



Editor, **DAVID C. WISLER (2008)**

Assistant to the Editor: **ELIZABETH WISLER**

Associate Editors

Gas Turbine (Review Chair)

A. J. STRAZISAR (2004)

Heat Transfer

T. ARTS (2005)

R. BUNKER (2006)

Structures and Dynamics

M. MIGNOLET (2006)

Turbomachinery

R. DAVIS (2005)

S. SJOLANDER (2005)

BOARD ON COMMUNICATIONS

Chair and Vice-President

OZDEN OCHOA

OFFICERS OF THE ASME

President, **HARRY ARMEN**

Executive Director, **VIRGIL R. CARTER**

Treasurer, **R. E. NICKELL**

PUBLISHING STAFF

Managing Director, Engineering

THOMAS G. LOUGHLIN

Director, Technical Publishing

PHILIP DI VIETRO

Production Coordinator

JUDITH SIERANT

Production Assistant

MARISOL ANDINO

Transactions of the ASME, Journal of Turbomachinery (ISSN 0889-504X) is published quarterly (Jan., Apr., July, Oct.) by The American Society of Mechanical Engineers, Three Park Avenue, New York, NY 10016. Periodicals postage paid at New York, NY and additional mailing offices. POSTMASTER: Send address changes to Transactions of the ASME, Journal of Turbomachinery, c/o THE AMERICAN SOCIETY

OF MECHANICAL ENGINEERS, 22 Law Drive, Box 2300, Fairfield, NJ 07007-2300.

CHANGES OF ADDRESS must be received at Society headquarters seven weeks before they are to be effective.

Please send old label and new address.

STATEMENT from By-Laws. The Society shall not be responsible for statements or opinions advanced in papers or ... printed in its publications (B7.1, Par. 3).

COPYRIGHT © 2004 by the American Society of Mechanical Engineers. For authorization to photocopy material for internal or personal use under those circumstances not falling within the fair use provisions of the Copyright Act, contact the Copyright Clearance Center (CCC), 222 Rosewood Drive, Danvers, MA 01923, tel: 978-750-8400, www.copyright.com. Request for special permission or bulk copying should be addressed to Reprints/Permission Department.

INDEXED by Applied Mechanics Reviews and Engineering Information, Inc. Canadian Goods & Services Tax Registration #126148048

Journal of Turbomachinery

Published Quarterly by ASME

VOLUME 126 • NUMBER 3 • JULY 2004



TECHNICAL PAPERS

- 333 Performance of Strongly Bowed Stators in a Four-Stage High-Speed Compressor (2003-GT-38392)**
Axel Fischer, Walter Riess, and Joerg R. Seume
- 339 A Numerical Investigation of the Flow Mechanisms in a High Pressure Compressor Front Stage With Axial Slots (2003-GT-38481)**
Ingo Wilke and Hans-Peter Kau
- 350 Advanced High Turning Compressor Airfoils for Low Reynolds Number Condition—Part I: Design and Optimization (2003-GT-38458)**
Toyotaka Sonoda, Yoshihiro Yamaguchi, Toshiyuki Arima, Markus Olhofer, Bernhard Sendhoff, and Heinz-Adolf Schreiber
- 360 Experimental Investigation of Unsteady Flow Field in the Tip Region of an Axial Compressor Rotor Passage at Near Stall Condition with Steroscopic Particle Image Velocimetry (2003-GT-38185)**
Baojie Liu, Hongwei Wang, Huoxing Liu, Hongjun Yu, Haokang Jiang, and Maozhang Chen
- 375 Numerical Investigation of Three-Dimensional Clocking Effects in a Low Pressure Turbine (2003-GT-38414)**
Andrea Arnone, Michele Marconcini, Alberto Scotti Del Greco, and Ennio Spano
- 385 The Effect of Real Turbine Roughness With Pressure Gradient on Heat Transfer (2003-GT-38738)**
Jeffrey P. Bons and Stephen T. McClain
- 395 Vortex Transport and Blade Interactions in High Pressure Turbines (2003-GT-38389)**
V. S. P. Chaluvadi, A. I. Kalfas, and H. P. Hodson
- 406 Aerodynamic Performance of a Very High Lift Low Pressure Turbine Blade With Emphasis on Separation Prediction (2003-GT-38802)**
Régis Houtermans, Thomas Coton, and Tony Arts
- 414 Experimental Surface Heat Transfer and Flow Structure in a Curved Channel With Laminar, Transitional, and Turbulent Flows (2003-GT-38734)**
P. M. Ligrani and C. R. Hedlund
- 424 Intermittency Transport Modeling of Separated Flow Transition (2003-GT-38719)**
J. Vicedo, S. Vilmin, W. N. Dawes, and A. M. Savill
- 432 Acoustic Resonance in Aeroengine Intake Ducts**
A. J. Cooper, A. B. Parry, and N. Peake

ANNOUNCEMENTS AND SPECIAL NOTES

- 442 Information for Authors**

(Contents continued on inside back cover)

This journal is printed on acid-free paper, which exceeds the ANSI Z39.48-1992 specification for permanence of paper and library materials. ™
 85% recycled content, including 10% post-consumer fibers.

The ASME Journal of Turbomachinery is abstracted and indexed in the following:

Aluminum Industry Abstracts, Aquatic Science and Fisheries Abstracts, AMR Abstracts Database, Ceramics Abstracts, Chemical Abstracts, Civil Engineering Abstracts, Compendex (The electronic equivalent of Engineering Index), Corrosion Abstracts, Current Contents, Ei EncompassLit, Electronics & Communications Abstracts, Energy Information Abstracts, Engineered Materials Abstracts, Engineering Index, Environmental Science and Pollution Management, Excerpta Medica, Fluidex, Fuel and Energy Abstracts, INSPEC, Index to Scientific Reviews, Materials Science Citation Index, Mechanical & Transportation Engineering Abstracts, Mechanical Engineering Abstracts, METADEX (The electronic equivalent of Metals Abstracts and Alloys Index), Metals Abstracts, Oceanic Abstracts, Pollution Abstracts, Referativnyi Zhurnal, Shock & Vibration Digest, Steels Alert

Performance of Strongly Bowed Stators in a Four-Stage High-Speed Compressor

Axel Fischer

Walter Riess

Joerg R. Seume

Turbomachinery Laboratory,
University of Hannover,
Appelstr. 9,
D-30167 Hannover, Germany

The FVV sponsored project "Bow Blading" (cf. acknowledgments) at the Turbomachinery Laboratory of the University of Hannover addresses the effect of strongly bowed stator vanes on the flow field in a four-stage high-speed axial compressor with controlled diffusion airfoil (CDA) blading. The compressor is equipped with more strongly bowed vanes than have previously been reported in the literature. The performance map of the present compressor is being investigated experimentally and numerically. The results show that the pressure ratio and the efficiency at the design point and at the choke limit are reduced by the increase in friction losses on the surface of the bowed vanes, whose surface area is greater than that of the reference (CDA) vanes. The mass flow at the choke limit decreases for the same reason. Because of the change in the radial distribution of axial velocity, pressure rise shifts from stage 3 to stage 4 between the choke limit and maximum pressure ratio. Beyond the point of maximum pressure ratio, this effect is not distinguishable from the reduction of separation by the bow of the vanes. Experimental results show that in cases of high aerodynamic loading, i.e., between maximum pressure ratio and the stall limit, separation is reduced in the bowed stator vanes so that the stagnation pressure ratio and efficiency are increased by the change to bowed stators. It is shown that the reduction of separation with bowed vanes leads to a increase of static pressure rise towards lower mass flow so that the present bow bladed compressor achieves higher static pressure ratios at the stall limit. [DOI: 10.1115/1.1649743]

Introduction

To optimize state of the art turbomachinery, it is necessary to control the flow in the end-wall regions. Therefore, the current development of new turbine and axial compressor blading is characterized by three-dimensional blading concepts. Leaned, bowed, and swept vanes are the subject in many numerical studies and wind tunnel experiments (e.g., [1–3]).

The characteristic features of a bowed vane are a positive lean angle at the hub and a negative lean angle at the shroud in comparison with a normal, radially stacked vane. The leaned vane induces radial forces on the fluid, so that at the acceleration part of the vane the streamlines are moved to the midspan section. At the deceleration part of the vane the streamlines are moved from the mid-span section towards the end walls. The loading of the flow in the end wall regions is reduced which can lead to lower end wall losses and reduce the tendency toward corner stall.

Joslyn [1] showed, that corner stall is one of the most important secondary flow-field effects in compressor stator vanes and that corner stall losses have great influence on overall losses. Breugelmanns [2] and Shang [3] showed with linear-cascade wind tunnel experiments, that corner stall can be reduced by leaned and bowed stator vanes. Because of the shift of mass flow towards the midspan section of the vane, the losses at midspan increased more than they decreased at the hub. Weingold et al. [4] demonstrated that a three-stage high-speed compressor, equipped with bowed stator vanes can increase pressure ratio and efficiency from the choke limit through surge conditions.

To study the effects of strongly bowed stator vanes on compressor performance and on the radial distribution of aerodynamic loading, the last two stages of the present test rig were equipped with strongly bowed stators, without change of the rotor blading and the vane count. The flow fields were measured by pneumatic

four-hole probes. On the suction and pressure side of the vane of the third stage, static surface pressures were measured to determine the local pressure distribution and to identify zones of separation. The performance map of the compressor with bowed vanes was determined and conditions of stall, choke, and best efficiency were identified at design speed. Detection of separation and of rotating stall were supported by unsteady pressure measurements. The effect of bow was predicted using commercial CFD codes. Pressure distributions, pressure rise and efficiency trends were predicted at design point and choke.

Modifications of Bowed Vanes

Figure 1 shows the stacking line of the bowed vane. The shift of stacking line is purely tangential. The lean angle at the hub is 35° , at the shroud it is 30° . At mid span, the vane is stacked radially. The vanes of the reference design are radially stacked over the entire span. Stagger angle and chord length of the bow vanes do not vary relative to the reference blades except of a small

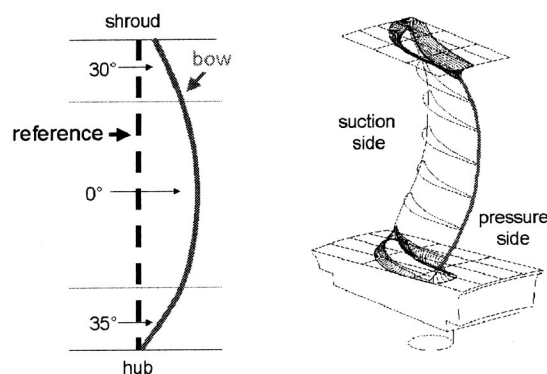


Fig. 1 Stacking line of bow vane and drawing of bowed stator 3

Contributed by the International Gas Turbine Institute and presented at the International Gas Turbine and Aeroengine Congress and Exhibition, Atlanta, GA, June 16–19, 2003. Manuscript received by the IGTI Dec. 2002; final revision Mar. 2003. Paper No. 2003-GT-38392. Review Chair: H. R. Simmons.

change at hub and shroud section which were twisted by 1 deg towards flow direction. The vane count of the reference design and the design with bowed vanes is equal.

Test Rig and Measurement Techniques

The test rig is driven by a 1300 kW DC motor. The compressor itself is a four-stage high-speed machine fully equipped with CDA blading. The maximum speed is 18,000 rpm, the design speed of the present tests is 17,100 rpm and the compressor generates an overall total pressure ratio of 2.65:1, [5]. **Figure 2** shows that the throttle of the compressor is located close to the last stage, so that the volume between outlet and throttle is small. This allows throttling the compressor until full-span rotating stall occurs without facing the risk of a low frequency surge.

The mass flow is metered by an orifice. The axial inlet flow conditions are measured by radially traversing with a Prandtl tube and a temperature probe. The outlet flow conditions and the flow field between the blade rows are measured by radially and circumferentially traversing with a pneumatic four-hole probe including

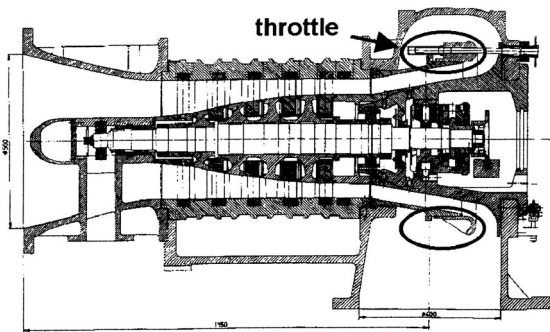


Fig. 2 4-stage axial compressor

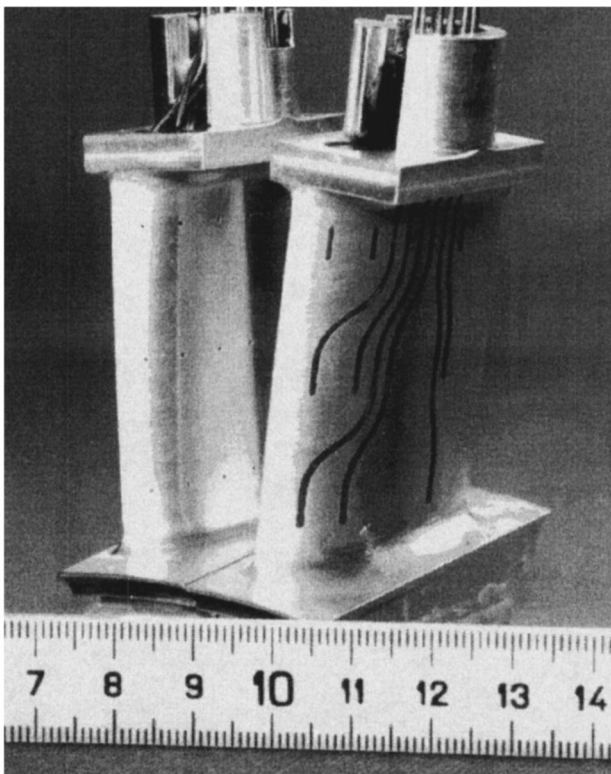


Fig. 3 Third stator instrumented reference vane

a temperature sensor. Efficiency and overall total pressure ratio are then computed from the flow field data. Static surface pressure distributions on the surface of the third stator are determined with instrumented vanes **Fig. 3**.

Static pressures at the casing are measured to determine the pressure ratios of the single blade rows and the stages. For investigations of stall inception and the initialization of full-span rotating stall, unsteady pressure transducers are installed in the casing and in an additional unsteady four-hole probe.

Three-Dimensional Navier-Stokes Computations

To investigate the effects of bowed blading numerically, the finite-volume based Navier-Stokes solver FINE™ Turbo by NUMECA International was applied. The complete compressor, including the inlet duct and the exhaust diffuser was meshed, **Fig. 4**, and the constant speed lines for the reference design and the configuration with bowed vanes were computed. The rotor/stator interaction was simulated by using quasi-steady mixing planes which average the flow properties at the rotor/stator interface, [6].

For symmetry reasons, only one pitch of every blade row needs to be computed. The inlet boundary is set to standard ambient conditions. At the compressor discharge, the static wall pressure is set. If this wall pressure is raised it is like closing the outlet throttle of the machine. For flow field analysis, the same planes are used as the probe traversing planes of the test compressor.

A portion of the mesh is shown in **Fig. 5**. Every single row is resolved with about 160,000 cells, including nine radial cell layers for the rotor tip clearance. The total compressor is meshed with 1.8 million cell volumes. The turbulence model is the algebraic Baldwin-Lomax model, because in comparison with multiple-equation models it is unsusceptible to numerical instability and accelerates the computation. The computation of one operating point takes half a day on a single-processor workstation equipped with a 750 MHz processor and 2.5 Gb memory.

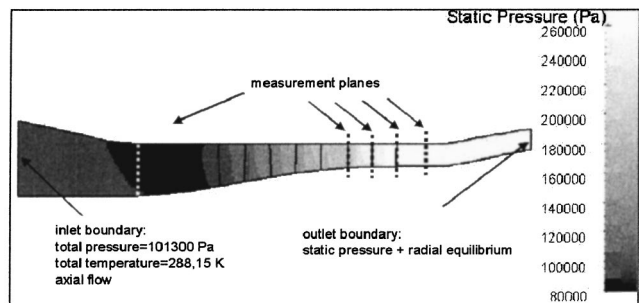


Fig. 4 Meridional view of the computational domain

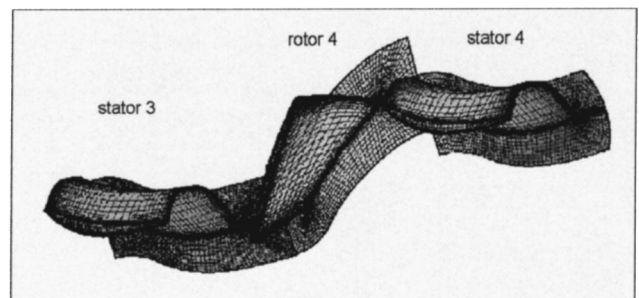


Fig. 5 Portion of the mesh

Results

Characteristics of the Present Axial Compressor. Figure 6 shows a typical constant-speed operating line of the present research compressor in terms of static pressure ratio. The static pressure ratio is the static outlet pressure divided by the static inlet pressure. Closing of the outlet throttle of the compressor leads to a rising static outlet pressure and a decreasing mass flow. Because the inlet dynamic pressure decreases with decreasing mass flow, the static pressure at the compressor inlet rises, if the inlet stagnation pressure is held constant as is the case for each constant speed operating line. While the static pressures behind each row of rotor blades and stator vanes, and at the outlet of the compressor rises up to the point at which the compressor stalls, the static pressure ratios of the individual stages and their product, the overall static pressure rise up to a maximum and then decrease as the outlet throttle is closed. Excessive aerodynamic loading of an airfoil generates such strong flow separation that turning is reduced, leading to a reduction of pressure ratio. Therefore, flow separation exists at the points of maximum static pressure ratio of single-blade rows and beyond towards the stall limit. Since the overall static pressure ratio is the product of the single-pressure ratios, its maximum indicates one or more blade rows with separated flow.

Depending on the system downstream of the compressor, rotating stall and/or surge occur at the left limit of the operation line, [7]. If the volume between compressor discharge and throttle can store enough compressed gas, the compressor will tend to surge at low frequency. If there is effectively no volume between the discharge and the throttle as in the present research compressor, a closing of the outlet throttle does not result in surge but in rotating stall. This property qualifies the present compressor test rig for investigations on flow separation and rotating stall without running the risk of damaging the rig.

Mechanism of the Bowed Vanes. At the front (acceleration) part of the suction side compressive normal blade forces act on the flow. In the case of positively leaned or bowed vanes, a radial component is superimposed on these forces which drives the flow towards the midspan section of the blade. Therefore, the flow near midspan of a bowed vane is faster than in the reference case while the velocity in the regions near the hub or shroud is reduced. At the aft (deceleration) part of the blade the fluid is driven from the midspan section towards the end walls by the suction normal blade forces. The higher acceleration in the front part at midspan implies a higher pressure rise and thus tends to cause separation in the deceleration part. Near the end walls, the effect is vice versa: The adverse pressure gradient in the deceleration part of the suction side is reduced and so is the tendency towards separation. In particular near the hub, the tendency toward corner stall is reduced.

The mechanisms of bow in a vane are demonstrated by stator 3 because the vanes of stator 3 have pressure taps. Figure 7 shows

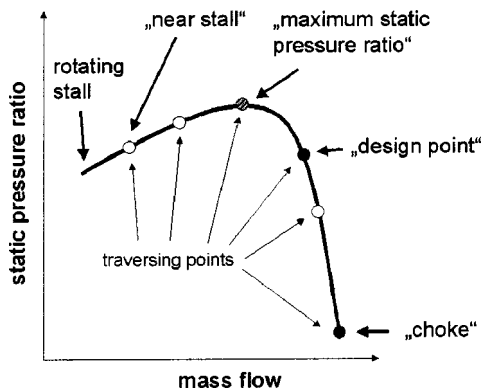


Fig. 6 Characteristic of the present axial compressor

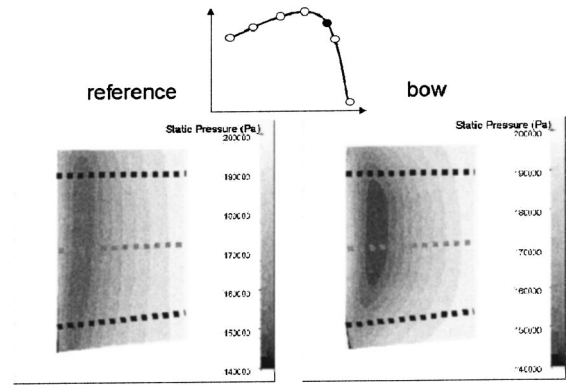


Fig. 7 Pressure distribution on suction side of stator 3

the computed static pressure distribution on the suction side of the reference and the bowed vane of the third stator at the design point. The dark gray and black zones indicate low pressure due to high acceleration. The flow is thus deflected from the end wall toward midspan in the front portion of the blade. The dotted lines in Fig. 7 represent 15%, 50% and 85% span. The relevant operating point is indicated in the pressure ratio versus mass flow diagram (from Fig. 6) in Figs. 7 through 11. In Figs. 8 and 9, the computed and measured (normalized with compressor discharge pressure) surface pressure distributions of the reference and the bow blading are shown for these three spanwise locations. In comparison with the reference vane, the acceleration at the front

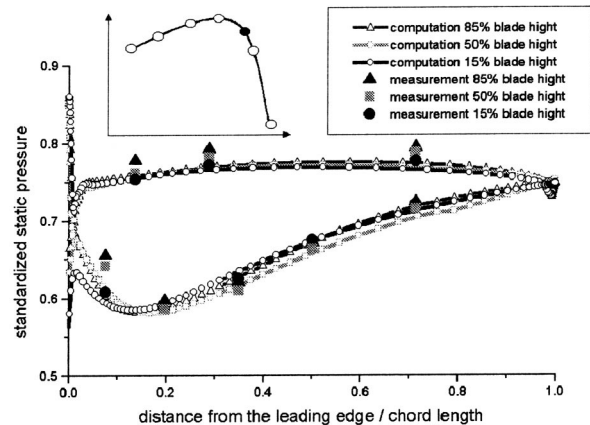


Fig. 8 Normalized surface pressure on the reference vane

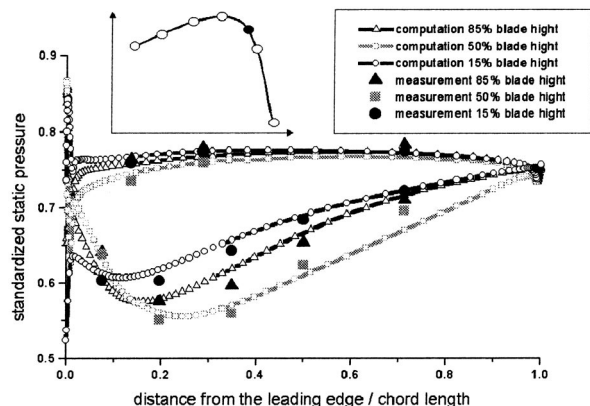


Fig. 9 Normalized surface pressure on the bowed vane

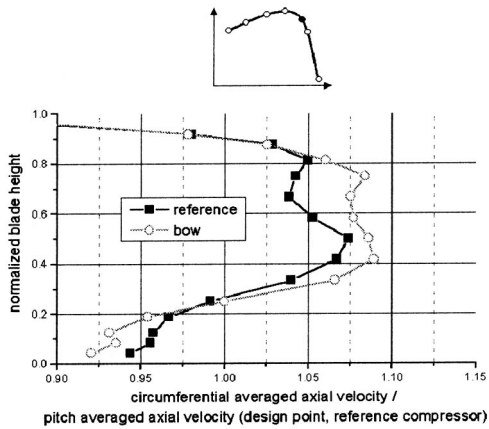


Fig. 10 Circumferentially averaged axial velocity at design point

portion of the bowed vane mid-span section increases while the acceleration is reduced in near wall zones of the bowed vanes when compared to the reference vane. This effect of reduced pressure decrease is more pronounced near the hub because of the lesser bow angle and the greater pitch to chord ratio at the shroud. Downstream from the pressure minimum on the suction side, the flow is decelerated and the pressure rises. In this deceleration area, where flow separation occurs if the gradient of pressure rise becomes too large, the gradient at mid span is increased by the bow while the gradient near the hub zone is decreased by bow.

Figure 10 shows the effect of bow in stator 3 on the axial velocity in the axial gap between stator 3 and rotor 4 at the design point. The values of velocities are circumferentially averaged from a 15×15 point traversing grid covering one pitch by a pneumatic four-hole probe which includes a thermocouple. Due to the higher acceleration at the mid span of the bowed vane, which causes a shift of mass flow towards mid span, the axial velocity at midsection of the duct increases, while the axial velocity near the hub decreases as a result of the lower acceleration here. Because of the higher axial velocities at midspan of the bowed vane the incidence angle at the inlet of the following rotor blade will decrease and the aerodynamic loading of the rotor will be reduced.

In summary, stator 3 shows two exemplary main effects of bowed vanes. Because the pressure rise from minimum pressure to trailing edge pressure of the bow-bladed near-hub section is less, the tendency towards separation is reduced. Near midspan, conversely the tendency towards flow separation increases. The second effect of bow on stator 3 is a displacement of mass flow from the near-wall zones towards the core flow zone in the decel-

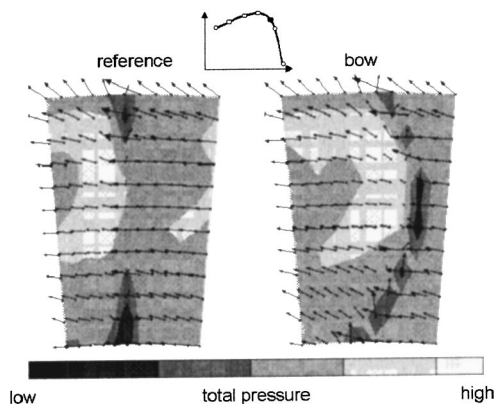


Fig. 11 Flow field downstream of stator 4, “design point”

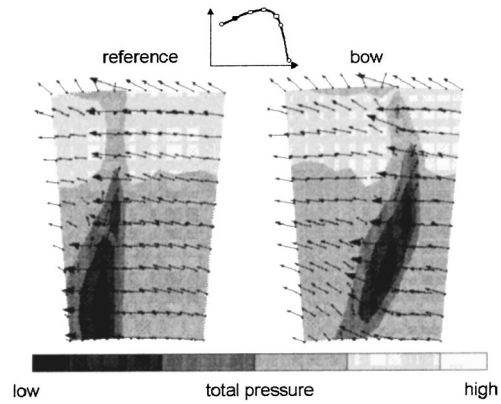


Fig. 12 Flow field downstream of stator 4, “near stall”

eration (aft) portion of the vane, resulting in a lower axial velocity of the near wall zones and a higher axial velocity in the mid section in the following axial gap at the design operating point.

Effects of the Present Bow on the Flowfield. **Figure 11** and **Fig. 12** show the results of flow field traverses on a 12×12 point grid for the reference and the bowed vane downstream of the fourth stator at different operation points. **Figure 11** is a plot of total pressure levels and velocity vectors at the design point of the compressor. **Figure 12** shows the same diagram at an operating point near stall. High values of total pressure show zones of undisturbed flow, low values of total pressure show zones of high losses like boundary layers, wake regions, or zones of separation.

At the design point, zones of losses are small. At the hub and the shroud of the reference design, small regions of thick boundary layers or small separation zones occur. These zones are reduced in the bowed stator vanes. The distinction of momentum deficit due to boundary-layer losses, separation losses, and wake losses was made in the present study by repeated flow field measurements along the complete constant-speed operating line from choke to stall. The plots are not shown here due to space constraints. In the near stall operation point big separation zones can be seen in both, the reference and the bowed vane designs.

In the reference blading, corner stall extends from the hub through midspan. In the bowed blading, the loading of the vane and therefore the separation is shifted from the hub towards midspan. This separation zone is removed from the hub so that there is no merging of corner stall separation with the separation on the suction side of the blade. The pitch-averaged value of total pressure of the bowed vane becomes higher, as indicated by a performance map. The effect of moving the loading and separation towards mid span is smaller in the third stator. Flow field data of the third stator are not shown in this paper. In the third row of vanes, the loading and the shape of separation zones is also moved towards midspan but in contrast to stator 4, the separation at the hub and the corner stall is not suppressed but merely reduced.

Effects of the Present Bow on Stage and Blade-Row Performance. **Figure 13** shows the static pressure rise of each stage in the reference and the bowed vane configuration at design speed. All values in **Figs. 13–17** were normalized with the design point conditions of the reference compressor. For the bowed configuration the pressure rise shifts such that the pressure rise of the stage 4 with bowed vanes increases while the pressure rise of stage 3 with bowed vanes decreases when compared with the reference design. The loss of pressure rise in bowed stator 3 and stage 3 is affected by the shift of mass flow to mid span and by the resulting higher velocity level in the midspan section which in turn results in lower deceleration. The higher axial velocity in the core flow at the outlet plane of stator 3 reduces the incidence inlet flow angle of rotor 4 at midspan and so effects a lesser loading of rotor 4. The

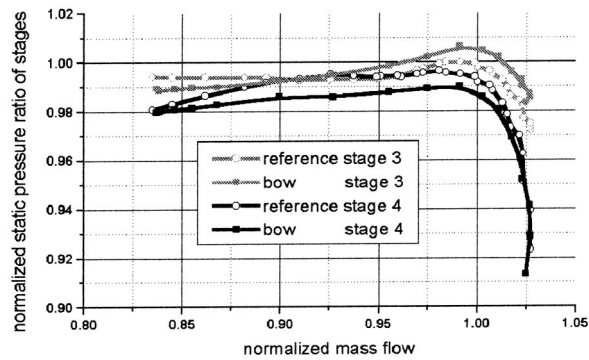


Fig. 13 Stage static pressure ratio of the reference and the bowed design

incidence flow angle of stator 4 increases which leads to an increased pressure ratio for the bowed stator 4 when compared with the reference. This effect decreases for decreasing mass flow, presumably because the acceleration zone of stator vanes becomes smaller for lower mass flow due to increasing inlet incidence angle.

Figure 14 shows the pressure ratio of the individual vanes of stator 3 and stator 4. The relative changes of the constant speed lines show the effects of the bowed stator vanes on the stator characteristic which are caused by the reduced separation. After passing the point of maximum pressure ratio towards lower mass flow, the loss of pressure ratio is reduced for the bowed stator vane 3 compared to the reference design. This is achieved by a reduction in flow separation. The loss of pressure ratio of stator 4,

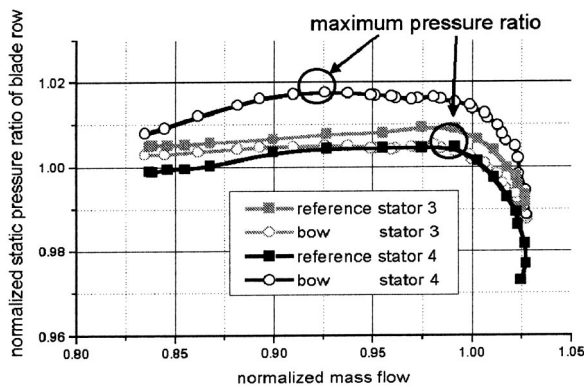


Fig. 14 Static pressure ratio of reference and bowed stator vanes 3 and 4

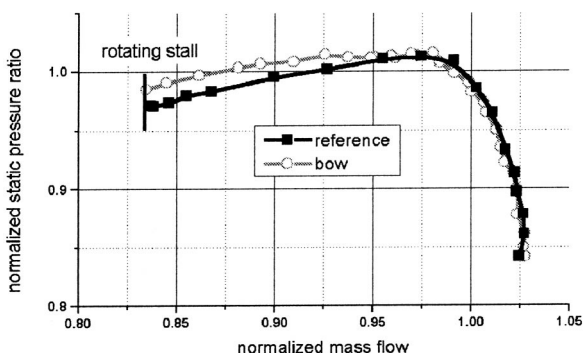


Fig. 15 Overall static pressure ratio

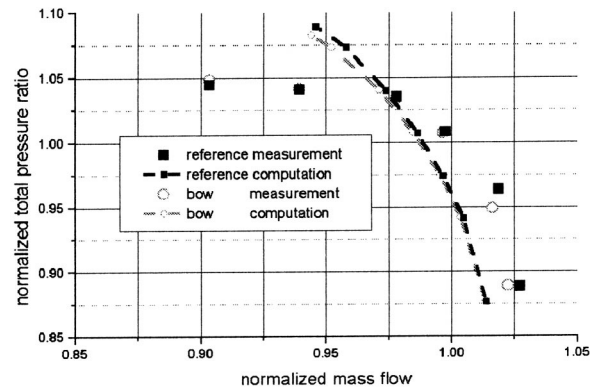


Fig. 16 Overall total pressure ratio

in which the corner stall was not just reduced but removed, is not just reduced but the point of maximum pressure ratio is also moved towards lower mass flow.

Effects of Bow on Compressor Performance. Figure 15 shows the static pressure ratio of the reference and the bowed compressor blading. The pressure ratio at constant speed of the bowed stator is reflected in the characteristics of the overall compressor. Beyond the maximum pressure ratio towards lower mass flow, the decrease of static pressure ratio is reduced by bow. From a normalized mass flow of 0.975 to 0.925, the constant speed line of the compressor with bowed vanes runs almost horizontal, indicating that the reduction of flow separation by the bowed vanes results in a higher static pressure rise if the machine is highly loaded. At a mass flow of 0.83, stable operation of the compressor is limited. Exceeding this limit leads to rotating stall, initialized in the first stage, [8]. Since the first stage is initializing the rotating stall, the bowed vanes do not affect this limiting mass flow. At the stall limit, the pressure rise of the bow-bladed compressor exceeds the pressure rise of the reference compressor by 1.4%.

Figure 16 shows the measured and computed overall total pressure ratio characteristic of the compressor at design speed with the reference and the bowed vane design. Figure 17 shows the corresponding isentropic efficiencies. The left-most measurement points (at normalized mass flow=0.9) in Fig. 16 and Fig. 17 are the last operating points where the flow probe could be traversed without the risk of initiating compressor instability by the blockage, caused by the probe itself. The relative error (in terms of 95%-confidence intervals) for mass flow is $\pm 0.5\%$. The relative error for total pressure is $\pm 0.32\%$ and for efficiency it is $\pm 0.4\%$ age points. From choke (normalized mass flow=1.025) to the

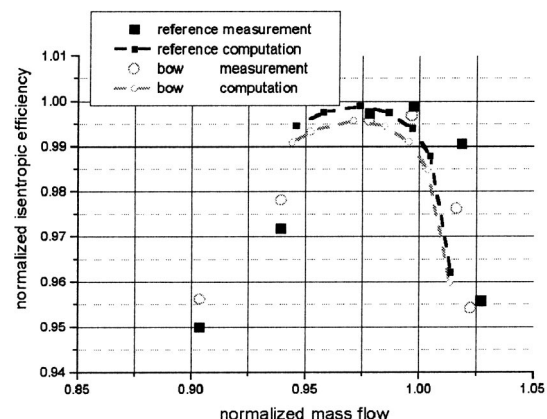


Fig. 17 Isentropic efficiency

point of maximum static pressure ratio (normalized mass flow = 0.975), the total pressure ratio and isentropic efficiency of the reference compressor is higher. At the point of maximum static pressure ratio, the measured lines overlap. From the point of maximum static pressure to the highly loaded point near stall (normalized mass flow = 0.9), the total pressure ratio and isentropic efficiency of the compressor with bowed vanes is higher by comparison. If not highly loaded, the higher losses of the bowed vanes are plausible, considering that the surface area of the bowed vane is about 7.5% larger in comparison with the basic vanes. The higher isentropic efficiency and overall total pressure of the bowed blading, when it is highly loaded, confirms the flow field measurements which showed reduction of the corner stall (Fig. 12).

The constant-speed lines of the Navier-Stokes computations show, in comparison with the measurements, a displacement towards lower mass flow of about 1.5%. The loss of isentropic efficiency and overall total pressure of the bowed vane design compared to the reference compressor from choke to the point of maximum static pressure rise match the measured results. The left-most points of the computations represent the respective points of maximum static pressure rise for each constant speed line. As described above, the static pressure defines the outlet boundary of the computation. If the static pressure at the outlet boundary is raised further, the computation becomes unstable. Figures 16 and 17 show that the computed overall total pressure rise and the isentropic efficiency to the left side of the measured point of maximum pressure ratio are too high, respectively. This failure is caused by the inability of the present computation to capture the separated flows in the last stator rows. Before the onset of the separation in the vanes, the computations become unstable.

Conclusions

Numerical and experimental results show that through a 35 deg bow angle at the hub and a 30 deg bow angle at the shroud, bowed stator vanes shift the flow from the near-wall regions to the midspan of the vanes in the front portion of the vanes. This leads to lower loading near the wall at the deceleration portion of the vane and reduces or eliminates corner stall at the hub, when compared with the reference, i.e., the radially stacked blade design. At the shroud, the effect is insignificant, because for conventional compressor designs, separation first arises at the hub. The higher loading of the midspan section of the bowed vane leads to earlier separation in this area. The increase of mass flow and thus the increase of axial velocity at midspan of stator 3 leads to a lesser loading of the following rotor 4 and to a shift of static pressure rise from stator 3 to the last stator 4.

The reduction of separation leads to an increase in overall static pressure rise, total pressure rise, and overall efficiency, when the compressor is highly loaded. For moderate loading, the static pressure rise does not change in comparison with the reference

blading design but efficiency is reduced because of higher friction losses caused by the larger in surface area of the bowed vanes. The constant-speed operating lines of bowed stators change so that in the case of stator 3, the decrease of static pressure ratio is reduced for high loading. In case of stator 4, the maximum static pressure ratio moves to lower mass flow for bowed vanes. At the stall limit, the static pressure rise of the bow-bladed compressor exceeds the static pressure rise of the reference compressor by 1.4%. In future engine designs, this effect can be used to move the surge limit towards higher static pressures. The loss of efficiency may be compensated by reducing the number of vanes which then need to achieve a higher pressure rise, which, as shown above, can be achieved by bowed vanes.

Acknowledgments

This report is the scientific result of a research project, sponsored by the FVV ("Forschungsvereinigung Verbrennungskraftmaschinen e.V." = Combustion Machinery Research Association, Frankfurt, Germany) and carried out at the Turbomachinery Laboratory, University of Hannover, Germany, under the direction of first Prof. W. Riess and then Prof. J. R. Seume. This work was partially (50%) financed by the German Ministry for Economics (BMWi) through the Society for Industry Research (AiF), (AiF-Nr. 067370).

The FVV would like to thank the initiator Prof. Riess, the advisor Prof. Seume, and the research assistant A. Fischer for the completion of the present project.

The authors would like to thank Bernhard Kuesters, Siemens Power Generation, Muelheim, for giving helpful advice and for guiding the working group "FVV Bow-Blading" and Uwe Schmidt-Eisenlohr, MTU Aero Engines, Munich, for the aerodynamic design of the compressor blading and for giving helpful advice.

References

- [1] Joslyn, H. D., 1985, "Axial Compressor Stator Aerodynamics," *ASME J. Eng. Gas Turbines Power*, **107**, pp. 484–493.
- [2] Breugelmans, F. A. H. et al., 1984, "Influence of Dihedral on the Secondary Flow in a Two-Dimensional Compressor Cascade," *ASME J. Eng. Gas Turbines Power*, **106**, pp. 578–584.
- [3] Shang, E. et al., 1993, "The Experimental Investigations on the Compressor Cascades With Leaned and Curved Blade," *ASME*, Paper No. 93-GT-50.
- [4] Weingold, H. D. et al., 1995, "Reduction of Compressor Stator Endwall Losses Through the Use of Bowed Stators," *ASME*, Paper No. 95-GT-380.
- [5] Walkenhorst, J., 2000, "Axialverdichter mit Wandkonturierten Leitschaufeln—Prüfstandsentwicklung und Strömungsuntersuchung," Ph.D. thesis, University of Hannover, Germany and VDI-Bericht Reihe 7, Nr. 390, Duesseldorf, Germany.
- [6] NUMECA Int., 2000, "Numeca's Flow Integrated Environment for Turbomachinery and Internal Flows," User Manual, Numeca Int., Brussels, Belgium.
- [7] Cumpsty, N. A., 1989, *Compressor Aerodynamics*, Longman Singapore Publishers Ltd., Singapore.
- [8] Hellmich, B. et al., 2002, "Estimation of the Rotating Stall Frequency From Rotor Frequency and Common Blade Number Integer Fractions in a Four Stage Axial Compressor," *Sixth Int. Conf. On Rotor Dynamics, Proceedings*, Vol. II, Sydney.

A Numerical Investigation of the Flow Mechanisms in a High Pressure Compressor Front Stage With Axial Slots

Ingo Wilke

Hans-Peter Kau

Technical University of Munich,
Ballmannstr. 15,
Garching 85747, Germany

This paper describes the impact of axial slots on the flow field in a transonic rotor blade row. The presented results are completely based on time-accurate three-dimensional numerical simulations of a high pressure compressor front stage with and without casing treatment. Two different axial positions of a casing treatment consisting of axial slots were tested for their impact on flow stability and efficiency. The first tested position (configuration 1) was chosen in a conventional way. The slots extend approximately from the leading up to the trailing edge of the rotor blades. As expected, the simulations of the compressor stage with this configuration showed a significant increase in flow stability near surge compared to the solid wall case. However, a non-negligible decrease in efficiency is also observed. Analyses of flow interactions between casing treatment and rotor blade rows under transonic conditions lead to the general conclusion that the stabilizing effect of circumferential grooves or axial slots mainly results from their impact on the tip leakage flow and its resulting vortex. A characteristic vortex inside the slots is observed in the simulations with the conventionally positioned casing treatment. This vortex removes fluid out of downstream parts of the blade passage and feeds it back into the main flow further upstream. The resulting impact on the tip leakage flow is responsible for the increased flow stability. However, the interaction between the configuration 1 casing treatment flow and the blade passage flow results in a significant relocation of the blade passage shock in the downstream direction. This fact is a main explanation for the observed decrease in compressor efficiency. A second slot position (configuration 2) was tested with the objective to improve compressor efficiency. The casing treatment was shifted upstream, so that only 25% of the blade chord remained under the slots. The simulations carried out demonstrate that this shift positively affects the resulting efficiency, but maintains the increased level of flow stability. A time-accurate analysis of the flow shows clearly that the modified casing treatment stabilizes the tip leakage vortex and reduces the influence on the flow inside the blade passage. [DOI: 10.1115/1.1731465]

Introduction

In highly loaded transonic compressor stages, with sufficient solidity to prevent an aerodynamic overloading of the rotor blades near surge, flow mechanisms inside the tip leakage and the resulting tip leakage vortex seem to be responsible for the loss of flow stability under stall conditions. Measurements and CFD simulations of several authors indicate that the tip leakage vortex in the rotor blade passage undergoes a dramatic change in topology if the compressor stage is operated near surge (Furukawa [1], Schlechtriem [2], Hofman [3], Wilke [4], and Hoeger [5]). Position, extension, and behavior of the tip leakage vortex directly depend on the loading of the compressor stage. As long as the compressor stage is loaded with moderate pressure ratios the tip leakage vortex is well structured and passes through the blade passage shock without significant effects. However, if the pressure ratio is increased above a certain limit a breakdown of the tip leakage vortex is observed. Detailed CFD simulations of transonic compressor stages indicate that high friction losses inside the vortex core are mainly responsible for this observed behavior (Wilke [4]). The vortex breakdown is equivalent to the onset of a local stagnation zone in the outer blade passage. Low-energy fluid,

which can not be transported through the pressure barrier of the passage shock, gets caught inside this stagnation zone. Low-energy fluid mainly results from the upstream tip leakage flow. Under stable conditions, the fluid inside the stagnation zone continuously becomes re-energized by mixing and diffusion effects with the high-energy main flow. This energy input prevents the breakdown area from a continuous expansion. At surge, however, this balance is severely disturbed. Therefore, more low-energy fluid flows into the stagnation zone than can be re-energized. Consequently the volume of the breakdown area grows rapidly. The resulting blockage finally causes vast flow separations in the rotor blade row and leads to compressor stall.

Experiments and CFD simulations demonstrate that casing treatments are able to delay stall, if flow mechanisms in the casing boundary layer and the tip leakage are responsible for the onset of instabilities (Greitzer [6], Crook [7], Wilke [4], Qing [8], Rabe [9], and Ghila [10]). In general their stabilizing effects can only be realized with a significant decrease in compressor efficiency. So far only few configurations are known which, under certain conditions, are able to delay stall without a negative impact on compressor efficiency (e.g. Qing [8] and Thompson [11]). In these cases the interaction between the casing treatment, the blade passage flow and the tip leakage has not yet been fully understood. At this point it has also not been explained in detail, in which important flow mechanisms these casing treatments differ from other configurations.

Contributed by the International Gas Turbine Institute and presented at the International Gas Turbine and Aeroengine Congress and Exhibition, Atlanta, GA, June 16–19, 2003. Manuscript received by the IGTI Dec. 2002; final revision Mar. 2003. Paper No. 2003-GT-38481. Review Chair: H. R. Simmons.

The presented results are based completely on numerical simulations and refer only to conditions of design speed. The impact of the slots at off design speeds has not yet been investigated.

Investigated Compressor Stage and Casing Treatments—Description of the CFD-Model Used for the Simulation

The investigated compressor stage is a transonic front stage of a modern high pressure compressor (HPC). At the design point the total pressure ratio of the front stage is 1.6 and the relative Mach number at the rotor tip is about 1.4. The modeled tip clearance of the rotor blades is about one percent of the axial tip chord length.

All presented results are based on three-dimensional, unsteady Reynolds-averaged CFD simulations. In order to conserve computational time, the modeling of the HPC front stage was reduced to a single rotor blade passage. Detailed steady-state simulations conducted during previous investigations (Wilke [4]) indicated that the exit stator row has little influence on the basic near stall flow mechanisms. Hence, the influence of the stator has been completely neglected in the presented simulation. A simplified exit condition defined by a circumferentially averaged static outlet pressure in radial equilibrium was used instead. As opposed to the stator blade row, the inlet guide vane (IGV) was substituted by boundary conditions calculated from steady state simulations of the complete HPC front stage. The IGV exit conditions were defined by circumferentially averaged radial profiles for total pressure, total temperature and the vector components of the velocity direction. In contrast to the original compressor stage, the IGV exit conditions were applied at about 1.1 times the axial tip chord length further upstream, measured from the leading edge of the rotor blade. These inlet conditions were kept constant for all simulated configurations and operating points. The ratio between rotor blade frequency and the acoustic transit time from the leading edge of the rotor blade to the upstream boundary is about 1 and from the trailing edge to the outlet boundary about 0.5.

The commercial solver NUMECA/EURANUS was used for the simulations. The integration in time is implemented in the implicit pseudo-time scheme. For the time-accurate simulation, 37 physical time steps per blade passage and 40 pseudo-time iterations with a CFL number of 3 within each physical time step, were performed. Single test runs with 67 physical time steps were carried out in order to prove that 37 time steps are enough to resolve all important information and give a time step independent solution. The algebraic Baldwin-Lomax model was used to introduce turbulence. The computation of at least one rotation of the rotor stage was necessary for each operating point in order to achieve convergence in the simulation runs. This time period was sufficient to distinguish stable operating points from unstable conditions at stall up an accuracy of 2500 Pa in static back pressure. Numerical stall appears as a transient flow field characterized by a continuous decrease in mass flow, total pressure ratio and efficiency. In the simulations, numerical stall was never a purely numerical phenomenon, but arose always from physical consequences due to distinctive flow mechanisms.

A block structured topology consisting of H-blocks for the inlet and outlet and a main O-block (surrounding the rotor blade) was used to model the rotor blade passage (Fig. 1). The whole rotor mesh—without casing treatment—consists of approximately 10^6 grid points. 81 grid points were used to model the blade passage in the spanwise as well as in the blade-to-blade direction. The O-grid has 241 grid points in the circumferential direction to ensure a high quality mesh at the leading and trailing edge of the rotor blade. The tip clearance is modeled by 17 grid points in the radial direction. Because of the low Reynolds description of the boundary layer in the Baldwin-Lomax model used, the mesh was stretched towards the solid boundaries in order to meet the resolution requirement of $y^+ \leq 2$. The meshing used proved to produce grid independent results in steady state simulations. So far, no detailed grid refinement studies have been carried out for the un-

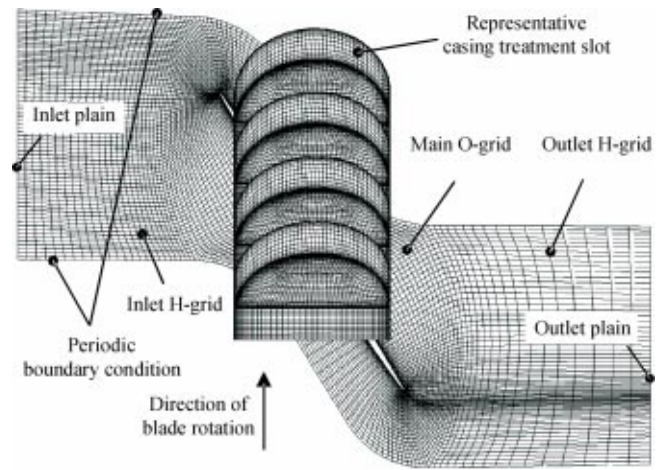


Fig. 1 Grid for blade passage and casing treatments

steady case due to massive computing time requirements. However, the authors believe that this meshing is suitable for unsteady simulations as well.

Figure 2 shows a representation of the design of the tested casing treatments. They consist of four identical axial slots per blade passage and have an open area of 50% in the circumferential direction. The slots are parallel to the rotation axis of the rotor and are inclined by 45 deg against a meridional plane in the direction of blade rotation. The slot shape is designed as a semicircle. In configuration 1, the position of the slots is centered above the rotor blade tip reaching from 7.5% to 92.5% of the chord length. In configuration 2, the slots are moved upstream so that only 25% of the blade chord length remains covered by the casing treatment. The slots have a butterfly topology and consist of 25 grid points in azimuthal and 57 grid points in main flow direction.

Considerations Relative to the Design of the Tested Casing Treatments

With its design and position casing treatment 1 represents a well-known type of casing treatment. This type has a significant stabilizing impact on rotor flows as shown by several authors (Fujita [12] and Takata [13]). The shape of the tested slots was designed as a semicircle. This was done to improve flow circulation inside the treatment by avoiding unnecessary stagnation zones. Experiments demonstrate that a slope of the slots in direction of blade rotation enhances the resulting effectiveness (Fujita [12] and Takata [13]). The authors believe that this behavior can be explained by an improved interaction with the tip leakage flow. Based upon this knowledge the slope of the tested casing treatment was set preliminarily to 45 deg. At this point literature available to us does not give any specific information about the number of slots per passage, the slot height or slot width for a given compressor configuration in order to achieve optimum results. For that reason configuration 1 was designed as a preliminary configuration with “average” geometric parameters. A main consideration was to reduce computation time as much as possible by choosing a small number of slots per blade passage. The intention of simulating treatment 1 was, in addition to the investigation of important flow mechanisms, a qualitative validation of the unsteady CFD computations. The simulations clearly demonstrate that this model is able to reproduce the stabilizing effect that was expected based upon the corresponding experiments. Numerical results at design speed indicate for casing treatment 1 a lowering of stalling mass flow by 20% and a decrease in maximum effi-

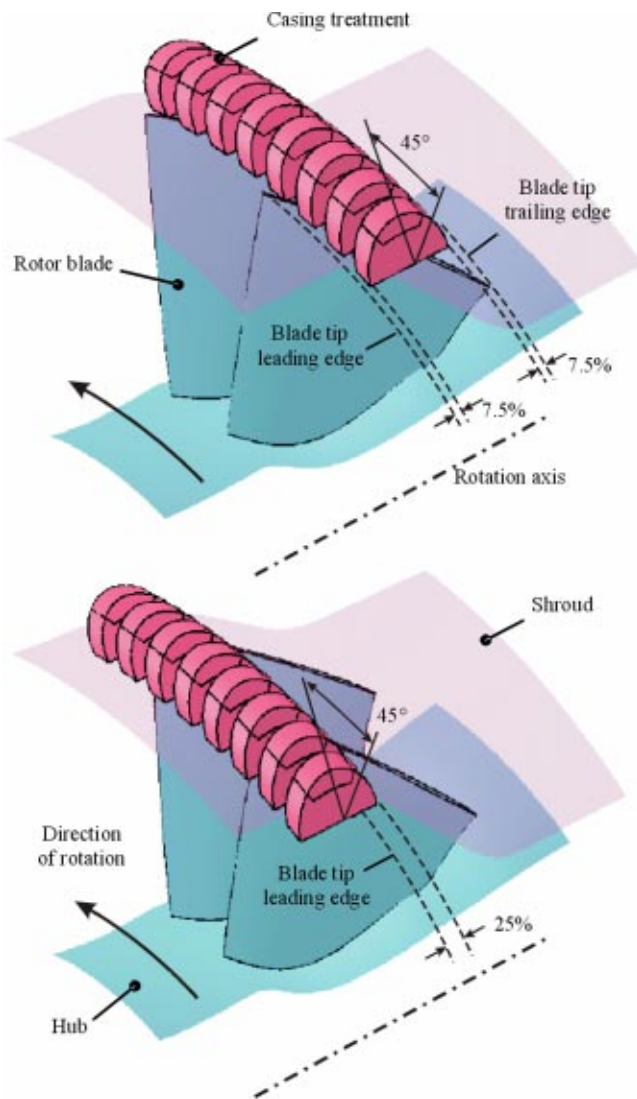


Fig. 2 Tested configurations of axial slots

ciency by 4%. This is in good correlation with experimental data from similar casing treatment designs (Fujita [12] and Takata [13]).

The authors believe that the stabilizing impact of casing treatments is mainly based on their impact on the tip leakage flow and its resulting vortex. The simulations show that especially the front part of the tip leakage flow is very significant for the stability of the tip leakage vortex. This can be concluded from the distribution of relative velocity inside the tip clearance (Fig. 3, Wilke [4,14]). It is, therefore, obvious, that manipulating the complete tip gap would not be more effective than simply using the high energy leakage flow near the leading edge. Moreover, slots reaching from the leading to the trailing edge of the rotor blades will unnecessarily increase the resulting leakage flow from downstream high-pressure areas. To improve this situation, a shift of the slots in the upstream direction would be an appropriate alternative. The modified casing treatment is expected to increase the flow stability and at the same time to improve the efficiency level. The criterion for the relocation was the distribution of the flow velocity inside the tip clearance for the solid wall case. Detailed simulations indicate that the highest velocities occur in the first 25% of the tip chord for the investigated rotor blade row (Fig. 3). Downstream of this location, the level of velocity reduces rapidly.

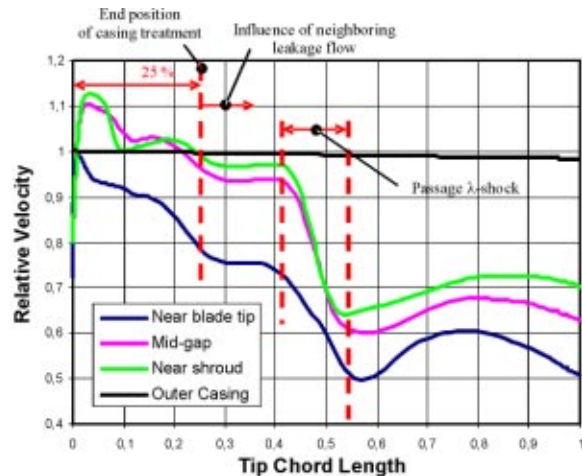


Fig. 3 Relative tip leakage velocity near stall for the solid case

At this point no optimization studies have been performed on the slots in configuration 1 and 2. Therefore, they are expected to have significant potential for further improvement. Possible geometric variables for a parametric study could be the position of the slot leading edge, the number of slots per passage and the slot height and width.

Flow Mechanisms Inside the Rotor Without Casing Treatment

The characteristics and mechanisms of the tip leakage flow and its resulting vortex have already been analyzed by several authors (Wilke [4], Gerolymos [15], and Hofmann [3]). For that reason, the investigation and description of the flow in the rotor stage without casing treatment will concentrate only on such phenomena that are essential to understand the impact of the tested casing treatment configurations on compressor flow stability.

Important Properties of the Tip Leakage Flow. The tip leakage flow can be seen mainly as a pressure enforced phenomenon driven by the pressure difference between the pressure and the suction side at the rotor blade tip. Therefore, the tip leakage flow is most intensive at operating points near stall where the aerodynamic blade loading reaches a maximum. The flow velocities inside the tip clearance continuously increase in the direction of the blade leading edge where the most intensive tip leakage flow occurs. This fact can be shown to have a negative impact on the losses inside the resulting tip leakage vortex and hence its stability (Wilke [4]). Usually, the radial tip gap extension is smaller than the overall thickness of the casing boundary layer. For that reason the tip leakage flow is never an isolated mechanism, but is always overlaid by the casing boundary layer. The properties of this boundary layer are essential for the behavior of the tip leakage flow and its resulting vortex. In particular, the axial velocity component of the boundary layer is very significant because this component is responsible for turning the upstream orientated tip leakage flow in the downstream direction.

In a similar way, mechanisms of the free main flow are superimposed upon the casing boundary layer near the blade tip. In particular, the blade passage shock does not appear in the following figures as clearly as it would in an inviscid flow. Near the blade tip, typical λ -shocks are observed instead.

Properties and Topology of the Tip Leakage Vortex. The tip leakage vortex develops from a rolling-up of the leakage flow after interacting with the incoming casing boundary layer. The rotation of the leakage vortex results in the formation of a characteristic trough in the static pressure distribution (Figs. 4 and 5).

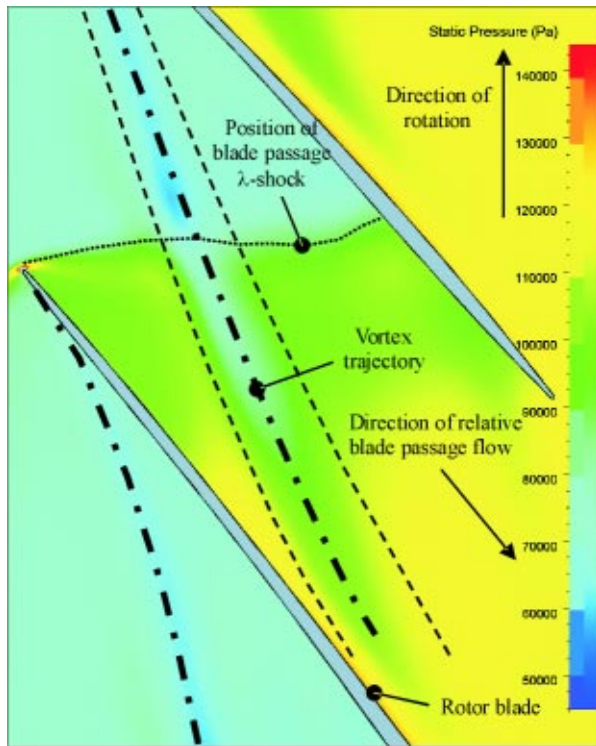


Fig. 4 Static pressure in the blade passage at maximum efficiency

This trough indicates the vortex trajectory. CFD simulations show that the flow velocities inside the vortex core rapidly decrease in the direction of the vortex trajectory. This can be explained by massive friction effects due to high gradients in the distribution of

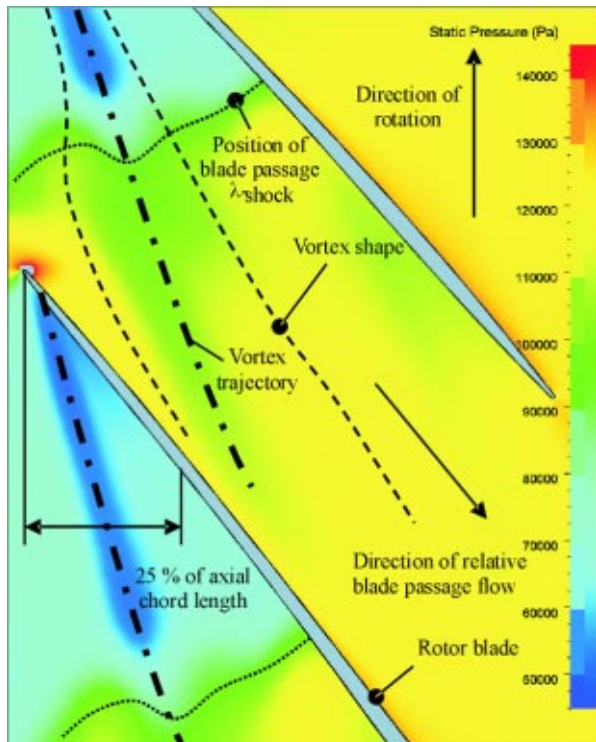


Fig. 5 Static pressure in the passage near blade tip at the onset of vortex breakdown

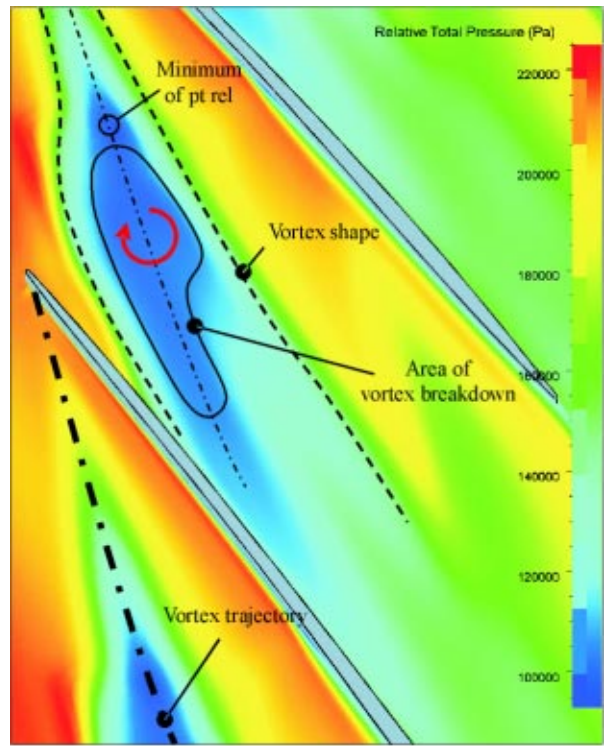


Fig. 6 Relative total pressure in the passage near blade tip at the onset of vortex breakdown

the angular velocity inside the vortex (Wilke [4]). The high gradients of angular velocity are the consequence of the distribution of the leakage flow velocity inside the tip clearance (highest at the leading edge and lowest at the trailing edge). The higher the velocities of the leakage flow are, the more intensive the friction losses inside the leakage vortex will be. It is obvious from Fig. 3 that the high-velocity zone in the first 20–30% of the blade chord has a dominating impact on the resulting losses. An appropriate method for the evaluation of losses inside the rotor flow is the computation of the total pressure in the relative system of the rotor. This value is highest at rotor inlet and losses of any kind cause a reduction of this initial value. In Fig. 6 the formation of a significant trough in the distribution of the relative total pressure is illustrated for an operating point at the onset of vortex breakdown. Figures 4–6 show pressure contour plots within the subsonic casing boundary layer. For that reason no losses occur in Fig. 6 at the location of the passage λ -shock. It is obvious from Fig. 6 that the losses in the rotor flow mainly concentrate in the vortex core and increase in the direction of the vortex trajectory. The relative total pressure reaches a minimum shortly ahead of the blade passage shock. If the compressor is operated at higher pressure ratios, the value of the relative total pressure in this minimum zone can even go beyond the level of the static pressure behind the passage shock (see Figs. 5 and 6). This lack of energy blocks the core part of the leakage vortex from passing through the pressure barrier of the blade passage shock. As a consequence the vortex core breaks down and the onset of a stagnation zone is observed. Low-energy fluid, which can not be transported through the blade passage shock, gets caught inside this stagnation zone. Under stable flow conditions the fluid inside the stagnation zone continuously gets re-energized by mixing and diffusion processes between the core and outer parts of the vortex. This energy input prevents the breakdown area from continuous expansion. At surge, however, the re-energizing effects are no longer sufficient to dampen an expansion of the stagnation zone. Hence, more low-energy fluid flows into the stagnation zone than can be re-energized. The volume of the breakdown zone rapidly grows until

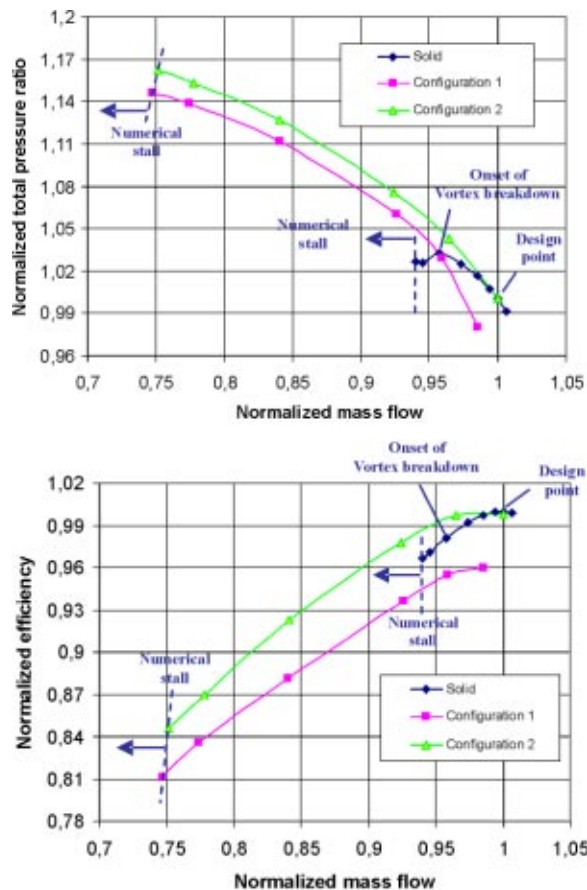


Fig. 7 Computed compressor map

the resulting blockage causes vast flow separations in the rotor flow. This mechanism finally leads to compressor stall.

In the simulations, the position and the angle of the vortex trajectory are found to be almost constant for operating points at higher pressure ratios. This behavior has also been described in other publications that investigate tip leakage flow in high-speed compressors (Hofman [3] and Hoeger [5]). The authors believe that this property is a characteristic of high-speed compressors and completely different from low-speed compressors. In low-speed compressor investigations a significant shift of the leakage vortex in the upstream direction is observed if the loading is increased (Saathoff [16]).

The simulations presented do not reveal an unsteady character of the leakage vortex. However, this fact is probably due to the numerical reduction of the computation model used to a single blade passage with periodic boundary conditions. Future investigations must take into account the unsteady interaction between neighboring blade passages.

Computed Compressor Map and Topology of the Tip Leakage Vortex at Design Speed. Figure 7 shows the characteristic speed line of the simulated rotor at design speed without casing treatment. Unsteady simulations were performed to evaluate the single operating points. At a normalized mass flow of 1.0, the compressor works at maximum efficiency (design point). The simulations indicate for this mass flow a well structured topology of the tip leakage vortex. The complete vortex is able to pass through the blade passage shock without significant disturbances (Fig. 4). At a normalized mass flow of 0.958, a breakdown of the vortex core is observed, leading to a local stagnation zone. With

increased back pressures, the breakdown zone rapidly grows until at a mass flow of 0.94, at which point the rotor reached numerical stall.

Flow Mechanisms Inside the Rotor With Casing Treatment

The plots in Fig. 7 show the influence of the tested casing treatments on the behavior of the simulated rotor at design speed. It is obvious from these data that a massive interaction with the rotor flow takes place if the slots are applied. The surge line as well as the efficiency are significantly affected by both casing treatment configurations. Configuration 1 results, as expected from corresponding experiments, in a stall point shift of about 20% to lower mass flows. This gain in flow stability correlates with a drastic decrease in efficiency over the whole operating range. At the design point the maximum efficiency gets reduced by 4%. A significant improvement resulted from the application of the configuration 2 casing treatment. The simulations revealed an identical increase in flow stability for this setup, but the impact on efficiency is much different. For mass flows higher than the design point, a moderate decrease in efficiency of only 0.2% is observed compared to the solid wall case. For mass flows lower than the design point, the compressor efficiency increases. The efficiency reaches the maximum value of the solid case.

Centered Positioned Axial Slots (Configuration 1)

Description of General Flow Mechanisms. Figure 8 shows the time-accurate interaction between casing treatment configuration 1 and the rotor flow near maximum efficiency (normalized mass flow 0.985). The contour plots show the distribution of static pressure in the blade passage near the blade tip and inside a representative slot (centerline). Additionally, the vector field of the flow velocity is given for the slot's midplane.

In the slot, a characteristic vortex in a counterclockwise orientation can be identified. This vortex, driven by the pressure gradient between the up- and downstream areas in the blade passage, draws fluid out of downstream parts of the blade passage and feeds it back into the main flow further upstream. The shock system in the blade passage gets significantly changed by this mechanism. Compared to the operating points of the solid case, a clear spatial separation of the front shock from the downstream passage shock is observed near the blade tip (Figs. 4, 5, and 8). This fact correlates with the loading of the blade tip. Figure 9 shows the time-averaged impact of casing treatment 1 on the distribution of static pressure at the blade tip. The leakage flow into the slots causes a pressure reduction in the back part of blade chord, whereas the flow out of the slots even increases the loading of the pressure side near the leading edge.

In the simulations, the blade passage shock is found to be almost steady in its position. Its changes in position are too small to be clearly detected in the presented contour plots. However, a small oscillation of the outgoing mass flow (about 0.1% of the total mass flow) is observed. This oscillation is periodic with the blade frequency and appears only in the outlet mass flow. This behavior is characteristic for all simulated operating points. The authors believe that the fluctuations in the outlet mass flow principally correlate with a periodic movement of the blade passage shock. At this point of the investigation, it is not yet clear, how much an unsteady behavior of the blade passage shock is suppressed by the computational reduction of the rotor stage to one single blade passage. Near maximum efficiency the maximum flow velocity inside the slots reaches approximately Mach 0.6 to 0.7. Due to this subsonic flow level, pressure information resulting from the front-shock and the low-pressure area at the suction side of the rotor blade are transported inside the slot in the clockwise direction. The frequency cycle of these pressure waves corresponds to the rotor blade frequency.

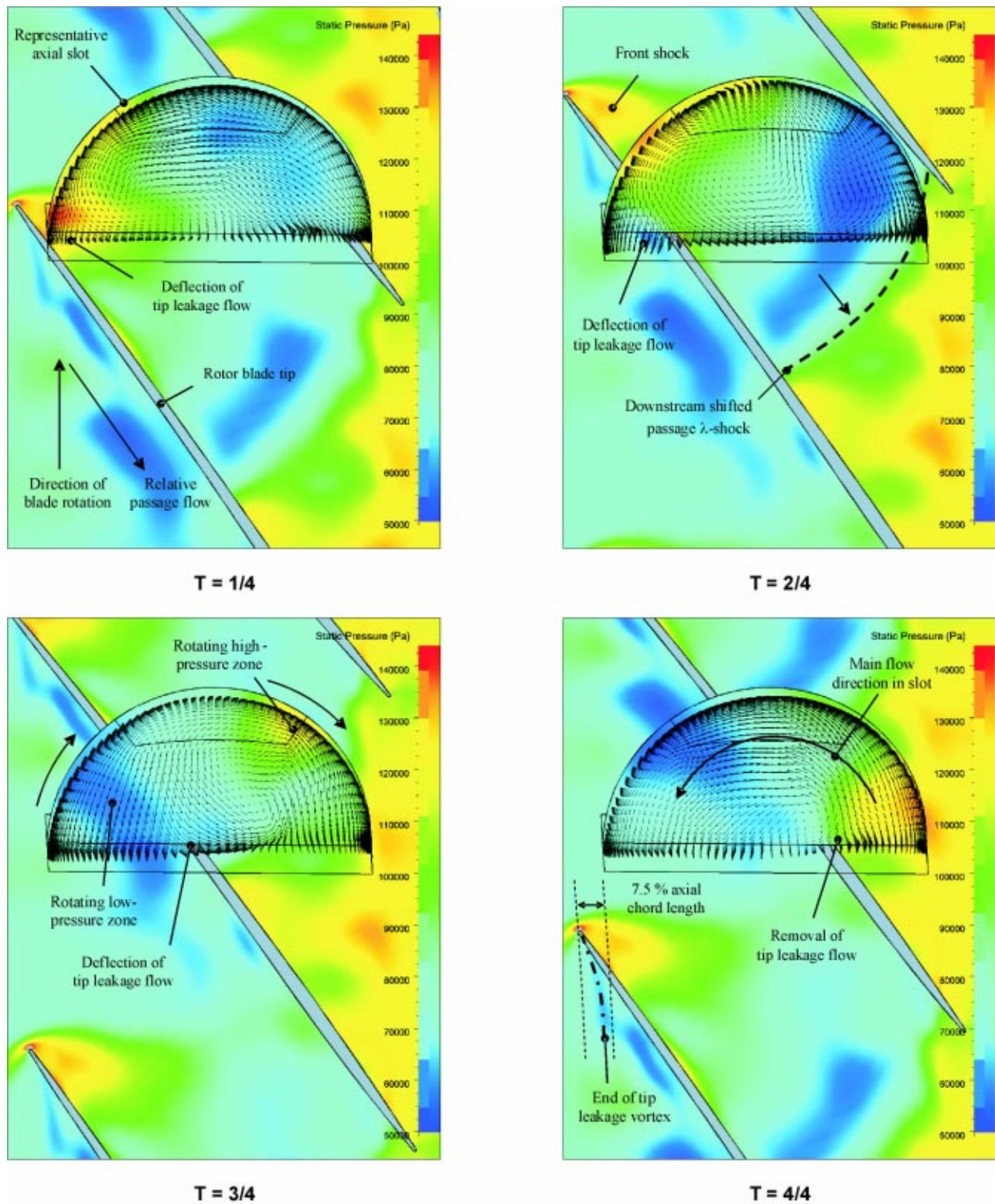


Fig. 8 Flow mechanisms with slot configuration 1 near maximum efficiency (normalized mass flow of 0.985)

Figures 10 and 11 show the distribution of static pressure near the blade tip and inside a slot for higher loadings. Here, no significant changes in the general flow mechanism can be detected near maximum efficiency. The maximum flow velocity inside the slot increases somewhat for higher pressure ratios. At a normalized mass flow of 0.84 a maximum flow velocity of 0.8 Mach is

observed (the flow vectors in Figs. 8, 10, and 11 are plotted with the same scale). The simulations show for all operating points that the total volume of casing treatment 1 is completely involved in the flow interaction. No “dead” volume exists. At a normalized mass flow of 0.959 the leakage flow that passes through the casing treatment is about 3.8% of the total mass flow at the design point.

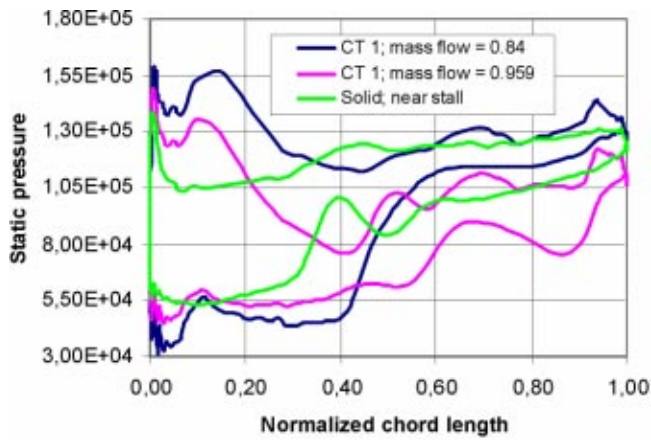


Fig. 9 Time-averaged loading of the blade tip, CT 1

This value increases for higher loadings. At a normalized mass flow of 0.84, the slot leakage flow reaches 5.3%. This is mainly due to an increased pressure level inside the blade passage.

Impact on Flow Stability. The high-pressure zone behind the blade passage shock mainly drives the flow inside the slots. Compressed air leaks continuously into the casing treatment and expands in the upstream direction. The mass flow by the slot vortex is responsible for a significant behavior change of the tip leakage flow and its vortex. In contrast to the untreated case, the spread of the tip leakage flow perpendicular to the blade chord is almost blocked. Depending on the flow field of the slot vortex, the tip leakage flow is drawn either into the casing treatment or is deflected radially inwards by the bleed air coming out of the slots. This mechanism prevents a loss-intensive rolling up of the tip leakage flow. In Figs. 8, 10, and 11 it can be seen that in the front part of the blade tip, which is not under the casing treatment, a tip

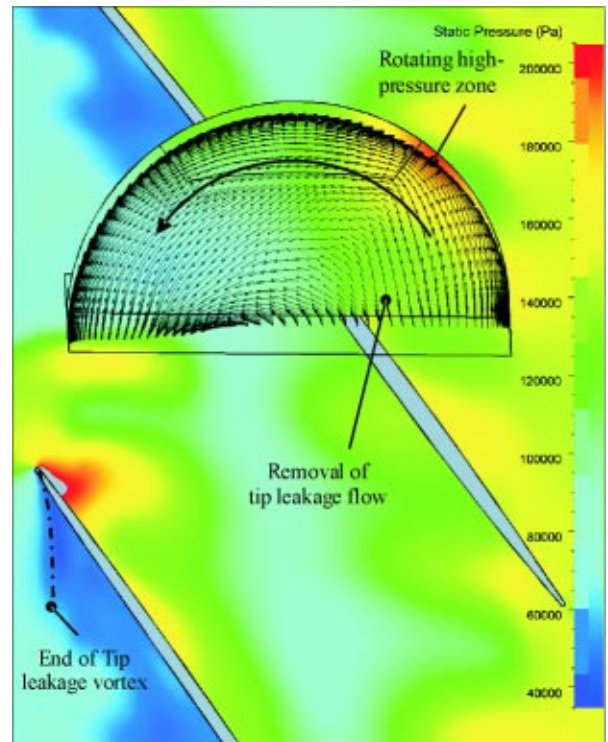


Fig. 11 Slot configuration 1 at a normalized mass flow of 0.84

leakage vortex develops like in the untreated case. A characteristic low-pressure trough in the first 7.5% of the blade chord indicates its trajectory. However, this vortex immediately disappears again at the leading edge of the casing treatment. This impact of the casing treatment minimizes the losses that would occur if the tip leakage vortex rolls up as in the solid case. Moreover, high-energy fluid transported from downstream parts of the blade passage continuously re-energizes the casing boundary flow in the upstream blade passage. By comparing the distribution of relative total pressure between slot configuration 1 (Fig. 12) and the untreated case (Fig. 6) it is obvious that the axial slots result in an improvement of the energy level near the blade tip (note the different color scales).

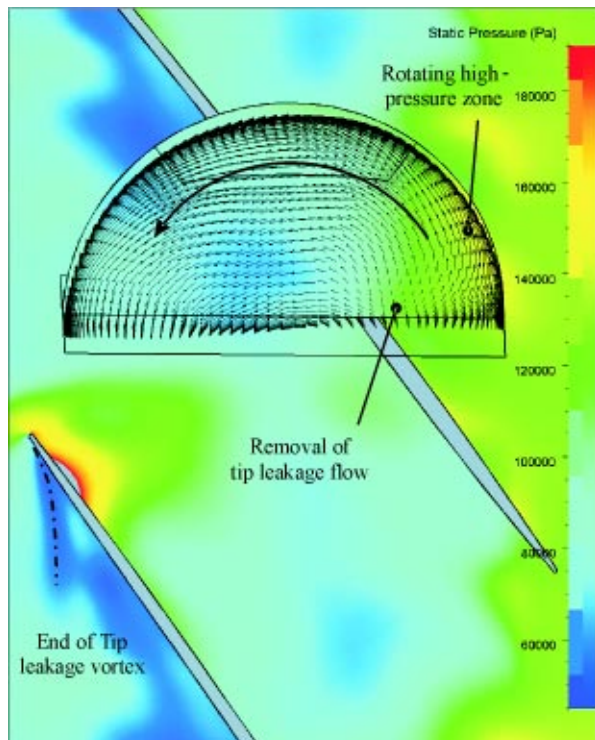


Fig. 10 Slot configuration 1 at a normalized mass flow of 0.959

Impact on Compressor Efficiency. Figures 8–11 indicate that with the application of casing treatment 1 a significant impact on the shock system, particularly that within the blade passage, is to be expected. As opposed to the solid case, the blade passage shock shifts significantly downstream due to the leakage flow through the slots. In Figs. 8 and 10 the blade passage shock clearly separates from the front shock at the blade leading edge. The shock-shifting impact of slot configuration 1 is not limited to the blade tip region, but extends significantly in the spanwise direction. By viewing the azimuthal averaged static pressure distribution in the blade passage this influence becomes very obvious. Figure 13 illustrates that almost the complete flow field in the blade passage is affected by the casing treatment. The dislocation of the shock system in the blade passage is one explanation for the observed decrease in efficiency. Another point is the slot leakage flow itself. As a result of the additional leakage flow, the already compressed air is decompressed again in a continuous cycle. Therefore, more work must be done by the compressor in order to maintain a certain pressure ratio. The computed slot leakage near maximum efficiency (about 3.8% of the mass flow at the design point) is nearly the same as the observed decrease in total efficiency of about 4%.

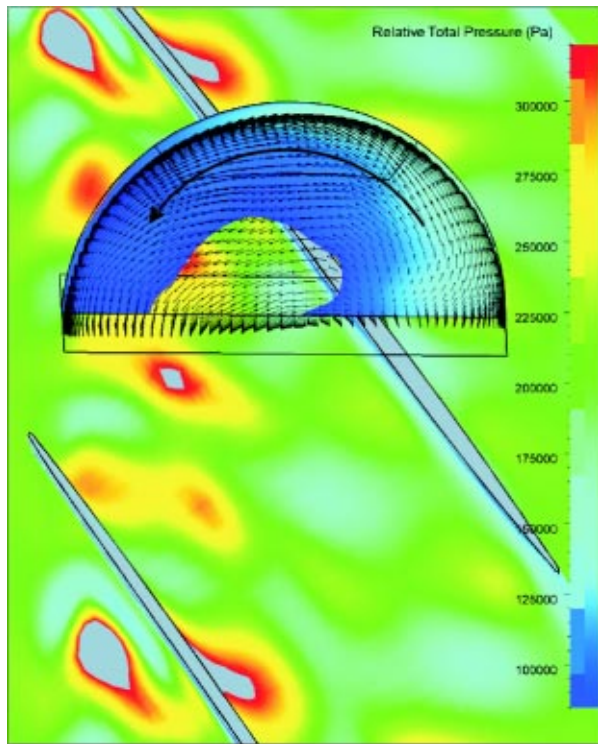


Fig. 12 Distribution of relative total pressure at a normalized mass flow of 0.959 for configuration 1

Upstream Positioned Axial Slots (Configuration 2)

Description of General Flow Mechanisms. As in configuration 1, the flow orientation inside the slots is dominated by a counterclockwise orientation. The driving force for the onset of the observed slot vortex is the high-pressure zone due to the front shock. It takes effect each time the blade leading edge passes a slot. Hence, the slot flow has a highly unsteady character. The simulations show that the velocities inside the slots significantly increase, mainly with the intensity of the front shock. Near maximum efficiency of configuration 2, the maximum velocity reaches only Mach 0.2–0.25, whereas at a normalized mass flow of 0.84, the maximum velocity rises to Mach 1.0 (the scaling of the velocity vectors is three times the scaling used for configuration 1). **Figure 14** shows the time-accurate interaction between slot configuration 2 and the rotor flow at a mass flow of 0.965. These illustrations reveal that each time the front shock passes the slot, fluid is drawn out of the blade passage into the casing treatment. The shock intensity at this loading is not high enough to cause a consistent flow circulation inside the complete slot volume. The main counterclockwise flow field in the slot has superimposed upon it secondary vortices that exhibit a clockwise orientation. This behavior changes for higher loadings. At a normalized mass flow of 0.84 a single strong slot vortex is observed. The mass flow that passes through the casing treatment is significantly less compared to configuration 1. Near maximum efficiency, the simulations result in a slot leakage flow of about 1.2% of the compressor's mass flow at the design point. This value increases to 3.8% if the normalized compressor mass flow is reduced to 0.84. The impact on the shock system inside the blade passage is not as intensive as it is observed with configuration 1. The location of the front and blade passage shock is not significantly affected. However, casing treatment 2 reduces the loading of the pressure side where the blade is under the slots. This fact can be seen in the azimuthal averaged static pressure in the blade passage (**Fig. 13**) and in the time averaged loading of the blade tip (**Fig. 15**).

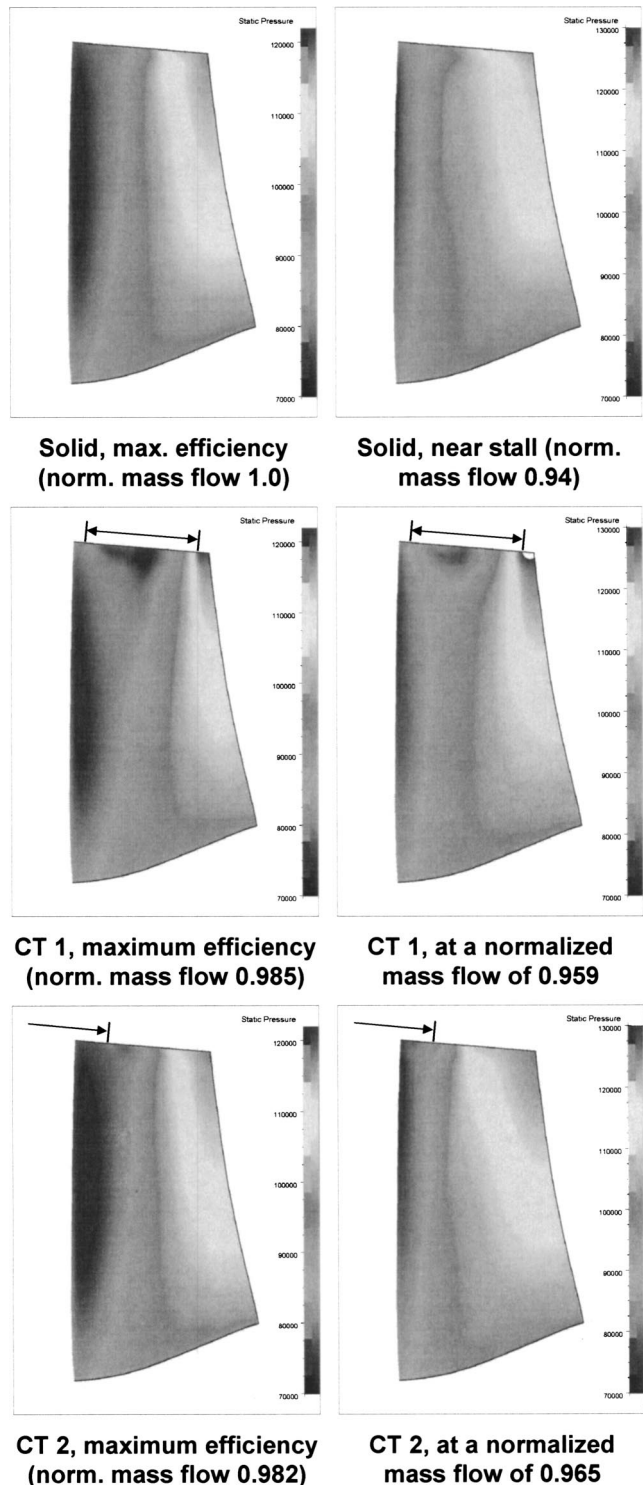
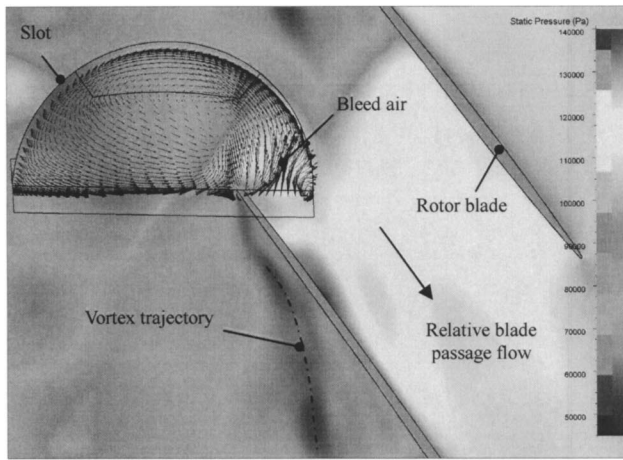
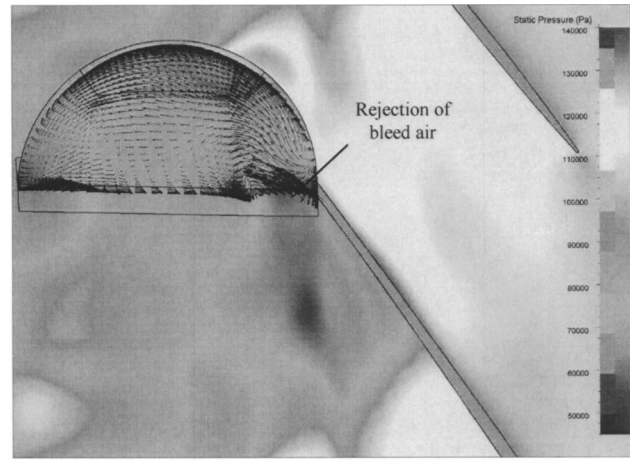


Fig. 13 Azimuthal averaged distribution of static pressure in the blade passage

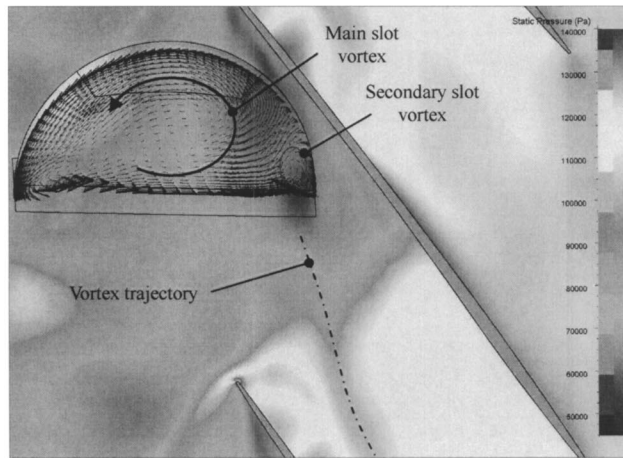
Impact on Flow Stability. The tip leakage vortex is not destroyed by the setup of casing treatment 2. However, its intensity is significantly reduced in comparison to the untreated case. This can be concluded from a visible weakening of the characteristic pressure trough in the blade passage. The observed impact of slot configuration 2 on the intensity of the tip leakage vortex is not constant for all operating points. It is smaller for low pressure ratios and grows with increasing blade loading. At very high pres-



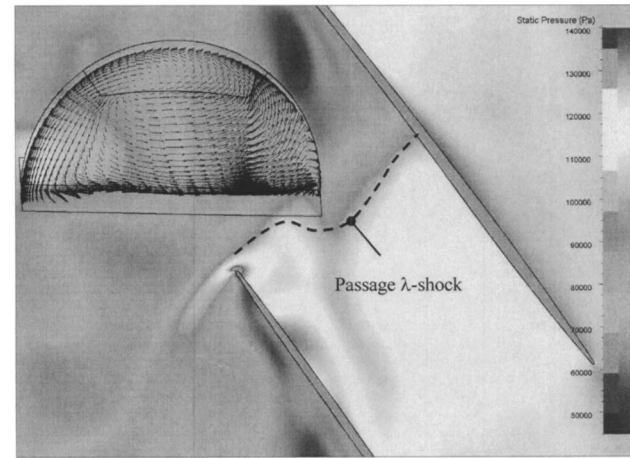
At a normalized mass flow of 0.965: $T = 1/4$



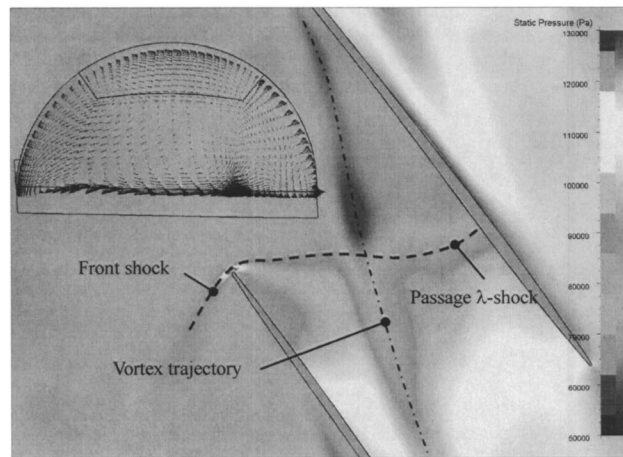
At a normalized mass flow of 0.965: $T = 2/4$



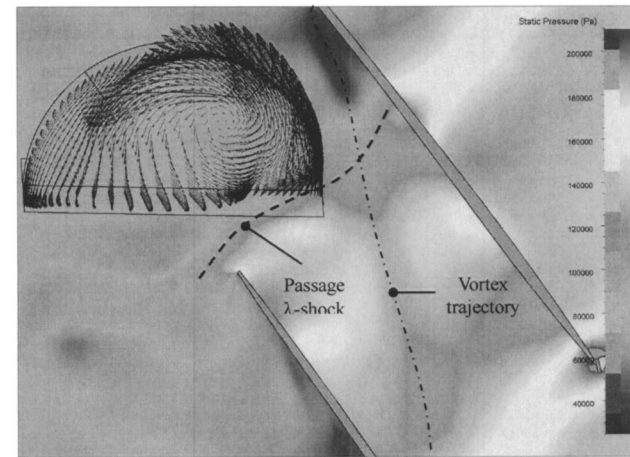
At a normalized mass flow of 0.965: $T = 3/4$



At a normalized mass flow of 0.965: $T = 4/4$



Under conditions of maximum efficiency: $T = 4/4$



At a normalized mass flow of 0.84: $T = 4/4$

Fig. 14 Flow mechanisms with slot configuration 2

sure ratios the onset of the tip leakage vortex is almost completely blocked in the first 25% of the blade chord (Fig. 13). The removal of tip leakage flow from the highly loaded pressure side through the slot opening is responsible for the intensity-lowering influence on the tip leakage vortex. This removed tip leakage flow is temporarily buffered inside the slots. Where this fluid leaves the slots again finally depends very much on the blade loading. For lower pressure ratios the outlet is mainly the low-pressure zone at the

blade suction side, whereas this outlet shifts upstream for higher blade loadings (Fig. 13). In the first 25% of the chord the resulting deflection of the tip leakage velocity component perpendicular to the blade dampens the loss-intensive rolling up of the tip leakage vortex. Hence, the losses inside the tip leakage vortex are reduced. This allows the tip leakage vortex to be stable even under conditions which, for the solid case, result in a vortex breakdown (Fig. 16).

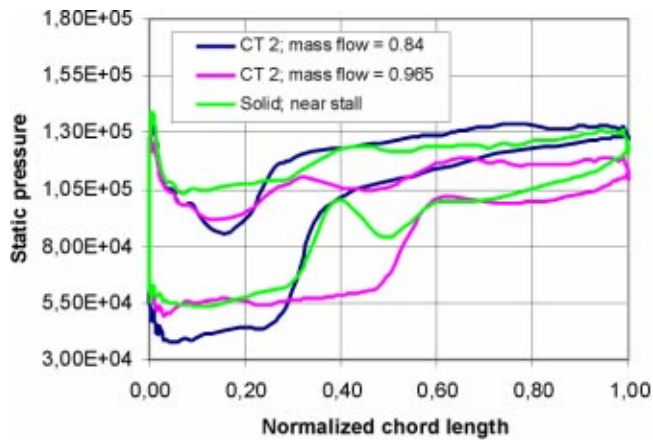


Fig. 15 Time-averaged loading of the blade tip, CT 2

Impact on Efficiency. When compared to configuration 1, configuration 2, the upstream shifted slots, has significantly less impact on the rotor flow field. The flow field and the shock system in the blade passage stay almost unchanged for lower pressure ratios. This explains the negligible decrease in efficiency within this operating range. In the solid wall case the properties of the tip leakage vortex become more and more important for higher pres-

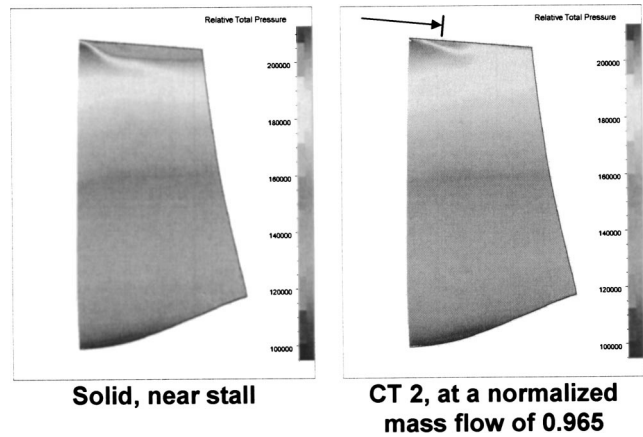
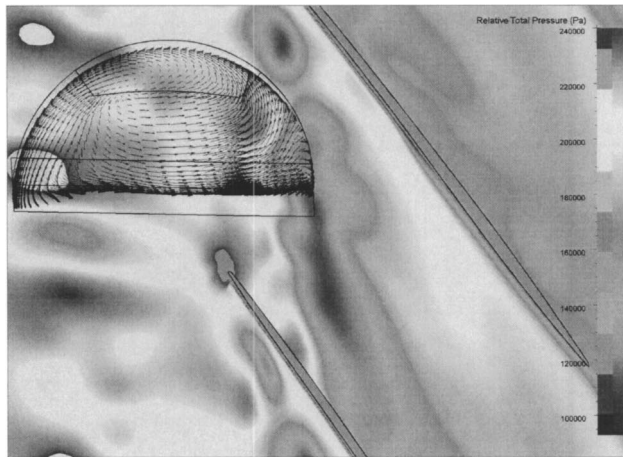


Fig. 17 Azimuthal averaged distribution of relative total pressure in the blade passage

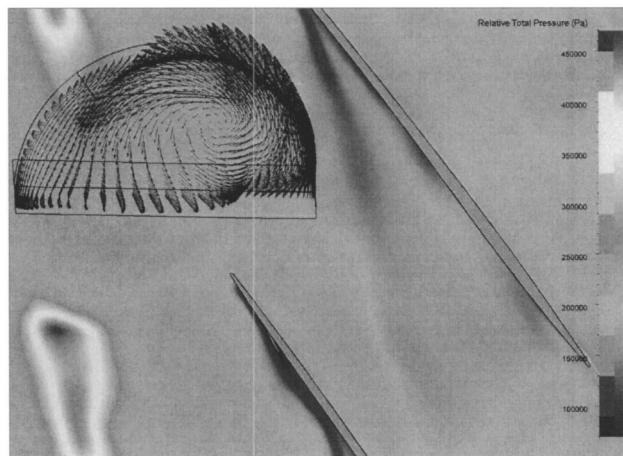
sure ratios. The tip leakage vortex is mainly responsible for losses in efficiency and blockage effects near the outer casing. Slot configuration 2 reduces the losses inside the leakage vortex (Fig. 17) and thus stabilizes its topology. This, of course, positively affects the compressor efficiency at higher pressure ratios.

Conclusion and Outlook

The simulations demonstrate that the stabilizing effects of the tested casing treatments are based on their impact on the tip leakage flow and its resulting vortex. Both configurations show the same effectiveness in delaying the onset of stall, but differ significantly in their resulting impact on efficiency. Configuration 1 leads to a massive destruction of the tip leakage vortex, whereas configuration 2 weakens the rolling up of the tip leakage flow. Hence, it can be concluded from the simulations that it is more advantageous to manipulate the tip leakage flow only in the very upstream part of the blade chord, than over the complete width. Configuration 2 represents a preliminary design. It surely has additional potential for efficiency improvement. The identification of design criteria, which are particularly advantageous to the weakening of the tip leakage roll up, will be the focus of future work. Investigations will concentrate on the question of how the flow inside the slot has to be directed in order to increase flow stability and efficiency as much as possible.



At a normalized mass flow of 0.965



At a normalized mass flow of 0.84

Fig. 16 Relative total pressure near blade tip, configuration 2

References

- [1] Furukawa, M., Inoue, M., Saiki, K., and Yamada, K., 1998, "The Role of Tip Leakage Vortex Breakdown in Compressor Rotor Aerodynamics," ASME Paper No. 98-GT-239.
- [2] Schlechtriem, S., and Lötzerich, M., 1997, "Breakdown of Tip Leakage Vortices in Compressors at Flow Conditions Close to Stall," ASME Paper No. 97-GT-041.
- [3] Hofman, W., and Ballmann, J., 2002, "Tip Clearance Vortex Development and Shock-Vortex-Interaction in a Transonic Axial Compressor Rotor," AIAA Paper No. 2002-0083.
- [4] Wilke, I., and Kau, H.-P., 2002, "A Numerical Investigation of the Influence of Casing Treatments on the Tip Leakage Flow in a HPC Front Stage," ASME Paper No. GT-2002-30642.
- [5] Hoeger, M., Fritsch, G., and Bauer, D., 1998, "Numerical Simulation of the Shock Tip Leakage Vortex Interaction in a HPC-Front Stage," ASME Paper No. 98-GT-261.
- [6] Greitzer, E. M., Nikkanen, J. P., Haddad, D. E., Mazzawy, R. S., and Joslyn, H. D., 1979, "A Fundamental Criterion for the Application of Rotor Casing Treatment," ASME J. Heat Transfer, **101**, pp. 237–243.
- [7] Crook, A. J., Greitzer, E. M., Tan, C. S., and Adameczyk, J. J., 1993, "Numerical Simulation of Compressor Endwall and Casing Treatment Flow Phenomena," ASME J. Turbomach., **115**, pp. 501–512.
- [8] Qing, Y., Qiushi, L., and Ling, L., 2002, "The Experimental Researches on Improving Operating Stability of a Transonic Fan," ASME Paper No. GT-2002-30640.
- [9] Rabe, D. C., and Hah, C., 2002, "Application of Casing Circumferential

Grooves for Improved Stall Margin in a Transonic Axial Compressor,” GT-2002-30641.

- [10] Ghila, A., and Tourlidakis, 2001, “Computational Analysis of Passive Stall Delay Through Vaned Recess Treatment,” ASME Paper No. 2001-GT-0342.
- [11] Thompson, D. W., King, P. I., and Rabe, D. C., 1997, “Experimental Investigation of Stepped Tip Gap Effects on the Performance of a Transonic Axial-Flow Compressor Rotor,” ASME Paper No. 97-GT-7.
- [12] Fujita, H., and Takata, H., 1984, “A Study on Configurations of Casing Treatment for Axial Flow Compressors,” JSME, **27**(230), pp. 1675–1681.

- [13] Takata, H., and Tsukuda, Y., 1976, “Stall Margin Improvement by Casing Treatment—Its Mechanism and Effectiveness,” ASME Paper No. 76-GT-A.
- [14] Wilke, I., and Kau, H.-P., 2000, “CFD-Simulationen von Verdichterstufen mit Casing Treatment,” DGLR Kongress 2000.
- [15] Gerolymos, G. A., and Vallet, I., “Tip-Clearance and Secondary Flows in a Transonic Compressor Rotor,” ASME Paper No. 98-GT-366.
- [16] Saathoff, H., and Stark, U., 2000, “Endwall Boundary Layer Separation in a High-Stagger Compressor Cascade and a Single-Stage Axial-Flow Low-Speed Compressor,” *Forschung im Ingenieurwesen*, **65**(8), pp. 217–224.

Toyotaka Sonoda
Yoshihiro Yamaguchi

Toshiyuki Arima
Honda R&D Co., Ltd.,
Wako Research Center,
Saitama 351-0193, Japan

Markus Olhofer

Bernhard Sendhoff
Honda Research Institute Europe GmbH,
63073 Offenbach, Germany

Heinz-Adolf Schreiber
German Aerospace Center (DLR),
Institute of Propulsion Technology,
D-51170 Köln, Germany

Advanced High Turning Compressor Airfoils for Low Reynolds Number Condition— Part I: Design and Optimization

High performance compressor airfoils at a low Reynolds number condition at ($Re = 1.3 \times 10^5$) have been developed using evolutionary algorithms in order to improve the performance of the outlet guide vane (OGV), used in a single low pressure turbine (LPT) of a small turbofan engine for business jet aircrafts. Two different numerical optimization methods, the evolution strategy (ES) and the multi-objective genetic algorithm (MOGA), were adopted for the design process to minimize the total pressure loss and the deviation angle at the design point at low Reynolds number condition. Especially, with respect to the MOGA, robustness against changes of the incidence angle is considered. The optimization process includes the representation of the blade geometry, the generation of a numerical grid and a blade-to-blade analysis using a quasi-three-dimensional Navier-Stokes solver with a $k-\omega$ turbulence model including a newly implemented transition model to evaluate the performance. Overall aerodynamic performance and boundary layer properties for the two optimized blades are discussed numerically. The superior performance of the two optimized airfoils is demonstrated by a comparison with conventional controlled diffusion airfoils (CDA). The advantage in performance has been confirmed by detailed experimental investigations, which are presented in Part II of this paper. [DOI: 10.1115/1.1737780]

Introduction

One approach to minimize the weight of small turbofan engines for business jet aircrafts is to design a single-stage low-pressure turbine together with an outlet guide vane: the OGV is set just downstream of the single-stage turbine in order to remove swirl. This way we hope to combine high efficiency at the cruise design point with the condition of a lightweight design.

The OGV had to be designed for high subsonic inlet speed, a high flow turning and a very low Reynolds number of about 1.3×10^5 at the cruise point. Although there are several publications on cascades at low Reynolds numbers, hardly any investigations have been reported on the detailed blade design for such high-turning low Reynolds number compressor blades. Almost all of the papers deal with low-speed cascades or with high-speed cascades but low turning airfoils. Rhoden [1] reported that for very-low-speed cascades with a large camber angle a fairly high suction peak near the leading edge of the suction surface seems to be effective to prevent a laminar separation. However, questions remain whether this concept is valid for high inlet speed regions. Furthermore, additional analysis is required to determine the important factors for boundary layer transition and for laminar separation bubbles for very low Reynolds numbers (e.g., [2]). The initial design of the high turning guide vane section, first carried out for ground condition ($Re = 0.86 \times 10^6$), was based on the concept of a controlled diffusion airfoil. A midspan cross section of the three-dimensional outlet guide vane and the design parameters are shown in **Fig. 1** and **Table 1**, respectively. The design inlet Mach number is 0.60 and the design turning angle is 43 deg. Because there is no streamtube contraction, the diffusion factor of 0.53 is relatively high. This blade is designated the baseline blade OGV-BASE.

Contributed by the International Gas Turbine Institute and presented at the International Gas Turbine and Aeroengine Congress and Exhibition, Atlanta, GA, June 16–19, 2003. Manuscript received by the IGTI December 2002; final revision March 2003. Paper No. 2003-GT-38458. Review Chair: H. R. Simmons.

In order to evaluate the performance of the baseline compressor blade experimentally, cascade tests have been carried out at DLR, Cologne [3] in a wide range of Reynolds numbers. The first results on the baseline cascade are given in **Fig. 2**, which shows the Reynolds number characteristics at two different incidence angles. It can be seen that for both cases the critical Reynolds number is about 2×10^5 and that the losses dramatically increase below this number. Therefore, it is very important to understand the corresponding flow mechanism first and in a second step to develop a new design concept for an improved blade element in this critical regime.

Recently, first results on the optimization of compressor airfoils have been reported [4,5]. The complete design method consists of a geometrical representation of the airfoil, a blade-to-blade flow solver and a numerical optimization algorithm. Koeller et al. [4] used a combination of stochastic and gradient algorithms for the optimization, and a third-order spline for the representation. Benini and Toffolo [5] used an evolutionary algorithm that belongs to the class of global stochastic optimization methods together with a Bezier spline. Both approaches used a viscous/inviscid solver (MISES [6]) for the blade-to-blade analysis. In both studies the Reynolds number was quite high (in the order of 2.5×10^6) which leads to a relatively simple flow field compared to the present condition ($Re = 1.3 \times 10^5$). Since in our project phenomena like large laminar separation bubbles and intensive turbulent separations are likely to play a dominant role, it seems inevitable to use a Navier-Stokes solver for the evaluation.

As shown in **Fig. 3**, two different methods belonging to the class of evolutionary algorithms, the evolution strategy (ES) and the multi-objective genetic algorithm (MOGA) have been employed for the optimization. We used a Navier-Stokes solver first during the optimization in a “fast” mode and later for validation before the experiments were executed in a “precise” mode. In the precise mode a new transition model adapted to the low Reynolds number regime with a fine mesh resolution in the boundary layer is used. Such a fine resolution is omitted in the fast mode in order

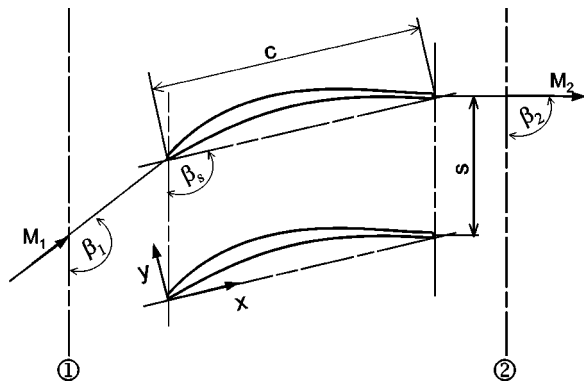


Fig. 1 Cascade parameters

to save computation time taking into account that during the optimization the flow solver will be called 6000 (ES) and 12000 (MOGA) times, repeating. The final designs were experimentally validated at DLR, Cologne, and additional flow analysis was carried out to support the interpretation of the experimental results.

It is well known that freestream turbulence occurring in real turbomachinery environments has a strong effect on the boundary layer; it tends to cause early transition from laminar to turbulent flow, [7], and it may alter the separation behavior. However, in the present work the freestream turbulence level for the optimization process has been set to the low turbulent level of 0.6% that is similar to the one in the planned experiments to allow a thorough and reasonable verification of the design.

In Part I of the two contributions the focus has been put on the results of the aerodynamic design optimization and in Part II on the validation and the flow analysis. Here the target was to elucidate why the optimized airfoils have a superior performance.

Validation of Fast Navier-Stokes Solver. As the fast flow solver, an in-house quasi-three-dimensional version of the Navier-Stokes flow solver, HSTAR (Honda Software for Turbomachinery

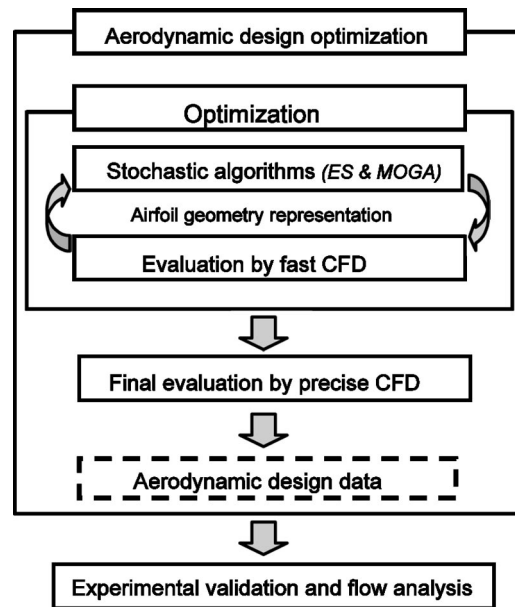


Fig. 3 Design approach for the high turning compressor airfoil for low Reynolds numbers

Aerodynamics Research) with a low Reynolds $k-\epsilon$ turbulence model proposed by Chien [8] is used. The quasi-three-dimensional flow solver is a modified three-dimensional Navier-Stokes code, [9], for the purpose of calculating aerodynamical performance of two-dimensional cascades in short time. The grid consists of 191×51 cells and the average value of y^+ near the wall is of the order of 1.0. The computation time for one run with this grid is about 3.5 minutes on an HP Alpha 21264 833MHz processor. In the optimization process, AVDR has been always fixed to 1.0.

A typical example for the validation of the fast flow solver (no transition model) is shown in Fig. 2. The CFD results do not clearly show a sudden increase below the critical Reynolds number as it is observed in the experiment. However, qualitatively the overall Reynolds number characteristics are well predicted. Fig.

Table 1 Design parameters of OGV-BASE

Aerodynamics		Geometry	
Inlet Mach Number, M_1	0.60	Stagger Angle, β	104.6°
Inlet Flow Angle, β_1	133.0°	Chord Length (mm), C	65.0
Exit Flow Angle, β_2	90.0°	Maximum Thickness	6.70%
Turning Angle, $\beta_1-\beta_2$	43.0°	solidity, C/S	1.734
Diffusion Factor, DF	0.53		
AVDR	1.0	Reynolds Number	8.7×10^5

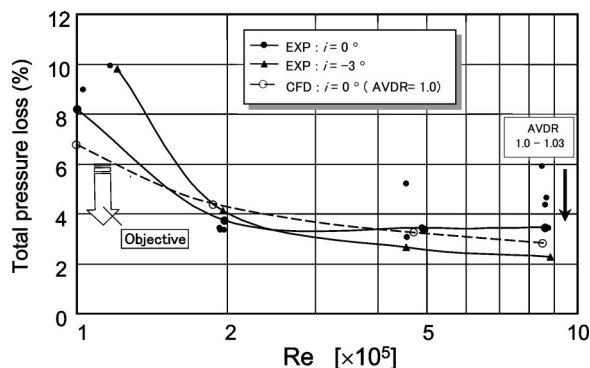


Fig. 2 Experimental and calculated Reynolds number characteristics of baseline CDA cascade

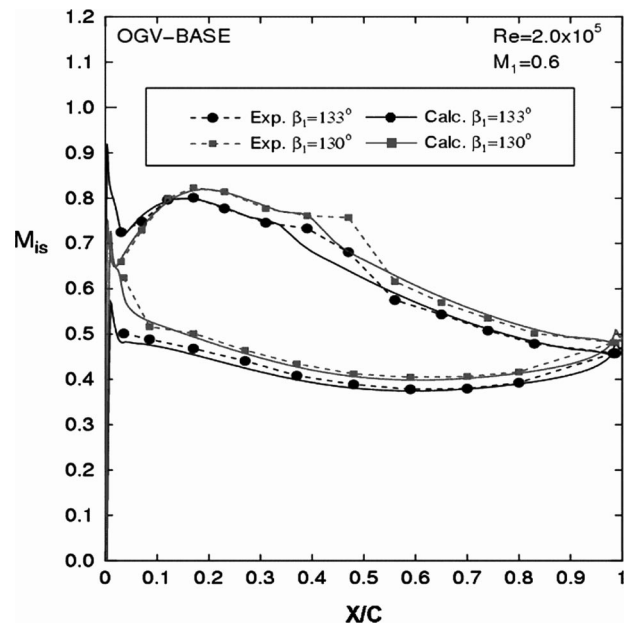


Fig. 4 Comparison of experiment and CFD simulation (no transition model) in profile Mach number distribution

Table 2 Summary of two global stochastic optimization methods used

Algorithm		(μ, λ)-CMA-ES	MOGA
Design parameters		42 (=14 of control points x 3)	14
Representation		NURBS (cyclic, 3rd order)	B-spline (3rd order)
Constraints	Thickness	$r_{LE} > 0.8\% \times c$	$b_1 > 0.8\% \times c$
		$r_{TE} > 1.1\% \times c$	$b_2 > 1.1\% \times c$
		$\Theta_{min} > 2.0\% \times c$	$\Theta_{min} > 2.0\% \times c$
		$\Theta_{max} > 6.7\% \times c$	$\Theta_{max} \rightarrow$ no constraint
Exit deviation angle		$-0.3^\circ > \beta_2 > +0.3^\circ$	$-1.0^\circ > \beta_2 > +1.0^\circ$
Objective function		Single objective (Eq. 1) weighted sum of 1. exit deviation angle constraint 2. pressure loss 3. four thickness constraints	Three objectives (Eqs. 3, 4, 5) f_1 = pressure loss f_2 = difference of pressure losses ($i=0^\circ$, f_3 = difference pressure losses ($i=0^\circ$, -
Population size		$\mu = 1, \lambda = 12$	80
Number of generations		500	50
Total number of NS-calls		6000 (=500x12)	12000 (=80x50x3)
Initial blade		OGV-BASE	Uniform distributed

ure 4 shows a blade surface Mach number distribution of the Reynolds number of 2×10^5 for two incidence angles. At design incidence ($\beta_1=133$ deg), the experimental Mach number distribution on the suction surface shows a laminar separation from about 30 to 55% of chord. A more extended bubble is obtained at the negative incidence ($\beta_1=130$ deg). Both lead to a certain amount of additional drag and performance deterioration. It is interesting to note that the $k-\epsilon$ model without an explicit transition model is able to simulate a similar midchord separation and provides a reasonable loss level. Therefore, it seems acceptable that this fast approach is applied during the optimization process.

Design Approach

Evolutionary Algorithms for Design Optimization. Evolutionary algorithms belong to the class of global stochastic optimization algorithms. They are based on principles of evolutionary biology, in particular on natural selection acting on a population of different designs called individuals. The variation operators produce genetic diversity and the selection directs the evolutionary search. Recombination or crossover which combines genetic material and mutation which introduces stochastic changes, are the main variation operators.

In this paper, we employ two algorithms that represent two different approaches to the search process with respect to the representation, to the variation operators and in particular to the design of the fitness function. The co-variance matrix adaptation-evolution strategy (CMA-ES), which was employed in the design of the OGV-ES blade, is a single-objective algorithm and belongs to the evolution strategies. The MOGA, which was employed in the design of the OGV-MOGA blade, belongs to the class of Pareto-based multi-objective algorithms, [10,11], and its evolutionary principles are based on the genetic algorithm.

For both optimizations, the inlet flow angle, the real chord length and the solidity are fixed by design requirements. In order to analyze a wide variety of possible design concepts, the geometrical constraints were not the same for the CMA-ES and the MOGA method. This has the drawback that the results cannot be directly compared from an optimization point of view. (see Table 2.)

Optimization With ES. In the design of the ES blade, a special variant of evolution strategies with so-called co-variance matrix adaptation (CMA) has been applied. The details of the CMA-ES are quite involved and the reader is referred to Hansen

et al. [12] for the implementation used here and to Olhofer et al. [13] for the application of the CMA-ES to design optimization problems.

Blade Profile Definition. A closed nonuniform third-order rational B-spline, [14], is used for the representation of the blade, as shown in Fig. 5. The control points are subject to the optimization and the resulting spline determines the contour of the represented blade. In this optimization, the parameter vector consists of 14 spline control points, where each control point is represented by three coordinates. Therefore, in total there are 42 parameters that are optimized. This allows a high degree-of-freedom for variations during the optimization. Nevertheless, the number of parameters is small enough to allow a convergence of the algorithm within a reasonable number of generations.

Objective Function. In order to calculate the fitness, three different criteria have to be considered: the pressure loss of the design, the deviation angle and the thickness of the blade. In principle, two different approaches are possible to cope with multiple criteria for the evaluation of the quality of the design: a weighted sum approach or a Pareto-based approach. In the design of the ES blade we employed the weighted sum approach as follows:

$$f = \sum_{i=1}^6 w_i t_i \rightarrow \text{minimize}, \tag{1}$$

where the w_i are weighting coefficients, which are fixed heuristically, and the t_i are given as follows:

$$t_1 = \max(0, |\beta_2 - \beta_{2,design}| - \delta\beta)$$

$$t_2 = \omega$$

$$t_3 = \max(0, r_{LE,design} - r_{LE})$$

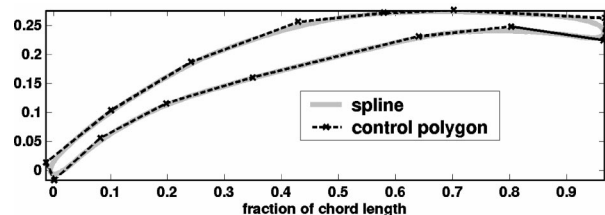


Fig. 5 Airfoil parameterization of ES

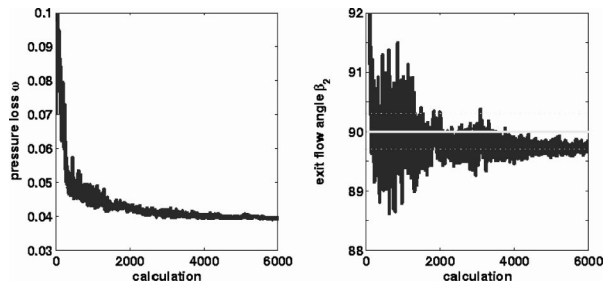


Fig. 6 Fitness values during optimization, (a) total pressure loss, (b) exit flow angle

$$\begin{aligned}
 t_4 &= \max(0, r_{TE,design} - r_{TE}) \\
 t_5 &= \max(0, \Theta_{min,design} - \Theta_{min}) \\
 t_6 &= \max(0, \Theta_{max,design} - \Theta_{max}). \quad (2)
 \end{aligned}$$

Constraints. The tolerance of the exit flow angle $\delta\beta$ is set to 0.3 deg. The values of $r_{TE,design}$, $r_{LE,design}$, $\Theta_{max,design}$, and $\Theta_{min,design}$ are lower limits. The first three are set identical to those of the BASE airfoil, and the last is set to $0.9 \times 2 \times$ radius of the trailing edge of OGV-BASE. No explicit criterion for the off-design incidence conditions is considered.

Convergence of the ES-CMA. In Fig. 6, the development of the pressure loss and the exit flow angle are shown. A (μ, λ) CMA-ES with one parent-individual ($\mu = 1$) and $\lambda = 12$ offspring-individuals in each generation was used. The optimization was initialized with a geometry similar to the BASE airfoil in the first generation. A fast decrease of the pressure loss as well as a rapid adaptation of the deviation angle can be observed. Later on the deviation angle fluctuates near the target angle of 0.3 deg, whereas the pressure loss is further decreased.

Optimization With MOGA. The basic algorithm of the MOGA is the same as the simple real-valued genetic algorithm. However, as the name suggests the MOGA approach incorporates extensions to allow a multi-objective search process with the target to approximate the Pareto surface, see [10,11], by the population of the final generation. A blade that belongs to the Pareto set is a nondominated solution, i.e., no other blade geometry exists which is superior in *all* objectives. Therefore, MOGAs can generate a set of Pareto solutions that demonstrate tradeoff relationships between the objective functions. These relationships can improve the decision-making process of the aerodynamic engineer and provide useful information for a design-parameter study. MOGAs have been successfully applied to the aerodynamic optimization of gas turbine blades, see, e.g., work by Yamaguchi et al. [15] and Oyama et al. [16].

Blade Profile Definition. The blade surface is described with a B-spline, [14], using four control points based on a *preliminary-camber* line. Note that the *preliminary-camber* line is different from the mean camber-line, since the control points on the suction surface and the pressure surface are defined independently in the optimization process. Furthermore, two points are used to describe the leading edge ellipse and the trailing edge ellipse for the pressure surface and the suction surface, respectively. Figure 7 shows a profile of the design parameterization.

Objective Functions. In this study, in addition to the performance at design condition, the off-design performance is considered as schematically shown in Fig. 8. The corresponding objective functions are defined as follows:

1. minimization of the pressure loss coefficient at design incidence

$$f_1 = \omega \rightarrow \text{minimize} \quad (3)$$

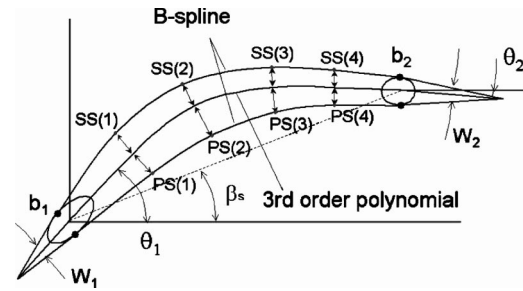


Fig. 7 Airfoil parameterization of MOGA

2. wide operating range for positive incidence

$$f_2 = |\omega_{design} - \omega_{design+5^\circ}| \rightarrow \text{minimize} \quad (4)$$

3. wide operating range for negative incidence

$$f_3 = |\omega_{design} - \omega_{design-5^\circ}| \rightarrow \text{minimize}. \quad (5)$$

Constraints. The tolerance of the outflow angle $|\beta_2 - \beta_{2,design}|$ is set to ± 1 deg. Furthermore, the lower bounds of Θ_{min} , b_1 and b_2 are given by $\Theta_{min,design} = 0.9 \times 2 \times$ (radius of the trailing edge) and by $r_{LE,design}$ and $r_{TE,design}$:

$$\Theta_{min} > \Theta_{min,design}; b_1 > r_{LE,design}; b_2 > r_{TE,design}. \quad (6)$$

Convergence in MOGA. In this optimization, the target is to obtain all Pareto solutions in a three dimensional space of objectives. In order to visualize the two-dimensional Pareto surface more clearly, we projected two objectives onto one in Figs. 9 and 10 resulting in two two-dimensional Pareto distributions. Figure 9 shows the distribution of individuals at the initial generation and the final generation on the f_1 versus f_2 objective plane. Figure 10 shows the corresponding distributions for the f_1 versus f_3 plane. From the individuals in the final generation in Figs. 9 and 10, one blade geometry highlighted by an arrow was selected as the

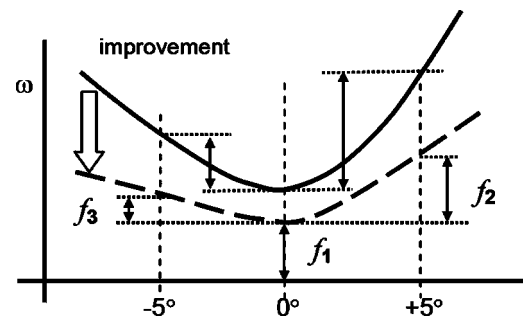


Fig. 8 Goal of optimization process of MOGA

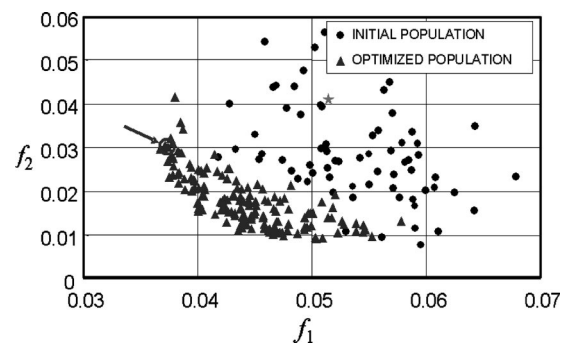


Fig. 9 Pareto distribution of the initial population and the optimized population projected on f_1 versus f_2 plane

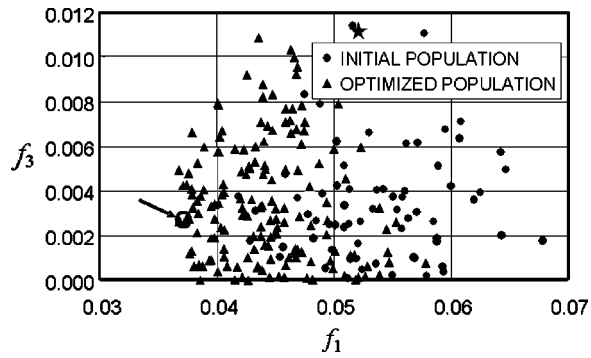


Fig. 10 Pareto distribution of the initial population and the optimized population projected on f_1 versus f_3 plane

MOGA airfoil, therefore, putting emphasis on the performance at design condition. For comparison, the baseline airfoil is represented by stars in **Figs. 9 and 10**.

Validation of Precise Flow Solver. As the precise flow solver, a $k-\omega$ turbulence model, [17], and an Abu-Ghannam/Shaw (AGS) transition model, [18], based on Drela's modification, [6], which has been successfully used in the MISES code, are implemented into the quasi-three-dimensional version of HSTAR, [9].

Transition Model. Transition starts when the momentum thickness Reynolds number Re_{δ_2} exceeds a critical transition Reynolds number Re_{tr} , and it is completed when $Re_{\delta_2} = 2 Re_{tr}$. The critical transition Reynolds number is calculated from the following relation used by Kuegeler [19], that is based on the modification by Drela [6] to remove the ill-posedness of the original AGS model:

$$Re_{tr} = 163 + 74.3 \left[0.55 + \tanh \left(\frac{10}{H_{12}} - 5.5 \right) + 1 \right] \cdot (0.94 \cdot n_{cr} + 1), \quad (7)$$

where $H_{12} = \delta_1 / \delta_2$. The influence of the freestream turbulence outside of the boundary layer Tu is given by the critical amplification factor n_{cr} :

$$n_{cr} = -8.43 - 2.4 \ln \left(\frac{Tu}{100} \right). \quad (8)$$

Outside the boundary layer the flow is assumed to be turbulent. The combination of the transition and the turbulence model is realized by introducing an intermittency function f_t to modify the turbulent viscosity μ_T obtained from the turbulence model, as follows:

$$\mu_T = f_t \frac{\rho k}{\omega}, \quad (9)$$

where

$$f_t = \left[25 \left/ \left[25 + 275 \left\{ 1 - \sin \left(\frac{\pi}{2} \cdot \frac{Re_{\delta_2} - Re_{tr}}{Re_{tr}} \right) \right\} \right] \right] \right]^3. \quad (10)$$

Validation. For the validation, the experimental data for the baseline cascade were used again. The computational grids are shown in **Fig. 11**. The grid consists of 251×81 cells, which is therefore finer than the one used in the fast mode (191×51). The average y^+ of the first grid point from the wall is about 0.3 for calculations at $Re \approx 2.0 \times 10^5$. The comparison between computed results and experimental data is shown in **Fig. 12**. In **Fig. 12(a)** the isentropic Mach number distributions obtained at $Re = 1.97 \times 10^5$, $M_1 = 0.60$, and $\beta_1 = 130$ deg are shown for the fully turbulent ($k-\omega$ and Chien's $k-\varepsilon$ model) and transitional analysis ($k-\omega$ plus transition model) in comparison to the measured data. The

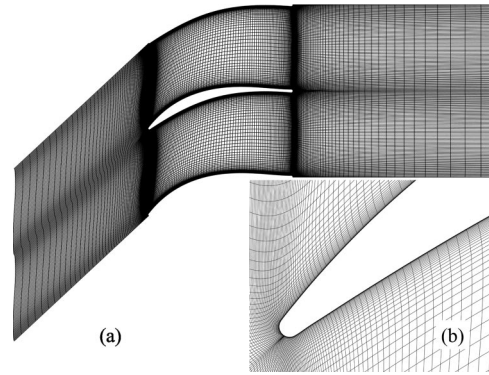


Fig. 11 Computational grid, (a) overall, (b) leading edge part in detail

measurement data show a nearly constant Mach number in the region of laminar separation between about 30% to 47% of the chord and a transition region with turbulent re-attachment and a large pressure recovery from about 45% to 57% of chord. In the computed results, this phenomenon can be predicted with the $k-\omega$ turbulence model and the transition model only.

A further validation is provided in **Fig. 12(b)**, that shows a comparison between simulated and experimental Reynolds number characteristics for $\beta_1 = 133$ deg and $M_1 = 0.6$. Compared to the case without the transition model, see **Fig. 2**, the prediction accuracy is considerably improved. As a last validation, a computed incidence characteristic for the subcritical conditions with high losses ($Re = 1.0 \times 10^5$) is shown in **Fig. 12(c)**. Although the experimental losses scatter around slightly high values ($\beta_1 = 133$ deg), the computed curve is qualitatively similar to the experimental one.

The computed flow field with the transitional analysis is shown in **Fig. 13**, again at $Re = 1.97 \times 10^5$, and $\beta_1 = 130$ deg. The computed skin friction coefficient with the isentropic Mach number along the suction surface is shown in **Fig. 13(a)**, the eddy viscosity contour in **Fig. 13(b)**, and the velocity vector with the static pressure contour in **Fig. 13(c)**. From **Fig. 13(a)** we notice that the laminar separation starts around 30% of chord on the blade suction surface. The augmentation of the eddy viscosity starts at approximately 45% chord, a position that corresponds to the Mach number or pressure kink in the suction side distribution. Downstream of the pressure kink the negative skin friction coefficient is amplified due to the high vorticity of the reverse flow and the turbulent entrainment process along the rear part of the bubble. Turbulent reattachment is simulated around 57% of chord, where the eddy viscosity increases. These observations agree well with the explanation of a separated-flow transition discussed, e.g., in the 1991 IGTI scholar lecture of Mayle [20] and the pattern of the computed skin friction coefficient is similar to the one shown by Walker [21].

Reynolds Number Effect on Boundary Layer of OGV-BASE

To analyze the effect of the Reynolds number in more detail, in **Fig. 14**, the computed blade Mach number distributions (top), the simulated boundary thickness parameters and form factor (middle), and the suction surface friction coefficient (bottom) are provided for Reynolds numbers of 1.0, 2.0 and 8.7×10^5 . As shown in **Fig. 12(b)**, the losses above a Reynolds number of 2.0×10^5 remain nearly constant, whereas for smaller Reynolds numbers a rapid increase can be observed. Since the computed Mach number distributions agree quite well with the experimental data, the computed boundary layer data and skin friction coefficient seem to be plausible.

For a high Reynolds number of $Re = 8.7 \times 10^5$ (including 4.9×10^6 , not shown here), the boundary layer transition occurs near the blade leading edge and flow remains turbulent all along the surface. However, the boundary layer thickens and the skin fric-

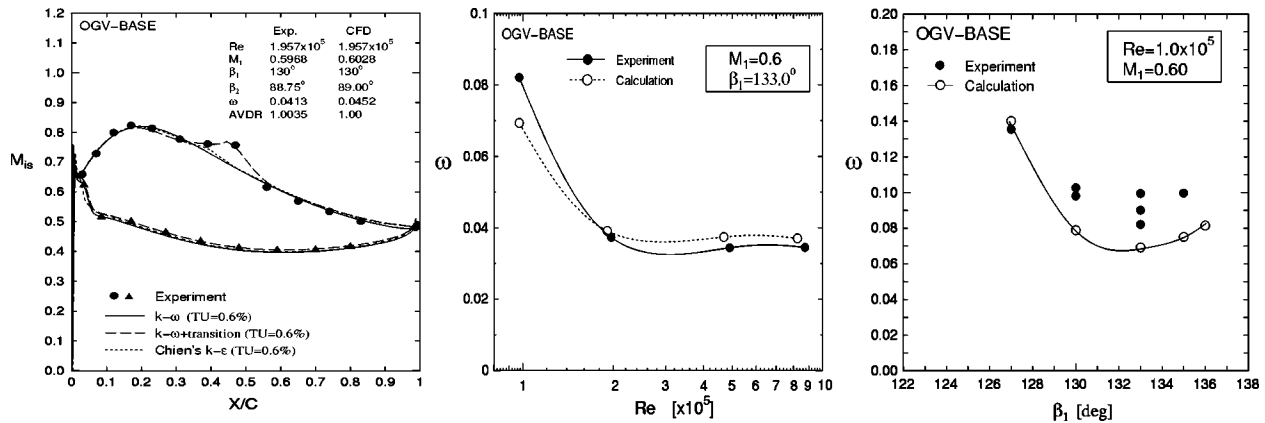


Fig. 12 Comparison of experimental and CFD results for OGV-BASE. In CFD, the $k-\omega$ model with transition model was applied. (a) Mach number distribution around critical Reynolds number, (b) Reynolds number characteristics, (c) incidence characteristics below critical Reynolds number.

tion coefficient decreases while moving toward the blade trailing edge. In reality, the boundary layer tends to separate from the rear part of the suction surface.

At the Reynolds number of 2.0×10^5 , a laminar separation bubble with transition and turbulent reattachment is observed between 25% and 48% of chord. The boundary layer thickness indicates that the laminar separation is less pronounced, and the bubble has little impact on the loss level. However, at lower Reynolds number ($Re = 1.0 \times 10^5$), an extended laminar separation is observed with a tendency not to re-attach on the surface, see Fig. 14 (right). This critical situation is often interpreted as “bubble burst” associated with a considerable loss increase. The present simulation predicts a loss of 6.9%.

Optimization Results

Airfoils Geometry. The airfoil geometry resulting from the two optimization methods ES and MOGA are shown together with the baseline profile in Fig. 15. Figures 15(a), (b), and (c) show all blade geometries with fixed LE points, the details of the LE parts and the chordwise suction surface curvature variations between 10% and 50% of the chord, respectively. Unique airfoil geometries have been obtained, having maximum thickness at around midchord (ES) and more in the rear part of the chord for the MOGA airfoil. The stagger angles of the two optimized blades are also significantly different. Furthermore, the LE thickness of

the MOGA profile is decreased, as shown in Fig. 15(b). The LE geometries of OGV-BASE, OGV-MOGA, and OGV-ES are circular, elliptic, and “arbitrary.” The present aerodynamic simulations show that the LE and suction side flow fields seem to be significantly controlled by the resulting variations of the suction-surface curvature of the optimized blades, as shown in Fig. 15(c). For the OGV-ES, the first local minimum of the curvature is located at about 15% chord, whereas for OGV-MOGA it is at 40% of chord.

Overall Aerodynamic Characteristics.

Reynolds Number Characteristics. As a main result, the computed loss versus Reynolds number characteristics for the two optimized airfoils ES and MOGA are shown in Fig. 16 for the design incidence (AVDR = 1.0) and compared to previous results of the baseline airfoil. The white circles for OGV-BASE are taken from Fig. 12(b) in which the AVDR was slightly adjusted to the experiments. Therefore, the losses of OGV-BASE have been recalculated at the design Reynolds number with AVDR = 1.0 and plotted as double circles.

The numerical results clearly demonstrate that both optimized blades are superior in the whole Reynolds number range and that a dramatic loss reduction was achieved at the design point with $Re = 1.3 \times 10^5$. There is no sign of a steep increase of the total pressure losses below a certain critical Reynolds number in the

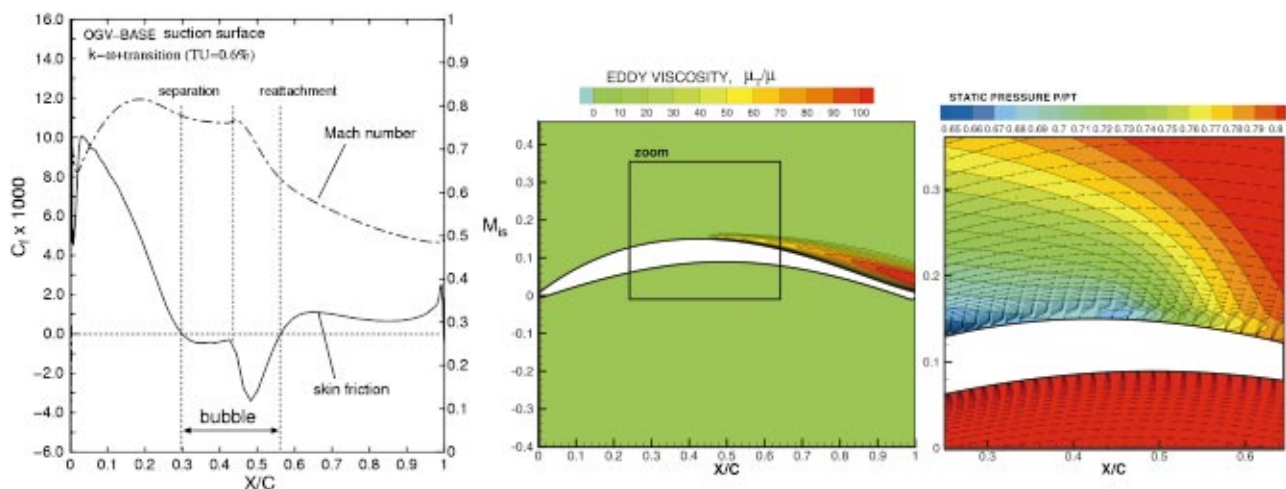


Fig. 13 Computed results with a $k-\omega$ turbulence and transition model at $Re \approx 2 \times 10^5$, $\beta_1 = 130^\circ$ (a) Skin friction coefficient and surface Mach number distribution, (b) eddy viscosity contour, (c) velocity vector and pressure contour.

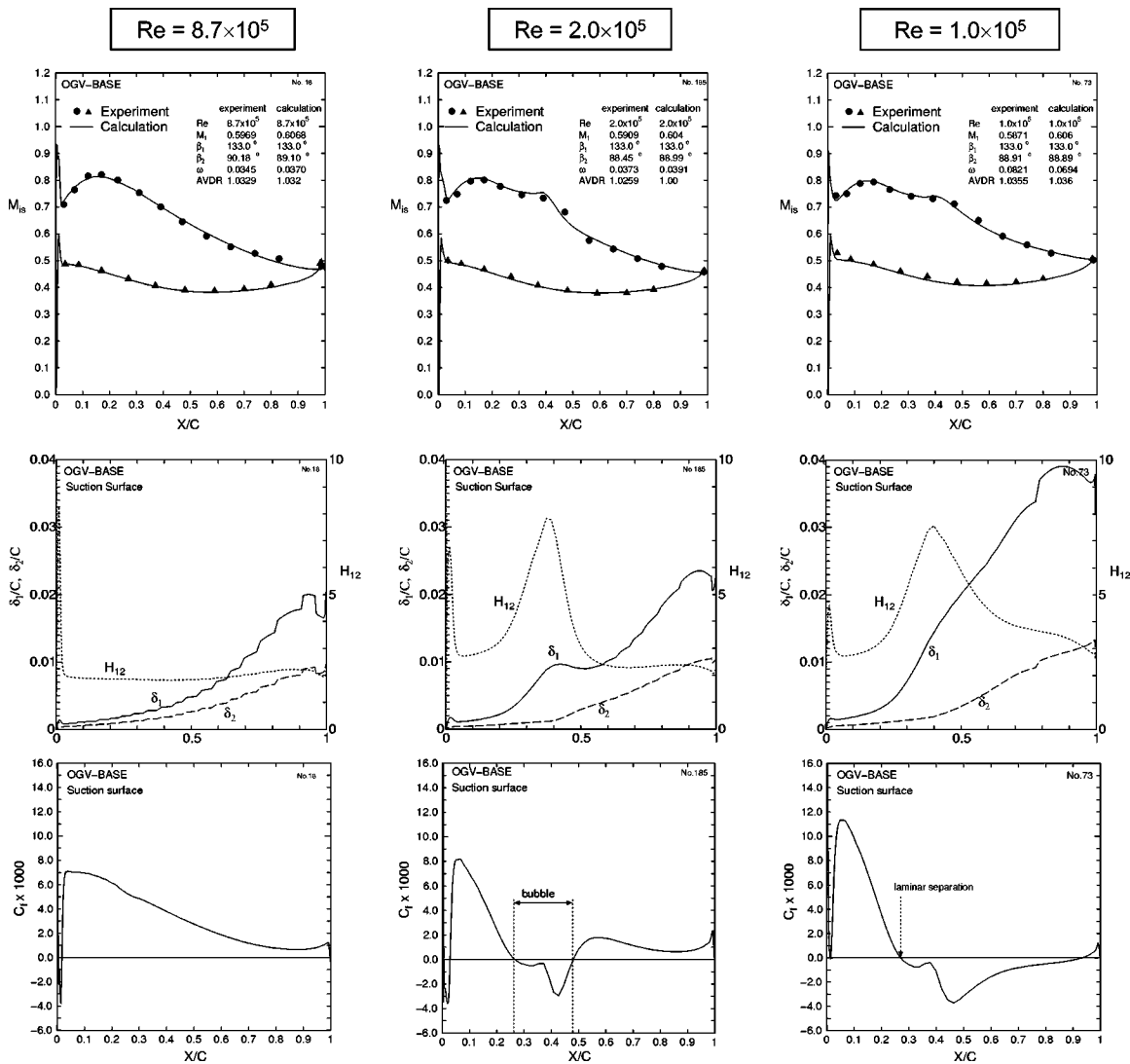


Fig. 14 Effect of Reynolds number on suction-side boundary layer property for OGV-BASE. Surface isentropic Mach number (top), boundary layer parameter (middle), and skin friction coefficient (bottom), $k-\omega$ turbulence and transition model applied

tested range. Another interesting point is that there seems to be a minimum loss point around $Re=1.8 \times 10^5$ for the MOGA airfoil; refer to Part II for a detailed discussion.

Incidence Angle Characteristics. A computed incidence angle characteristics for the optimized airfoils and for the baseline profile is shown in **Fig. 17** for the design Reynolds number of 1.3×10^5 and AVDR=1.0. Again the performance of OGV-BASE at the design Reynolds number with AVDR=1.0 is recalculated and plotted as double circles. The incidence range is fairly increased both for the negative as well as for the positive incidence range. Especially, the OGV-MOGA results show lower losses between 134 deg and 137 deg compared to OGV-ES but slightly higher ones at very negative incidences.

An explanation for these differences can be obtained from the blade surface Mach number distribution at the design incidence angle of 133.0 deg: As shown in **Fig. 18 (top)** the Mach number distribution is very different between the OGV-ES and MOGA profile. One reason why two different types of loading patterns have been obtained is the difference between the constraints for the ES and the MOGA optimization. In the case of OGV-ES, which was optimized for the design incidence only, the Mach number distribution shows an extreme front loading type, while

the maximum LE peak Mach number of OGV-MOGA is slightly decreased to achieve lower losses at the high incidences. As a result of the simulations **Fig. 17** clearly reflects that OGV-MOGA with a smaller peak Mach number shows superior performance on the positive incidence side and OGV-ES seems to be marginally better at the very negative incidences.

It is interesting to note that the optimized blades show a similar performance around the design flow angle of 133.0 deg, although both airfoil geometries are very different from each other. The Mach number distribution of the OGV-ES has an extreme forward located suction side Mach number maximum—a distribution similar to the one found in the low-speed C4-cascade tests of Rhoden [1] with minimum losses. Here, earlier boundary layer transition from laminar to turbulent flow seems to be important for low Reynolds numbers, and the well-controlled front loading airfoil leads to a good performance.

Boundary Layer Characteristics at Design Reynolds Number. **Figure 18** shows the computed isentropic profile Mach number distributions (top), the computed boundary layer parameter on the suction surface (middle), and the skin friction coefficient (bottom) for OGV-BASE, OGV-ES, and OGV-MOGA, respectively, for the design Reynolds number of 1.3×10^5 . In **Table**

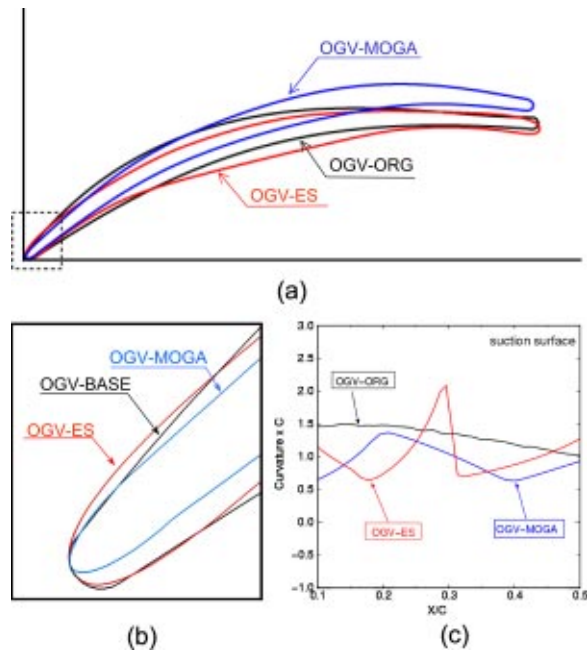


Fig. 15 Two optimized airfoils compared to baseline geometry, (a) blade profile, (b) leading edge part in detail, (c) curvature of suction surface

3 the corresponding aerodynamic parameters for the three cascades are summarized. For OGV-BASE, a well developed laminar separation bubble is observed on the suction surface in Fig. 18 (left). The laminar separation occurs at around 25% of chord and extends to approximately 90% of chord; a situation at which a “bubble burst” associated with high losses ($\omega=0.06$) can be expected. For OGV-ES, an early laminar separation bubble and transition at around 21% of chord is observed due to the strong adverse pressure gradient right from the beginning (Fig. 18 center). Downstream of transition this gradient is continuously relaxed toward the TE to keep the boundary layer far apart from turbulent separation. The computed result shows that the laminar separation starts around 7% of chord from leading edge. Turbulent re-

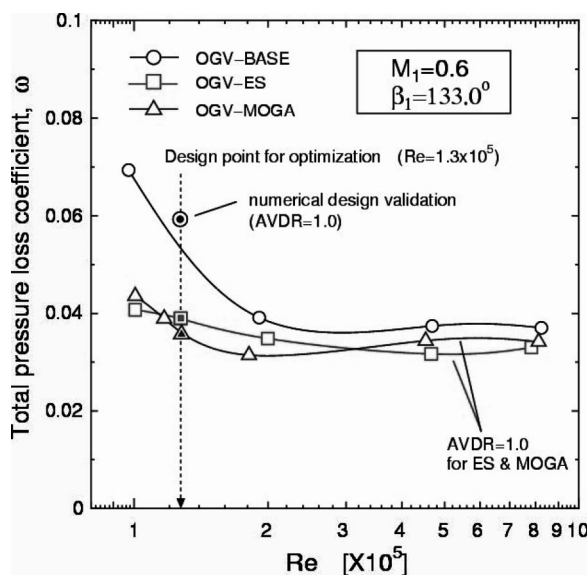


Fig. 16 Computed Reynolds number characteristics of three airfoils at design inlet flow angle of 133°

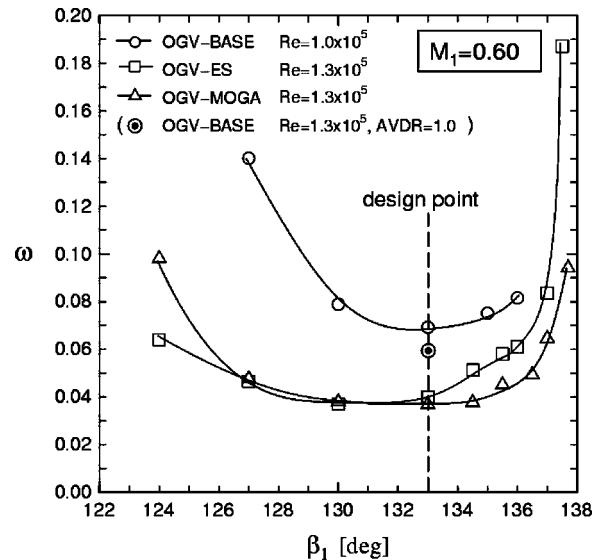


Fig. 17 Computed incidence characteristics of three airfoils at low Reynolds number of about 1.2×10^5

attachment is observed at approximately 25% of chord. On the MOGA airfoil, a small LE separation bubble is observed (Fig. 18 right), however, transition is not completed. The flow re-laminarizes due to a weak re-acceleration at around 10% to 20% of chord and the boundary layer thickness remains thin, see δ_1 and δ_2 in Fig. 18 (right). Laminar separation finally occurs at around 31% to 50% of chord with turbulent re-attachment.

The bubble positions for the two optimized blades correspond to local curvature minima at positions of about 15% (OGV-ES) and about 40% (OGV-MOGA) as shown in Fig. 15(c). On the other hand, the curvature for the baseline airfoil is monotonically decreased downstream but shows a higher level in the bubble position in relation to those of ES and MOGA. It seems that the boundary layer development is significantly controlled by the airfoil surface curvature underneath the bubble.

Conclusions

Evolutionary optimization methods, namely evolution strategy and the multi-objective genetic algorithm, have been applied to the design of a high turning compressor airfoil at very low Reynolds numbers together with a Navier-Stokes solver with Chien’s low Reynolds $k-\varepsilon$ turbulence model. Furthermore, the aerodynamic characteristics and the boundary layer properties for the baseline blade OGV-BASE and the two optimized airfoils OGV-ES and OGV-MOGA have been numerically analyzed using a newly developed flow solver that combines a $k-\omega$ turbulence model with an Abu-Ghannam/Shaw (AGS) transition model. The following conclusions can be drawn.

1. The results from the optimization algorithms without an explicit transition model in the flow solver show better performance for a wide range of Reynolds numbers in the numerical design validation than the baseline.
2. The superior performance of the optimized airfoils for very low Reynolds numbers is gained without losing performance at high Reynolds numbers.
3. The boundary layer analysis shows a large separation bubble for the baseline airfoil which is close to “bubble burst,” but relatively smaller separation bubbles with less drag for the two optimized airfoils.
4. In the case of OGV-ES, which was optimized only at the design incidence angle, a well-controlled front loading airfoil leads to an earlier boundary layer transition which in turn leads to a high performance for low Reynolds numbers.

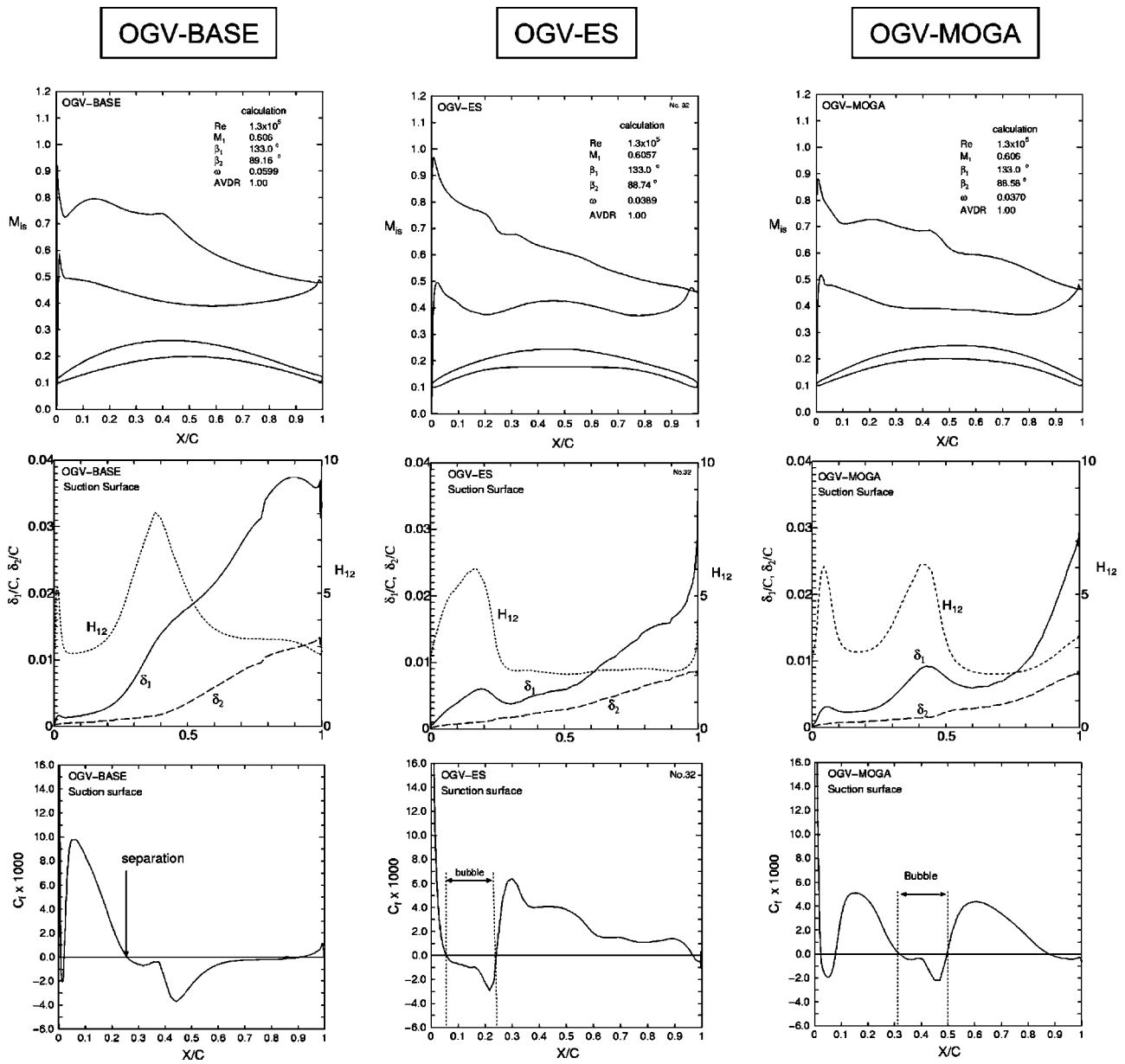


Fig. 18 Computed surface isentropic Mach number (top), boundary layer parameters (middle), and skin friction coefficient (bottom) at design point ($Re=1.3 \times 10^5$, $M_1=0.6$, and $\beta_1=133$ deg for the baseline airfoil (OGV-BASE) and two optimized airfoils (OGV-ES and OGV-MOGA)

- The OGV-MOGA cascade, which was optimized at off-design incidences as well as design incidence, obtained a slightly reduced velocity maximum at the leading edge with moderate local pressure gradients and the suction side partly remained laminar until about mid chord.
- The bubble positions for the optimized blades correspond to the positions with local curvature minima of the airfoil suction surface. Therefore, the curvature underneath the bubble seems to play an important role to minimize the bubble height and the associated drag and losses.

Table 3 Computed performance for two optimized airfoils and baseline airfoil at low Reynolds number

	$Re \times 10^{-5}$	M_1	M_2	β_1	β_2	p_2/p_1	AVDR	ω
OGV-ES	1.3	0.606	0.397	133°	88.74°	1.134	1	0.0389
OGV-MOGA	1.3	0.606	0.398	133°	88.58°	1.136	1	0.037
OGV-BASE	1.3	0.606	0.399	133°	89.16°	1.123	1	0.0599

7. The experimental validation of the performance of the optimized airfoils and additional analysis are carried out in Part II of this paper.

Acknowledgments

The authors are grateful to Wolfgang Steinert, who performed the test series, to Anton Weber and Harald Greza (all from the Institute of Propulsion Technology, DLR) and to Yaochu Jin and Edgar Körner (both from Honda Research Institute Europe) for helpful discussions and useful comments on the CFD simulation and the optimization. Finally, we thank Honda R&D Co., Ltd. for the permission to publish these results.

Nomenclature

AVDR = axial velocity density ratio: $AVDR = (\rho_2 u_2) / (\rho_1 u_1)$
 c = chord length
 C_f = skin friction coefficient = $\tau_w / (0.5 \rho_1 u_1^2)$
 H_{12} = shape factor = δ_1 / δ_2
 i = incidence angle
 k = turbulent kinetic energy
 M = Mach number
 p = pressure
 r = radius
 Re = Reynolds number = $\rho_1 u_1 c / \mu_1$
 s = blade spacing
 Tu = freestream turbulence level, in %
 u = velocity
 x = chordwise coordinate
 y = see Fig. 1
 y^+ = dimensionless distance from wall
 β = flow angle with respect to cascade front
 β_s = stagger angle
 δ_1 = boundary layer displacement thickness
 δ_2 = boundary layer momentum thickness
 $\delta\beta$ = tolerance for exit flow angle
 μ = dynamic viscosity
 μ_T = turbulent viscosity
 ρ = density
 τ_w = wall shear stress
 θ = blade metal angle
 ω = total pressure loss coefficient: $\omega = (p_{t1} - p_t) / (p_{t1} - p_1)$, or specific dissipation of turbulent kinetic energy
 Θ_{\min} = minimum thickness of blade
 Θ_{\max} = maximum thickness of blade

Additional Nomenclature for the Optimization

b_1 = minor axis of leading edge ellipse
 b_2 = minor axis of trailing edge ellipse
 $PS(i)$ = control points on pressure surface
 $SS(i)$ = control points on suction surface
 W_1 = wedge-in angle
 W_2 = wedge-out angle
 r_{L12} = ratio of minor to major axis of leading edge ellipse
 r_{T12} = ratio of minor to major axis of trailing edge ellipse

Subscripts

1 = inlet plane upstream of leading edge
 2 = exit plane downstream of trailing edge
 is = isentropic entity
 LE = leading edge
 TE = trailing edge
 t = total
 tr = transition

References

- [1] Rhoden, H. G., 1952, "Effects of Reynolds Number on the Flow of Air through a Cascade of Compressor Blades," ARC, R&M No. 2919.
- [2] Roberts, W. B., 1975, "The Effect of Reynolds Number and Laminar Separation on Axial Cascade Performance," ASME J. Eng. Gas Turbines Power, **97**, pp. 261–274.
- [3] Schreiber, H. A., Steinert, W., Sonoda, T., and Arima, T., 2003, "Advanced High Turning Compressor Airfoils for Low Reynolds Number Condition, Part II: Experimental and Numerical Analysis," ASME J. Turbomach., to be published.
- [4] Koeller, U., Moenig, R., Kuesters, B., and Schreiber, H. A., 2000, "Development of Advanced Compressor Airfoils for Heavy-Duty Gas Turbines, Part I: Design and Optimization," ASME J. Turbomach., **122**, pp. 397–405.
- [5] Benini, E., and Toffolo, A., 2002, "Development of High-Performance Airfoils for Axial Flow Compressor Using Evolutionary Computation," J. Propul. Power, **18**(3), pp. 544–554.
- [6] Drela, M., 1998, "MISES Implementation of Modified Abu-Ghannam/Shaw Transition Criterion (Second Revision)," M.I.T. Aero-Astro.
- [7] Schreiber, H. A., Steinert, W., and Kuesters, B., 2002, "Effect of Reynolds Number and Free-Stream Turbulence on Boundary Layer Transition in a Compressor Cascade," ASME J. Turbomach., **124**, pp. 1–9.
- [8] Chien, J. Y., 1982, "Predictions of Channel and Boundary Layers With a Low-Reynolds-Number Two Equation Model of Turbulence," AIAA J., **20**, pp. 33–38.
- [9] Arima, T., Sonoda, T., Shirotori, M., Tamura, A., and Kikuchi, K., 1999, "A Numerical Investigation of Transonic Axial Compressor Rotor Flow Using a Low-Reynolds-Number $k-\epsilon$ Turbulence Model," ASME J. Turbomach., **121**, pp. 44–58.
- [10] Goldberg, D. E., 1989, *Genetic Algorithms in Search, Optimization, and Machine Learning*, Addison-Wesley, Reading, MA.
- [11] Fonseca, C. M., and Fleming, P. J., 1993, "Genetic Algorithms for Multiobjective Optimization: Formulation, Discussion, and Generalization," Proceedings of the 5th International Conference on Genetic Algorithms.
- [12] Hansen, N., and Ostermeier, A., 1996, "Complete Derandomized Self-Adaptation in Evolution Strategies: The Covariance Matrix Adaptation," in *Proceedings 1996 IEEE International Conference on Evolutionary Computation*, IEEE Press, Piscataway, NJ, pp. 312–317.
- [13] Olhofer, M., Arima, T., Sonoda, T., Fischer, M., and Sendhoff, B., 2001, "Aerodynamic Shape Optimization Using Evolution Strategies," *Optimization in Industry*, I. C. Parmee and P. Hajela, eds., Springer-Verlag, New York, pp. 83–94.
- [14] Piegel, L., and Tiller, W., 1997, *The NURBS Book*, 2nd Ed., Springer-Verlag, New York.
- [15] Yamaguchi, Y., and Arima, T., 2002, "Aerodynamic Optimization for the Compressor Stator Blade," *Optimization in Industry*, I. C. Parmee and P. Hajela, eds., Springer-Verlag, New York, pp. 163–172.
- [16] Oyama, A., and Liou, M. S., 2002, "Multiobjective Optimization of a Multi-Stage Compressor Using Evolutionary Algorithm," AIAA Paper 2002-3545.
- [17] Wilcox, D. C., 1988, "Reassessment of the Scale-Determining Equation for Advanced Turbulence Models," AIAA J., **26**(11), pp. 1299–1310.
- [18] Abu-Ghannam, B. J., and Shaw, R., 1980, "Natural Transition of Boundary Layers—The Effects of Turbulence, Pressure Gradient, and Flow History," J. Mech. Eng. Sci., **22**(5), pp. 213–228.
- [19] Kuegeler, E., Weber, A., and Lisiewicz, S., 2001, "Combination of a Transition Model With a Two-Equation Turbulence Model and Comparison with Experimental Results," The 4th European Turbomachinery Conference, ATI-CST-076/01.
- [20] Mayle, R. E., 1991, "The Role of Laminar-Turbulent Transition in Gas Turbine Engines," ASME J. Turbomach., **113**, pp. 509–531.
- [21] Walker, G. J., 1993, "The Role of Laminar-Turbulent Transition in Gas Turbine Engines: A Discussion," ASME J. Turbomach., **115**, pp. 207–217.

Experimental Investigation of Unsteady Flow Field in the Tip Region of an Axial Compressor Rotor Passage at Near Stall Condition With Stereoscopic Particle Image Velocimetry

Baojie Liu

Hongwei Wang

Huoxing Liu

Hongjun Yu

Haokang Jiang

Maozhang Chen

School of Jet Propulsion,
Beijing University of Aeronautics and
Astronautics,
Beijing 100083, China

Stereoscopic particle image velocimetry (SPIV) was applied to a large-scale low-speed compressor facility with the configuration of the two CCD cameras placed on each side of the light sheet to make the measurement of the vortices in the cross flow section possible and to avoid the disturbance from the light sheet containing periscope-type probe. Instantaneous velocity and vorticity distributions were successfully documented at the tip region of the rotor at near stall condition. The measurement results clearly revealed the generation and evolution of the tip leakage vortex. Comparing to design condition, the tip leakage vortex at near stall condition generates and breaks down earlier and interacts more violently with mainstream, which causes large blockage and much loss. Whether corner vortex exists or not is the primary difference between near stall and design condition. Differing from the leakage vortex, the corner vortex is composed of multiple vortices developed from the suction surface of the rotor blade. The key mechanism for the generation of the corner vortex is that the rotation of the rotor has different effect on the evolution of positive vortices and negative vortices, which makes the positive vortices dissipates faster than the negative ones, the vortices at the rotor exit therefore bear mainly negative vortices, which induces the fluids to rotate clockwise at the corner and forms the corner vortex. [DOI: 10.1115/1.1748367]

Introduction

The flow in the tip region of a compressor rotor is always complicated. Due to the interactions among various flows such as end-wall flow, blade boundary layer, tip leakage flow, and the influence of the rotating blade, there exist complex flow structures such as tip leakage vortex, corner vortex, local separation, radial and circumferential transportation of low-energy fluids, and the interaction between leakage flow and shock in high speed condition. Loss generated in the tip region is the major source of compressor rotor inefficiency, and is often the cause of compressor rotor stall. Mechanism of the complex flow in the tip region, therefore, is a hot issue in compressor aerodynamics. Investigation on the generation and evolution of the vortices in the tip region, and the relationship between them with compressor loss and stall is important for the development of high performance compressor. The study on the tip region flow is difficult even with current advanced measurement techniques and computational fluid dynamics (CFD).

Simple theoretical models have been established to describe leakage flow based on observation and experimental research, which include Rains' jet model, [1], Lakshminaragana's compound vortex model, [2], and Chen's similarity analysis of leakage vortex, [3], etc. These simple models successfully described the basic characteristic of leakage flow, and also demonstrated its inviscid characteristic. Detailed structure of tip leakage flow was experimentally investigated on planar cascades and large-scale

compressor facilities. Stable leakage vortex, tip separation vortex, and secondary vortex were successfully found by detailed measurement on stationary planar cascades, [4,5]. In contrast, the measurement results on compressor facilities are different from each other, [6–13]. Few of them have detected the stable leakage vortex at the rotor exit, and their position, intensity, and scale are much different from those in the planar cascades. The detail structure of the leakage vortex in the rotor passage was not successfully measured because of the obvious measurement difficulties in the rotor, except for some very limited results by LDV whose spatial resolution was not adequate. These complex measurement results represent the unsteady and viscous nature of the tip leakage flow. Two explanations were proposed to explain why there is no leakage vortex at the rotor exit on most compressor facilities. The first one considers that the leakage flow is mixed into the main flow before it can roll up into a leakage vortex, [12]. Another considers that the leakage vortex has broken down in the rotor passage. Recent unsteady CFD simulations on tip leakage flow, [14–16], show that the leakage vortex breaks down in the rotor passage in high-speed compressors or low-speed compressors working at near-stall condition. However, at the working point of most low-speed compressor facilities, CFD results are different from most experimental results in that a stable leakage vortex exists at the rotor exit. In summary, steady characteristics of rotor tip leakage flow are well understood based on mean flow, turbulence characteristics, and pressure distribution on the casing after more than half-century study. However, the measurements and computations on the tip region flow are far more than sufficient to analyze the formation, evolution, and dissipation of the leakage vortex and corner vortex. Breakthrough techniques such as stereoscopic particle image velocimetry (SPIV) should be applied to the

Contributed by the International Gas Turbine Institute and presented at the International Gas Turbine and Aeroengine Congress and Exhibition, Atlanta, GA, June 16–19, 2003. Manuscript received by the IGTI December 2002; final revision March 2003. Paper No. 2003-GT-38185. Review Chair: H. R. Simmons.

Table 1 Parameters of the test compressor

Outer diameter (m)	1.0
Aspect ratio	0.6
Design speed	1200 rpm
Design mass flow rate	22.4 kg/s
Flow coefficient	0.58
Pressure rise coefficient	0.4
Vortex design	Free vortex
Configuration	IGV+ rotor+ stator
Number of blades	36+17+20
Airfoil type	C4
Blade camber angle	17.4+26.5+49.1
Blade chord (mm)	100+180+180
Reynolds number	7.5×10^5
Rotor tip clearance	0.5%
(As percentage of blade height)	

study of complicated unsteady flow in the tip region of compressor rotor. In the present study, SPIV was used on a single-stage low-speed large-scale compressor facility to obtain the three-dimensional instantaneous velocity distribution. Measurement was acquired on a few cross sections at the tip region of the rotor passage at near stall condition. The structure and the mechanism of the tip leakage flow and corner vortex were discussed in the paper based on the instantaneous results to give insight on the issues proposed above.

Compressor Facility

Measurements were acquired in the low-speed large-scale compressor facility in Beijing University of Aeronautics & Astronautics. A full specific of the geometric and aerodynamic characteristics for the experiment facility was given here for the consideration of the influence by them for further comparison and analysis. The key parameters of the compressor facility are as **Table 1**. The facility is a typical single-stage low-speed compressor facility and the flow in the tip region should be able to represent most low-speed compressors. Performance of the compressor is shown as **Fig. 1**, and the inlet stagnation pressure and axial velocity distribution 15 mm before the leading edge of the rotor are as **Fig. 2**. A curved glass casing window with length of 420 mm, width of 280 mm and thickness of 5 mm is located at the rotor's tip region for optical measurement.

The layout of the measurement cross-sections is as **Fig. 3**. Eight cross sections were arranged from 30% to 110% chord length with interval of 10% chord length. The cross sections were near the suction surface of the rotor blade with a width of half of the rotor passage and a height of half of the rotor blade. The effective area of the cross sections, however, was different due to the intensive light reflection from the hub and the random movement of the seeding, most with a height of one-third the blade height. The

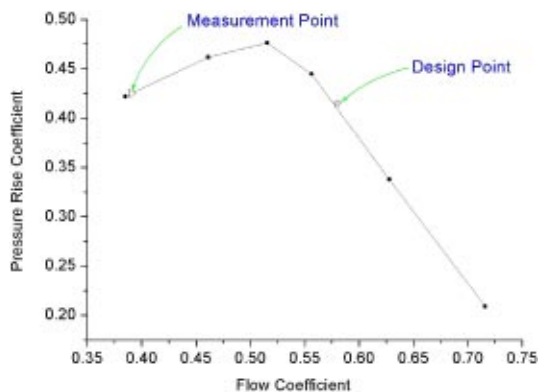


Fig. 1 Compressor characteristic

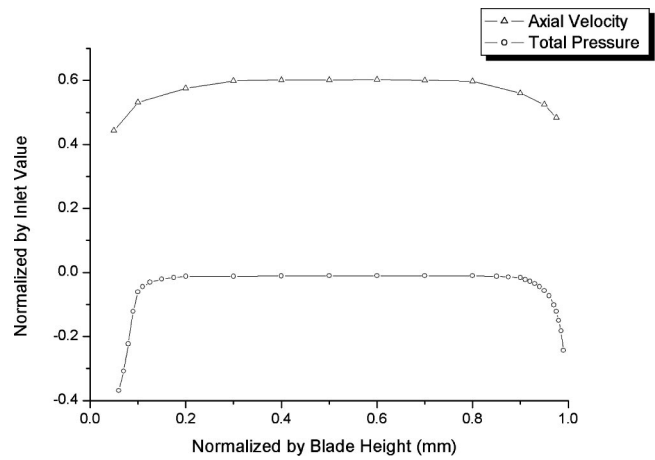


Fig. 2 Rotor inlet axial velocity and total pressure distributions

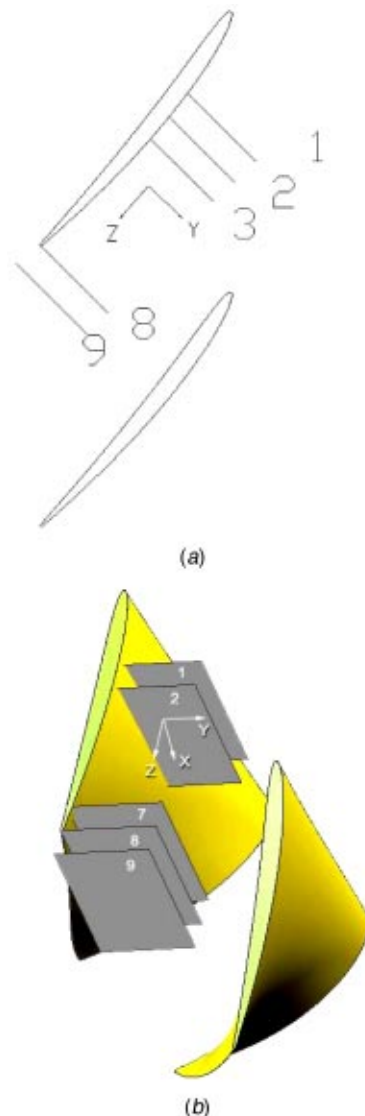


Fig. 3 SPIV measurement cross sections

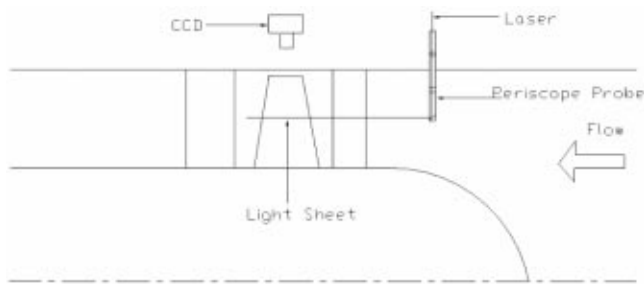


Fig. 4 Measurement scheme of PIV

coordinate is based on the measurement cross sections, which were perpendicular to the tip chord of the blade. The velocity axis X , Y , and Z for velocity u , v , and w are shown on the Fig. 3.

SPIV System

Particle image velocimetry (PIV) breaks through the limit of single-point measurement techniques because of its capability of measuring the instantaneous velocity distribution of an unsteady complex flow. It also allows the advantages of nonintrusive, high spatial resolution, huge data acquisition capacity, and fast testing operation, [17–19]. The accuracy of PIV is comparable to LDV now, [17,20]. It has been widely used in the studies range from low-speed to high-speed, from large scale to microscale, and from external flow to internal flow, especially for the unsteady flows.

Stereoscopic particle image velocimetry (SPIV) offers the potential to shed light on the problem of streamwise vortex measurement in turbomachinery. Two CCD cameras are used in the SPIV measurement, which can be placed on the same side of the light sheet or on each side of the light sheet, and there must be certain angle between the optics axis of each camera and the light sheet. Comparing to the PIV configuration shown in Fig. 4, these features ensured SPIV to obtain not only the instantaneous three-dimensional velocity distribution in the cross section of blade passage as shown in Fig. 5, but also the application in multistage turbomachinery.

SPIV with two CCD cameras placed at each side of the light sheet was applied to the measurement of rotor tip leakage flow and corner flow in the low-speed large-scale research compressor facility in this paper. Instantaneous velocity and vorticity distribution in eight cross sections of the rotor passage were successfully documented at near stall condition. The whole SPIV system is manufactured by TSI incorporation. As described in Table 2, it is built with high performance CCDs and is applicable for common cases. Phase locking was used to make sure the measurement was in the same position relative to the same blade in the experiment. The instantaneous flow field characteristics taken in the same cross-section do not relate with each other directly since the ac-

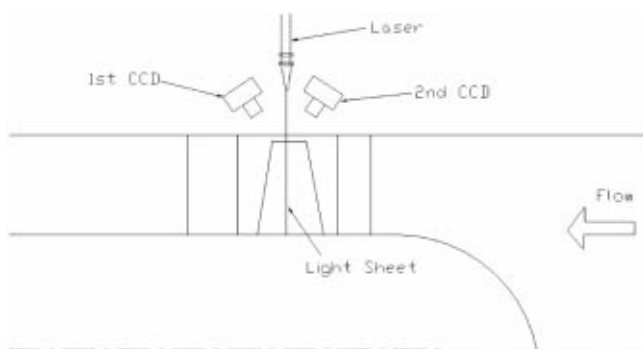


Fig. 5 Measurement scheme of SPIV

Table 2 Parameters of the SPIV system

Light resource	Dual-cavity YAG laser, 150 mJ/pulse, 30 Hz
CCD	1280×1024 Pixels, 3.7 Hz, minimum time interval 0.5 μ s
Synchronizer Acquisition and analysis software	TSI model 6300 TSI INSIGHT3

quisition frequency of the SPIV is far lower than the blade passing frequency, which should be noticed in the analysis later.

Seeding

Seeding is the key for the optical techniques such as LDV or PIV when they are applied on compressor facilities. An effective method is to seed only around the measurement region to avoid the difficulty caused by the huge flow rate and complicated flow in such facilities. A smoke generator was built and placed 5–6 meters in front of the inlet of the compressor to scatter the seed uniformly. The seed is not very uniform in the measurement region due to the unstable movement of the incoming air, which is the reason that a region of insufficient measurement results was documented at each cross section.

More details of the measurement and data processing please refer to the previous paper, [21]. All the units are international ones except those specified in the paper.

Results and Discussion

There are many results concerning the rotor tip leakage flow using single point measurement, most of which were measured at design condition and at rotor exit. The discussion here will focus on the instantaneous flow structure in the rotor passage and the mechanism of evolution of leakage flow as well as corner flow at near stall condition.

The vortex mentioned in this paper means a concentrated vortex with definite size that rotates around a vortex core with pure vorticity, such as the leakage vortex. It is unreliable to recognize a vortex from the velocity distribution in a complex flow with multiple vortices since the result will depend on the location of an observer. The vortex distribution as well as velocity distribution was used to do this. The result shows that the vortex recognition based on the vorticity distribution is more reliable than the one based on the velocity distribution. All the analysis is in the rotor frame since the vorticity distribution was calculated based on relative velocity. To achieve a high spatial resolution, the measurement area was limited to be half of the passage's width, which is 60 mm due to the limitation of the pixels of the CCD. The achieved resolution is around 1 mm, however, it is more than adequate to recognize the small-scale structure of the turbulence flow. Concerning the light reflection from the blade surface, all resulted measurement areas are 4 mm away from the blade suction surface, which means that no data is in the boundary layer.

Evolution of Tip Leakage Flow and Corner Flow

Figure 6 are the measurement results at 30% chord. The vectors in the figures represent projected velocity on the observed plane. A clear leakage vortex is detected here, which means the leakage vortex is generated in upstream. The streamwise velocity of the vortex core is much lower than the velocity in the mainstream, which indicates the leakage vortex is not very stable. Some low-speed regions exist near the blade suction surface at this cross section, and they bear high positive or negative vorticity. Mainstream flow should achieve maximum speed here since the 30% chord cross section is the maximum thickness location for the blade for this rotor. The low-speed regions indicate that the flow near the blade suction surface becomes unstable and presents

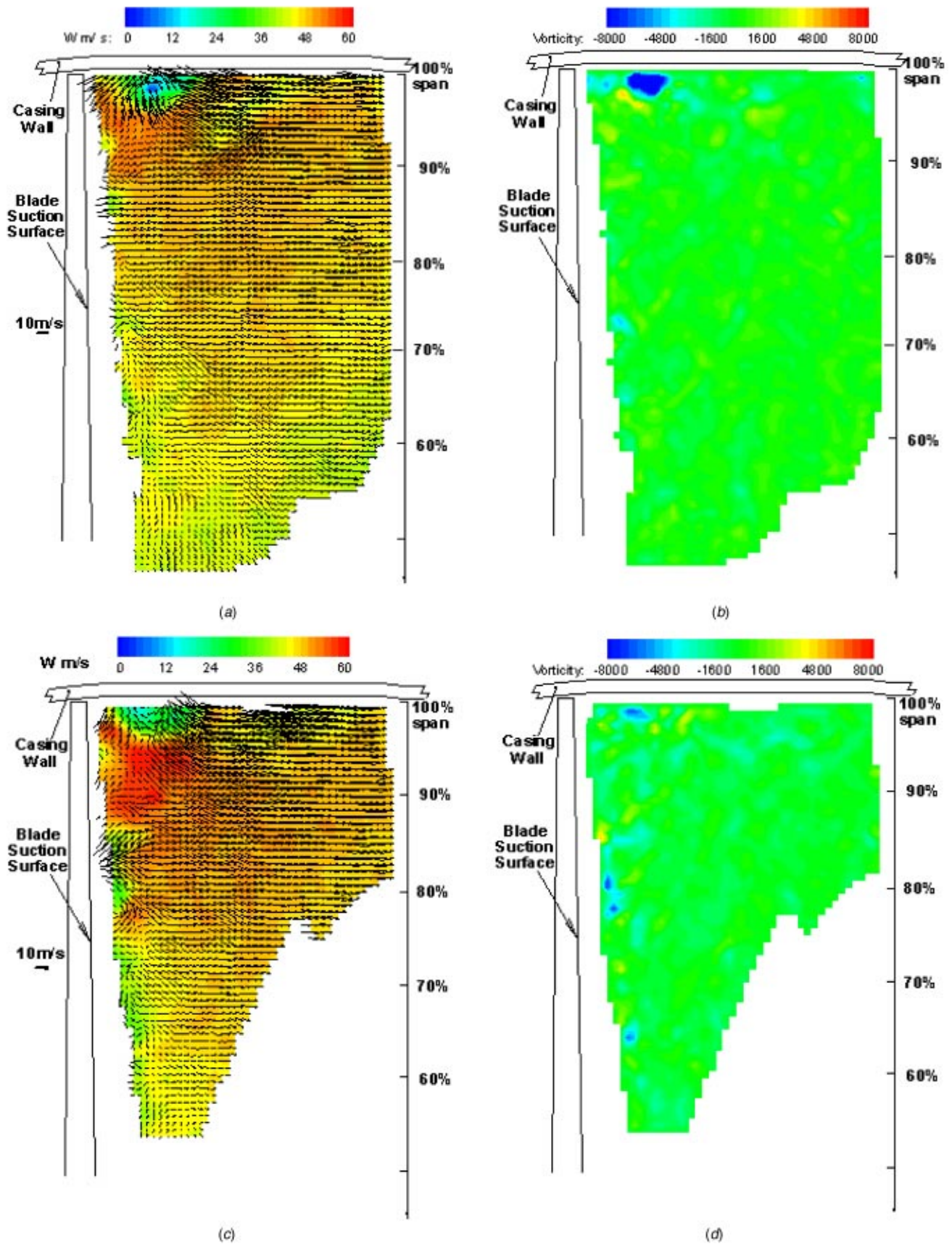


Fig. 6 Two instantaneous measurement results at 30% chord at near stall condition (left: velocity w distribution; right: corresponding vorticity distribution)

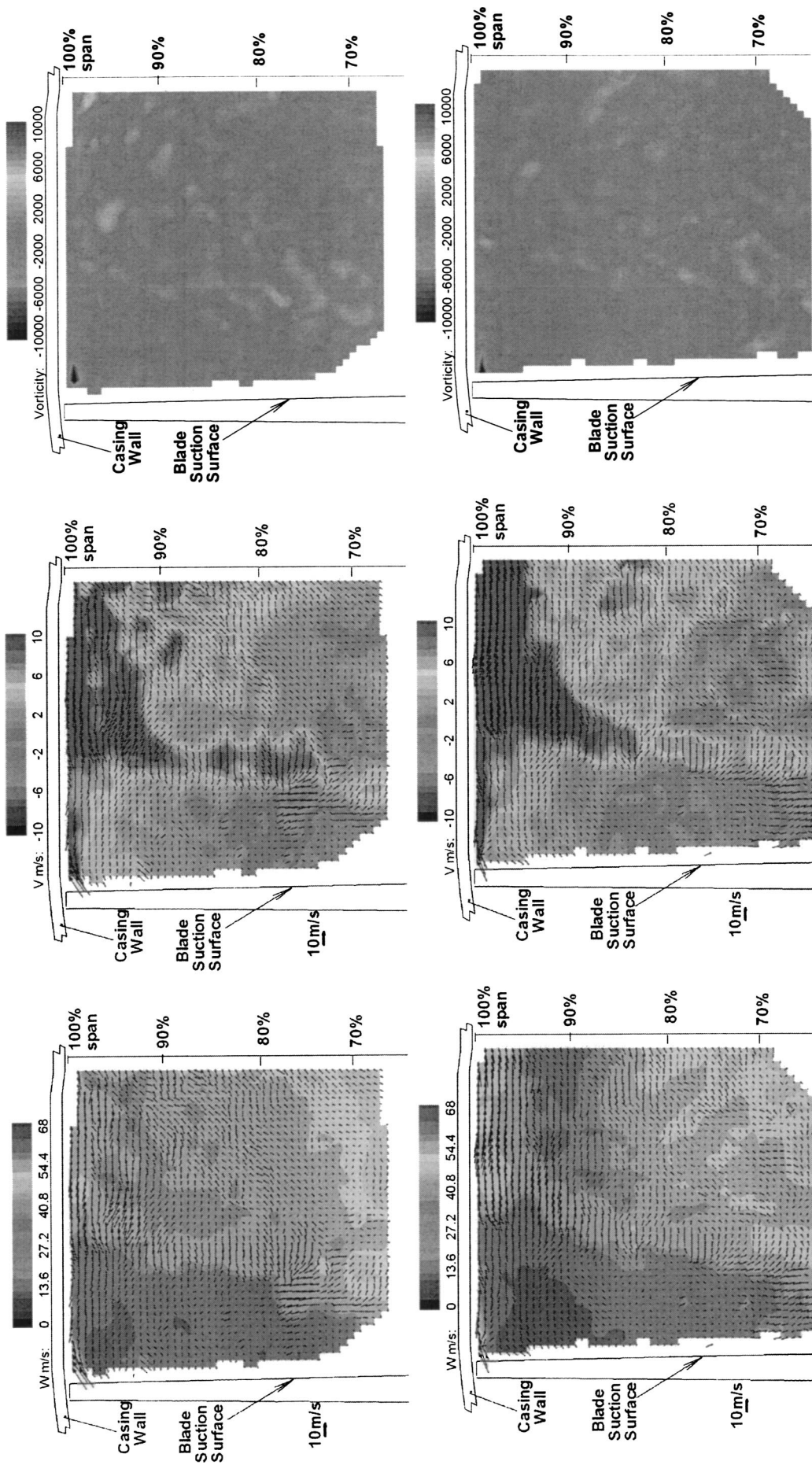


Fig. 7 Two instantaneous measurement results at 30% chord at design condition (left: velocity w distribution; middle: velocity v distribution; right: corresponding vorticity distribution)

a three-dimensional characteristic although the flow does not separate in the whole. The wake of IGV is not clearly shown in **Fig. 6**; however, it can be clearly discerned at design condition as shown by **Fig. 7**, especially in the figure of velocity v distribution, which means that the wake of IGV diffuses earlier at near stall condition.

The measurement results at 40% chord are shown in **Fig. 8**. The leakage vortex appears less concentrated at some instants and its shape varies. The first leakage vortex appears spiral divergence and the vorticity at the vortex core begin to split in the figure, which indicates the leakage vortex becomes unstable. In addition, the local low-speed regions near the blade suction surface continue to develop and connect to each other, but they do not transport in radial direction.

The measurement results at 50% chord are shown in **Fig. 9**. The leakage vortex has broken down here, but the splitted vortex core does not interact violently with mainstream at the beginning. After the leakage vortex breaks down, the vortex folds because the velocity in the vortex core is much lower than its exterior margin, so some small vortex spots with positive-vorticity appears in the core region after the leakage vortex breaks down. The low-speed regions near the suction surface continue to develop and begin to merge together. While the low-speed regions are flowing downstream, their streamwise velocity decreases continually due to adverse pressure gradient. Some of the low-speed regions almost stagnate at this section—as shown in the right figure of **Fig. 9**. Large velocity difference between the low-speed region and mainstream causes the vortex near the suction surface to fold rapidly, which forms some streamwise vortices with positive or negative vorticity and arise intermittently.

Thanks to the entrainment of these streamwise vortices, the low-speed flow near the suction surface is energized by the mainstream, which prevents the flow separation. The unsteady nature of flow makes the measurement results vary with each other remarkably. As shown in **Fig. 9**, sometimes the flow near the suction surface is relatively uniform and the streamwise vortices are relatively weak: sometimes are near stagnated and the streamwise vortices are very strong, which are comparable to the broken leakage vortex. Also, the near-stagnation low-speed flows begin to transport up in the radial direction. Although the leakage vortex has broken down and the low-speed flows near the suction surface are fully developed, they are still separated apart by the mainstream.

Thanks to the entrainment of these streamwise vortices, the low-speed flow near the suction surface is energized by the mainstream, which prevents the flow separation. The unsteady nature of flow makes the measurement results vary with each other remarkably. As shown in **Fig. 9**, sometimes the flow near the suction surface is relatively uniform and the streamwise vortices are relatively weak: sometimes are near stagnated and the streamwise vortices are very strong, which are comparable to the broken leakage vortex. Also, the near-stagnation low-speed flows begin to transport up in the radial direction. Although the leakage vortex has broken down and the low-speed flows near the suction surface are fully developed, they are still separated apart by the mainstream.

The measurement results at 70% chord cross-section are shown in **Fig. 10**. The broken leakage vortex begins to interact with mainstream violently now, which can be concluded from instantaneous rate of shear strain distribution, where the region with high rate of shear strain and low energy is much larger in the tip area than the one at 50% chord section. The resulted low-speed flow blocks the mainstream, and the interaction causes much loss. Low-speed flows near the suction surface continually develop and begin to transport in radial direction together. Pushed by the radial transportation fluid, the flow near the casing wall also begins to transport circumferentially. The low-speed flow near the suction surface begins to merge together with the low-energy leakage flow in this cross section.

The measurement results at 90% chord cross-section are shown in **Fig. 11**. The low-energy core of the broken leakage vortex has moved out of the measurement area. The low-energy fluid transported up radially from the suction surface begins to concentrate at the corner. The concentration could happen because of the flow turning at the corner and the large amount of negative vorticity vortices inside the low-energy fluid. The low-energy fluid concentrated in the corner has a large scale and blocks the mainstream, as shown in **Fig. 11**, which is obvious because the mainstream flow speed near the corner is much higher than that in other regions.

The measurement results at 100% and 110% chord cross sections are shown in **Fig. 12** and **Fig. 13**, respectively. Corner vortex has developed in these locations. From the instantaneous measurement results in these two cross-sections, numerous vortices transported from the suction surface concentrate at the corner and form a large corner vortex with a scale of one third of the blade height. This kind of corner vortex is different than the typical concentrated vortex, since it is formed by many discrete vortices. Because of the numerous negative vorticity vortices concentrated in the corner region, the flow there is always rotating clockwise no matter whether or not an apparent corner vortex exists. In addition, the results in **Fig. 12** and **Fig. 13** reveal that not all the vortices transported from the suction surface have concentrated in the corner, some of them move further to the middle of the rotor passage along the casing wall, which also transports low-energy fluid to the region.

There are more than ten instantaneous measurement results at each cross section; their average results could represent the mean characteristics of the leakage flow and corner flow at near stall condition. **Figure 14** and **Fig. 15** are the integration of the measurement results in all cross sections for the average and instantaneous streamwise velocity w and streamwise vorticity. (The instantaneous results at each cross section in the figure do not relate to each other directly since they were not measured at the same time.)

Before the leakage vortex breaks down, its location and scale are stable and its circumferential outer edge is easily identified by the static pressure measurements on the casing wall. Once the leakage vortex breaks down, its circumferential outer edge, especially the edge near the suction surface is hard to identify by the static pressure. As shown in **Fig. 14** and **Fig. 15**, when the leakage vortex breaks down, it splits into many small vortices and these vortices form the core of the low-energy leakage flow and its circumferential outer edge moves to the pressure side of the passage quickly. (The static pressures on the case are not presented in this paper.)

Vortex breakdown is the key for the track of leakage vortex turn rapidly: First, when leakage vortex is stable, the pressure at the suction surface of blade tip is low due to vortex entrainment, which make the leakage vortex stay near the blade suction surface. Once it breaks down, the broken leakage vortex moves to pressure surface rapidly due to the lost of entrainment effect. Secondly, fluid in the leakage vortex is thrown out when the vortex breaks down and spreads out circumferentially due to the effect of casing shear flow, which causes the outer edge of broken leakage vortex to spread more rapidly.

From the difference between the averaged and instantaneous results of velocity and vorticity shown in **Fig. 14** and **Fig. 15**, although the average field can represent the development of the tip leakage flow and the corner flow, the detail flow structures and their unsteady characteristics are not covered, especially for the distribution of vorticity, which indicate the importance of unsteady measurement against statistical information.

The measurement results in all the cross-sections indicate that the break of the leakage vortex, the interaction between the broken vortex and mainstream, and the unstable flow on blade suction surface, the interaction between the corner vortex and mainstream is the trigger for the loss for a compressor at near stall condition. The comparison between the averaged and instantana-

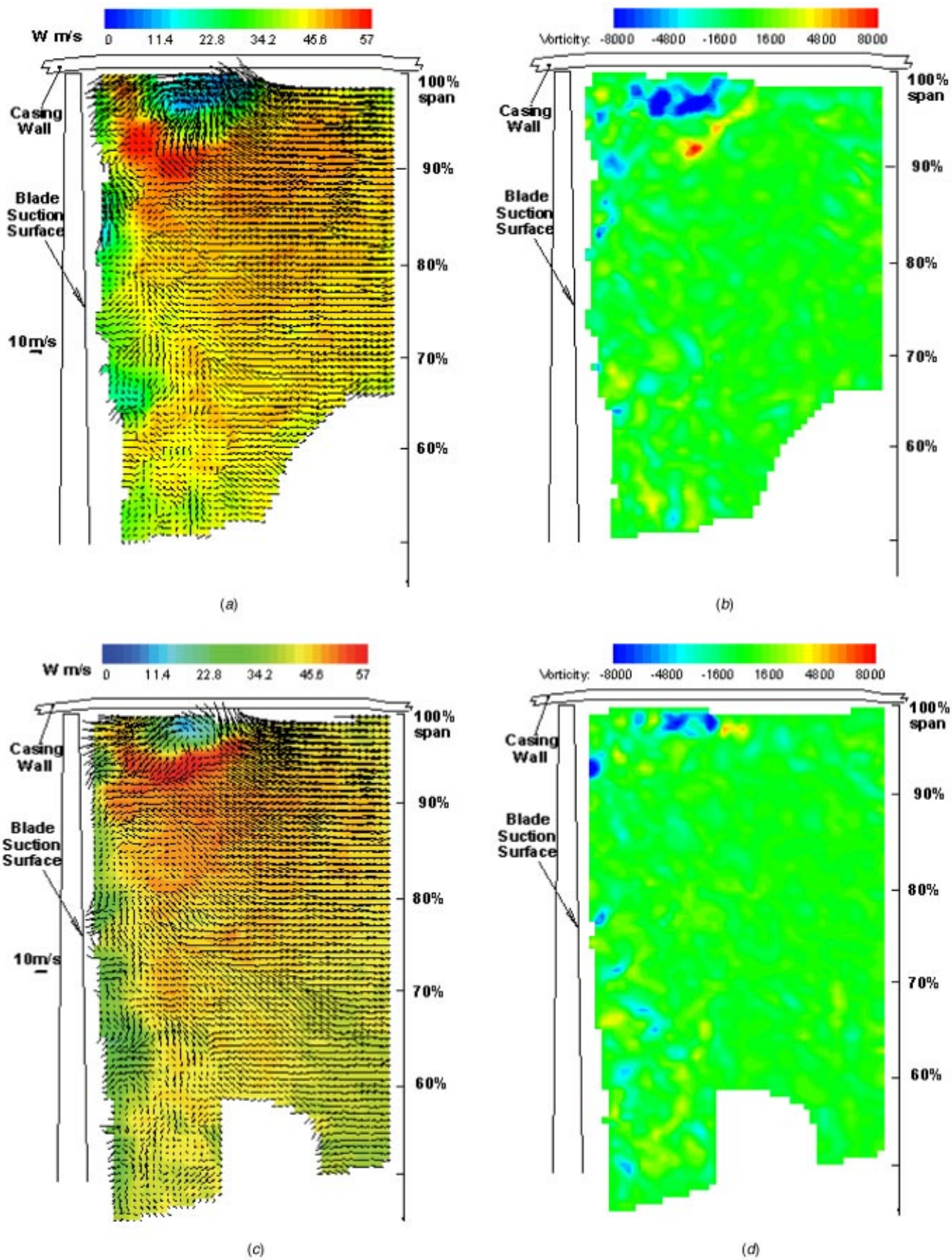


Fig. 8 Two instantaneous measurement results at 40% chord at near stall condition (left: velocity w distribution; right: corresponding vorticity distribution)

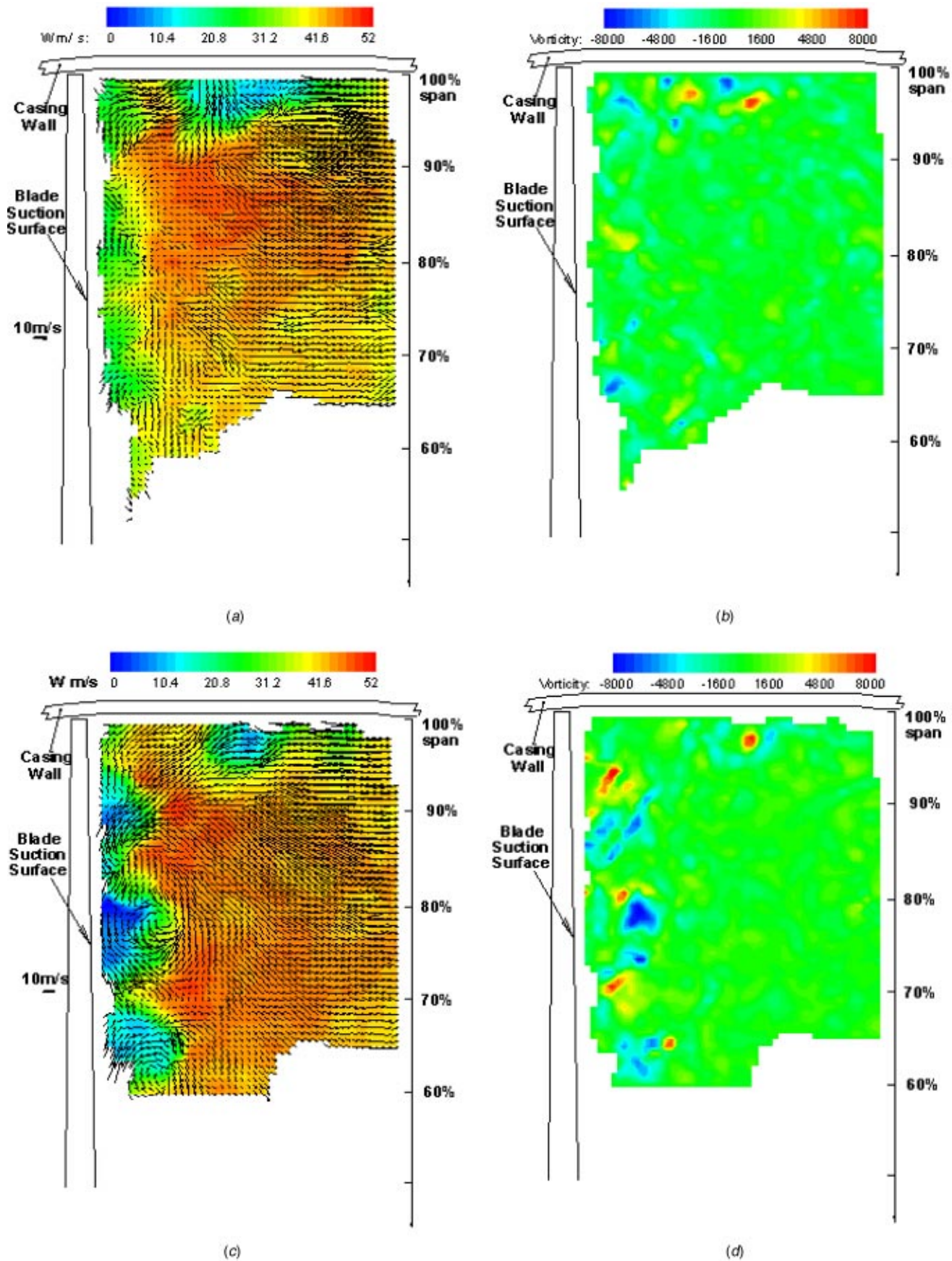


Fig. 9 Two instantaneous measurement results at 50% chord at near stall condition (left: velocity w distribution; right: corresponding vorticity distribution)

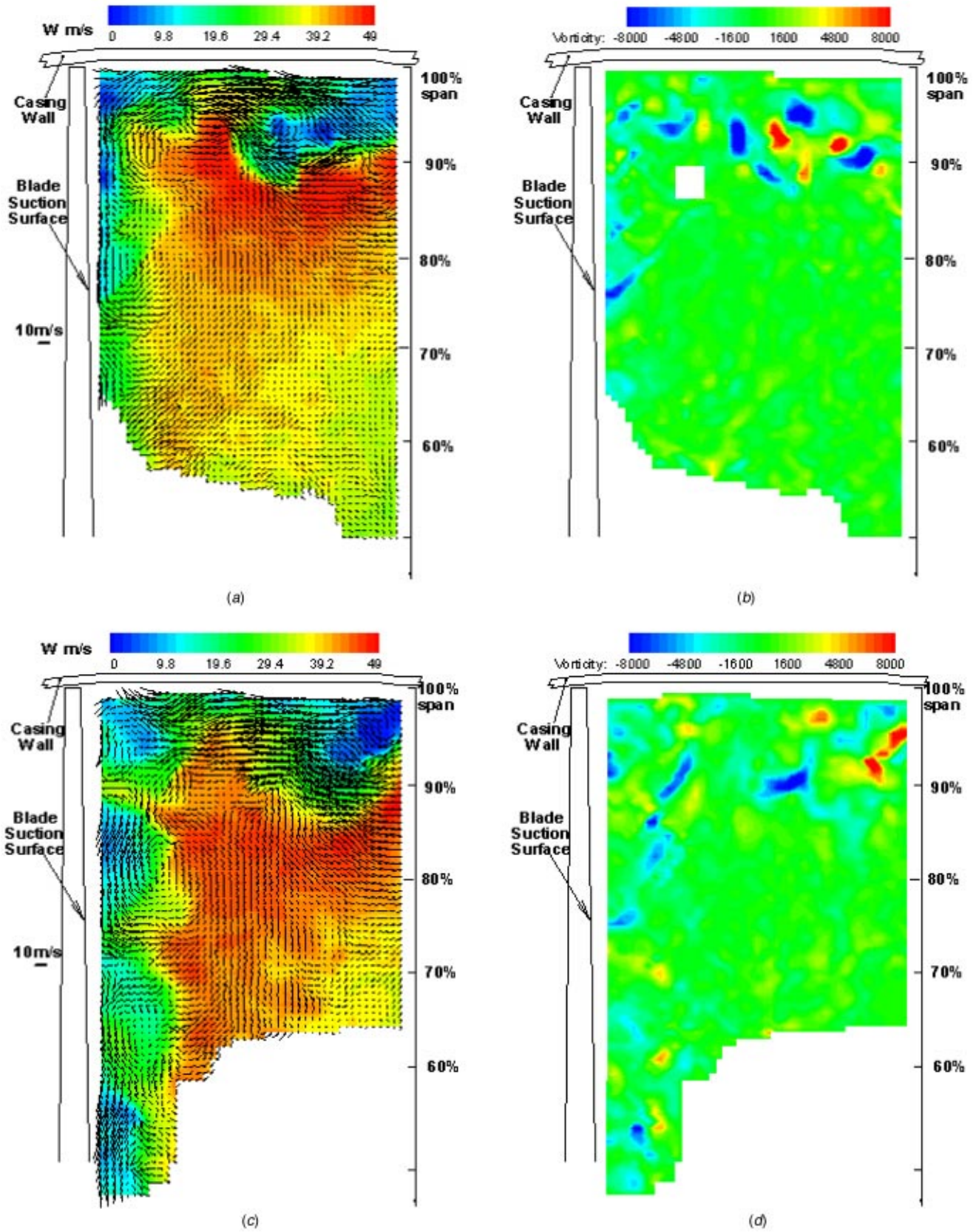


Fig. 10 Two instantaneous measurement results at 70% chord at near stall condition (left: velocity w distribution; right: corresponding vorticity distribution)

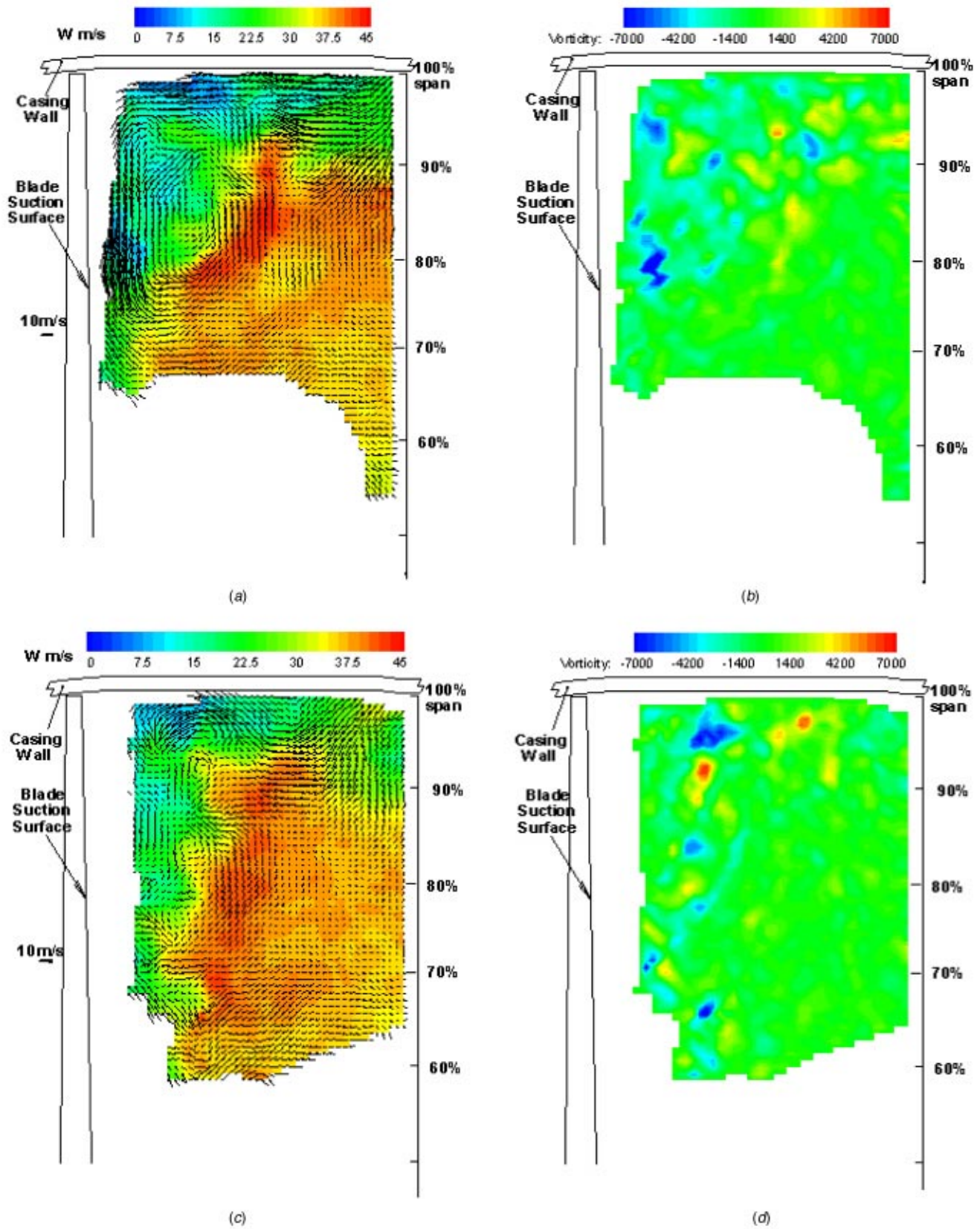


Fig. 11 Two instantaneous measurement results at 90% chord at near stall condition (left: velocity w distribution; right: corresponding vorticity distribution)

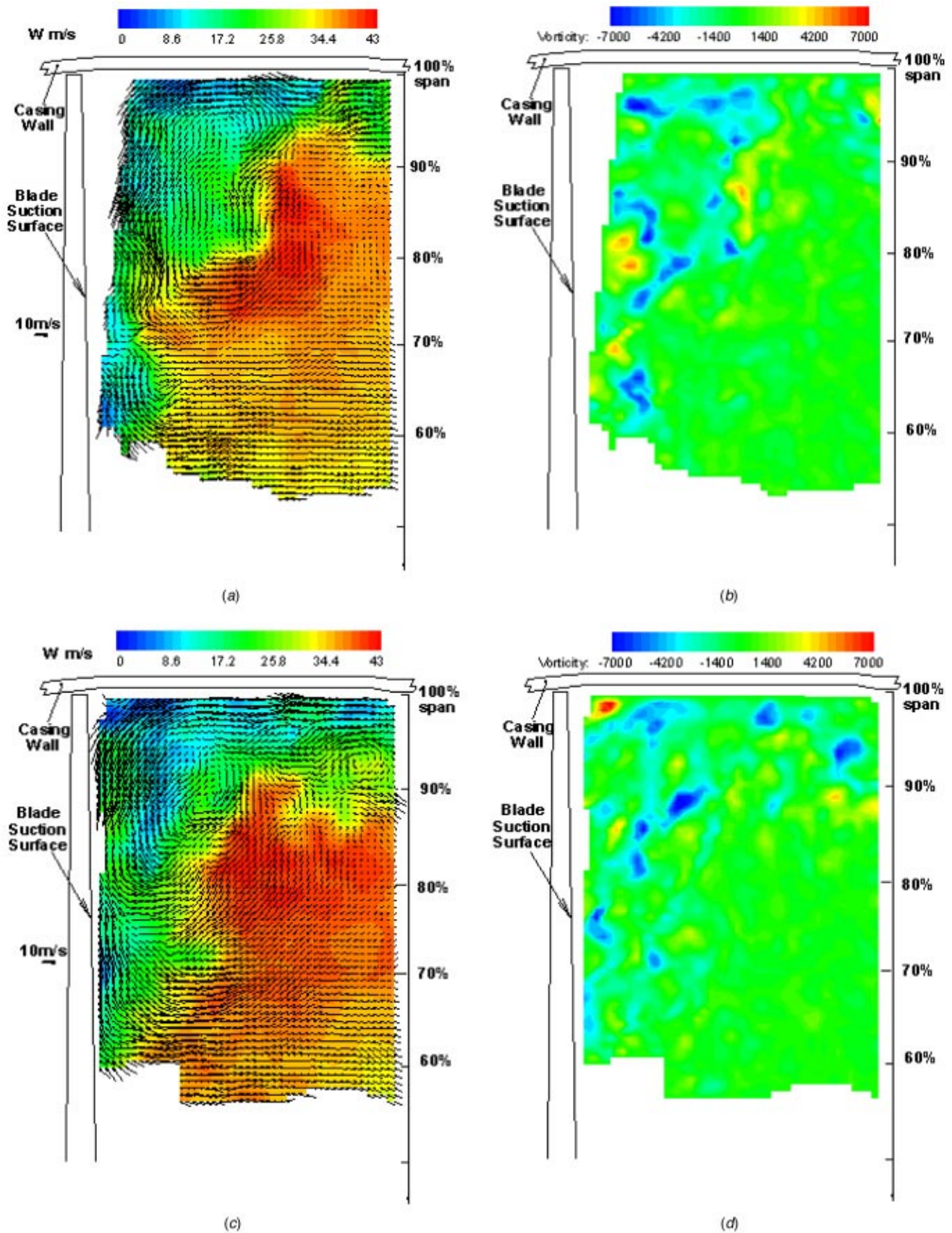


Fig. 12 Two instantaneous measurement results at 100% chord at near stall condition (left: velocity w distribution; right: corresponding vorticity distribution)

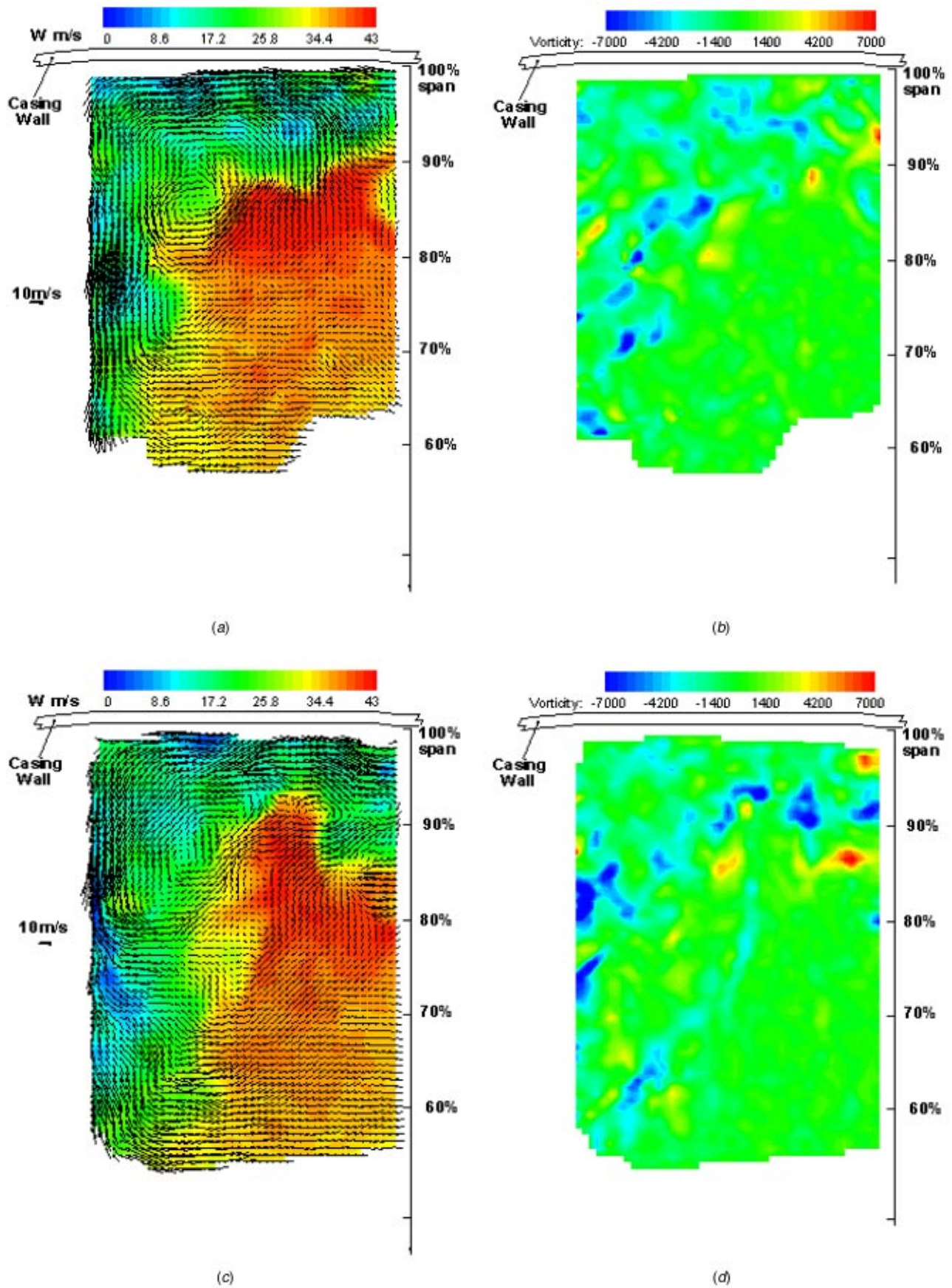


Fig. 13 Two instantaneous measurement results at 110% chord at near stall condition (left: velocity w distribution; right: corresponding vorticity distribution)

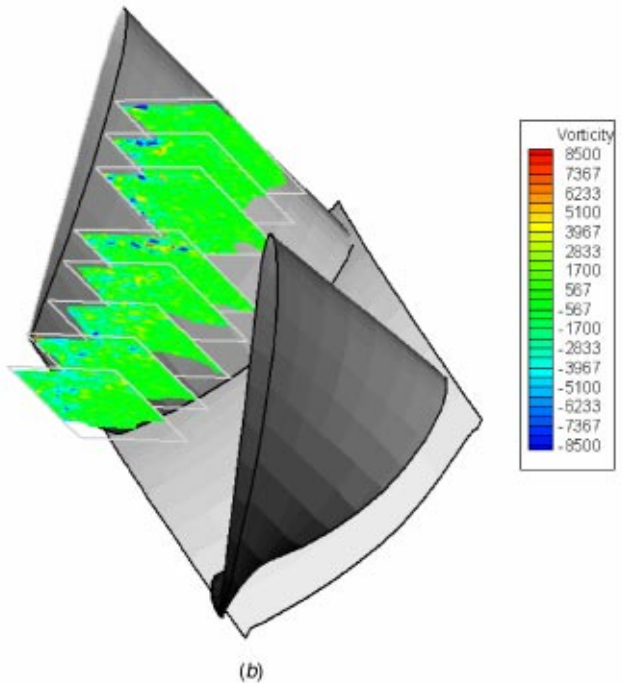
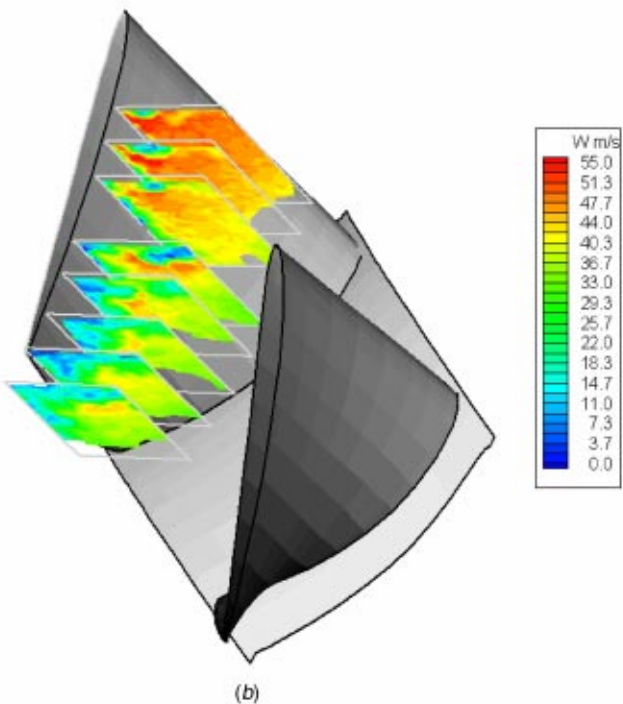
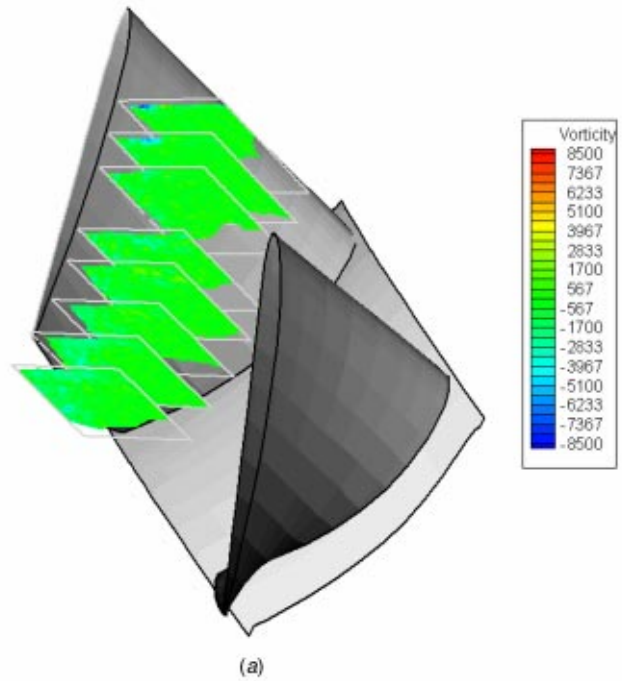
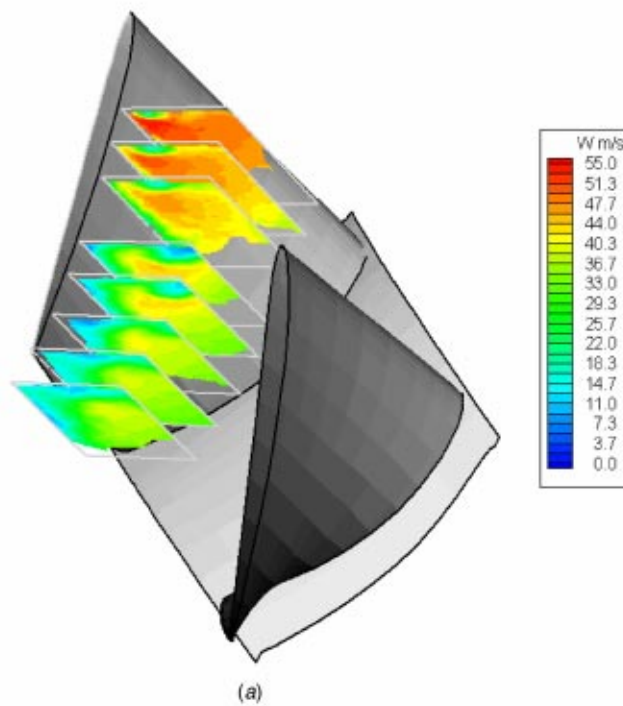


Fig. 14 Composite figure of velocity w distribution at near stall condition (left: average results; right: instantaneous results)

Fig. 15 Composite figure of vorticity distribution at near stall condition (left: average results; right: instantaneous results)

neous flow fields and the complex flow in compressors such as the breakdown of vortices, flow instability, and interaction between various vortices and the mainstream reveals that the turbulence model used in compressors can improve its validation and accuracy only by considering more physics information.

Mechanism of Corner Vortex Formation

At near-stall condition, a key to the formation mechanism of the corner vortex is that most of the vortices in the corner bear

amount of negative vorticity near the rotor exit. That is to say, the development of vortices is selected by the rotation of the compressor.

The vorticity transportation equation in incompressible condition is as follows:

$$\frac{D\vec{\omega}}{Dt} - \vec{\omega} \cdot \nabla \vec{u} = \nabla \times \vec{F} + \nu \nabla^2 \vec{\omega} \quad (1)$$

As in Eq. (1), source terms that can change the vortex vorticity in

low-speed compressors are the two right-hand side terms. In rotational coordinate, due to the Coriolis force, not all the body force added to the fluid is potential. Look at Eq. (2).

$$\nabla \times \vec{F} = \nabla \times (2\vec{\Omega} \times \vec{u}) \quad (2)$$

When vortex is expanding or contracting, the left-hand side in Eq. (2) is not zero and vorticity of vortex changes. From the evolution of the positive or negative vortices near the blade suction surface, the scale of the vortices varies gradually while flowing downstream. In this case, although the left-hand side of Eq. (2) is not zero, it should be a small quantity and does not affect the vorticity of the vortices very much.

Viscosity is another factor to the evolution of the vortices in compressors. Viscous dissipation is the ultimate reason for vortex dissipation. The dissipation is associated with not only the viscosity of the fluid but also the magnitude and distribution of the vorticity of a vortex. When the rotational direction of the vortex is the same of the compressor's rotation, Coriolis force enhances the pressure difference between the vortex center and its edge (main flow). The Coriolis force effect is reverse when the rotational direction of a vortex is opposite to the direction of compressors. This effect can make vortices with negative vorticity more stable than the ones with positive vorticity, which results in that positive vortices dissipate faster than negative vortices.

Magnitude of the Coriolis force relative to the inertia force is indicated by the Rossby number R_o , as defined in Eq. (3).

$$R_o = \frac{U_v}{\Omega L_v} \approx \frac{10}{125.7 \times 0.01} = 8 \quad (3)$$

The Rossby number of the vortex near the suction surface of the rotor blade can be estimated according to the vortex in Fig. 8, which is approximately 8. This indicates that the Coriolis force could have an important influence on vortex stability

The difference for dissipation speed of the positive and negative vorticity bearing vortices is the key reason for the selectivity of the evolution of the streamwise vortices in compressors. So the negative vortices are dominant in the corner near the rotor exit.

Conclusions

Instantaneous velocity field measurement was performed at typical cross sections in the low-speed large-scale compressor facilities in BUAA which have relatively small tip clearance and high Reynolds number working at near stall condition using SPIV technique. The mechanism of the formation, development, and evolution of the leakage vortex as well as the formation and evolution process of the corner vortex were discussed. The conclusions below are more suitable to low-speed compressors since the experiment was done on a low-speed compressor facility.

1. Flow phenomenon such as the formation, evolution and breakdown of the leakage vortex as well as the interaction between the broken leakage vortex and mainstream at near-stall condition are described and explained based on the instantaneous measurement results.
2. The breakdown of the leakage vortex causes the track of leakage vortex to turn abruptly and strong unsteady vortices form there. Losses mainly come from the viscous and turbulent mixing before the leakage vortex breaks down and strong interaction between the vortices and mainstream after the leakage vortex breaks down. The loss by the latter is much greater and is the main part of tip flow loss as indicated by the instantaneous rate of shear strain distribution in these sections in Fig. 16.
3. The occurrence of a corner vortex is the main difference for rotor tip flow at near stall condition compared to design condition. In difference to the leakage vortex, the corner vortex is a compound vortex with its vortex core composed by multiple vortices. The evolution of the low-energy flow

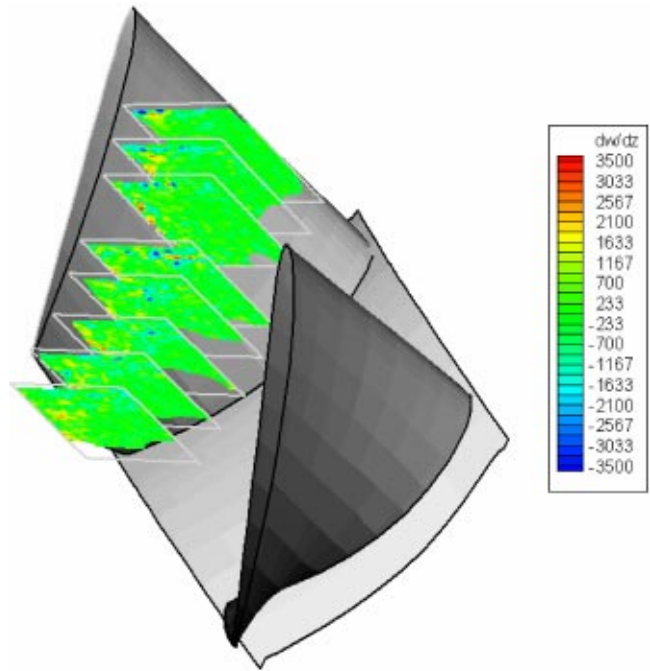


Fig. 16 Composite figure of instantaneous rate of shear strain distribution at near stall condition

near the blade suction surface and the mechanism of the corner vortex formation are described and discussed.

4. At near-stall condition, the low-energy large-scale corner vortex causes the flow at the rotor exit to present strong three-dimensional characteristic. Loss from the corner vortex is the main part of the loss from rotor tip corner flow; also, part of the low-energy fluid from the blade suction surface transports even to the middle passage near the casing wall and causes loss there.
5. A key mechanism for the generation of the corner vortex is the rotation of the compressor has a different effect to the negative or positive vorticity bearing vortices near the blade suction side. This selectivity causes the vortices concentrated at the corner to bear mainly negative vorticity and form corner vortex by the inducement of these vortices in the corner near the rotor exit.

Acknowledgments

The authors would like to acknowledge the support of National Science Foundation of China, Grant No. 50006001, and the support of National Foundation Research Project, Grant No. 1999022305. The authors also would like to thank the help and contributions of Mr. Huijing Yuan and Prof. Yueting Xu.

Nomenclature

- \vec{F} = body force vector
 L_v = vortex scale
 R_o = Rossby number
 U_v = rotation speed at the vortex edge
 t = time variable
 u, v, w = velocity with respect to X , Y , and Z
 ν = kinematic viscosity
 $\vec{\omega}$ = vorticity
 $\vec{\Omega}$ = compressor rotation speed

References

- [1] Rains, D. A., 1954, "Tip Clearance Flows in Axial Flow Compressors and

- Pumps," California Institute of Technology, Hydrodynamics and Mechanical Engineering Laboratories, Report No. 5.
- [2] Lakshminarayana, B., 1970, "Methods of Predicting the Tip Clearance Effects in Axial Flow Turbomachinery," *ASME J. Basic Eng.*, **112**, pp. 609–617.
- [3] Chen, G. T., Greitzer, E. M., Tan, C. S., and Marble, F. E., 1991, "Similarity Analysis of Compressor Tip Clearance Flow Structure," *ASME J. Turbomach.*, **113**, pp. 260–271.
- [4] Storer, J. A., and Cumpsty, N. A., 1991, "Tip Leakage Flow in Axial Compressor," *ASME J. Turbomach.*, **113**, pp. 252–259.
- [5] Kang, S., and Hirsch, C., 1993, "Experiment Study on the Three-Dimension Flow within a Compressor Cascade With Tip Clearance: Part I—Velocity and Pressure Fields," *ASME J. Turbomach.*, **115**, pp. 444–452.
- [6] Hunter, I. H., and Cumpsty, N. A., 1982, "Casing Wall Boundary Layer Development Through an Isolated Compressor Rotor," *ASME Journal Engineering for Power*, **104**, pp. 805–818.
- [7] Inoue, M., Kurou, M., and Fukuhara, M., 1986, "Behavior of Tip Leakage Flow behind an Axial Compressor Rotor," *ASME J. Eng. Gas Turbines Power*, **108**, pp. 7–14.
- [8] Inoue, M., and Kurou, M., 1989, "Structure of Tip Clearance Flow in an Isolated Axial Compressor Rotor," *ASME J. Turbomach.*, **111**, pp. 250–256.
- [9] Goto, A., 1992, "Three-Dimensional Flow and Mixing in an Axial Flow Compressor With Different Rotor Tip Clearances," *ASME J. Turbomach.*, **114**, pp. 675–685.
- [10] Stauter, R. C., 1993, "Measurement of the Three-Dimensional Tip Region Flow in an Axial Compressor," *ASME J. Turbomach.*, **115**, pp. 468–476.
- [11] Lakshminarayana, B., et al., 1982, "Three-Dimensional Flow Field in the Tip Region of a Compressor Rotor Passage, Parts I and II," *ASME J. Eng. Gas Turbines Power*, **104**, pp. 760–781.
- [12] Lakshmirayana, B., Zaccaria, M., and Marathe, B., 1995, "The Structure of Tip Clearance Flow in an Axial Flow Compressor," *ASME J. Turbomach.*, **117**, pp. 336–347.
- [13] Hongwei, Ma, and Haokang, Jiang, 2000, "Three-dimensional Turbulent Flow of the Tip Leakage Vortex in an Axial Compressor Rotor Passage," *ASME Paper 2000-GT-503*.
- [14] Schlechtriem, S., and Lotzerich, M., 1997, "Breakdown of Tip Leakage Vortices in Compressors at Flow Conditions Close to Stall," *ASME Paper No. 97-GT-41*.
- [15] Furukawa, M., Inoue, M., Saiki, K., and Yamada, K., 1999, "The Role of Tip Leakage Vortex Breakdown in Compressor Rotor Aerodynamics," *ASME J. Turbomach.*, **121**, pp. 469–480.
- [16] Furukawa, M., Saiki, K., Yamada, K., and Inoue, M., 2000, "Unsteady Flow Behavior Due to Breakdown of Tip Leakage Vortex in an Axial Compressor Rotor at Near-Stall Condition," *ASME Paper 2000-GT-666*.
- [17] Adrian, R. J., 1991 "Particle Imaging Techniques for Experimental Fluid Mechanics," *Annu. Rev. Fluid Mech.*, **23**, pp. 261–304.
- [18] Grant, J., 1997, "Particle Imaging Velocimetry: A Review," *Proc. Inst. Mech. Eng.: Part C*, **211**, pp. 55–76.
- [19] Raffel, M., Willert, C., and Kompenhans, J., 1998, *Particle Image Velocimetry: A Practical Guide*, Springer-Verlag, New York.
- [20] Yao, C., and Paschal, K., 1994, "PIV Measurements of Airfoil Wake-Flow Turbulence Statistics and Turbulent Structure," *AIAA Paper No. 94-0085*.
- [21] Baojie, L., et al., 2002, "SPIV Application in the Measurement Leakage Flow of Compressor Rotor," *Optical Technology and Image Processing For Fluids and Solids Diagnostics*, SPIE/Beijing.

Andrea Arnone

Michele Marconcini

e-mail: Michele.Marconcini@arnone.de.unifi.it

Alberto Scotti Del Greco

“Sergio Stecco” Department of Energy
Engineering,
University of Florence,
Via di Santa Marta, 3,
50139 Firenze, Italy

Ennio Spano

Fiat Avio S.p.A.—Direzione Tecnica,
Via Nizza, 312,
10127 Torino, Italy

Numerical Investigation of Three-Dimensional Clocking Effects in a Low Pressure Turbine

One and a half stages of a low pressure turbine were investigated using a three-dimensional time-accurate viscous solver. Unsteady analyses were carried out by varying the circumferential relative position of consecutive vanes to study the effects of clocking on performance. Assuming that efficiency improvements by clocking are linked to the wake tangential position with respect to the successive blade, a certain circumferential shift in this position can be observed along the blade height due to blade twist and nonradial stacking, giving different contributions. In order to assess this phenomenon, results from three-dimensional computations were compared with a quasi-three-dimensional analysis at mid-span. The effects of clocking on wake interaction mechanisms and unsteady blade loadings are presented and discussed. [DOI: 10.1115/1.1740780]

Introduction

The real flow in multistage turbomachines is inherently unsteady because of the relative blade row motion. This causes unsteady interaction of pressure fields, shock waves, and wakes between stators and rotors. These unsteady flows cause mixing and losses which need to be accounted for in order to include state-of-the-art predictions in design phase simulations.

In the last few years a lot of attention has been dedicated to the development of unsteady solvers used to investigate the physics of rotor-stator interactions. This research has led to a better understanding of the interaction mechanisms and showed how some unsteady effects can be successfully employed to reduce the number of components while still maintaining good performance. Many authors pointed out how high-lift (see Cobley et al. [1] and Curtis et al. [2]) and ultra-high-lift (see Haselbach et al. [3] and Howell et al. [4]) airfoils can be operated with losses control by taking advantage of wake-induced transition effects in LPT low Reynolds number flows (e.g., Schulte and Hodson [5] and Howell et al. [6]).

The clocking technique operates on the relative circumferential positions of fixed and rotating blade rows in consecutive stages. The axial and circumferential relative position of the rows, together with the blade count ratio between consecutive fixed and rotating rows, impact on the flow field unsteadiness, and consequently on the performance. Larger efficiency benefits can be achieved if the blade count ratio of consecutive stator and rotor rows is near 1:1, while practically no effect can be detected if it is far from unity (e.g., Arnone et al. [7]).

Many researchers have assessed the potential of exploiting airfoil clocking effects to enhance stages performance. In particular, both experimental (e.g., [8–10]) and numerical (e.g., [11–16]) investigations have shown how the time-averaged turbomachine efficiency is a periodic function of stator and rotor clocking positions.

For compressors, the effects of airfoil clocking have been predicted by Gundy-Burlet and Dorney [17,18]. The numerical results for a 2 1/2 stage compressor showed efficiency variations between 0.5% and 0.8% as a function of stator clocking position. Dorney et al. [15] showed how the effects of the wake are due

both to steady and unsteady mechanisms; the first are linked to the flow angle variation across the wake, the latter increment the loss level.

Cizmas and Dorney [14] investigated the effects of *full clocking* (i.e., simultaneously clocking stator and rotor rows) in a three-stage steam turbine. Arnone et al. [16] investigated the same effects in a three-stage LP turbine in two operating conditions. They showed that further benefit can be achieved from the rotor rows clocking.

Besides the total efficiency, clocking effects influence the unsteady blade row pressure distribution. Many authors agree on the fact that larger amplitudes of unsteady pressure on the blades correspond to higher efficiency configurations (e.g., for turbine blades: [11,19]; for compressor blades: [15,17,18]), however, contrasting behavior has also been detected, [13,20].

Tests by Hsu and Wo [21] in an axial compressor rig pointed out the beneficial use of clocking for the reduction of unsteady blade loading in a rotor/stator/rotor configuration.

The numerical investigations on a transonic HP turbine stage carried out by Hummel [22] have shown how wake-shock interactions can produce a reduction in the intensity of the shock itself at the stage exit, thus introducing potential for clocking of downstream blade rows.

Although there seems to be a lot of research activity aimed at investigating clocking mechanisms and their effects, very little is published about fully three-dimensional analyses.

The experimental results reported by Huber et al. [9] for a two-stage HP turbine showed a 0.3% overall efficiency variation due to clocking of the 2nd stage stator. With a spanwise comparison the tip and mid-span best clocking position were found to be 50% pitch out of phase with each other, and this was suspected to be in close link with the wake skewness. A two-dimensional numerical analysis performed by Griffin et al. [13] for the same turbine, correctly predicted the optimum clocking positions but the estimated efficiency variation was only 0.5% compared to the measured one of 0.8% at midspan.

Gombert and Höhn [23] performed experimental investigation on a three-stage LP turbine varying the stators circumferential position. They found that the efficiency variations as a function of clocking positions were significantly out of phase moving from hub to tip.

Reinmüller et al. [10] performed both experimental and numerical investigations to study clocking effects in a 1 1/2 stage axial turbine with untwisted blades. They used a three-

Contributed by the International Gas Turbine Institute and presented at the International Gas Turbine and Aeroengine Congress and Exhibition, Atlanta, GA, June 16–19, 2003. Manuscript received by the IGTI Dec. 2002; final revision Mar. 2003. Paper No. 2003-GT-38414. Review Chair: H. R. Simmons.

dimensional time accurate viscous solver with phase-shifted periodic boundary conditions for the single blade channel computations. The maximum variation of efficiency at mid-span found for the measurements was about 1.0% and about 0.7% for the numerical simulations. The maximum and minimum efficiency clocking positions agreed within 3° over an angular pitch of 10° .

The current study is aimed at investigating the three-dimensional flowfield in a 1 1/2 stage LP turbine while clocking the second stator. In three-dimensional flows unsteadiness is additionally generated due to hub and tip boundary layers, leakage flows and secondary flows transport through successive blade rows. In order to assess these contributions, a detailed comparison between three-dimensional and quasi-three-dimensional unsteady viscous flow computations was performed. The analysis confirmed the major effects of clocking due to the relative position between the wake of the 1st and the leading edge of the 2nd stator. Moreover a close link between optimum efficiency position and unsteadiness was detected.

Computational Procedure

The time-accurate release of the TRAF code (Arnone et al. [24]) was used in the present work. The unsteady three-dimensional, Reynolds-averaged Navier-Stokes equations are written in conservative form in a curvilinear, body-fitted coordinate system and solved for density, absolute momentum components, and total energy.

The code has recently been used to compute trailing edge wake shedding (Arnone and Pacciani [25]) and rotor-stator interaction in turbine and compressor stages (Schmitt et al. [26] and Arnone et al. [27]).

Numerical Scheme. The space discretization is based on a cell-centered finite volume scheme. The artificial dissipation model used is basically the one originally introduced by Jameson et al. [28]. In order to minimize the amount of artificial diffusion inside the shear layers, the eigenvalue scaling of Martinelli and Jameson [29] and Swanson and Turkel [30] was implemented to weigh these terms (cf. Arnone and Swanson [31]). The system of governing equations is advanced in time using an explicit four-stage Runge-Kutta scheme.

Residual smoothing, local time-stepping, and multigriding are employed to speed up convergence to the steady-state solution. The time step is locally computed on the basis of the maximum allowable Courant number, typically 5.0, and accounts for both convective and diffusive limitations, [31].

A dual time-stepping method (Arnone and Pacciani [32] and Jameson [33]) is used to perform time accurate calculations. By introducing the dual time-stepping concept, the solution is advanced in nonphysical time, and acceleration strategies, like local time stepping, implicit residual smoothing, and multigriding are used to speed up the residual to zero to satisfy the time-accurate equations.

Inflow and outflow boundaries are treated according to the theory of characteristics: The flow angles, total pressure and temperature are imposed at the subsonic first row inlet while the outgoing Riemann invariant is taken from the interior. At the subsonic last row outlet, static pressure is prescribed, and the density and the momentum components are extrapolated.

The link between rows is handled by means of sliding interface planes. Consecutive rows have a common interface plane and the match is provided through appropriate calculation of phantom cell values. The phantom cells relative to the interface plane lie on the adjacent blade passage, and linear interpolations are used to provide the flow variable values. This approach, similar to the one used on periodic boundaries, where grids do not match, is not strictly conservative. However, relative errors in the conservation of mass, momentum, and energy were always less than 10^{-5} , which was considered accurate enough.

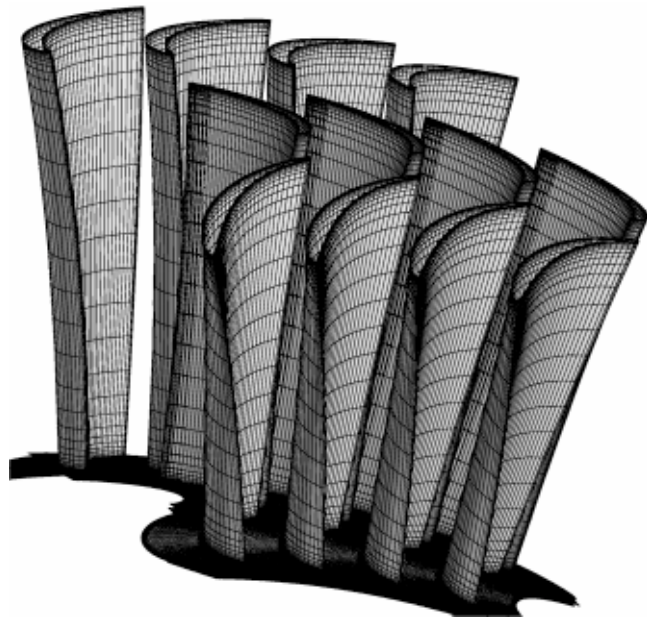


Fig. 1 Three-dimensional view of the grid

Turbulence and Transition Modeling. A two-layer algebraic model based on the mixing length concept (Arnone and Pacciani [34]) was used for turbulence closure.

The location of transition onset is determined by the Abu Ghanam and Shaw [35] criterion. Downstream of the onset of transition the model proposed by Solomon et al. [36] is used for the distribution of intermittency. The intermittency function is computed from 5% to 95% of the blade span and then is interpolated with the assumption that the boundary layer is considered turbulent on both hub and tip endwalls. More details on the transition model implementation can be found in Arnone et al. [37].

Geometry and Computational Grids

The turbine being studied features typical aspects of the current design practices of aircraft engine LP blades (see Fig. 1), with shrouded rotors and relatively high aspect ratios. Detailed geometrical data are protected by Fiat Avio S.p.A and can not be made available.

Figure 2 shows a blade-to-blade view of the H-type grids ($177 \times 73 \times 33$) chosen for the two stators and for the rotor. The value of y^+ for the first grid point above the wall, was approximately 2.0 for all blade rows. With an H-type structure it is relatively easy to control the uniformity and density of the grid before the blade passage to prevent an excessive smearing of the incoming wakes. In order to reduce the mesh skewness, the grids are of the nonperiodic type. Based on past grid dependence analyses performed for the midspan section of the same turbine (Arnone et al. [16]), the selected grid size were considered to be an adequate compromise between modeling the clocking effects and obtaining reasonable computation times.

The vane/blade count ratio was very close to one. In order to end up with reasonable memory and computer time requirements, approximate configuration was considered: the rotor pitch was slightly modified to match an exact 1:1 vane/blade count ratio. The pitch alteration of the rotor blade row was of the order of 0.2% and, based on experience (Arnone and Pacciani [32]), it was considered negligible.

Figure 3 shows the five different clocking locations for the 2nd stator. This pitch discretization is considered sufficiently accurate in order to appreciate clocking effects, [8,10,14].

For the quasi-three-dimensional computations, the midspan section of the turbine was selected using the stream-tube thickness

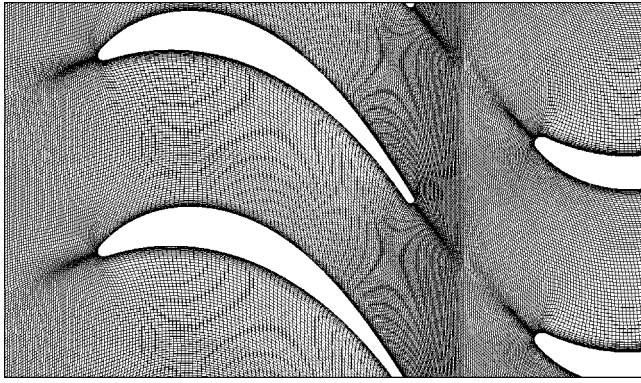


Fig. 2 H-type grid for the midspan section (177x73)

and radius distributions determined on the basis of the three-dimensional calculation. The chosen tangential reference position for the clocking analysis was the same for the midspan section of the fully three-dimensional case. In this way all the results are directly comparable without any tangential shift.

The nondimensional blade lift coefficient based on pressure distribution was used to monitor the time-periodic convergence. Starting from an initial steady-state solution, up to 20 rotor passing periods were needed to obtain a periodic solution. Figure 4 shows the evolution of the nondimensional lift coefficient amplitude. The first three Fourier harmonics were plotted over 25 periods for the 1st rotor and for the 2nd stator.

Quasi-Three-Dimensional and Fully Three-Dimensional Clocking Analyses

Efficiency Variations. In this investigation, the total-to-total average efficiency is calculated using the mass-average of the time-averaged total pressure and total temperature:

$$\eta = \frac{1 - \frac{T_{t2}}{T_{t1}}}{1 - \left(\frac{p_{t2}}{p_{t1}}\right)^{\gamma-1/\gamma}} \quad (1)$$

Clocking effects are evidenced by turbine efficiency variation with respect to the average value $\Delta\eta = \eta - \eta_{av}$. Figure 5 displays the variation in the overall efficiency as the 2nd vane is clocked over a circumferential distance equal to one pitch. Results from quasi-three-dimensional and fully three-dimensional analyses are reported. Both predictions show a sinusoidal pattern of $\Delta\eta$ versus clocking position. The comparison clearly indicates a good agreement in detecting the best and the worst configurations, while the amplitude appears to be overestimated in the quasi-three-dimensional approach. In particular the three-dimensional

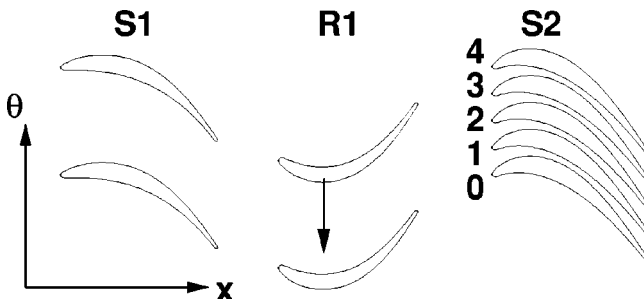
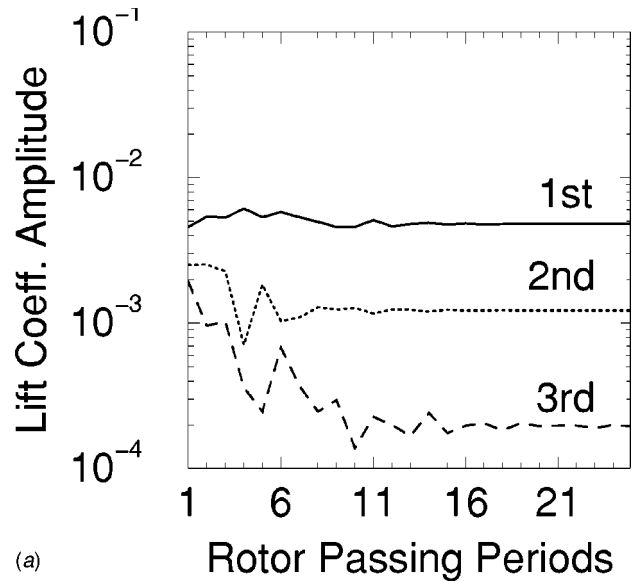
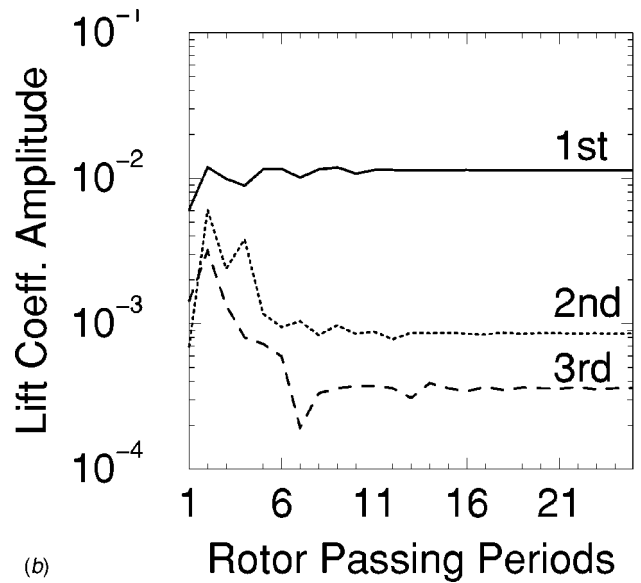


Fig. 3 Investigated clocking positions



(a)



(b)

Fig. 4 Evolution of the nondimensional lift coefficient amplitude harmonics; (a) 1st rotor, (b) 2nd rotor

computations predict a 0.7% overall efficiency variation, while the quasi-three-dimensional estimate was 1.1% for the midspan section.

Effects on Wake Trajectories. Clocking effects seem to be directly linked to wake trajectories. Numerical results obtained by many authors with different numerical methods and turbulence models suggest that maximum efficiencies can be achieved when the wake generated by a stator/rotor blade impinges upon the leading edge of the next stator/rotor blade. Lower performance would correspond to wake trajectory crossing the next stator/rotor vane, [e.g., [9,11–14]].

The wake from the 1st stator blade is convected downstream, chopped by the passing rotor into discrete spots and then approaches the 2nd stator row.

When this flow is time-averaged, stator wake paths appear as continuous entropy stripes and their tangential location, compared to the successive stator leading edge, varies as a function of the circumferential position. The stator wake path is visible in Figs. 6 (a)–(b) for the maximum and the minimum efficiency configurations, respectively. As can be observed, two separate wake paths

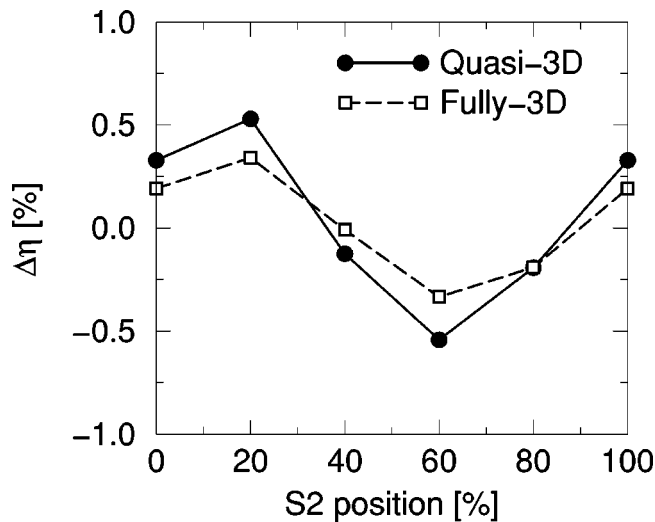


Fig. 5 Efficiency variation versus 2nd stator clocking position

are actually present in the time-averaged flow field of both the two reported cases. One corresponds to a wake path crossing the vane while the other impinges near the blade leading edge.

Unfortunately it is difficult to distinguish the difference between the two stripes only on the basis of time-averaged entropy contours. For a better characterization, a detailed analysis of the instantaneous flow field is essential.

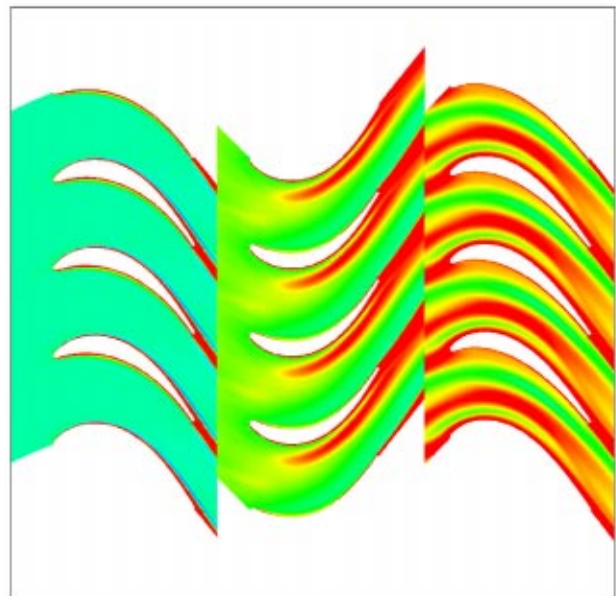
Figures 7 (a)–(e) present a series of five predictions of the unsteady flow at midspan during one blade passing period for the maximum and the minimum efficiency configurations respectively. Here, instantaneous contours of vorticity are plotted rather than entropy, because more extensive information can be obtained.

The wake leaving the stator one blade row consists of two parts, placed side by side, with opposite vorticity and which are seen as a red and a blue zone in Figs. 7 (a)–(e). They come from either side of the blade (pressure and suction surface respectively) and the distinction persists even when they are convected downstream.

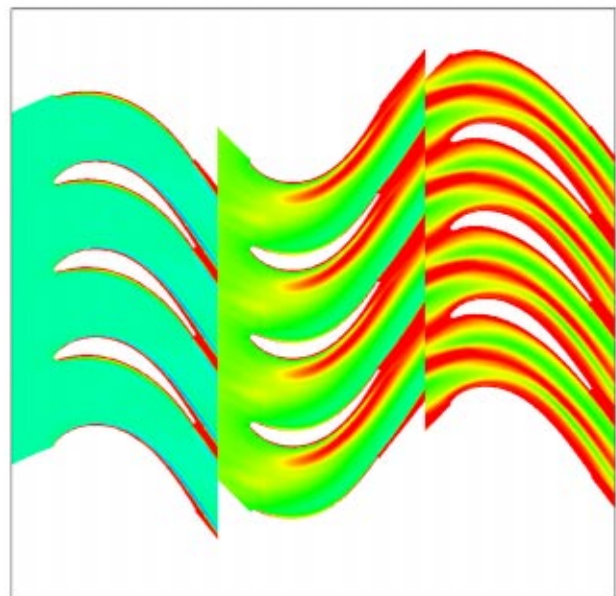
The movement of wakes through succeeding rotor blade rows has been explained by many authors using a simple kinematic theory, which accounts for three different mechanisms: bowing, shearing and stretching, [38,39]. Bowing is due to variations in transport velocity across the passage and is responsible for the distortion of the wake centerline; shearing is a consequence of the velocity gradient between the pressure and suction sides and causes the reorientation of the wake; stretching occurs because of the velocity gradients near the leading edge and makes the wake width become extended, especially on the suction surface.

A comprehensive way to describe the wake-blade interaction is plotting the unsteady velocity vectors in the rotor relative reference frame (see Fig. 8). The unsteady velocity vectors are defined as the instantaneous local velocity minus the local time-mean velocity. In Fig. 8 they are superimposed on vorticity contours. It is rather easy to recognize the typical vortex structure, the so-called negative jet. It consists of a pair of counterrotating vortices, which are convected downstream and distorted. Furthermore, Fig. 8 clearly indicates a direct correspondence with the two zones of opposite vorticity shed by the 1st stator blade row.

Once generated, these recirculating unsteady flow patterns leave the rotor passage and approach the 2nd vane sliding over the rotor wake. For clarity in Figs. 7 (a)–(e) we highlighted the counterclockwise and the clockwise rotating regions with black and white arrows respectively. Such vorticity spots enter the succeeding stator vane in different tangential locations and are convected downstream following the two separate paths evidenced in the time-averaged entropy field (Figs. 6 (a)–(b)). As a direct result of



(a)



(b)

Fig. 6 Time-averaged entropy contours for maximum and minimum efficiency; (a) maximum efficiency, (b) minimum efficiency

this study it now appears that the wake path impinging the blade leading edge is associated with the upstream vortex (red spot) for the maximum efficiency configuration and with the downstream one (blue spot) for the minimum one. The stripe in the midvane is instead produced by the other counterrotating vortex.

Additionally, Figs. 7 (a)–(e) show that when the 2nd vane blade row is optimally clocked, the spots entering one passage come from adjacent 1st stator blades, while in the worst configuration they are shed by the same one.

A further distinction between the two wake segments arises when the effects on stagnation pressure are investigated. Figures

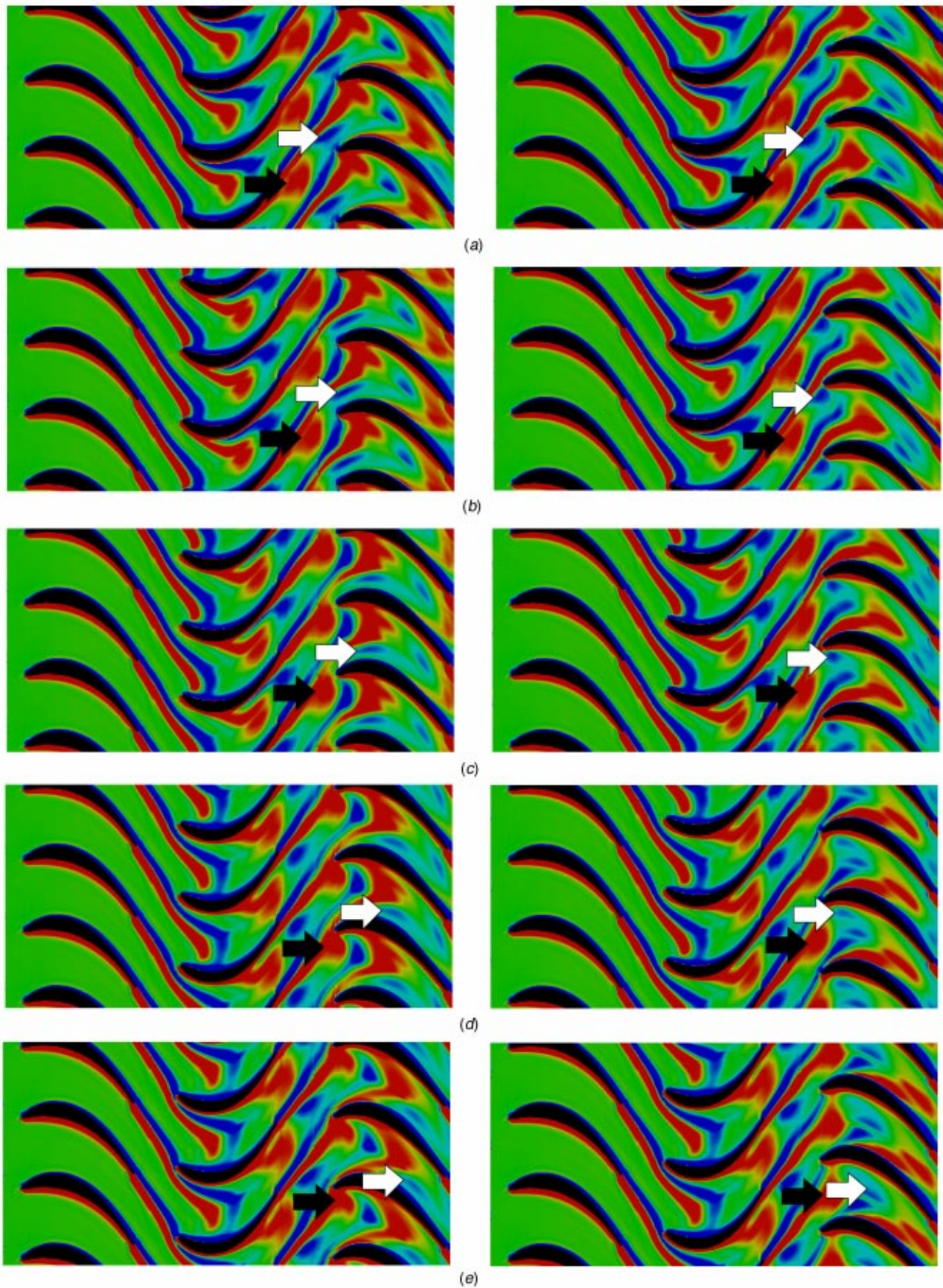


Fig. 7 Instantaneous vorticity contours for maximum (left column) and minimum (right column) efficiency; (a) $t/T=0.0$, (b) $t/T=0.2$, (c) $t/T=0.4$, (d) $t/T=0.6$, (e) $t/T=0.8$

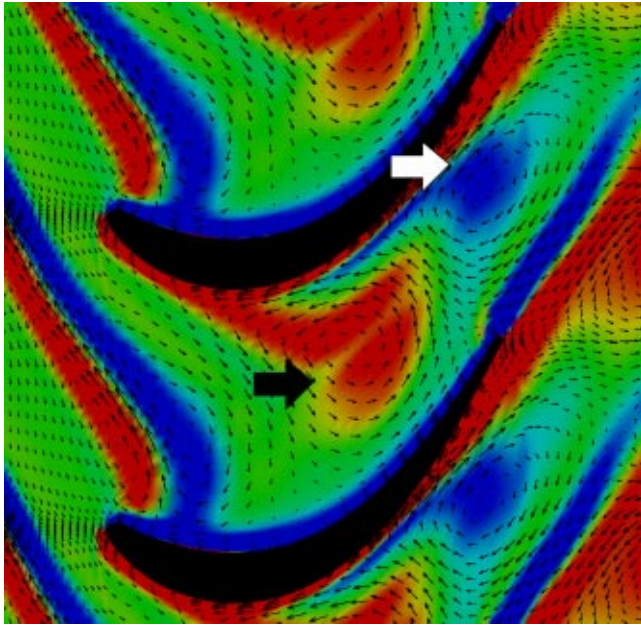


Fig. 8 Instantaneous vorticity contours and unsteady velocity vectors

9 (a)–(b) report time-averaged total pressure variation traverses at midspan in front of the 2nd stator for the maximum and the minimum efficiency clocking position, respectively. Results from fully three-dimensional and quasi-three-dimensional computations are compared and a substantial agreement is found, although the quasi-three-dimensional approach tends to overestimate positive peaks.

These distributions clearly indicate that only one significant energy defect can be detected all over the pitch, while previous plots of time-averaged entropy contours evidenced the presence of two separate wake paths in the 2nd stator blade passage. More exactly a comparison between **Figs. 6 (a)–(b)**, and **Figs. 9 (a)–(b)**, shows that in both the two clocking configurations investigated the turbine performance strictly depends on the circumferential position of the upstream wake segment (indicated with a black arrow in **Fig. 8**) while the downstream one (white arrow) has no remarkable effects on losses.

Such a circumstance is probably due to the larger dimensions of the upstream vortex with respect to the downstream one, as **Fig. 8**, illustrating the unsteady velocity vectors, seems to suggest.

With reference to the total pressure defect, it appears so confirmed that best performance improvements occur when the 1st vane wake impinges upon the leading edge, while the minimum efficiency is associated with a wake path entering the midchannel.

The above analysis was carried out to demonstrate that time-averaged stagnation pressure can be profitably used to detect clocking effects and was therefore repeated for the three-dimensional case, too.

In the three-dimensional environment, the radial gradients can be important. The decrease in total pressure from the tip to the hub section is, in fact, more pronounced than circumferential variations and so a direct plot of stagnation pressure would not be clear enough.

Consequently, in order to highlight the energy defects associated with the presence of wake segments, the following quantity was defined:

$$\bar{p}_t(\vartheta, r) = \frac{p_t(\vartheta, r) - p_{t,av}(r)}{p_{t,ref}} \quad (2)$$

where $p_{t,av}$ is the pitchwise average value of total pressure. Con-

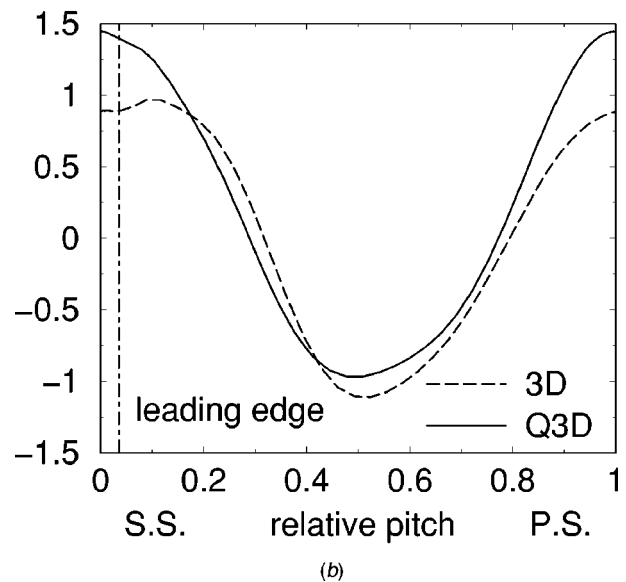
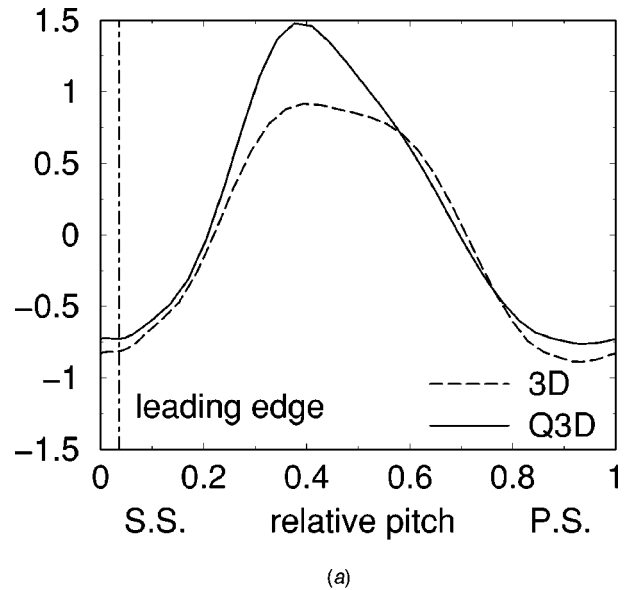


Fig. 9 Time-averaged total pressure pitchwise distribution in front of the 2nd stator, three-dimensional midspan and quasi-three-dimensional; (a) maximum efficiency, (b) minimum efficiency

tours of \bar{p}_t on the 2nd vane blade rows inlet plane are depicted in **Figs. 10 (a)–(b)**, which refer to maximum and minimum efficiency configurations respectively.

The 1st vane wake is seen as a blue region representing the minimum peak in stagnation pressure, while the red zones correspond to high values. Both images show a rather similar pattern, except for an apparent rotation about the turbine axis which clearly shows the different circumferential position of the wakes in the two cases.

It is worthwhile to notice that the predicted time-averaged 1st vane wake at hub is skewed relative to the 2nd vane leading edge, while it appears to be quite aligned in the remaining span. This is probably due to the nonradial stacking of upstream stator and rotor blade rows and to the interactions with their secondary flow field in the hub and tip regions.

This bowed contour implies that near the hub the relative position of the wake with respect to the blade leading edge differs from the situation at tip and midspan.

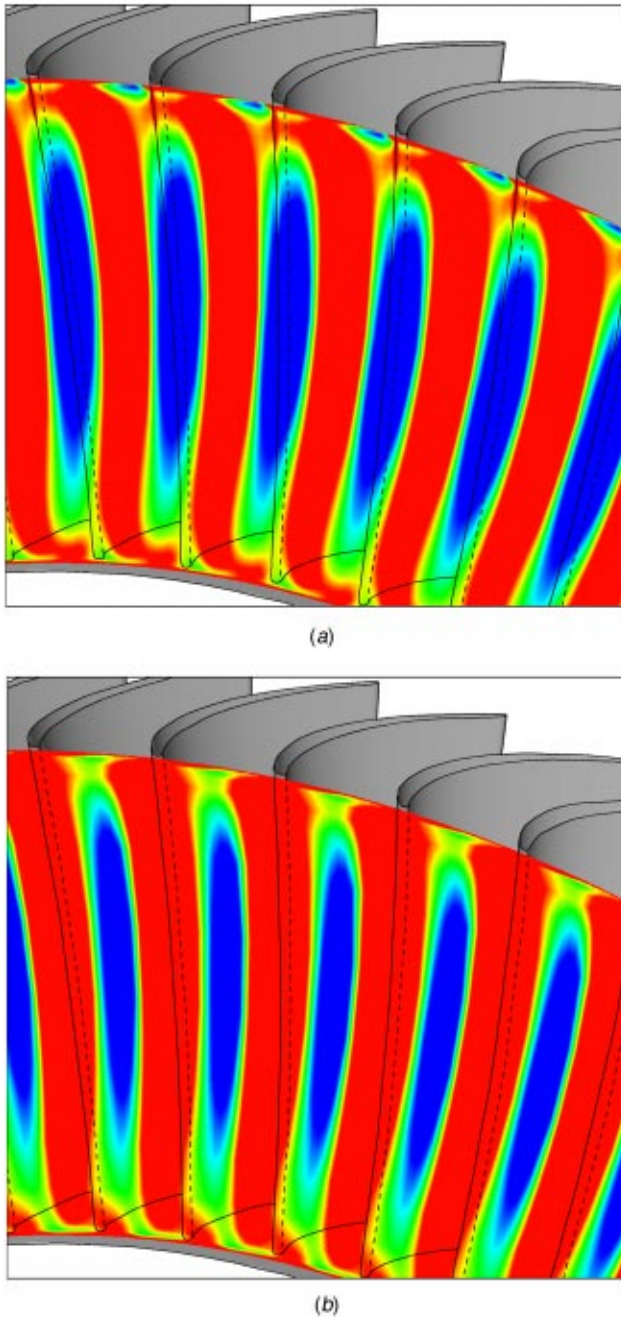


Fig. 10 Time-averaged \bar{p}_t contours in front of the 2nd stator; (a) $\eta_{\max} - \Delta\theta_{s2} = 20\%$, (b) $\eta_{\min} - \Delta\theta_{s2} = 60\%$

As far as best clocking position is concerned, near the mid-span and the tip section, the minimum peak in total pressure is located just near the stator leading edge, whereas about the hub it is close to mid-pitch. The opposite situation occurs for the minimum efficiency configuration: in this case the wake is generally placed in the midchannel except near the hub where a shift towards the stator pressure side can be observed.

The situation depicted in **Figs. 10 (a)–(b)** is supported by **Figs. 11 (a)–(c)**, which show the time-averaged stagnation pressure pitchwise distributions in front of the 2nd stator at 10%, 50%, and 90% of the span height, respectively. The minimum peak in total pressure is predicted to shift about 20% between the hub and either the midspan or the tip section.

The spanwise shape of the convective wake entering the 2nd

vane tends to explain the discrepancies in predictions from fully three-dimensional and quasi-three-dimensional computations shown in **Fig. 5**. Due to the fact that the 1st vane wake changes its circumferential position with the radius, turbine efficiency is a result of different, sometimes conflicting, contributions. For example, in the maximum efficiency configuration, beneficial effects arising from the situation at tip and midspan are reduced by the flow behavior at hub. On the other hand, in the worst clocking position, for the same reason, the hub region prevents a larger performance drop.

The quasi-three-dimensional approach instead does not account for these compensating effects and consequently it tends to overestimate either efficiency gain or loss, thus making turbine performance become more sensitive to row indexing.

It should be noticed however that, due to the mass-average operation, various contributions are differently weighted. Consequently, the wake behavior in the tip and the midspan region, where a higher mass flow rate is swallowed, mainly affects turbine efficiency.

Effects on Blade Loading. The relative motion of adjacent stator and rotor blade rows induces a variety of unsteady flow phenomena, among which the potential-flow interaction and the wake interaction are the most significant ones in a low pressure turbine. Row indexing affects both mechanisms and, depending on clocking position, different modifications can be observed. The kinematics of wake-blade interactions was discussed above. The present section addresses the problem of clocking effects on potential-field interactions.

The study of flow unsteadiness concerned the 2nd vane blade row. Due to the unsteady flow field, at a fixed location of the stator surface, pressure is not a constant, but varies cyclically. These fluctuations have been stored for every point of both the suction and pressure sides and signal properties have been analyzed. In order to compare unsteadiness levels in different configurations, the unsteady pressure amplitude was used. The unsteady pressure coefficient is defined by

$$C_{p,\max} - C_{p,\min} = \frac{p_{\max} - p_{\min}}{p_{t,\text{ref}}} \quad (3)$$

where p_{\min} and p_{\max} are the minimum and maximum values of the instantaneous pressure registered over one period.

Unsteady pressure coefficient distributions were obtained in the quasi-three-dimensional and in the fully three-dimensional approach for both maximum and minimum configuration. In the three-dimensional case, moreover, the analysis was repeated at 10%, 50%, and 90% of the span height. Results from fully three-dimensional computations are presented in **Fig. 12**. The plots relative to 50% and 90% span show that when the 2nd vane is optimally clocked, unsteadiness near the leading edge is higher than in the minimum efficiency position, while at 10% no offset in levels is observed and the values appear comparable with each other.

A plausible explanation of high unsteadiness levels registered close to the leading edge at tip and at mid-span for the maximum efficiency configuration can be given if we compare **Figs. 12 (a)–(c)** and **Figs. 11 (a)–(b)**. It appears that the amplitude of static pressure disturbances is greatest when the 1st vane wake impinges upon the leading edge, while a decrease occurs if the wake enters the mid-channel. The phase-lag detected at the hub section in the previous analysis of time-averaged stagnation pressure accounts for the different behavior of unsteadiness distribution at 10% span.

Since pressure fluctuations are related to the wake circumferential position, which also affects turbine performance, a relation-

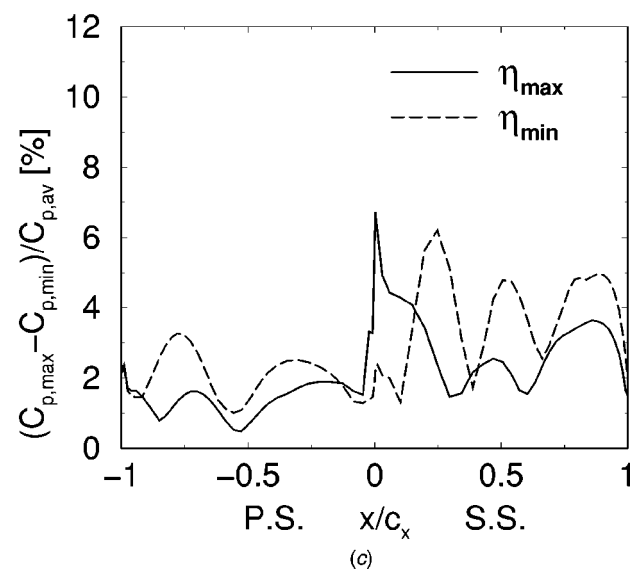
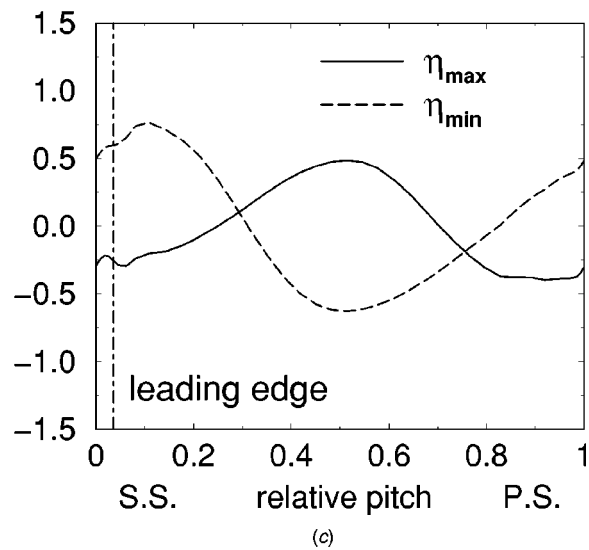
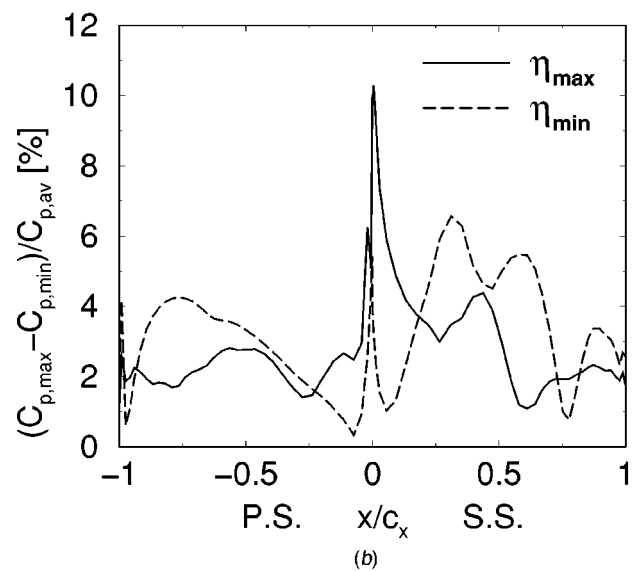
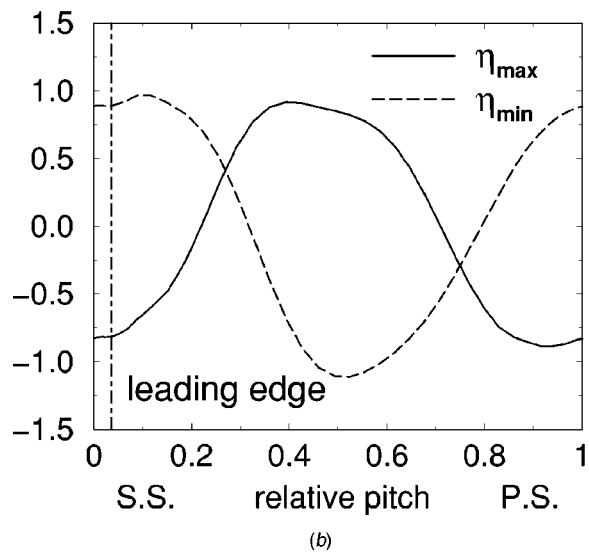
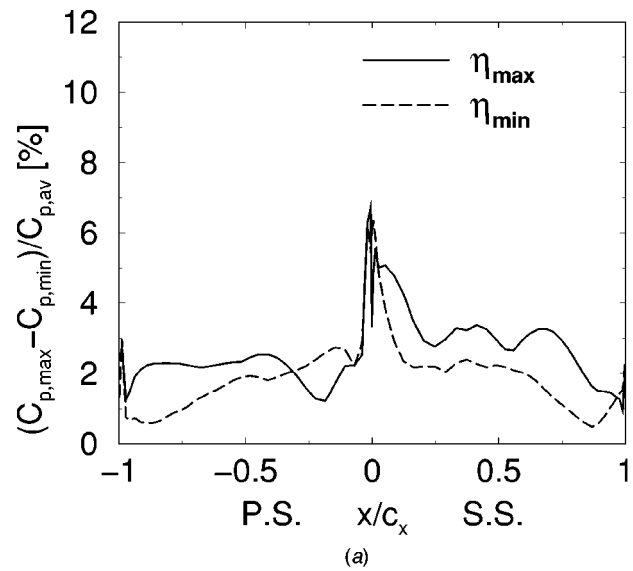
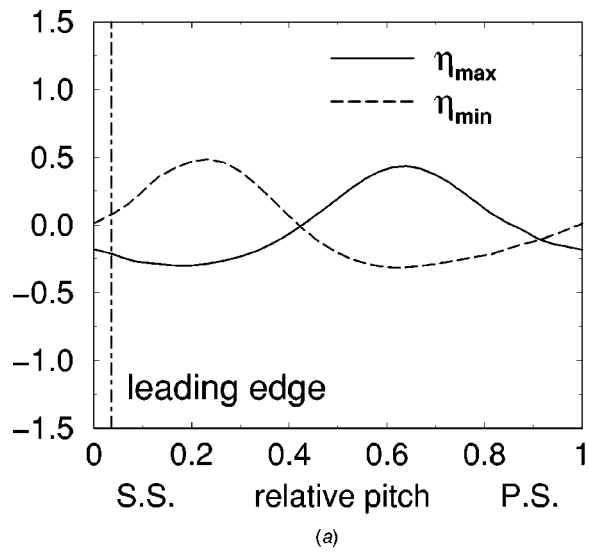


Fig. 11 Time-averaged total pressure pitchwise distributions in front of the 2nd stator at 10%, 50%, and 90% of the span; (a) 10% span, (b) 50% span, (c) 90% span

Fig. 12 Unsteady pressure coefficient distributions for the 2nd stator at 10%, 50%, and 90% of the span; (a) 10% span, (b) 50% span, (c) 90% span

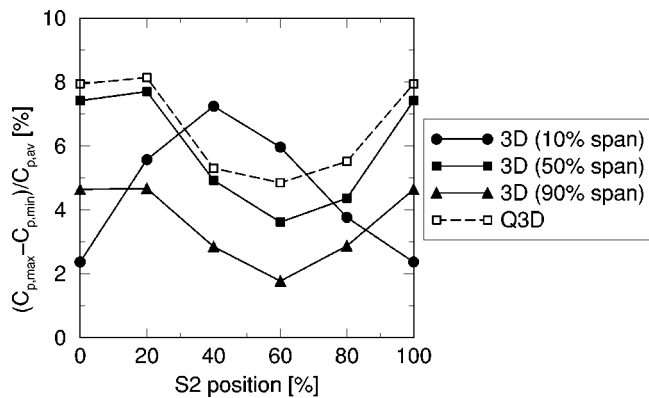


Fig. 13 Unsteady pressure coefficient at leading edge versus clocking positions

ship is expected between efficiency variation and leading edge unsteadiness. To assess this phenomenon, the unsteady pressure coefficient in the vicinity of the leading edge was analyzed not only for the best and the worst clocking positions, but also for the intermediate cases.

The unsteady pressure coefficient is a local quantity, strictly dependent on the point where it is computed. In particular, in the leading edge zone, sudden variations can occur, even between locations very close to each other. In order to characterize the unsteadiness in this region, an averaged value is therefore more suitable than a punctual one. The average operation conventionally concerned a symmetrical portion of the blade surface around the leading edge.

Figure 13 gives the variation of the unsteady pressure coefficient in the leading edge zone with the clocking position at 10%, 50%, and 90% span. Results from quasi-three-dimensional computations are also reported for comparison.

A good agreement is found at 50% span between the quasi-three-dimensional and the fully three-dimensional approach; however a certain offset in levels occurs, especially for the minimum efficiency configuration. This overestimate, also detected for the plots of \bar{p}_t at midspan, can probably be explained by the fact that the quasi-three-dimensional approach tends to concentrate effects otherwise distributed all over the span in a fully three-dimensional environment.

Another point to be noticed is that the hub section is out-of-phase with the tip and midspan ones, while the amount of variations and the mean value are comparable with those found at 50% span. At 90% span, instead, we observe a general decrease in levels, as well as in amplitude.

A comparison between **Fig. 13** and **Fig. 5** clearly shows that, in the quasi-three-dimensional approach, turbine performance and leading edge unsteadiness have a very similar pattern with maximum and minimum at the same locations. Provided that these two aspects are closely related to each other, a broader validity seems to be suggested. In particular in the three-dimensional case, analyzing unsteadiness levels in the region close to the leading edge could result in an alternative method to detect the best and the worst clocking position for each radius.

Assuming therefore that maximum efficiency is associated with the maximum unsteadiness in the leading edge zone, the present analysis showed that the hub best clocking position was about 20% pitch out-of-phase with the tip and the midspan ones, while for the worst configuration, discrepancy rose to about 40% pitch. Such values are consistent with the shift in total pressure defect location previously observed between hub and either midspan or tip section (see **Fig. 9**) and seem to support the above considerations.

With reference to **Figs. 12 (a)–(c)** we notice that, except for the leading edge region, lower unsteadiness levels are associated with

the best clocking position, while higher values correspond to the minimum efficiency configuration. This behavior was observed at 50% and 90% span, whereas, due to the wake skewness we discussed above, the opposite situation occurs at 10% span.

These results show that row indexing affects flow unsteadiness in different way depending on blade surface location. This makes the correlation with performance become not so direct and could also explain the contrasting findings by previous works (c.f. [11,13,19,20]).

Finally, it is worth noticing that in this study, only the unsteady pressure amplitude distributions were analyzed while the influence of the phase angles was not investigated. This information can be relevant when dealing with aeroelasticity problems (e.g., Novinski and Panovsky [40]), but is beyond the scope of the present paper.

Conclusions

A three-dimensional unsteady Navier-Stokes analysis was used to investigate the flow physics associated with clocking in a 1 1/2 stage LP turbine. A quasi-three-dimensional approach was used for the midspan section in order to obtain a comparison and highlight three-dimensional effects. Various aspects of the unsteady flow interactions associated with clocking effects were studied. Such aspects concerned efficiency variations, wake interaction patterns and flow unsteadiness.

Vorticity visualizations resulted in a meaningful contribution and were profitably used in order to monitor the 1st vane wake evolution through succeeding blade rows. Instantaneous contours, as well as unsteady velocity vectors, highlighted flow structures otherwise difficult to detect with traditional studies simply based on entropy. In particular the interaction between counterrotating vortices and the 2nd vane blade row was investigated for both best and worst clocking position.

The three-dimensional analysis, also supported by quasi-three-dimensional computations, confirmed the fundamental role played by the circumferential position of wakes and showed that the greatest benefits are achieved when the wake just impinges on the 2nd stator leading edge, while an efficiency drop was observed if the wake path entered the midchannel. It was remarked, too, that in a fully-three-dimensional environment, the not-perfect alignment between wake and leading edge further reduces potential improvements which instead, in a quasi-three-dimensional approach make the turbine become more sensitive to clocking effects.

Finally, an extensive review of unsteadiness and its relationship with efficiency was conducted showing a different behavior of the leading edge region with respect to the remaining blade surface. In particular it was noticed that, whereas lower unsteadiness levels on either pressure or suction side are usually associated with better turbine performance, the opposite situation occurred in the zone around the leading edge. Additionally an alternative method based on leading edge unsteadiness analysis was suggested in order to detect the best clocking position for every radius.

As a result of this study it was found that, although basic interaction mechanisms are confirmed, three-dimensional effects can be relevant and they should be accounted for to exploit the benefit of row indexing technique.

Acknowledgments

Special thanks to Prof. Ennio Carnevale and to Dr. Roberto Pacciani of University of Florence for the helpful comments. The authors wish also to express their gratitude to the Technical Division of Fiat Avio S.p.A. and in particular to Drs. Emilio Ferrari and Claudia Schipani.

Nomenclature

c = chord
 C_p = unsteady pressure coefficient

p = pressure
 PS = pressure surface
 r = radial direction
 SS = suction surface
 T = period
 t = time
 x = axial direction

Greek

η = total-to-total efficiency
 γ = ratio of specific heats (c_p/c_v)
 ϑ = tangential angle, tangential direction

Subscripts

1 = inlet
 2 = outlet
 av = averaged
 max = maximum value
 min = minimum value
 ref = reference value
 t = total value, turbine
 x = axial direction

References

- [1] Cogley, K., Coleman, N., Siden, G., and Arndt, N., 1997, "Design of New Three Stage Low Pressure Turbine for the BMW Rolls-Royce BR715 Turbofan Engine," ASME Paper 97-GT-419.
- [2] Curtis, E. M., Hodson, H. P., Baniaghbal, M. R., Denton, J. D., Howell, R. J., and Harvey, N. W., 1997, "Development of Blade Profiles for Low Pressure Turbine Applications," ASME J. Turbomach., **119**, pp. 531–538.
- [3] Haselbach, F., Schiffer, H. P., Horsman, M., Dressen, S., Harvey, N. W., and Read, S., 2002, "The Application of Ultra High Lift Blading in the BR715 LP Turbine," ASME J. Turbomach., **124**, pp. 45–51.
- [4] Howell, R. J., Hodson, H. P., Schulte, V., Stieger, R. D., Schiffer, H. P., Haselbach, F., and Harvey, N. W., 2002, "Boundary Layer Development in the BR710 and BR715 LP Turbines—The Implementation of High-Lift and Ultra-High-Lift Concepts," ASME J. Turbomach., **124**, pp. 385–392.
- [5] Schulte, V., and Hodson, H. P., 1998, "Unsteady Wake-Induced Boundary Layer Transition in High Lift HP Turbines," ASME J. Turbomach., **120**, pp. 28–35.
- [6] Howell, R. J., Ramesh, O. N., Hodson, H. P., Harvey, N. W., and Schulte, V., 2001, "High Lift and Aft-Loaded Profiles for Low-Pressure Turbines," ASME J. Turbomach., **123**, pp. 181–188.
- [7] Arnone, A., Marconcini, M., and Pacciani, R., 2000, "On the Use of Unsteady Methods in Predicting Stage Aerodynamic Performance," *Unsteady Aerodynamics, Aeroacoustics and Aeroelasticity of Turbomachines—Conference Proceedings*, Presses Universitaires de Grenoble (PUG), 9th ISUAAAT, Sept. 4–8, Lyon, France, pp. 24–36.
- [8] Sharma, O. P., Ni, R. H., and Tanrikut, S., 1994, "Unsteady Flow in Turbines—Impact on Design Procedure," AGARD Lecture Series 195, Turbomachinery Design Using CFD, Technical Report.
- [9] Huber, F. W., Johnson, P. D., Sharma, O. P., Staubach, J. B., and Gaddis, S. W., 1996, "Performance Improvement Through Indexing of Turbine Airfoils: Part I—Experimental Investigation," ASME J. Turbomach., **118**, pp. 630–635.
- [10] Reinmüller, U., Stephan, B., Schmidt, S., and Niehuis, R., 2002, "Clocking Effects in a 1.5 Stage Axial Turbine—Steady and Unsteady Experimental Investigations Supported by Numerical Simulations," ASME J. Turbomach., **124**, pp. 52–60.
- [11] Dorney, D. J., and Sharma, O. P., 1996, "A Study of Turbine Performance Increases Through Airfoil Clocking," AIAA Paper 96-2816.
- [12] Eulitz, F., Engel, K., and Gebing, H., 1996, "Numerical Investigation of the Clocking Effects in a Multistage Turbine," ASME Paper 96-GT-26.
- [13] Griffin, L. W., Huber, F. W., and Sharma, O. P., 1996, "Performance Improvement Through Indexing of Turbine Airfoils: Part II—Numerical Simulation," ASME J. Turbomach., **118**, pp. 636–642.
- [14] Cizmas, P., and Dorney, D., 1998, "Parallel Computation of Turbine Blade Clocking," AIAA Paper 98-3598.
- [15] Dorney, D. J., Sharma, O. P., and Gundy-Burlet, K. L., 1998, "Physics of Airfoil Clocking in a High-Speed Axial Compressor," ASME Paper 98-GT-082.
- [16] Arnone, A., Marconcini, M., Pacciani, R., Schipani, C., and Spano, E., 2002, "Numerical Investigation of Airfoil Clocking in a Three-Stage Low Pressure Turbine," ASME J. Turbomach., **124**, pp. 61–68.
- [17] Gundy-Burlet, K. L., and Dorney, D. J., 1997, "Investigation of Airfoil Clocking and Inter-Blade-Row Gaps in Axial Compressors," AIAA Paper 97-3008.
- [18] Gundy-Burlet, K. L., and Dorney, D. J., 1997, "Physics of Airfoil Clocking in Axial Compressors," ASME Paper 97-GT-444.
- [19] Cizmas, P. G. A., and Dorney, D. J., 1999, "The Influence of Clocking on Unsteady Forces on Compressor an Turbine Blades," ISABE Paper 99-7231.
- [20] Dorney, D. J., Croft, R. R., Sondak, D. L., Stang, U. E., and Twardochleb, C. Z., 2001, "Computational Study of Clocking and Embedded Stage in a 4-Stage Industrial Turbine," ASME Paper 2001-GT-509.
- [21] Hsu, S. T., and Wo, A. M., 1998, "Reduction of Unsteady Blade Loading by Beneficial Use of Vortical and Potential Disturbances in an Axial Compressor With Rotor Clocking," ASME J. Turbomach., **120**, pp. 705–713.
- [22] Hummel, F., 2002, "Wake-Wake Interaction and Its Potential for Clocking in a Transonic High-Pressure Turbine," ASME J. Turbomach., **124**, pp. 69–76.
- [23] Gombert, R., and Höhn, W., 2001, "Unsteady Aerodynamical Blade Row Interaction in a New Multistage Research Turbine—Part I: Experimental Investigation," ASME Paper 2001-GT-306.
- [24] Arnone, A., Liou, M. S., and Povinelli, L. A., 1992, "Navier-Stokes Solution of Transonic Cascade Flow Using Non-Periodic C-Type Grids," J. Propul. Power, **8**(2), pp. 410–417.
- [25] Arnone, A., and Pacciani, R., 1997, "Numerical Prediction of Trailing Edge Wake Shedding," ASME Paper 97-GT-89.
- [26] Schmitt, S., Eulitz, F., Wallscheid, L., Arnone, A., and Marconcini, M., 2001, "Evaluation of Unsteady CFD Methods by Their Application to a Transonic Propfan Stage," ASME Paper 2001-GT-310.
- [27] Arnone, A., Liou, M. S., and Povinelli, L. A., 1993, "Multigrid Time-Accurate Integration of Navier-Stokes Equations," AIAA Paper 93-3361-CP.
- [28] Jameson, A., Schmidt, W., and Turkel, E., 1981, "Numerical Solutions of the Euler Equations by Finite Volume Methods Using Runge-Kutta Time-Stepping Schemes," AIAA Paper 81-1259.
- [29] Martinelli, L., and Jameson, A., 1988, "Validation of a Multigrid Method for Reynolds Averaged Equations," AIAA Paper 88-0414.
- [30] Swanson, R. C., and Turkel, E., 1987, "Artificial Dissipation and Central Difference Schemes for the Euler and Navier-Stokes Equations," AIAA Paper 87-1107-CP.
- [31] Arnone, A., and Swanson, R. C., 1993, "A Navier-Stokes Solver for Turbomachinery Applications," ASME J. Turbomach., **115**, pp. 305–313.
- [32] Arnone, A., and Pacciani, R., 1996, "Rotor-Stator Interaction Analysis Using the Navier-Stokes Equations and a Multigrid Method," ASME J. Turbomach., **118**, pp. 679–689.
- [33] Jameson, A., 1991, "Time Dependent Calculations Using Multigrid With Applications to Unsteady Flows Past Airfoils and Wings," AIAA Paper 91-1596.
- [34] Arnone, A., and Pacciani, R., 1998, "IGV-Rotor Interaction Analysis in a Transonic Compressor Using the Navier-Stokes Equations," ASME J. Turbomach., **120**, pp. 143–155.
- [35] Abu Ghannam, B. J., and Shaw, R., 1980, "Natural Transition of Boundary Layers—The Effect of Turbulence, Pressure Gradient and Flow History," J. Mech. Eng. Sci., **22**(5), pp. 213–228.
- [36] Solomon, W. J., Walker, G. J., and Gostelow, J. P., 1996, "Transition Length Prediction for Flows With Rapidly Changing Pressure Gradients," ASME J. Turbomach., **118**, pp. 744–753.
- [37] Arnone, A., Marconcini, M., Pacciani, R., and Spano, E., 1999, "Numerical Prediction of Wake-Induced Transition in a Low Pressure Turbine," ISABE Paper 99-058.
- [38] Korakianitis, T., 1993, "On the Propagation of Viscous Wakes and Potential Flow in Axial-Turbine Cascade," ASME J. Turbomach., **115**, pp. 118–127.
- [39] Hodson, H. P., 1998, "Blade Row Interactions in Low Pressure Turbines," *Blade Row Interference Effects in Axial Turbomachinery Stages*, Von Kármán Institute, Lecture Series 1998-02.
- [40] Novinski, M., and Panovsky, J., 2000, "Flutter Mechanisms in Low Pressure Turbine Blades," ASME J. Turbomach., **122**, pp. 82–88.

The Effect of Real Turbine Roughness With Pressure Gradient on Heat Transfer

Jeffrey P. Bons

Department of Mechanical Engineering,
Brigham Young University,
Provo, UT 84602
e-mail: jbons@byu.edu

Stephen T. McClain

Department of Mechanical Engineering,
The University of Alabama at Birmingham,
Birmingham, AL 35294
e-mail: smcclain@eng.uab.edu

Experimental measurements of heat transfer (St) are reported for low speed flow over scaled turbine roughness models at three different freestream pressure gradients: adverse, zero (nominally), and favorable. The roughness models were scaled from surface measurements taken on actual, in-service land-based turbine hardware and include samples of fuel deposits, TBC spallation, erosion, and pitting as well as a smooth control surface. All St measurements were made in a developing turbulent boundary layer at the same value of Reynolds number ($Re_x \cong 900,000$). An integral boundary layer method used to estimate c_f for the smooth wall cases allowed the calculation of the Reynolds analogy ($2St/c_f$). Results indicate that for a smooth wall, Reynolds analogy varies appreciably with pressure gradient. Smooth surface heat transfer is considerably less sensitive to pressure gradients than skin friction. For the rough surfaces with adverse pressure gradient, St is less sensitive to roughness than with zero or favorable pressure gradient. Roughness-induced Stanton number increases at zero pressure gradient range from 16–44% (depending on roughness type), while increases with adverse pressure gradient are 7% less on average for the same roughness type. Hot-wire measurements show a corresponding drop in roughness-induced momentum deficit and streamwise turbulent kinetic energy generation in the adverse pressure gradient boundary layer compared with the other pressure gradient conditions. The combined effects of roughness and pressure gradient are different than their individual effects added together. Specifically, for adverse pressure gradient the combined effect on heat transfer is 9% less than that estimated by adding their separate effects. For favorable pressure gradient, the additive estimate is 6% lower than the result with combined effects. Identical measurements on a “simulated” roughness surface composed of cones in an ordered array show a behavior unlike that of the scaled “real” roughness models. St calculations made using a discrete-element roughness model show promising agreement with the experimental data. Predictions and data combine to underline the importance of accounting for pressure gradient and surface roughness effects simultaneously rather than independently for accurate performance calculations in turbines. [DOI: 10.1115/1.1738120]

Introduction/Background

Flows of engineering interest occur over surfaces that are not smooth. Surface roughness has been shown to influence both the aerodynamics and heat transfer of fluid devices. Understanding the full effects of surface roughness is perhaps no where more critical than in a gas turbine engine. In the turbine section of a modern gas turbine, the accurate prediction of heat transfer is paramount. Underestimating the turbine inlet temperature by 25°C can reduce the blade life by a factor of two, [1]. In a compressor, stage efficiency is generally of greater importance (though recent advances in gas turbine performance have been in some cases limited by the high pressure compressor exit temperature). Roughness-induced aerodynamic losses aggravate airfoil wakes in the compressor, upsetting the tenuous balance of vane-blade interaction that is so critical to peak efficiency.

To properly account for roughness-induced effects requires a proper understanding of an imposing list of flow phenomena, including boundary layer transition, secondary (three-dimensional) flows, and turbulent (momentum and energy) transport. Consequently, roughness is still an active topic of research nearly a century after the initial pipe flow experiments of Nikuradse [2]. A summary of some of the more recent studies in this area is contained in Bons [3], to include an extensive (though certainly not

exhaustive) reference list. The bulk of experimental work with roughness has been conducted in the laboratory environment with simulated roughness elements (e.g., sand, [4,5], cylinders, [6], spherical segments, [7], cones, [8], pedestals, [9], etc.). Laboratory findings show the quantitative effects of roughness to be significant. Measured augmentation factors range from $1.5 < c_f/c_{fo} < 3.5$ and $1.1 < St/St_o < 1.6$. These values can be even greater when boundary layer transition is initiated prematurely due to roughness. Empirical correlations, [10,11], have been more or less successful at capturing the significant trends in the laboratory data. However, since the correlations are created to match laboratory findings rather than the complex flow environment of a gas turbine, it is not surprising that they are less effective when applied to turbomachinery flows, [12,13]. Nonetheless, full rig tests with roughness clearly show its effects, [14,15], thus it can not simply be neglected.

More sophisticated roughness models combined with computational fluid dynamics calculations have proven more effective than empirical correlations and have provided greater insight into the fundamental flow physics. The discrete-element method in particular has been developed and tailored to provide good agreement in c_f and St over a wide range of roughness types, [16,17]. But once again, most comparisons are with laboratory findings which lack many of the complexities of turbomachinery flow fields. Two of these complicating factors that have been addressed by the authors are freestream turbulence, [3], and nonzero pressure gradients.

Combustor exit measurements of freestream turbulence range

Contributed by the International Gas Turbine Institute and presented at the International Gas Turbine and Aeroengine Congress and Exhibition, Atlanta, GA, June 16–19, 2003. Manuscript received by the IGTI Dec. 2002; final revision Mar. 2003. Paper No. 2003-GT-38738. Review Chair: H. R. Simmons.

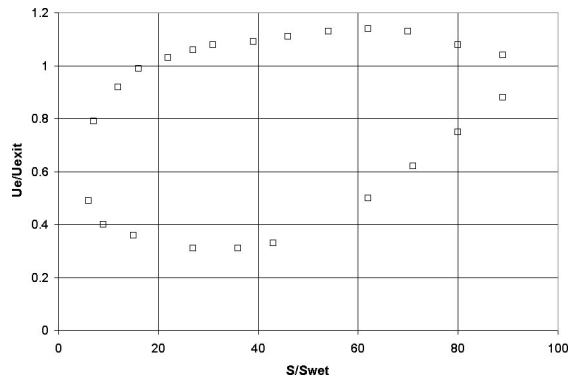


Fig. 1 Experimental velocity data (U_e normalized by exit velocity from stage) versus wetted surface distance for typical turbine airfoil (Fig. 5 from [19])

from 10–17%, [18]. This extreme level decays somewhat by the second turbine stage, yielding levels below 10% thereafter. Intuition might suggest that such elevated turbulence levels would completely overwhelm the effects of surface roughness, making it negligible. However, results reported in [3] show just the opposite effect. St and c_f levels with turbulence and roughness combined exceeded those for the two independent effects superposed by up to 20% in some cases. This synergy has been documented by other researchers as well. Though some of the heat transfer increase can be attributed to an increase in wetted surface area due to roughness, the reported values exceed the increased surface area ratio (S_w/S) by up to a factor of three.

Pressure gradients in turbines likewise vary over a considerable range. **Figure 1** [from [19]] shows a typical velocity distribution for a modern turbine nozzle. Acceleration parameters (K) ranging from 2×10^{-6} to -6×10^{-6} on the pressure surface and 2×10^{-6} to -0.3×10^{-6} on the suction surface are not uncommon. Bons et al. [20] showed that significant surface roughness can occur in any location on a turbine blade, depending on the blade design and the operating environment. Thus, the turbine designer and operator are left with the dilemma of how to account for roughness effects over the entire envelope of possible pressure gradients. The bulk of experimental roughness research has been conducted at zero-pressure gradient or in fully developed pipe flow, neither of which accurately models the boundary layers on a turbine blade. Consequently, correlations based on these laboratory data lack sensitivity to variable pressure gradients.

There have been a handful of experimental studies with combined roughness and variable pressure gradient. Coleman et al. [21] added densely packed spheres to a heat transfer facility used previously by Moretti and Kays [22], and repeated a series of accelerated freestream profiles with a turbulent boundary layer. The original smooth plate study of Moretti and Kays compared St at the same x -location for two flows: one at constant U_e and one at the same constant U_e followed by an accelerated zone just prior to the St measurement location. In this configuration, St in the accelerated zone was actually lower than St with constant U_e . The authors remarked that acceleration causes a thinning of the turbulent boundary layer accompanied by a suppression of boundary layer turbulence (even relaminarization in some cases). Turbulence suppression has a particularly marked effect on the convective heat transfer coefficient (h) and the resultant St ($=h/\rho c_p U_e$). Thus when St is normalized by a higher (accelerated) U_e , it decreases at the same streamwise (x) location. When Coleman et al. added the densely packed spheres to this facility, they found a 10–20% increase in St when comparing favorable pressure gradient (FPG) to zero pressure gradient (ZPG) for the same roughness. The acceleration-thinned boundary layer resulted in a larger k/δ ratio and a greater roughness influence compared to the ZPG case. This augmentation more than overcame the St

reduction of the smooth model with FPG. Chakroun and Taylor [23] expanded on the findings of Coleman et al. in a nearly identical experimental facility but with hemispheres rather than spheres as the rough-wall characterization. They reported a 10% drop in St with acceleration for a smooth surface, again citing the drop in turbulent fluctuations. The roughened wall more than overcame this decrease, resulting in a 5–15% increase in St (depending on Re) for a rough FPG versus the rough ZPG case.

Researchers at NASA have likewise been very active in the roughness arena through their extensive research into the effects of icing on external airfoils. Poinatte et al. [24,25] added a staggered array of 2-mm diameter hemispheres to the leading edge of a NACA-0012 airfoil to study icing effects on heat transfer. Roughness did increase the local St , but the authors indicated that this was probably related to premature boundary layer transition. Varying the angle of attack (α) of the artificially-roughened airfoil (and thus changing the pressure gradient just after the leading edge to be more strongly adverse) did show an increase in heat transfer as α was increased from zero. Again, the suction surface boundary layer was found to transition closer to the leading edge because of the increasingly adverse pressure gradient in the artificially roughened zone. This appeared to explain the increased heat transfer. Interestingly, in a limited test series with elevated freestream turbulence and roughness (at constant α), the authors registered surprise at finding that freestream turbulence actually amplified the effect of roughness (a finding corroborated in [3]).

A second NASA study by Dukhan et al. [26,27] employed aluminum castings of real ice formations and studied the interrelation of pressure gradient and roughness. The boundary layer over the smooth baseline casting was not turbulent and showed only a slight variation in St with the accelerated freestream. Increasing FPG delayed boundary layer transition to higher values of Re_x in accordance with linear stability theory, thus St values were lower in the transition zone with higher FPG at the same Re_x . The upper bound of Dukhan et al.'s smooth plate data ended in the transition zone, so no information was available on turbulent boundary layer heat transfer over a smooth plate with pressure gradient. For the rough castings, increasing FPG increased St for the same Re_x by 10–40% at high values of Re_x . For $Re_x < 400,000$, the favorable pressure gradient case actually showed a reduced St at matched Re_x . Some of this low Reynolds number observation may be attributed to delayed transition effects.

A final study that combined roughness and variable pressure gradient is reported by Turner et al. [28]. Roughness was modeled by an array of pyramid shaped elements and only a single set of favorable pressure gradient data are reported. In this one case, FPG does increase rough wall St at the same Re_x by roughly 5% for $Re_x > 500,000$ (beyond the transition affected zone). Acceleration parameters for this study were lower than for some of the other researchers ($K \approx 1.5 \times 10^{-7}$) and no adverse pressure gradient data were presented.

Piecing together these scattered sets of roughness data, it seems evident that pressure gradient is an important parameter that must be considered when estimating rough wall heat transfer. However, without a clearer documentation of the interdependence between roughness and pressure gradient in a turbulent boundary layer, existing roughness correlations become suspect when applied much beyond the mild camber (and angle of attack) of a typical external airfoil. Experimental data are needed to determine the combined effects of both favorable and adverse pressure gradient with roughness. A significant finding of Bons [3] was that simulated roughness falls short of providing an accurate roughness model for both c_f and St . It is expected that this disparity will only be exacerbated with variable pressure gradients. Thus, to be accurate, the wall condition in any roughness study should be actual roughness, reproduced from the turbine environment that is being modeled, rather than simulated roughness using homogeneous elements. This report contains the findings of just such a study. Employing the same facility used in [3], St was measured

Table 1 Surface statistics for scaled wind tunnel models of “real” rough surfaces

Type	Scaling	Ra (mm)	Rz (mm)	Rt (mm)	α_{rms} (deg)	S_w/S	Rz/θ
Pitted	28.5	0.12	1.14	2.08	7.23	1.02	0.57
Spalled	28.1	0.84	4.51	6.43	16.4	1.08	2.26
Fuel	34.3	1.17	5.96	7.3	20.6	1.22	2.98
Deposits							
Erosion/ deposits	57.7	0.52	3.83	4.23	25.3	1.20	1.92

over scaled roughness models in both adverse and favorable pressure gradient conditions. Though the levels of pressure gradient ($-2 \times 10^{-7} < K < 5 \times 10^{-7}$) are lower than those found in an actual turbine, they are large enough to show a measurable effect, and thus provide valuable insight into expected trends. Also, comparisons are made with discrete-element model calculations using the same real-roughness characterizations. Results of this comparison establish this model’s viability as a tool for predicting St in more engine representative pressure gradients.

Surface Roughness Characterization

Data reported in this study employ the same roughness characterizations used in previous studies by the authors [3,17,20]. Surface measurements were made on nearly 100 land-based turbine components assembled from four manufacturers: General Electric, Solar Turbines, Siemens-Westinghouse, and Honeywell Corporation. The articles were selected by each manufacturer to be representative of surface conditions generally found in the land-based gas turbine inventory. Chord dimensions on the assembled blades and vanes ranged from 2 to 20 cm and included samples with thermal barrier coatings (TBC). In order to respect proprietary concerns of the manufacturers, strict source anonymity has been maintained for all data in this publication.

Extensive two-dimensional and three-dimensional surface measurements were made on the assembled hardware using a Taylor-Hobson Form Talysurf Series 2 contact stylus measurement system. The complete results are reported in [3,20]. Of the surfaces available for study, four were chosen for this study. These include one pitted surface, one coated/spalled surface, one fuel deposit surface, and one erosion/deposit surface. The full statistics for each of the four surfaces are included in [3] along with representative two-dimensional traces. **Table 1** contains a subset of these statistical measurements. The surfaces were scaled to match the roughness to boundary layer height ratio of the turbine environment as well as the roughness classification of the flow (smooth, fully rough, or transitionally rough). The scaled models were fabricated into 280 mm×360 mm test panels using a StrataSys Inc. GeniSys Xi 3D plastic printer.

Description of Experimental Facility

The research facility used for the experiments is described in detail in [3] and only a brief summary will be given here. The open-loop wind tunnel located at Wright-Patterson AFB uses a centrifugal blower to provide a nominal mass flow of 1.2 kg/s to the test section (**Fig. 2**). A heat exchanger can be used to vary the flow temperature from 18 to 54°C. The flow enters a conditioning plenum of 0.6-m diameter before reaching the rectangular test section. The freestream turbulence level at the test section is 1%. At 1.22 m from the plenum exit a knife-edge boundary layer bleed with suction removes the bottom 1.27 cm of the growing boundary layer, making the aspect ratio (span/height) of the final test section approximately 1.7 (with no pressure gradient). The top wall of this final section is adjustable in order to set non-zero pressure gradients in the tunnel. Since the goal of this study is to assess the effect of pressure gradient on rough surfaces, this top wall was adjusted to create three different (roughly linear) pres-

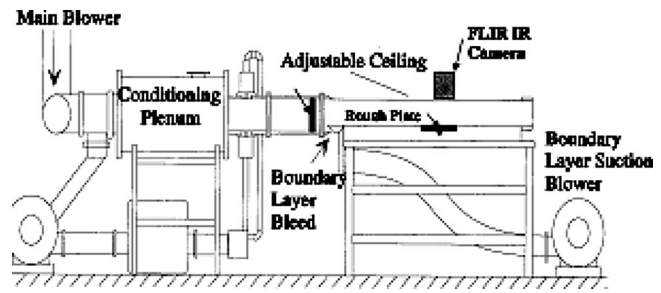


Fig. 2 Schematic of variable pressure gradient wind tunnel at AFRL

sure gradients. Velocity measurements at multiple axial locations along the tunnel centerline are shown in **Fig. 3**. The location of the roughness test plate (centered at $x = 1.18$ m) is also indicated in the figure, and was chosen as the point of intersection of the three $U_e(x)$ profiles. External flow heat transfer data is generally reported as St versus Re_x . St normalizes the heat transfer coefficient by the rate of available thermal capacity in the flow ($\rho c_p U_e$). Using St allows comparisons to be made for different fluids and flow conditions. Re_x identifies the hydrodynamic boundary layer state and maturity. Plotting St versus Re_x allows heat transfer assessments to be made independent of fluid type, flow character, or boundary layer state. However, since both St and Re_x employ the local value of U_e , they contain no direct information about the upstream variation of U_e . Thus, when comparing St and Re_x data from different experiments with pressure gradients, it is important to understand the manner in which the pressure gradient was imposed (relative to the measurement location) as this will have a significant impact on the relevance of comparisons between results.

Coleman et al. [21] and Chakroun and Taylor [23] made comparisons at the same streamwise location for a turbulent boundary layer that either had a constant U_e or a constant U_e followed by an accelerated zone just prior to the measurement location. Thus, comparisons were made of St versus x with the same U_e far upstream but different Re_x values at the measurement location (since U_e at the measurement site is different with or without acceleration). Incidentally, these studies also employed a significant unheated starting length in an effort to lessen the dependency of the thermal boundary layer development on the hydrodynamic boundary layer development. By contrast, the NASA work by Dukhan et al. [27] used constant acceleration from the leading edge of the roughened test plate and reported heat transfer as St versus Re_x . There is a short unheated starting length in the NASA facility as well. The focus of the present study is turbine blade heat transfer, though the findings are more broadly applicable to a variety of

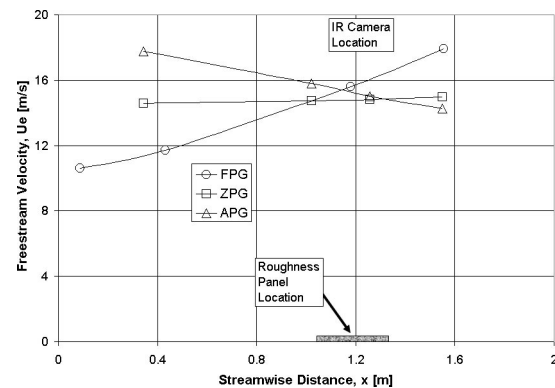


Fig. 3 Freestream velocity distribution for three pressure gradients in AFRL wind tunnel

Table 2 Smooth-wall data from experiment and calculation (at $x=1.2$ m)

	APG	ZPG	FPG
K	-2.25×10^{-7}	3.52×10^{-8}	4.73×10^{-7}
Re_x	939,000	901,000	932,000
St-experimental	0.00199	0.00220	0.00248
St-BLACOMP	0.00208	0.00225	0.00257
St-Ambrok [31]	0.00206	0.00217	0.00245
c_f -BLACOMP	0.00304	0.00375	0.00446
c_f -White [33]	0.00299	0.00376	0.00456
Reynolds analogy-BLACOMP	1.37	1.20	1.15

industrial applications. Since pressure gradients on turbine blading begin at the leading edge, it was decided to compare St versus Re_x at the same x -location. This is done in the present facility by starting the flow at $x=0$ with a U_e value that is higher or lower than the zero pressure gradient constant U_e value, and then decreasing or increasing U_e up to the measurement location (see Fig. 3). Also, to more faithfully simulate the turbine environment, the thermal and velocity boundary layers begin simultaneously at $x=0$ (without an unheated starting length).

One attribute of the facility that does not necessarily mirror the turbine blade application is the wall roughness character leading up to the measurement location. The roughness panels are preceded by 1.04 m of smooth plexiglas wall (of comparable thermal properties to the plastic panels). Accordingly, the flow experiences a transition from a smooth to rough wall condition at the leading edge of the roughness panels. This experimental setup departs from traditional roughness experiments in which the entire development length of the boundary layer is roughened. Previous work by other researchers (referred to in [3]) suggests that St recovers its rough wall value within three to four boundary layer thicknesses. To mitigate the effect of this transition region, the heat transfer data were taken on the downstream half of the roughness section (beyond the expected adjustment length). That said, the turbine roughness measurements reported by Bons [20] show rapid spatial variations in surface character. So, this experimental configuration may actually be more representative of the real turbine blade surface than constant roughness from the leading edge of the tunnel.

For the heat transfer measurements, a FLIR Thermacam SC 3000 infrared camera system is mounted over a hole in the plexiglas ceiling of the tunnel. The camera setup and data reduction procedure is documented in [3]. The optical port is sealed to the camera lens using a cylindrical housing. This prevents air from exiting or entering through this port during tests with variable pressure gradient. For this study, the focal distance of the camera was kept constant regardless of the height of the adjustable tunnel ceiling. The camera field of view is roughly 70×90 mm, centered at $x=1.2$ m. The surface temperatures recorded by the camera were area-averaged to obtain the surface temperature history required by the St calculation algorithm. The Stanton number was determined from this surface temperature history using the method of Schultz and Jones [29]. This transient technique uses Duhamel's superposition method to calculate the surface heat flux given the surface temperature history. It assumes the panels are a semi-infinite solid at constant temperature at the start of the transient. To accomplish this, the entire test section was soaked at room temperature for several hours prior to testing. Using the flow heat exchanger, hot air flow was then initiated instantaneously while monitoring the freestream velocity and temperature as well as the average surface temperature (with the IR camera). The heat transfer coefficient (h) at each time step was then calculated using the expression in [3]. With this procedure, smooth plate, zero pressure gradient St values were found to be within 3% of the accepted correlations. Repeatability was within $\pm 5\%$ and bias uncertainty was estimated at ± 0.00015 for the smooth plate measurement of $St=0.00219$ at ($Re_x=900,000$).

Discrete-Element Computational Model

The discrete-element model used for comparison in this report is outlined in detail in [17] and was implemented in a finite difference, boundary layer code, BLACOMP, developed at Mississippi State University for educational use, [30]. The discrete-element model was formulated for roughness elements with three-dimensional shapes for which the element cross-section distribution can be defined at every height, y . The differential equations including roughness effects are derived by applying the basic conservation statements for mass, momentum, and energy to a control volume located below the roughness peaks. Basic to this approach is the idea that the two-dimensional time-averaged turbulent boundary layer equations can be applied in this flow region. The flow variables are spatially averaged over the transverse (z) direction and the streamwise (x) direction. The physical effects of the roughness elements on the fluid in the control volume are modeled by considering the flow blockage, the local element heat transfer, and the local element form drag. The turbulence model is not modified to include roughness effects since the physical effects of the roughness on the flow are explicitly included in the differential equations. The Prandtl mixing length with van Driest damping is used for turbulence closure. Closure in the energy equation is achieved using a turbulent Prandtl number, Pr_t , of 0.9. $U_e(x)$ and $T_e - T_w(x)$, as well as the inlet flow at $x=0$ are required inputs for the calculation.

Results and Discussion

Data are presented first for the smooth baseline panels at three pressure gradients. This is followed by a presentation of the rough wall data, and finally a comparison between the rough data and the computational model calculation.

Smooth Wall With Pressure Gradient. Smooth wall tests were conducted both to provide a benchmark for comparison with the rough-wall data and to establish the suitability of the experimental facility. Table 2 shows the St data and corresponding Re_x for each of the three pressure gradients with smooth walls. The zero pressure gradient (ZPG) case actually has a nonzero value of K . However, the value is an order of magnitude less than the absolute value of K for both pressure gradient cases. Thus, it is referred to as the zero pressure gradient reference. St increases and decreases both by about 10% for favorable pressure gradient (FPG) and adverse pressure gradient (APG), respectively. This result for a smooth wall turbulent boundary layer appears to run counter to the aforementioned findings of Moretti and Kays [22] in which freestream acceleration suppressed turbulent fluctuations, reducing St for constant x . Though it is unclear from the data presentation in [22], it is quite possible that their St data would actually show a slight increase with FPG if comparisons could be made at matched Re_x conditions (as in the present study). However, there are other mitigating factors to consider as well. The leading 1/3rd of the Moretti and Kays wind tunnel is non-heated. Thus the hydrodynamic boundary layer is significantly larger than the thermal boundary layer. Since the thermal boundary layer resides in the near wall log-law region in this configura-

ration, an acceleration-induced suppression of turbulent fluctuations would have a significant impact on the energy exchange with the wall. By contrast, the present heat transfer experiment is conducted in a transient mode. The entire tunnel floor ($x \geq 0$) sees the same blast of hot air, and the velocity and thermal boundary layers are more comparable in size. A second difference is related to the boundary layer history upstream of the measurement location. Moretti and Kays compare acceleration to constant U_e after a considerable constant velocity zone. As such, the boundary layer size at the measurement site would only be slightly thinner in the accelerated case. Since the present study uses approximately linear freestream velocity gradients from $x=0$ (Fig. 3), U_e and Re_x are matched at the measurement location, but the boundary layer thicknesses vary dramatically (42 mm, 27 mm, and 12 mm for APG, ZPG, and FPG, respectively). This disparity in boundary layer size with comparable U_e and T_e creates considerably different boundary layer gradients and exchange rates.

To verify the magnitude of the smooth-wall St variation with pressure gradient, calculations were made using both BLACOMP and the method of Ambrok [31]. Ambrok's empirically based integral method employs an assumed relationship between the surface heat flux and the energy thickness of the boundary layer to solve the energy integral equation. An implicit assumption of this method is that the thermal and hydrodynamic boundary layers develop independently. This limitation aside, Ambrok's method has been used by a number of researchers, [22,32], for a reasonably accurate and robust prediction of St with variable U_e and $T_e - T_w$. Initially, the two calculations were conducted with a constant $T_e - T_w$ assumption, using the experimental value from the measurement location ($x=1.2$ m). This produced matching trends in the calculated St (increase for FPG and decrease for APG), but the magnitude of the change was only 1/3rd that of the experimental result. Upon closer consideration, it was discovered that both calculation procedures are quite sensitive to the $T_e - T_w$ variation with x . Unfortunately, T_w was only measured at $x=1.2$ m in the experiment, and no other information (e.g., thermal boundary layer profiles) was available to infer $T_w(x)$. Since the wall is modeled as a semi-infinite surface with constant T_w at $t=0$, the thermal wall boundary condition during the experiment is neither constant T_w nor constant q_w (much like a turbine blade, incidentally). Because both boundary layers develop from the leading edge, it is reasonable to assume that for ZPG, $T_e - T_w$ would be ≈ 0 at $x=0$, rising steeply during the initial stages of boundary layer development, then approaching the measured value of 25°C at $x=1.2$ m asymptotically. Since the FPG is constantly accelerating from $x=0$ to 1.2 m, the boundary layer growth is slower, and $T_e - T_w$ would not adjust as sharply with x . The APG boundary layer, on the other hand, would experience rapid growth near the leading edge and may indeed be well approximated by a constant $T_e - T_w$ thereafter (the thick boundary layer providing a significant deterrent to variations in T_w from $x=0$ to 1.2 m). These three intuition-based $T_e - T_w(x)$ distributions are depicted in Fig. 4 (normalized by $T_e - T_w$ at $x=1.2$ m). Employing these variable $T_e - T_w$ distributions in the BLACOMP and Ambrok calculations yielded closer agreement with the experimental data as shown in Table 2. Since the roughness panels only occupy the region from $1.04\text{ m} < x < 1.32\text{ m}$ in the wind tunnel, it was assumed that these T_w distributions would change very little with different roughness panels. Accordingly, they were employed in the BLACOMP rough-wall calculations as well.

Though the focus of this paper is on heat transfer, the BLACOMP calculation also yields a prediction of c_f . With the view of shedding light on the applicability of Reynolds analogy ($St \approx c_f/2$) in nonzero pressure gradients, Table 2 also includes the BLACOMP c_f prediction and the resulting value of $2St/c_f$. Reynolds analogy is based on the equivalence of the turbulent eddy diffusivities for heat and momentum. The BLACOMP value for c_f agrees favorably with that obtained using a standard integral calculation from White [33], also shown in the table. The Reynolds

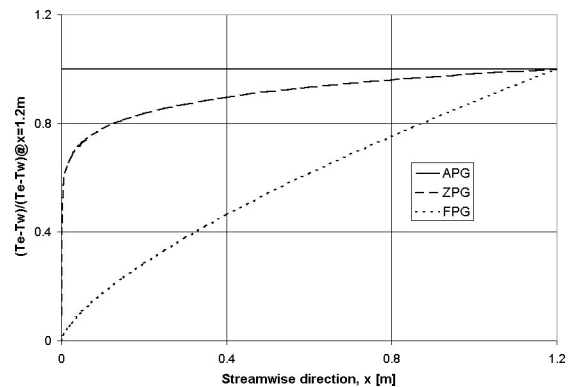


Fig. 4 Empirical $T_e - T_w$ distributions used in St calculations (nondimensionalized by measured $T_e - T_w$ at $x=1.2$ m)

analogy trend shown in the table bears some explanation. It appears that the predicted Reynolds analogy is not independent of pressure gradient. Indeed, it increases with APG and decreases with FPG. This indicates that heat transfer (the numerator) is much less sensitive to pressure gradient than skin friction (the denominator). This finding has been noted by others, dating back to the nozzle flow experiments of Back et al. [32,34]. In two different cases, Reynolds analogy dropped from the 1.2–1.3 range at ZPG to approximately 0.7 in the accelerated zone of the nozzle. Acceleration parameters were considerably higher for these flows ($K \approx 2 \times 10^{-6}$) than for the present study (Table 2), explaining the more significant drop in Reynolds analogy with acceleration. Back et al. [34] flatly state that the Colburn equation (Reynolds analogy) “fails badly” in regions of variable U_e . Boundary layer temperature and velocity measurements indicate that the thermal resistance of the boundary layer (the enthalpy thickness) is much less responsive to acceleration than the momentum thickness (θ). Indeed, temperature profiles taken in the converging nozzle vary only slightly with axial distance while the velocity profiles show a large shift of momentum down toward the wall. This disparity between c_f and St with pressure gradient was treated analytically by So [35]. So extended the equilibrium turbulent boundary layer analysis of Mellor and Gibson [36] to the thermal boundary layer. With both boundary layers then fully characterized, So was able to plot Reynolds analogy versus Clauser's equilibrium parameter β (Fig. 5). Though the current experiments are not equilibrium turbulent boundary layers in the classical sense, the trends are remarkably in line (see data plotted with So's theoretical trends in Fig. 5). This effect also explains the relatively low Reynolds analogy values (≈ 0.95) reported for recent pipe flow experiments

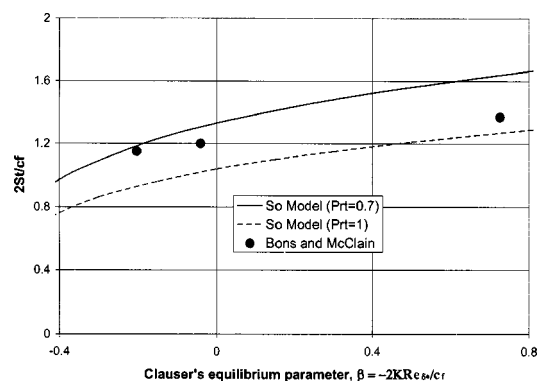


Fig. 5 Reynolds analogy predictions from So [35] compared with results using smooth-wall predictions from BLACOMP computation

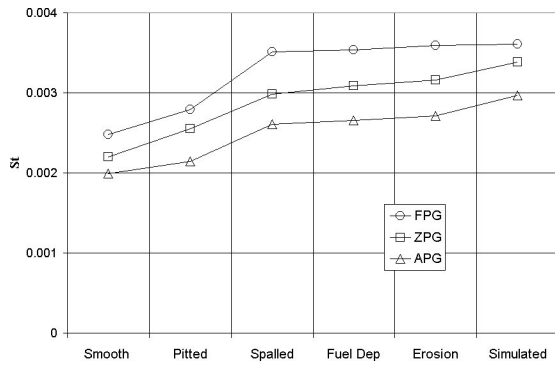


Fig. 6 Experimental St data for six panels and three pressure gradients ($Re_x=9 \times 10^5$)

of Belnap et al. [37]. Though a fully developed turbulent pipe flow is different in several ways from an external, developing boundary layer, the favorable axial pressure gradient does result in a lower Reynolds analogy than for ZPG (1.1–1.2). This finding is particularly critical for experimentalists who often infer heat transfer from skin friction measurements or vice versa, [38]. If pressure gradients are considerable, the two exchange mechanisms do not behave in unison.

Rough Wall With Pressure Gradient. As mentioned earlier, four distinct roughness models were used in this study: pitted, spalled, fuel deposit, and erosion/deposits. A fifth surface was also constructed using a staggered array of cones (height=2 mm, base diameter=5 mm, spacing=5 mm). This simulated rough surface (also reported in [3]) was designed to have similar roughness statistics to the erosion/deposits surface in this paper. The St data for all six surfaces is shown in **Fig. 6**. St increases with both roughness and favorable pressure gradient at constant Re_x . There are several different ways to dissect the data in this figure. **Figures 7 and 8** show two such treatments. **Figure 7** plots the roughness-induced change in St (rough minus smooth) as a percent of the smooth-wall St value, all evaluated at the same pressure gradient. This change is calculated for each of the three pressure gradients and all five rough surfaces. (The smooth panel is not plotted since it would be self-referenced and thus identically equal to zero.) The lower roughness-induced St augmentation for APG appears to be universal across all surface types (on average 7% less than the roughness effect at ZPG). The results with FPG are not so universal. The roughest three scaled models show a +3% difference in roughness effect between FPG and ZPG, while the pitted and simulated surfaces actually show a lower roughness-induced effect on St . This should not be misinterpreted as a reduction in St

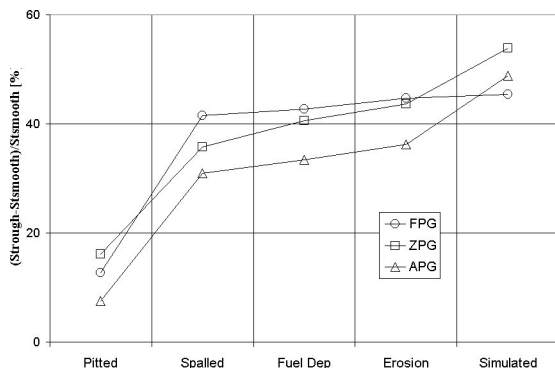


Fig. 7 Experimental data for five panels ($Re_x=9 \times 10^5$). Roughness-induced change in $St(St_{Rough} - St_{Smooth})$ as a percent of St_{Smooth} at matching pressure gradient.

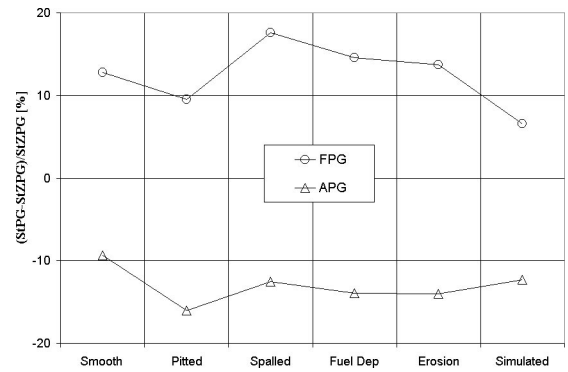


Fig. 8 Experimental data for six panels ($Re_x=9 \times 10^5$). Pressure gradient induced change in $St(St_{PG} - St_{ZPG})$ as a percent of St_{ZPG} for the same rough surface.

with FPG for these cases (as is clear from the raw St data in **Fig. 6**). Rather it implies that the percent increase in heat transfer due to roughness for FPG is less than the observed percent increase in heat transfer due to roughness for ZPG. **Figure 8** plots the pressure gradient induced change in St (nonzero pressure gradient minus zero pressure gradient) as a percent of the St value at zero pressure gradient for the same rough surface. Data is shown for FPG and APG only since the ZPG curve would be identically zero. Pressure gradient has the same qualitative effect for all of the six surfaces shown (FPG increases St while APG decreases St at constant roughness). The APG data again show some universal trends (all rough panels are lower than the smooth baseline), while the FPG data show mixed results when compared to the smooth case. The range of accelerated freestream St augmentation (7–18%) shown in **Fig. 8** is comparable to that reported by other researchers. Coleman et al. reported increases from 10–20%, while Chakroun and Taylor measured 5–15% increases (data was presented for roughness with FPG compared to roughness with ZPG). These studies both reported St at constant x (not Re_x). Dukhan et al. reported St versus Re_x and showed 10–40% augmentation (larger with higher Re_x). Finally, Turner et al. reported 5% augmentation. An exact comparison is difficult to make due to the number of variables in the different wind tunnels (unheated starting length, flow history, etc.), yet the level of augmentation due to FPG is consistent.

Of critical importance to the designer is whether heat transfer augmentation due to pressure gradient alone can simply be added to results with roughness alone to approximate the effect when both are present. If true, this would imply a lack of synergy between the two mechanisms. This is attractive to the designer because it allows correction factors to be simply superposed without additional parametric testing. One way to determine the degree to which these two mechanisms are synergistic is to compare the augmentation results obtained with both mechanisms present to that achieved by adding or compounding their individual effects. For example, if the smooth plate St augmentation due to favorable pressure gradient was 10% and the St augmentation of a rough plate (with zero pressure gradient) was 40%, the additive prediction for the rough plate with FPG would be 50%. For the same case, the compound method would predict a combined effect of 54%. These three measures can be written algebraically as follows:

$$\text{Synergistic: } \frac{St_{RPG}}{St_o} - 1 \equiv \frac{\Delta St}{St_o} \quad (1)$$

$$\text{Compound: } \frac{St_R}{St_o} \frac{St_{PG}}{St_o} - 1 \quad (2)$$

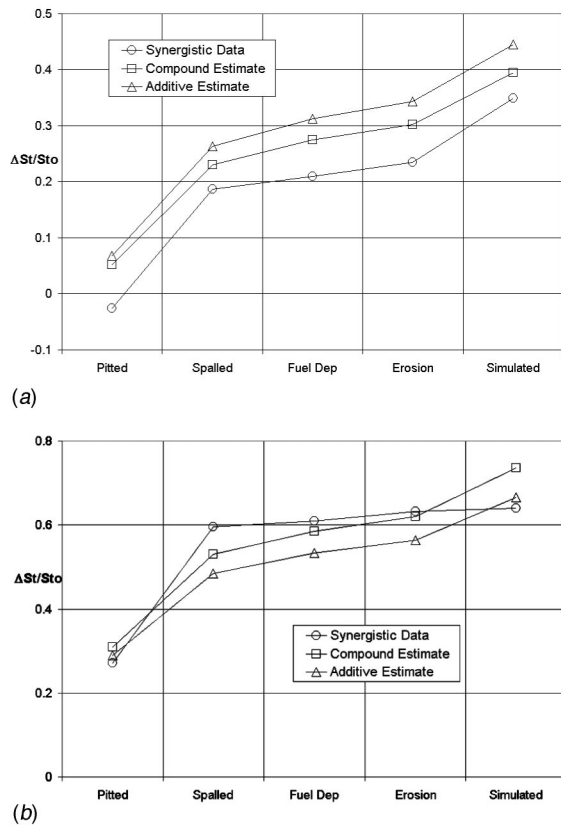


Fig. 9 Comparison of combined (synergistic) roughness/pressure gradient effects on St with compound and additive estimates using individual effects of roughness alone and pressure gradient alone. Data for five rough surfaces and (a) APG or (b) FPG. ($Re_x=9 \times 10^5$).

$$\text{Additive: } \left(\frac{St_R}{St_o} - 1 \right) + \left(\frac{St_{PG}}{St_o} - 1 \right). \quad (3)$$

The subscripts “R,” “PG,” and “RPG” represent St measurements with roughness only, nonzero pressure gradient only, and the two effects combined, respectively. An identical analysis was conducted in [3] looking for synergies between roughness and freestream turbulence. **Figures 9(a,b)** contain these measures for all five surfaces at APG and FPG, respectively. An interpretation of the APG plot is that the additive St estimate would overpredict the actual St by 10% on average, while the compound estimate overpredicts the actual St by only 6%. This is a negative synergy. The FPG plot again has a mixed result. The three roughest “real” models show an average of 8.5% positive synergy relative to the additive estimate while the pitted panel and the simulated panel both show slightly negative synergies (up to an average of -7% relative to the compound estimate). The magnitude of the synergy in St is not as significant as those reported in [3] for roughness and freestream turbulence (5–20%). However, it is expected that the synergies will grow with pressure gradient (K), and the values of K in this study are lower than for a typical turbine blade. Thus, the error that would be incurred by estimating the synergistic St augmentation by the simple superposition of the two separate effects could be substantial in practice. Also, measured and calculated c_f synergies with roughness and pressure gradient indicate much stronger synergies in aerodynamics than in heat transfer. For example, BLACOMP calculations of c_f for the erosion/deposit surface with favorable pressure gradient yield a 216% additive estimate for c_f augmentation (roughness and pressure gradient effects assessed independently) compared with the synergistic result of 266% (roughness and pressure gradient effects combined). This

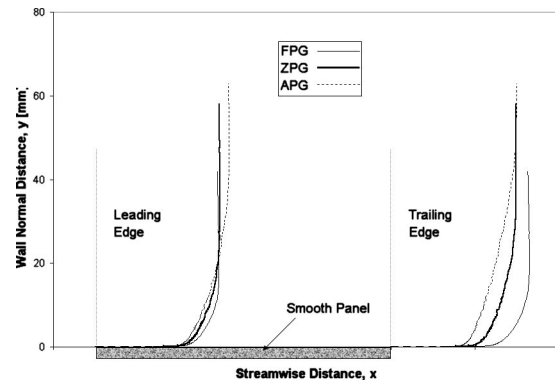


Fig. 10 Mean velocity profiles (U) at leading and trailing edge of smooth panels: adverse, zero, and favorable pressure gradients. ($Re_x=9 \times 10^5$).

50% under prediction is due to the strong positive synergy of favorable pressure gradients and roughness and is similar to experimental c_f measurements (not presented in this paper) for the erosion/deposit surface. There is, of course, a clearer physical mechanism for c_f synergy with pressure gradient and roughness. The bulk of c_f increase with roughness is due to the form drag on the individual roughness elements. Favorable pressure gradient (like elevated freestream turbulence) has a tendency to increase the near wall momentum, thus producing an even larger increase in c_f (due to a disproportionate increase in form drag) than would be predicted for pressure gradient and roughness separately. The opposite would be true for APG.

There is no “form drag” equivalent for heat transfer, so the link between pressure gradient and roughness is less obvious. Ultimately, the wall heat transfer occurs by conduction, so synergies must either interrupt (APG) or accelerate (FPG) this process. Previous researchers, [22], have identified the pressure gradient influence on turbulent fluctuations in the boundary layer as a possible suppression/enhancement mechanism. To explore this possibility, boundary layer profiles were taken at the leading and trailing edges of three different panels (smooth, erosion/deposits, and simulated) at the three pressure gradients. Because the heat transfer tests are transient, these velocity measurements were not made simultaneously with the St measurements. Rather, T_e was set to a constant value (close to the value used in the transient heat transfer tests) and the wall temperature was not controlled in any way. Thus, there was little or no $T_e - T_w$. The profiles were taken with a single-element hotwire. **Figure 10** shows the mean velocity (U) profiles for the smooth panel and three pressure gradients at leading and trailing edges.

With so many flow variables, it was necessary to synthesize these boundary layer data into their essential results. Accordingly, the boundary layer momentum thickness (θ) and streamwise turbulent kinetic energy (u'^2) flux (q) were computed for both leading and trailing profiles:

$$\theta = \int_0^\delta \frac{U}{U_e} \left(1 - \frac{U}{U_e} \right) dy \quad (4)$$

and

$$q = \int_0^\delta u'^2 U dy. \quad (5)$$

The change in these values from trailing to leading edge was then calculated to arrive at the net change of momentum thickness ($\Delta\theta$) and streamwise turbulent kinetic energy flux (Δq) across the test panels. In the same way that the rough-wall St data were compared to the smooth-wall St data for reference, the smooth-wall trailing-to-leading-edge difference ($\Delta\theta_{\text{smooth}}$) was then sub-

Table 3 Boundary layer parameter variation across test panels

Surface	PG	$\Delta\theta = \theta_{TE} - \theta_{LE}$	$\Delta\theta_{rough} - \Delta\theta_{smooth}$	$\Delta q = q_{TE} - q_{LE}$	$\Delta q_{rough} - \Delta q_{smooth}$
		(mm)	(mm)	(m ⁴ /s ²)	(m ⁴ /s ³)
Smooth	FPG	0.11		0.021	
Smooth	ZPG	0.75		0.036	
Smooth	APG	2.14		0.071	
Ero/dep	FPG	1.17	1.07	0.167	0.146
Ero/dep	ZPG	1.4	0.65	0.135	0.099
Ero/dep	APG	2.47	0.33	0.163	0.092
Simulated	FPG	0.97	0.87	0.112	0.091
Simulated	ZPG	1.41	0.66	0.124	0.088
Simulated	APG	2.58	0.45	0.154	0.083

tracted from the rough-wall ($\Delta\theta_{rough}$) value at the same pressure gradient (to try to isolate the effect of roughness only for a given pressure gradient). The result is in **Table 3** for the erosion/deposits and simulated surfaces. The table includes the $\Delta\theta$ and Δq values for all three surfaces at the three pressure gradient values. $\Delta\theta$ values are positive since the boundary layer momentum thickness increases from leading edge to trailing edge. Δq values are also positive since the difference between the streamwise turbulent kinetic energy exiting and entering the control volume over the test panels represents the net production of TKE in the developing boundary layer. The 4th and 6th columns in **Table 3** contain the comparison of rough to smooth values (the change due to roughness at constant pressure gradient).

Looking first at the “real” erosion/deposit roughness data, the APG boundary layer has less roughness-induced momentum deficit (0.33) and less roughness-induced TKE generation (0.092) when referenced to the smooth wall APG values than ZPG or FPG with the same roughness. It would then be expected that this roughness would have less effect on St for APG than for ZPG or FPG since St is influenced both by turbulent fluctuations and the near-wall velocity profile. This is again evidence of a negative synergy. The opposite is seen for the FPG data, where a positive synergy is implied (for this roughness panel). The rough surface generates 0.099 (m⁴/s³) more streamwise turbulent kinetic energy (Δq) than a smooth surface at zero pressure gradient, while in an accelerating flow the rough surface generates 0.146 (m⁴/s³) more Δq than if the surface were smooth. A physical mechanism for this observed variation in Δq with pressure gradient may be the stretching of turbulent eddies generated from roughness elements in the boundary layer. The thinner favorable pressure gradient boundary layer has a steeper mean velocity gradient which will increase the transfer of mean kinetic energy to turbulent kinetic energy via the vortex stretching mechanism. The opposite would be true for the adverse pressure gradient case. Also, in terms of the k^+ regimes established by Schlichting [10], the favorable pressure gradient flow (with higher c_f at constant Re_x) increases the k^+ of a given roughness, possibly moving it from aerodynamically smooth ($k^+ < 5$) to transitionally rough or even to fully rough ($k^+ > 60$). Incidentally, the smooth case in the present study shows the same drop in streamwise turbulent kinetic energy generation (Δq) with favorable pressure gradient that was reported by Moretti and Kays [22] for a smooth wall.

Turning attention to the simulated roughness panel, we note that despite the matched roughness statistics for the two panels, the effect of pressure gradient is markedly different. The range of momentum thickness increase is not as broad and the increased turbulent kinetic energy generation with FPG is significantly less than for the “real” roughness counterpart. This underscores the finding from [3] that statistically “equivalent” ordered roughness surfaces may be tuned to match the c_f of “real” roughness, but they will not necessarily match the St (generally yielding a higher St). The explanation offered in [3] for this shortcoming was that the lower St of “real” roughness may be due to the range and

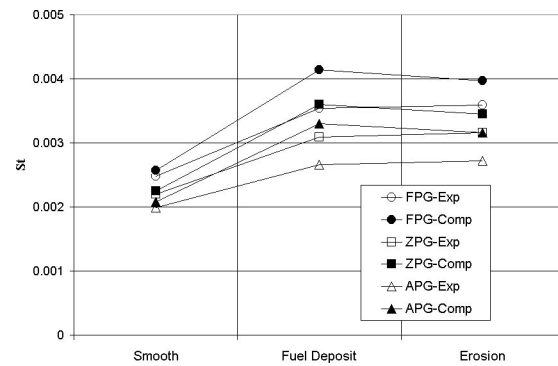


Fig. 11 Comparison of experimental St data with discrete-element method prediction for three panels and three pressure gradients. ($Re_x = 9 \times 10^5$).

random distribution of roughness scales in the “real” case. Shed vorticity from the larger roughness elements may be disrupted downstream by smaller elements and rendered less effective at augmenting heat transfer. This was the finding with no pressure gradient. The present data adds to this finding by showing that the two statistically equivalent surfaces do not respond to FPG similarly. The simulated roughness model already elicits a more elevated heat transfer augmentation without pressure gradient. Thus, when a favorable pressure gradient is imposed, the simulated roughness model does not have as much room to enhance St as the “real” roughness model.

Nuances such as these are missed by equivalent sandgrain type empirical roughness correlations. Likewise, CFD applications that adjust the van Driest damping in the turbulence closure relation to account for roughness effects are also limited in this regard. By contrast, the discrete-element method considers the particular roughness geometry of each surface, assessing the individual contributions to c_f and St of each roughness element. As reported in [17], the BLACOMP code was able to match c_f within 7% and St within 16% for a range of real and simulated roughness panels. For this study, the same code was exercised for three of the panels from the experimental study (smooth, fuel deposits, and erosion/deposits) at three pressure gradients. The experimental $U_e(x)$ distribution was input along with the intuitively based $T_e - T_w(x)$ distribution discussed previously (**Fig. 4**). The results for these three surfaces are compared with the experimental St data in **Fig. 11**. As expected from the data in **Table 2**, the smooth St values match within 5%. For zero pressure gradient, the computed St values for the two rough panels are an average of 12% higher than the measured values. This discrepancy aside, the effect of pressure gradient for a given roughness panel is quite well matched. The difference in computed St from FPG to APG for the two rough surfaces is 23% of the ZPG St value. For the experimental St measurements, this same difference is 28% of the ZPG St value. While there are still areas for improvement, this level of agreement in heat transfer calculations with roughness is significant. Clearly, the capabilities of the discrete-element method make it a formidable prediction tool for “real” roughness.

Summary and Conclusions

Heat transfer measurements have been made on roughness panels in a low-speed wind tunnel at three different pressure gradients. The roughness panels are scaled models of actual turbine surfaces rather than the traditional simulated roughness using sand or ordered arrays of cones or spherical segments. Based on the findings, the following conclusions are made:

1. For a smooth-wall turbulent boundary layer, favorable pres-

sure gradient increases St for the same Re_x compared to no pressure gradient. Adverse pressure gradient has the opposite effect.

- Heat transfer is less sensitive to pressure gradient variations than skin friction for a smooth wall turbulent boundary layer. This phenomenon results in a variable Reynolds analogy with pressure gradient.
- Combined roughness and pressure gradient have negative (for APG) and positive (for FPG) synergies on heat transfer. Adding the measured effects of roughness alone and adverse pressure gradient alone on heat transfer to arrive at an estimate for St when both are present would overpredict the actual St by 10% on average. Conversely for FPG, this additive estimate would underpredict the St by 8%. Synergies are less pronounced when the St data are compared to compound estimates.
- A simulated roughness panel with matched roughness statistics to a "real" roughness test model does not show the same heat transfer or boundary layer behavior.
- A discrete-element method CFD computation is able to capture the variation in St with pressure gradient for three different roughness panels.

Acknowledgments

The authors are indebted to numerous personnel at the four industrial partners for providing the turbine hardware. Primary among these are: Dr. Boris Glezer formerly of Solar Turbines, Dr. Ron Bunker and Mr. Paul Suttman at General Electric, Mr. Mohan Hebbar at Siemens-Westinghouse, and Dr. William Troha and Mr. Shawn Pollock of Honeywell Corporation. In addition, collaborations with Dr. Keith Hodge at Mississippi State University and Drs. Richard Rivir and Rolf Sondergaard of the Air Force Research Lab (AFRL) are appreciated. The testing was conducted at the Air Force Research Lab Aero-thermal research laboratory with technical support from Mr. William Nilson, Mr. Jay Anderson, and Mr. Andy Pitts. The assistance of Ms. Nikki Widmor at the University of Dayton Research Institute in determining the plastic properties is gratefully acknowledged. This work was sponsored by the U.S. Department of Energy–National Energy Technology Laboratory through a cooperative agreement with the South Carolina Institute for Energy Studies at Clemson University. The views expressed in this article are those of the author and do not reflect the official policy or position of the Department of Energy or U.S. Government.

Nomenclature

APG = adverse pressure gradient
 FPG = favorable pressure gradient
 K = acceleration parameter, $\nu(dU_e/dx)/U_e^2$
 Pr_t = turbulent Prandtl number
 Ra = centerline average roughness
 Re_x = Reynolds number ($U_e x/\nu$)
 Rt = maximum peak to valley roughness
 Rz = average peak to valley roughness
 S = surface area of sample without roughness
 S_w = wetted surface area of sample with roughness
 St = Stanton Number, $h/(\rho c_p U_e)$
 T = temperature ($^{\circ}C$)
 U = mean velocity (m/s)
 ZPG = zero pressure gradient
 c_f = skin friction coefficient, $\tau_w/(0.5\rho U_e^2)$
 c_p = specific heat at constant pressure
 h = convective heat transfer coefficient
 k = average roughness height ($\approx Rz$)
 k^+ = ku_τ/ν
 q = streamwise flux of boundary layer streamwise turbulent kinetic energy
 u' = fluctuating velocity (rms)

u_τ = friction or shear velocity $\sqrt{\tau_w/\rho}$
 x = streamwise distance from tunnel leading edge
 y = surface normal distance
 Δ = change in quantity from trailing to leading edge of panels
 α = airfoil angle of attack
 α_{rms} = rms deviation of surface slope angles
 β = Clauser's equilibrium parameter,
 $\beta = -2\delta_d(dU_e/dx)/(c_f U_e)$
 δ = boundary layer thickness
 δ_d = boundary layer displacement thickness
 ν = kinematic viscosity
 θ = boundary layer momentum thickness
 ρ = density
 τ_w = wall shear

Subscripts

e = freestream (boundary layer edge) value
 o = smooth plate reference
 PG = pressure gradient only
 R = roughness only
 RPG = roughness and pressure gradient
 rough = rough wall value
 smooth = smooth wall value at the same pressure gradient
 w = surface value

References

- Rivir, R. B., 2002, private communication.
- Nikuradse, J., 1933, "Laws for Flows in Rough Pipes," VDI-Forschung. 361, Series B, 4 (English Translation NACA TM 1292, 1950).
- Bons, J. P., 2002, "St and c_f Augmentation for Real Turbine Roughness With Elevated Freestream Turbulence," ASME J. Turbomach., **124**, pp. 632–644.
- Acharya, M., Bornstein, J., and Escudier, M., 1986, "Turbulent Boundary Layers on Rough Surfaces," Exp. Fluids, **(4)**, pp. 33–47.
- Pinson, M. W., and Wang, T., 2000, "Effect of Two-Scale Roughness on Boundary Layer Transition Over a Heated Flat Plate: Part 1—Surface Heat Transfer," ASME J. Turbomach., **122**, pp. 301–307.
- Goldstein, R., Eckert, E., Chiang, H., and Elovic, E., 1985, "Effect of Surface Roughness on Film Cooling Performance," ASME J. Eng. Gas Turbines Power, **107**, pp. 111–116.
- Taylor, R. P., Scaggs, W. F., and Coleman, H. W., 1988, "Measurement and Prediction of the Effects of Nonuniform Surface Roughness on Turbulent Flow Friction Coefficients," ASME J. Fluids Eng., **110**, pp. 380–384.
- Bogard, D. G., Schmidt, D. L., and Tabbita, M., 1998, "Characterization and Laboratory Simulation of Turbine Airfoil Surface Roughness and Associated Heat Transfer," ASME J. Turbomach., **120**, pp. 337–342.
- Barlow, D. N., Kim, Y. W., and Florschuetz, L. W., 1997, "Transient Liquid Crystal Technique for Convective Heat Transfer on Rough Surfaces," ASME J. Turbomach., **119**, pp. 14–22.
- Schlichting, H., 1979, *Boundary Layer Theory*, 7th Ed., McGraw-Hill, New York.
- Dipprey, D. F., and Sabersky, R. H., 1962, "Heat and Momentum Transfer in Smooth and Rough Tubes at Various Prandtl Numbers," Int. J. Heat Mass Transfer, **6**, pp. 329–353.
- Boyle, R. J., 1993, "Prediction of Surface Roughness and Incidence Effects on Turbine Performance," ASME Paper No. 93-GT-280.
- Tolpadi, A. K., and Crawford, M. E., 1998, "Predictions of the Effect of Roughness on Heat Transfer From Turbine Airfoils," ASME Paper No. 97-GT-087.
- Blair, M. F., 1994, "An Experimental Study of Heat Transfer in a Large-Scale Turbine Rotor Passage," ASME J. Turbomach., **116**, pp. 1–13.
- Guo, S. M., Jones, T. V., Lock, G. D., and Dancer, S. N., 1998, "Computational Prediction of Heat Transfer to Gas Turbine Nozzle Guide Vanes With Roughened Surfaces," ASME J. Turbomach., **120**, pp. 343–350.
- Hosni, M. H., Coleman, H. W., and Taylor, R. P., 1991, "Measurements and Calculations of Rough-Wall Heat Transfer in the Turbulent Boundary Layer," Int. J. Heat Mass Transfer, **34**, pp. 1067–1082.
- McClain, S. T., Hodge, B. K., and Bons, J. P., "Predicting Skin Friction and Heat Transfer for Turbulent Flow Over Real Gas-Turbine Surface Roughness Using the Discrete-Element Method," ASME Paper No. GT-2003-38813.
- Goebel, S. G., Abuaf, N., Lovett, J. A., and Lee, C.-P., 1993, "Measurements of Combustor Velocity and Turbulence Profiles," ASME Paper No. 93-GT-228.
- Dorney, D. J., Ashpis, D. E., Halstead, D. E., and Wisler, D. C., 1999, "Study of Boundary Layer Development in a Two-Stage Low-Pressure Turbine," Paper No. AIAA 99-0742.
- Bons, J. P., Taylor, R., McClain, S., and Rivir, R. B., 2001, "The Many Faces of Turbine Surface Roughness," ASME J. Turbomach., **123**, pp. 739–748.
- Coleman, H. W., Moffat, R. J., and Kays, W. M., 1981, "Heat Transfer in the

- Accelerated Fully Rough Turbulent Boundary Layer," ASME J. Heat Transfer, **103**, pp. 153–158.
- [22] Moretti, P. M., and Kays, W. M., 1965, "Heat Transfer to a Turbulent Boundary Layer With Varying Free-Stream Velocity and Varying Surface Temperature—An Experimental Study," *Int. J. Heat Mass Transfer*, **8**, pp. 1187–1201.
- [23] Chakroun, W., and Taylor, R. P., 1993, "The Effects of Moderately Strong Acceleration on Heat Transfer in the Turbulent Rough-Wall Boundary Layer," ASME J. Heat Transfer, **115**, pp. 782–785.
- [24] Poinsatte, P. E., VanFossen, G. J., and Newton, J. E., 1991, "Heat Transfer Measurements From a Smooth NACA 0012 Airfoil," *J. Aircr.*, **28**(12), pp. 892–898.
- [25] Poinsatte, P. E., VanFossen, G. J., and DeWitt, K. J., 1991, "Roughness Effects on Heat Transfer From a NACA 0012 Airfoil," *J. Aircr.*, **28**(12), pp. 908–911.
- [26] Dukhan, N., Masiulaniec, K. C., and DeWitt, K. J., 1999, "Experimental Heat Transfer Coefficients From Ice-Roughened Surfaces for Aircraft Deicing Design," *J. Aircr.*, **36**(6), pp. 948–956.
- [27] Dukhan, N., Masiulaniec, K. C., DeWitt, K. J., and VanFossen, G. J., 1999, "Acceleration Effect on the Stanton Number for Castings of Ice-Roughened Surfaces," *J. Aircr.*, **36**(5), pp. 896–898.
- [28] Turner, A. B., Hubbe-Walker, S. E., and Bayley, F. J., 2000, "Fluid Flow and Heat Transfer Over Straight and Curved Rough Surfaces," *Int. J. Heat Mass Transfer*, **43**, pp. 251–262.
- [29] Schultz, D. L., and Jones, T. V., 1973, "Heat-Transfer Measurements in Short-Duration Hypersonic Facilities," Advisory Group for Aerospace Research and Development, No. 165, NATO.
- [30] Gatlin, B., and Hodge, B. K., 1990, "An Instructional Computer Program for Computing the Steady, Compressible Turbulent Flow of an Arbitrary Fluid Near a Smooth Wall," Department of Mechanical Engineering, Mississippi State University, Second printing.
- [31] Ambrok, G. S., 1957, "Approximate Solution of Equations for the Thermal Boundary Layer With Variations in Boundary Layer Structure," *Soviet Physics*, **2**(2), pp. 1979–1986.
- [32] Back, L. H., and Cuffel, R. F., 1971, "Turbulent Boundary Layer and Heat Transfer Measurements Along a Convergent-Divergent Nozzle," ASME J. Heat Transfer, **93**, pp. 397–407.
- [33] White, F. M., 1991, *Viscous Fluid Flow*, 2nd Ed., 1991, McGraw-Hill, New York.
- [34] Back, L. H., and Seban, R. A., 1965, "On Constant Property Turbulent Boundary Layers With Variable Temperature or Heat Flow at the Wall," ASME J. Eng. Gas Turbines Power, **87**(1), pp. 151–156.
- [35] So, R. M. C., 1994, "Pressure Gradient Effects on Reynolds Analogy for Constant Property Equilibrium Turbulent Boundary Layers," *Int. J. Heat Mass Transfer*, **37**, pp. 27–41.
- [36] Mellor, G. L., and Gibson, D. M., 1966, "Equilibrium Turbulent Boundary Layers," *J. Fluid Mech.*, **24**, pp. 225–253.
- [37] Belnap, B. J., vanRij, J. A., and Ligrani, P. M., 2002, "A Reynolds Analogy for Real Component Surface Roughness," *Int. J. Heat Mass Transfer*, **45**, pp. 3089–3099.
- [38] Abuaf, N., Bunker, R. S., and Lee, C. P., 1998, "Effects of Surface Roughness on Heat Transfer and Aerodynamic Performance of Turbine Airfoils," ASME J. Turbomach., **120**(3), pp. 522–529.

Vortex Transport and Blade Interactions in High Pressure Turbines

V. S. P. Chaluvadi

A. I. Kalfas

H. P. Hodson

Whittle Laboratory,
Cambridge University Engineering Department,
Maddingley Road,
Cambridge CB3 0DY, UK

This paper presents a study of the three-dimensional flow field within the blade rows of a high-pressure axial flow steam turbine stage. Half-delta wings were fixed to a rotating hub to simulate an upstream rotor passage vortex. The flow field is investigated in a low-speed research turbine using pneumatic and hot-wire probes downstream of the blade row. The paper examines the impact of the delta wing vortex transport on the performance of the downstream blade row. Steady and unsteady numerical simulations were performed using structured three-dimensional Navier-Stokes solver to further understand the flow field. The loss measurements at the exit of the stator blade showed an increase in stagnation pressure loss due to the delta wing vortex transport. The increase in loss was 21% of the datum stator loss, demonstrating the importance of this vortex interaction. The transport of the stator viscous flow through the rotor blade row is also described. The rotor exit flow was affected by the interaction between the enhanced stator passage vortex and the rotor blade row. Flow underturning near the hub and overturning towards the midspan was observed, contrary to the classical model of overturning near the hub and underturning towards the midspan. The unsteady numerical simulation results were further analyzed to identify the entropy producing regions in the unsteady flow field.

[DOI: 10.1115/1.1773849]

1 Introduction

The most significant contribution to the unsteadiness in a turbine is due to the periodic chopping of the wake (Hodson [1]) and secondary flow vortices from the upstream blade row by the downstream blade row (Chaluvadi et al. [2,3], Sharma et al. [4], Boletis and Sieverding [5], Walraevens et al. [6], and Ristic et al. [7]). As modern engine design philosophy places emphasis on higher blade loading and smaller engine length, the effects of these interactions become even more important. For a turbine with a low aspect ratio and high blade turning angle, secondary flow interactions could become more important than those due to wakes. Sharma et al. [4,8] showed that the interaction of the first rotor secondary flows with the succeeding second stator blade row appears to dominate the flow field. All the earlier studies were conducted in a stage environment wherein various forms of secondary flows (blade wake, hub and casing secondary flow and tip leakage flow) occur simultaneously in the blade row. This makes it difficult to isolate the cause and effect of a particular secondary flow interaction with the downstream blade row.

Chaluvadi et al. [9] demonstrated the use of half-delta wings for simulating the passage vortices of a rotor in a turbine. The same concept was used in the scope of the present paper too, where the interaction of these well-known vortices shed from the half-delta wings, with the downstream blade row is investigated. This paper also examines the impact of upstream streamwise vortices on the performance of the downstream blade row. The study focuses on understanding of the transport mechanism and the unsteady mixing process of the passage vortices inside the downstream blade row. These objectives are met through a comprehensive experimental investigation and numerical simulation program.

Contributed by the International Gas Turbine Institute and presented at the International Gas Turbine and Aeroengine Congress and Exhibition, Atlanta, GA, June 16–19, 2003. Manuscript received by the IGTI December 2002; final revision March 2003. Paper No. 2003-GT-38389. Review Chair: H. R. Simmons.

2 Experimental and Numerical Approach

2.1 Test Rig and Instrumentation. The present work has been carried out in a subsonic large-scale, axial flow high-pressure turbine with a casing diameter of 1.524 m and a hub-tip ratio of 0.8. Hodson [1] and Chaluvadi [10] described the test facility in detail. **Figure 1** shows the schematic diagram of the test facility and the planes of measurement. The large scale of the rig makes it possible to measure the flow field inside the blade passage, upstream and downstream of the blade rows. Trip wires of 1.2 mm diameter were used to ensure that the boundary layers at the hub ($\delta^*/h=0.008$, $H=1.31$) and the casing ($\delta^*/h=0.0077$, $H=1.30$) are turbulent at the inlet to the delta wing row. These are located at two stator axial chords upstream of the delta wing row. Further details of the turbine and the design condition of the test rig are given in **Table 1**. **Figure 2(a)** presents the three-dimensional solid model of the rig showing the delta wing row, the stator row and the rotor row with shroud arrangement. **Figures 2(b)** and **2(c)** show the stator vane and rotor blades, respectively.

Half-delta wings were fixed to the rotating hub of a single-stage low-speed rotating turbine upstream of the stator blade row. The relative air angle at the inlet to the delta wing row varies from 74 deg at the hub to 70 deg at the tip. The delta wings were fixed to the hub at 85 deg to the axial direction to maintain an incidence angle of 10 deg to represent a typical rotor passage vortex (Chaluvadi et al. [9]). Initial experiments with 42 delta wings (equal to the number of rotor blades) upstream of the stator were not successful. This was due to the large amount of blockage created by the delta wings as they have a stagger angle of 85 deg. After several trials, it was decided to use 21 delta wings instead of 42, resulting in less mass flow blockage and associated flow distortion.

A Scanivalve system with integral pressure transducer is fitted to the rotor. Slip rings transfer power to and signals from the rotor mounted instruments. The rotor is designed to accommodate a three-axis relative frame traverse system in order to measure the flow field within and at the exit of the rotor. Area traverses were carried out downstream of the blade rows using a five-hole probe.

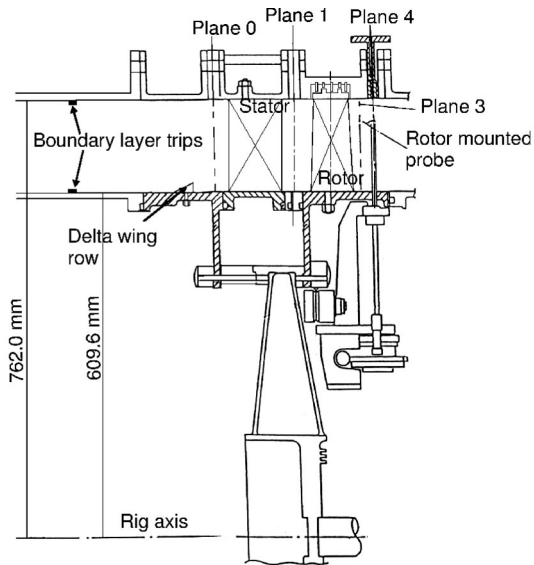


Fig. 1 Schematic diagram of the test configuration

The five-hole probe has a diameter of 2.05 mm with cone semi-angle of 45 deg and side pressure holes drilled perpendicular to the side of the cone. In all of the measurements, the probes were small relative to the blade having diameters of less than 1.5% of the blade pitch. The axes of the probes were aligned parallel to the mean flow direction in order to minimize the errors.

The probe calibration was performed over ± 30 deg yaw and ± 30 deg pitch in a low speed calibration tunnel at the typical velocities encountered in the area traverses downstream of the blade row. Calibration coefficients were chosen to give good resolution over most of the calibrated range. The traversing was achieved using a computer-controlled stepper motor system. The probes were traversed radially from hub to tip in 26 steps and circumferentially over one pitch in 45 steps. Fine data grid resolution was used in the region of large gradients of total pressure such as the blade wake and secondary flows.

2.2 Hot Wire Anemometry. The development of the delta wing flow inside the stator and rotor blade passage was investigated using a miniature three-axis hot wire probe. The probe had a measurement volume of 2 mm in diameter and is made up of three different single-axis inclined sensors arranged perpendicular to each other as shown in Fig. 3. Due to the length-diameter ratio

Table 1 Turbine geometry and test conditions

	Stator	Rotor
Flow coefficient (V_{x1}/U_m)		0.35
Stage loading ($\Delta h_0/U_m^2$)		1.20
Stage reaction		0.5
Midspan upstream axial gap (mm)		41.2
Hub-tip radius ratio	0.8	0.8
Number of blades	36	42
Mean radius (m)	0.6858	0.6858
Rotational speed (rpm)		550
Midspan chord (mm)	142.5	114.5
Midspan pitch-chord ratio	0.84	0.896
Aspect ratio	1.07	1.33
Radial shroud clearance (mm)		1.0
Inlet axial velocity (m/s)	13.85	
Midspan inlet angle (from axial)	0.0 deg	13.46 deg
Midspan exit angle (from axial)	71.03 deg	-70.86 deg
Chord based Reynolds number	5.24×10^5	4.12×10^5
Inlet absolute Mach number	0.038	
Exit absolute Mach number	0.13	
Inlet freestream turbulence	0.25%	

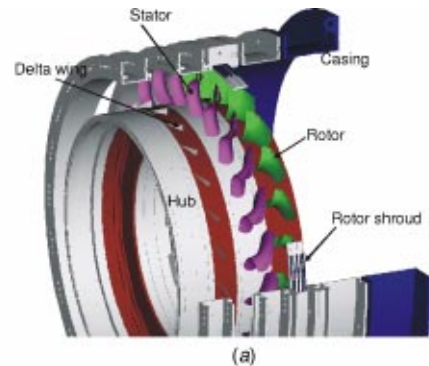


Fig. 2 (a) Large-scale rotating delta wing in the turbine rig, (b) stator vane, (c) rotor blade

of the hot wire sensors (~ 200), it was not appropriate to use the “cosine law” or its modifications to represent the response of the sensors at different angles of attack (Champagne et al. [11]). For this reason, a technique similar to that used for calibrating a five-hole pneumatic probe was developed. The technique relies on the interpolation of the data contained in a look-up table. A fixed, low turbulence, constant velocity jet was used for probe calibration in a low speed calibration tunnel. The probe angular response was calibrated by varying the yaw, pitch angles of the probe (± 30 deg) with respect to the calibration jet. Two nondimensional coefficients, derived from the apparent velocities indicated by the three sensors were used as coordinates for the table. The nondimensional calibration constants were selected to give good resolution over the calibration range and have been checked for uniqueness for the calibration function.

Each anemometer output signal was recorded at a logging frequency of 5.2 KHz using a computer controlled 12-bit transient-capture system. All the measured voltages were converted to velocities before the determination of the statistical quantities. The acquisition of the data was triggered using a once-per-revolution signal. For the phase locked data measurements, 48 samples were recorded in the time taken for the rotor to move past three stator pitches. The data was ensembled over 200 revolutions and about 300 points (17 points pitchwise, 19 points radially), were taken within the area traverse.

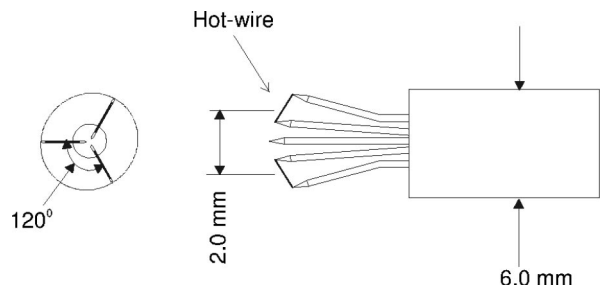


Fig. 3 Schematic of the three-axis hot-wire probe

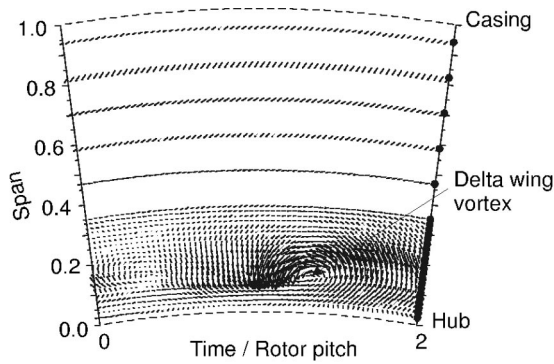


Fig. 4 Secondary velocity vectors at delta-wing exit (plane 0)

2.3 Numerical Approach. The numerical simulations discussed in this paper were performed with a steady Navier-Stokes solver “MULTIP99” and time-accurate Navier-Stokes solver “UNSTREST” of Denton [12–14]. These codes solve the three-dimensional modified Reynolds averaged Navier-Stokes equations on a structured, nonadaptive mesh. The equations of motion are discretized to second-order accuracy and integrated forward in time. A mixing length model with wall function is used for modelling the turbulence in the flow. For the steady-state calculations, a full multigrid method and local time stepping are used to accelerate the convergence. A sliding interface plane between the blade rows allows properties to pass from one blade row to another. The calculation is taken to be converged after a periodic solution is obtained in one blade passing period.

A grid of $61 \times 111 \times 45$ for the delta wing, $61 \times 92 \times 45$ points for the stator and $61 \times 105 \times 45$ points for the rotor has been employed in these numerical simulations in the pitchwise, streamwise and spanwise directions, respectively. Grid expansion ratios of 1.3 near the endwalls and 1.2 near the blade surfaces were used in these computations. A total of nine cells have been employed inside the end-wall boundary layer thickness ($\sim 4\%$ blade span) to represent the vorticity accurately at the inlet to the stator blade row. Unless otherwise indicated, all the experiments and computations have been carried out at the design operating condition.

3 Results and Discussion

3.1 Delta Wing Exit Flow. Measurements were carried out at the exit planes of the delta wing row, the stator row and the rotor blade row. As there was no access for rotating traverse gear at the measurement location behind the delta wing, relative frame traverses were not carried out. Instead, radial and area traverses were carried out in the absolute frame of reference with a five-hole probe to quantify the loss generated due to the delta wing vortex. The losses measured thus include the effect of potential interaction of the stator vane downstream of the delta wing.

The unsteady velocity field downstream of the delta wing trailing edge was measured using a single slant hot-wire technique described by Kuroumaru et al. [15] and developed by Goto [16]. Figure 4 presents the secondary velocity vectors at the exit of the delta wing measured using a single slant hot-wire (23% of stator C_x before the stator leading edge, plane 0) at one circumferential location. The time variation of the measured velocity is expressed as a fraction of the rotor blade-passing period. The secondary velocity vector is defined as the difference between the local velocity vector and the average velocity vector at that spanwise direction throughout the paper. The delta wing vortex can be identified from 5% to 25% of blade span with a center at 17% span and rotating in the counterclockwise direction. A comparison between the vortex generated by the half-delta wing and a typical

rotor passage vortex (in size, velocity deficit and vorticity) indicate that the delta wing vortex is a good simulation of a rotor passage vortex at the hub (Chaluvadi et al. [9]).

3.2 Stator Exit Flow. The flow field at the exit of the stator is investigated with the help of measurements at plane 1, located at 8.4% of stator C_x downstream of the stator trailing edge in the absolute frame of reference. The results are compared between two test configurations.

3.2.1 Datum Configuration. In this configuration, the half-delta wings were not fixed in front of the stator row; instead it had a rotating end-wall. This configuration is referred to as the datum configuration. Figure 5(a) presents the contours of stagnation pressure loss coefficient (Y). The loss regions due to the blade wake can be identified in the middle of the plot. In addition to blade wake, there is a loss core near the casing and the hub from the end-wall secondary flow.

3.2.2 Delta Wing Configuration. In this configuration, half-delta wings were fixed to the rotating end-wall upstream of the stator row. Figure 5(b) presents the contours of stagnation pressure loss coefficient (Y) at the exit of stator row. The axial location and the contour intervals are the same as Fig. 5(a). After comparing the Fig. 5(b) with Fig. 5(a), it can be observed that the stator wake is stronger in the delta wing configuration than the datum configuration. The loss core near the hub is larger in size and higher in loss. It occupies almost 60% of the stator pitch. This is due to the hub passage vortex. Also another region of loss (region A) near the pressure surface can be observed.

Figure 5(c) presents the contours of the predicted stagnation pressure loss coefficient (Y) from the steady numerical simulations. It can be observed that the loss contours agree well with the measurements except near the region corresponding to the hub passage vortex. In computations, the loss core corresponding to the hub passage vortex can be observed at a higher radial location of 30% blade span instead of 10% blade span from the measurements. The size and the strength of the loss core are also much larger than the measurements indicating that the steady computations did not accurately predict the stator flow. The flow at this location is a combination of the interaction between the delta wing vortex and the stator blade row.

Figure 5(d) presents the phase averaged time mean turbulence intensity (\overline{Tu}) measured using a three axis hot-wire. It can be observed that the turbulence intensity contours are in good agreement with the loss coefficient contours at various viscous regions in the flow like the blade wake and the passage vortices. The maximum turbulence intensities of 11.7% can be seen in the center of the vortex as compared to around 8% in the center of the wake and 1.8% in the freestream regions. The passage vortex region near the casing has lower turbulence intensity levels of 8% compared to the hub region. The turbulence intensity on the pressure side of the blade (region A) is around 4% and coincides with the loss region as noticed in Fig. 5(b).

Figure 6 gives the comparisons of the pitch-wise average of the stagnation pressure loss coefficient for the datum and delta-wing configurations. The loss coefficient (Y) is derived using the mass averaged primitive variables in the pitchwise direction throughout the paper. The reference stagnation pressure for both of the measurements is the mean stagnation pressure measured at the inlet of the rig at mid radius location. The loss behind the stator for “delta wing” configuration includes the loss and work exchange from the delta wings. The loss coefficient corresponding to the passage vortex at the hub increased to 0.054 for the datum configuration and can be observed at 15% span. A larger increase in loss coefficient to 0.11 for the delta wing configuration is observed at 15% span. Some of this loss is due to the delta wing vortex and some due to the interaction between the delta wing vortex and the stator blade row as shown below. After 30% blade span no difference between the two configurations can be observed.

The measured stagnation pressure loss behind the airfoil row

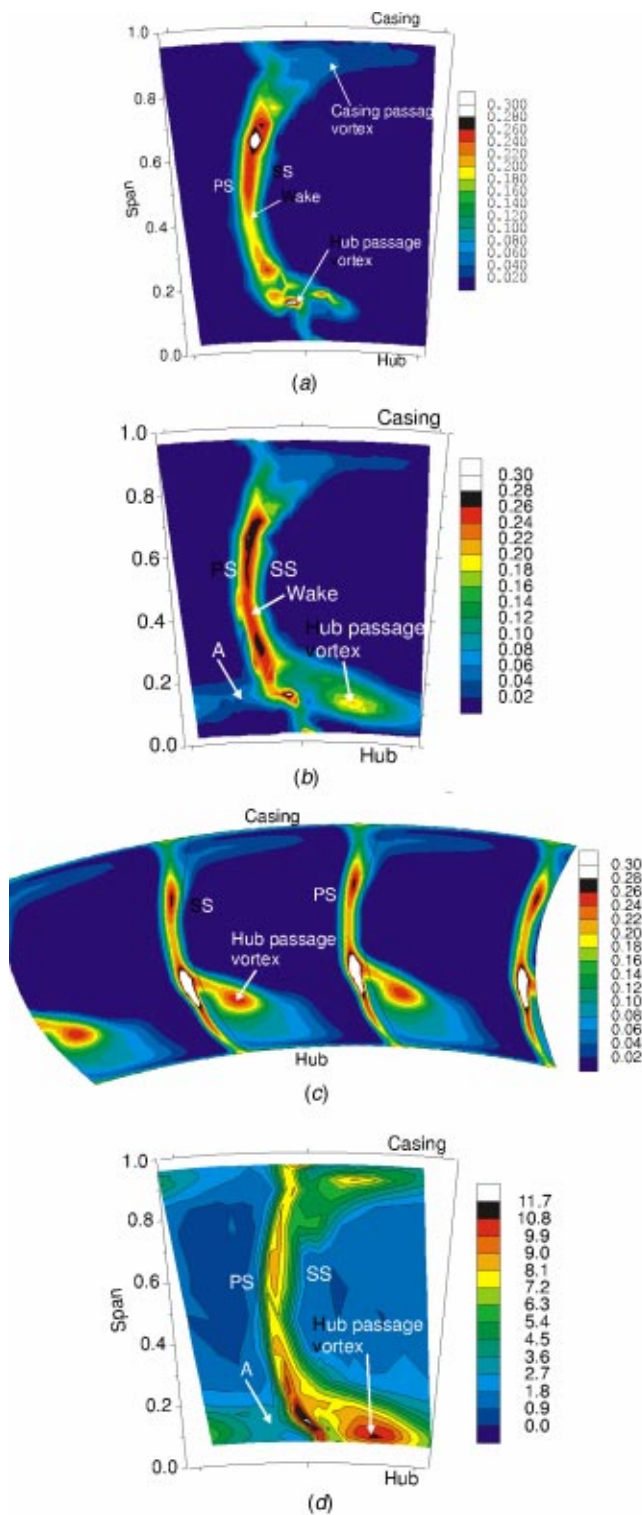


Fig. 5 Flow field at stator exit (8.7% C_x downstream of stator TE , plane 1); (a) Y contours for datum configuration, (b) Y contours for Δ -wing configuration, (c) Y contours from steady simulations with Δ -wings, (d) average turbulence intensity contours with Δ -wings

and the associated mixing losses are mass weighted and integrated over the measurement area. The “mixed-out” losses were obtained by using control volume method mixing the non-uniform pressures to a uniform static pressure distribution far downstream of the measurement plane. **Table 2** presents the area-integrated

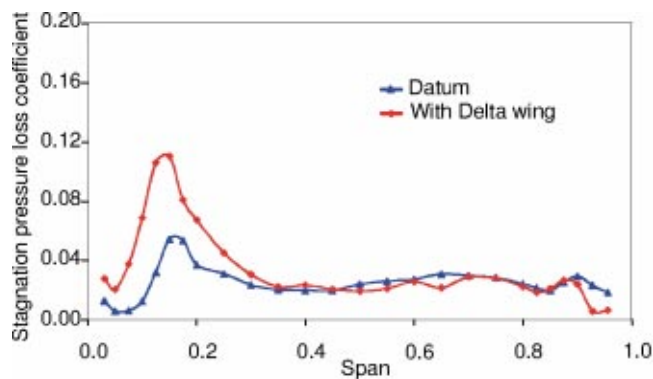


Fig. 6 Pitchwise averaged spanwise variations of Y stator exit (plane 1)

values of loss coefficient for the two test cases. The uncertainty analysis has been carried out for the measurement system using the method of Arts et al. [17]. The uncertainty in measuring velocity is ± 0.128 m/sec, for the flow density is ± 0.002 kg/m³, for the mass flow rate is ± 0.108 kg/sec. Similarly, the uncertainty associated with the measurement of loss coefficient in the stationary frame of measurements can be calculated as ± 0.0015 . **Table 2** shows the integrated loss coefficient behind the stator for the datum case is 0.0246, while the loss coefficient for the delta wing configuration is 0.0375. The integrated loss coefficient measured behind the delta wing is 0.0077, which is 31.3% of the datum loss. The delta wing loss includes the mixing loss associated with the vortex in a constant volume. The difference in loss between the delta wing and the datum test configuration can be evaluated as 52.4% of the datum stator loss. After considering the contribution of the loss from delta wing (31.3%), the additional loss generated in the stator is 0.0052 or 21.1% with an error of $\pm 6.1\%$ of the datum stator loss. Hence, this additional loss can be due to the interaction between the delta wing vortex and the downstream stator blade. These results show that the additional loss generated in the stator blade is significant.

Another parameter, which characterises the flow, is the yaw angle. **Figure 7(a)** presents the contours of the absolute yaw angle from five-hole probe measurements. The flow overturning caused by the strong hub secondary flow at suction side corner can be observed, so is the flow overturning near the casing. The overturning near the hub can be seen up to 10% blade span while the flow underturning can be observed from 10% to 25% of blade span. This whole region corresponds to the loss core as presented in **Fig. 5(b)** and associated with the hub passage vortex.

Figure 7(b) presents the secondary velocity vectors calculated from the measured data. Near the hub, a strong secondary flow pattern occupying almost 20% blade span can be identified. The casing secondary flow is weaker than the hub and occupies up to 20% blade span from casing. Another vortical flow is also observed near region “A” rotating opposite in direction to the hub secondary flow at 20% blade span. It is the same region “A” observed in **Fig. 5(b)** and associated with a loss core on the pres-

Table 2 Area integrated loss at stator exit (Plane 1)

		Datum	Δ -Wing
Delta wing exit	Y_{measured}	-	0.0077
	% of datum	-	31.3
Stator exit	Y_{measured}	0.0246	0.0375
	% of datum	100.0	152.4
Additional loss (% of datum)	Total	-	52.4
	Δ -wing	-	31.3
	loss due to vortex transport	-	21.1

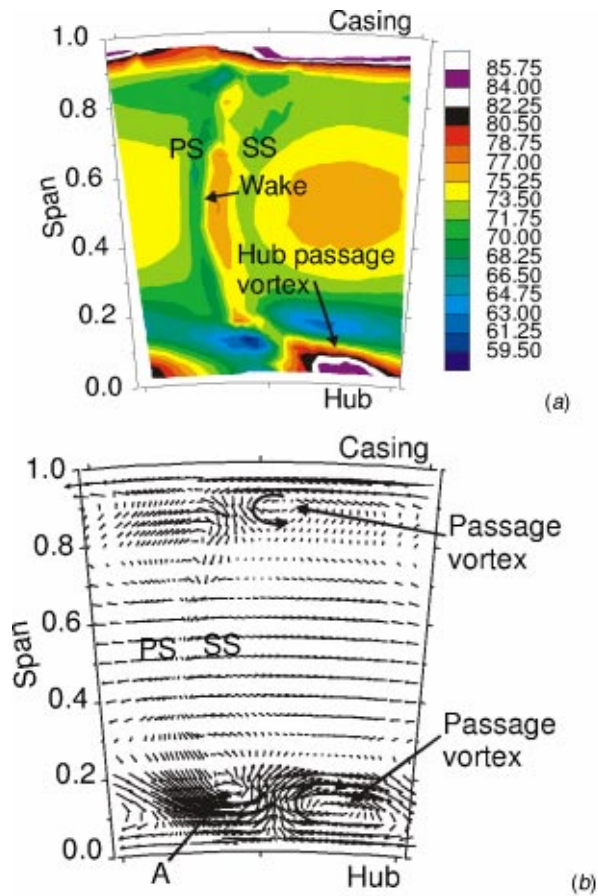


Fig. 7 Flow field at stator exit (plane 1); (a) yaw angle, (b) secondary velocity vectors

sure side of the stator. This vortical flow is further discussed in Section 3.3 with the help of the unsteady measurements.

Figure 8 presents the pitch-wise averages of the measured yaw angle data for the two test configurations. The flow overturning near the hub region and underturning towards the midspan, indicating a classical vortex pattern, can be observed at around 10% blade height for the datum test configuration. The yaw angle variation is larger for the delta wing configuration indicating increased strength of the passage vortex compared with the datum test configuration. At all other locations from 40% blade span to casing there is little or no variation in the flow angle between the

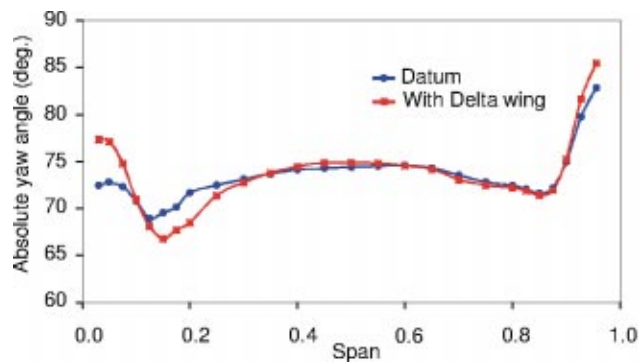


Fig. 8 Pitchwise averaged spanwise variations of yaw angle at stator exit (plane 1)

two configurations. This indicates that above 30% span, there is no influence of delta wing vortex on the yaw angle of the stator exit flow.

3.3 Unsteady Stator Exit Flow Field. It has been shown in the previous section that there is a difference between the steady numerical predictions and the measurements indicating the effect of unsteadiness on the stator flow field. This unsteadiness arises due to the relative motion between the delta wing vortex and the stator row. Extensive time resolved data has been obtained downstream of the stator (plane 1, 8.4% of stator C_x downstream of stator trailing edge) using a three-axis hot-wire probe in an absolute frame of reference. This measurement plane is selected at the same location as that of the five-hole probe measurement plane for easy comparison. One appearance of the delta wing vortex behind the stator can be expected over two rotor blade passing periods.

Figure 9 presents the contours of the instantaneous turbulence intensity (Tu) in two rotor-passing periods. The stator wake, the hub and the casing passage vortices can be identified by the high-turbulence intensity regions, as marked in the figure. The maximum turbulence intensities correspond to the passage vortex at the hub and in the intersection between the wake and the vortex. The turbulence levels are as high as 11.7% in the center of hub passage vortex compared to 7% in the center of the wake. It can be observed that in the regions corresponding to hub passage vortex, the turbulence intensity varies with time during the two-rotor wake passing periods. This region has a minimum value of 9.9% at time $t/\tau=0.750$ and a maximum value of 11.7% at time $t/\tau=1.50$, where τ is defined as time taken by the one rotor blade to travel through the stator pitch. The turbulence intensity corresponding to region A of Fig. 5(b) is observed to vary from 1.8% ($t/\tau=0.0$) to 5.3% ($t/\tau=0.75$) in one wake passing period indicating the periodic nature of this region. After considering the secondary velocity vector plots (Fig. 7(b)), loss measurements (Fig. 5(b)), it can be concluded that this structure may be due to the pressure leg of the delta-wing vortex.

The structure of the stator secondary flow near the suction surface is similar at all instants of time with little variations from one time instant to another. The turbulence intensity results combined with the yaw and pitch angle data (not presented in this paper) suggests that the delta-wing vortex has mixed with the stator passage vortex at the hub, hence cannot be identified as a separate entity. Nevertheless, the presence of the delta-wing vortex inside this region is confirmed using frequency spectrum data presented in Section 3.5.

3.4 Unsteady Numerical Simulations. Unsteady numerical simulations were carried out with a three-dimensional multistage solver "UNSTREST." Denton [18] illustrates that the accurate measure of loss in a flow is entropy. Entropy is a particularly convenient measure because, unlike stagnation pressure, stagnation enthalpy or the kinetic energy, its value does not depend upon the frame of reference. The numerical results are discussed by analysing the entropy function contours in quasi-orthogonal planes at various time instants over one vortex passing period. The entropy function is defined as $e^{(-\Delta s/R)}$. For a cascade with uniform inlet flow, this function reduces to the stagnation pressure recovery coefficient (P_{02}/P_{01}). The reference stagnation pressure is taken as the midpassage inlet stagnation pressure at the blade midspan location. A value of 1.0 for the entropy function corresponds to the flow with no losses and any value less than 1.0 represents a loss.

Figure 10 presents the entropy function contours at 8.4% stator C_x distance downstream of the stator trailing edge over two rotor passing periods. This plane is at the same location as that of the measurement plane for the "delta wing" test case as discussed in Section 3.2.2. At time, $t/\tau=0.0$, the secondary flow near the stator hub is significant and covers up to 50% of the passage width. A variation in the magnitude of the hub secondary flow can be ob-

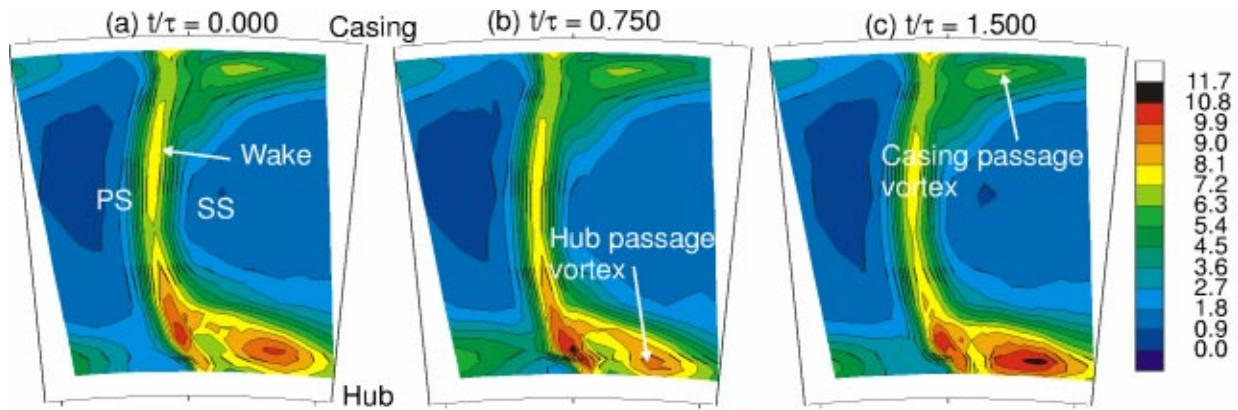


Fig. 9 Unsteady Tu contours at stator exit (plane 1)

served with a maximum size of the secondary flow at time $t/\tau = 1.6$. At this axial plane, the delta wing vortex can no longer be distinguished from the rest of the flow.

This is in agreement with the measurements carried out at the same location with a three-axis hot-wire and shown in Fig. 9. These results indicate that the stator viscous flow variation with the rotor-passing period is not substantial. A comparison of the contours of measured turbulence intensity in Fig. 9 and the present unsteady predictions indicate the similar stator hub secondary flow. The stator hub passage vortex can not be observed as a loss core in the middle of the blade passage in numerical simulations, instead, it is attached to the stator blade wake. The discrepancy between the turbulence intensity measurements and the predicted entropy function contours may be due to the type of mixing model used in the present numerical simulation. Nevertheless, the unsteady numerical simulations were in good agreement in predicting the location and size of the stator passage vortex at the hub.

Figure 11 shows the results at 10% rotor axial chord upstream of the rotor leading edge over one stator blade-passing period, where τ is defined as time taken by the one rotor blade to travel

through the stator pitch. This plane is $25.2\% C_x$ downstream of the stator trailing edge. Measurements are not available at this axial location to compare the computational results. The stator blade wakes can be identified by the contours of lower entropy function in the middle of the passage. In addition to the stator wakes, the loss cores can be observed corresponding to the stator hub and casing passage vortices in Fig. 11(a). At time $t/\tau = 0.4$, the secondary flow near the hub has increased and also at the casing. At this instant in time (Fig. 11(b)), the wake is restricted to the middle of the blade for about 15% blade span, while the secondary flow at the hub and the casing occupied rest of the blade span. The hub secondary flow can be observed for about 75–80% blade pitch. After another 40% of vortex passing period at $t/\tau = 0.8$, the magnitudes of the entropy function corresponding to the stator flow has reduced to lower levels.

The variation in the stator flow restricted to the hub secondary flow. The time varying flow field presented in Fig. 11 shows otherwise, a large variation in the incoming stator flow to the rotor row. The axial plane is very close to the rotor leading edge ($10\% C_x$ upstream of the rotor leading edge). This suggests that this variation in the stator flow may be due to the potential field of the

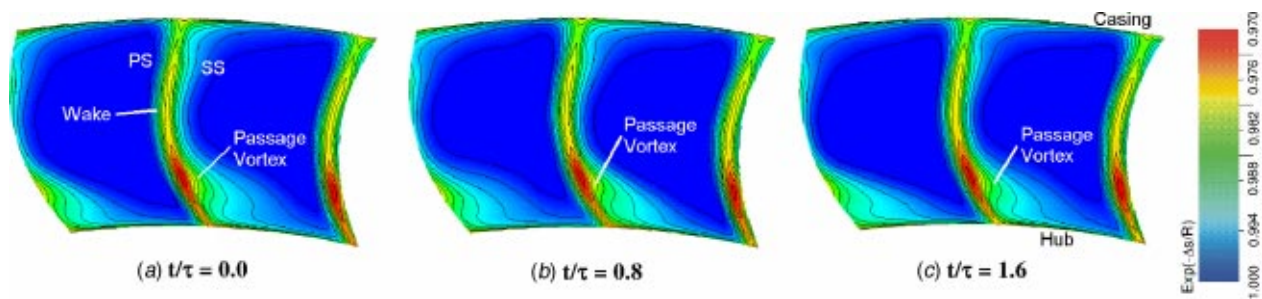


Fig. 10 Computed contours of entropy function at stator exit ($8.4\% C_x$ downstream of the stator TE)

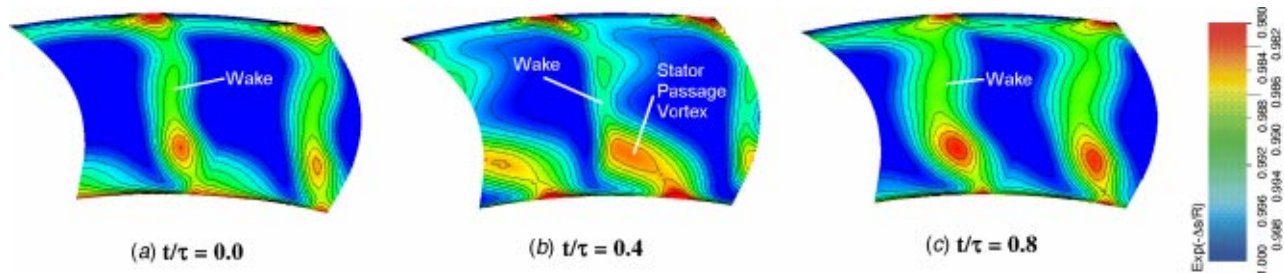


Fig. 11 Computed contours of the entropy function at rotor inlet in one stator wake passing period ($25.2\% C_x$ downstream of stator $TE/10\%$ upstream of rotor LE)

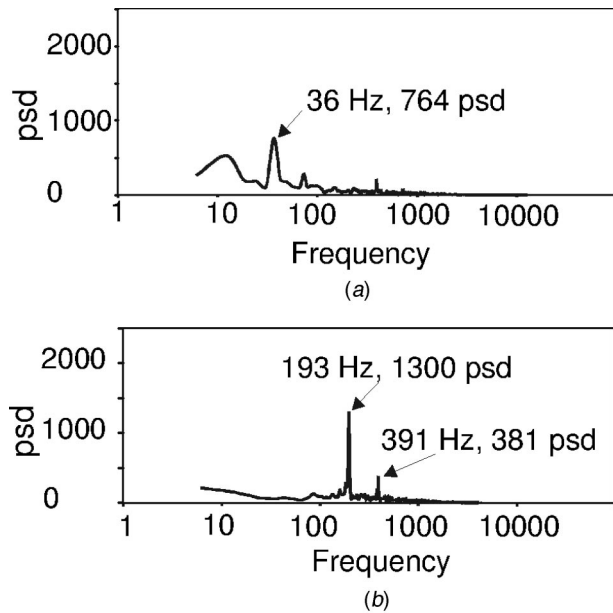


Fig. 12 Power spectral density inside the stator hub passage vortex; (a) datum configuration, (b) delta-wing configuration

rotor. It can also be due to the passage vortex interaction of the stator with the rotor leading edge, which results in the turbulence generation as suggested by Binder et al. [19]. This phenomenon has to be further investigated either numerically or by measurements.

3.5 Spectral Analysis at Stator Exit. Spectral analyses have been carried out at the measurement location (plane 1) by recording the velocity from the three wires of three-axis hot-wire probe over a long period of time. The data has been sampled at various important locations in the area traverse such as the centres of the wake, hub and casing passage vortices and in the free stream. The data are logged at a frequency of 10 KHz to capture all the frequency ranges of interest. The spectral analysis was carried out using a fast Fourier transformation (FFT) of the tangential velocity data. The spectral analysis of the axial and radial components of the velocity also resulted in similar conclusions and hence only the tangential velocity data (this component being dominant in the total velocity) is presented here.

Figure 12(a) presents the results from the spectral analysis for the datum test configuration at 8.4% C_x downstream of the stator trailing edge (plane 1) inside the stator passage vortex near the hub. No predominant frequencies can be observed at this location. It is observed that the power spectral density (psd) at the main frequencies is reduced inside the viscous regions. It is worth noting at this point that the number of half-delta wings is half of the blade number resulting to a passing frequency exactly half of the blade passing frequency, which is also a subharmonic of the blade passing frequency. **Figure 12(b)** presents the spectrum acquired behind the stator for the “delta wing” test configuration. The spectrum in the center of the hub passage vortex is different when compared to **Fig. 12(a)**. There are two dominant frequencies at this location. One is 193 Hz and the other is at 391 Hz. These frequencies correspond to the delta wing and the rotor passing frequencies, respectively. This suggests that the delta wing vortex is responsible for the dominance at these frequencies. This also indicates that the vortex near the hub is a result of the combination of the stator hub passage vortex and the upstream delta-wing vortex.

3.6 Rotor Exit Flow. The flow field at the rotor exit is discussed with the help of measurements at the measurement plane 3

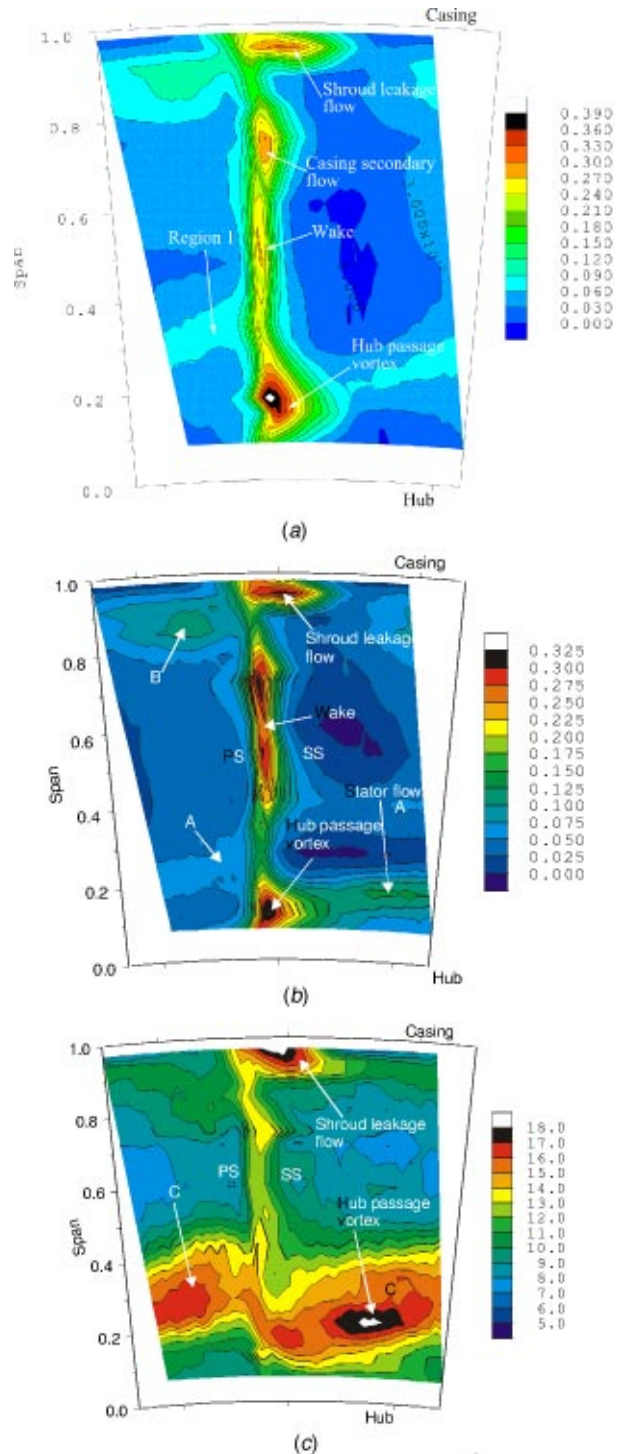


Fig. 13 Flow field at rotor exit (10% C_x downstream of rotor TE, plane 3); (a) Y contours for datum configuration, (b) Y contours for delta wing configuration, (c) TU contours for delta-wing configuration

which is located 10% of rotor C_x distance downstream of the rotor trailing edge, in the relative frame of reference. **Figure 13(a)** presents the contours of the relative stagnation pressure loss coefficient at plane 3 for the datum configuration. The data obtained from five radially disposed rotor leading edge Pitot tubes have been interpolated to provide reference stagnation pressure for the traverse data at each radius. The rotor wake can be identified with the high loss region with a loss of 0.27 in the middle of the blade

passage. The loss cores corresponding to the secondary flows at the hub ($Y_{\max}=0.39$) and the casing ($Y_{\max}=0.3$) and corresponding to the leakage flow ($Y_{\max}=0.33$) can also be observed. Another loss core can be identified on the pressure side of the blade at 35% span (region 1, $Y_{\max}=0.09$).

It has been shown in Section 3.2 that the interaction between the delta-wing vortex and the stator blade row resulted in a strong stator passage vortex at the hub. It occupied almost 60 to 75% of the blade pitch and up to 20% of the blade height. This strong stator passage vortex interacts with the downstream rotor blade and generates a complex flow field in the rotor blade row. The flow field at the rotor exit for the delta wing configuration is discussed with the help of measurements at plane 3, same axial location as that of the datum configuration in Fig. 13(a). Figure 13(b) presents the contours of relative stagnation pressure loss coefficient (Y) from five-hole probe measurements. The rotor wake can be identified as a thin loss region in the center of the area traverse. The loss core corresponding to the hub and the casing secondary flow and shroud leakage flow are found at 12%, 73% and 95% blade span, respectively. In addition to these features, another loss core can be identified to the right of the hub secondary flow occupying the entire blade pitch (region A) and on the pressure side of the blade near casing region and denoted by B.

A comparison of the contours of the loss coefficient between the datum configuration case in Fig. 13(a) and the delta wing configuration case in Fig. 13(b) indicate that the rotor flow field is very similar including the magnitude of loss. The loss corresponding to the region "A" in Fig. 13(b) is much higher ($Y_{\max}=0.15$) compared to the datum configuration case in Fig. 13(a) (region 1, $Y_{\max}=0.09$) indicating the effect of stronger stator hub passage vortex.

Figure 13(c) presents the contours of the phase averaged time-mean turbulence intensity (\overline{Tu}) measured with a three-axis hot-wire at the same measurement plane. The turbulence intensity in the center of the wake is 13%, with maximum of 18% in the center of shroud leakage flow and hub passage vortex. The high turbulence region near the hub extends from suction side to the pressure side of the passage, occupying the whole blade pitch. The location of this region on the pressure side (35% blade span) is much higher than on the suction side (17% blade span) similar to the observed for region A in Fig. 13(b). The secondary velocity vectors (not presented in this paper) at this location (region A) indicate a vortical structure rotating opposite in direction to the main hub passage vortex. It has been shown in Chaluvadi et al. [2,3] that this region is a result of the manifestation of the pressure leg of the stator hub passage vortex at the exit of the rotor.

The turbulence intensity in the free stream region is higher at 8% compared to the stator exit value of 1.8%. Hence, it can be said that the rotor freestream turbulence has increased as a result of the interaction of the stator wake flow with the rotor flow field. The increase in turbulence intensity is also observed in the center of the wake (13%) compared to the corresponding stator wake value of 9%. The overall results of turbulence intensity match well with the stagnation pressure loss contours from five-hole probe measurements.

The pitchwise averaged spanwise distributions of the measured flow for two test cases are presented in Fig. 14 at the exit of the rotor (plane 3, 10% C_x downstream of the rotor trailing edge). Figure 14(a) presents the relative yaw angle distributions for the two test configurations: datum and delta wing. The classical overturning near the hub end-wall and underturning towards the midspan is seen in the case of datum configuration with a vortex at around 17% blade span. An entirely different phenomenon is observed for the delta-wing test case. Large underturning near the hub region (up to 15% blade span) and overturning towards the midspan region (from 20% to 40% blade span) can be observed for the delta wing case. This is similar to the results obtained by Sharma et al. [4].

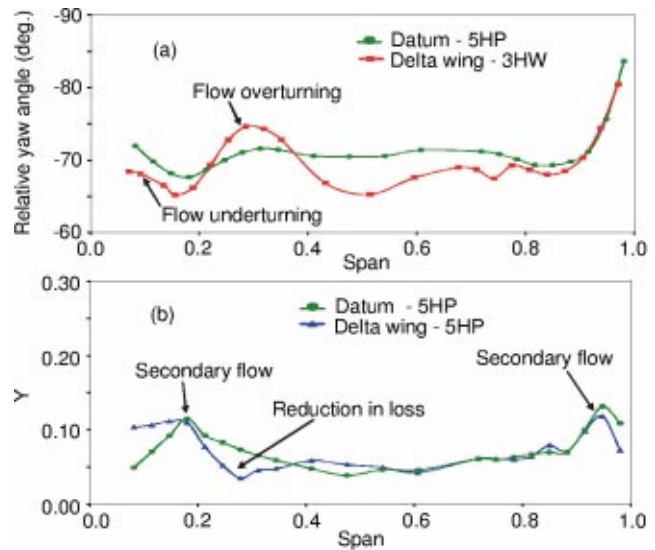


Fig. 14 Pitchwise averaged spanwise variations at rotor exit

The flow overturning near 30% span corresponds to the loss core (region A) in Fig. 13(b). The results from stator exit traverses show that the passage vortex behind the stator is strong, occupies the whole stator pitch and has same sense of rotation as a classical stator passage vortex. The stator passage vortex while transporting through downstream blade produced an overturned flow at 30% span while in the "datum" configuration it did not result in overturned flow. This indicates that the flow overturning towards the midspan is due to the interaction of the stator flow with the rotor. At other spanwise locations, a good agreement between both test configurations from 90 to 100% blade span can be observed indicating, little or negligible effect of the delta wing vortex transport on the shroud leakage flow. The difference in yaw angle distribution from 40 to 90% blade span between the two configurations also indicate the effect of the stator vortex transport on the rotor flow field.

The pitchwise averaged variations of the relative stagnation pressure loss coefficient (Y) are shown in Fig. 14(b). The local increase in loss is observed corresponding to the secondary flow regions at the hub and the casing. A difference in magnitudes of loss between the two test cases is observed from the hub region to up to 38% blade span. The reduction in loss for the delta wing case from 20% span to 38% span can be observed and may be attributed to the reduction in rotor secondary flow in the delta-wing test case.

The uncertainty associated with the measurement of loss coefficient in the rotating frame of measurements is given as ± 0.002 . The integrated loss coefficient behind the rotor for the datum configuration is 0.0691 and the corresponding value for the delta wing configuration is 0.0687. This reduction in loss coefficient is within the uncertainty limits. This loss coefficient data still indicate that the loss has remained constant if not reduced in this delta-wing case in spite of having a strong incoming stator hub passage vortex.

3.7 Unsteady Rotor Exit Flow Field. Extensive time resolved data has been obtained downstream of the rotor (Plane 3, 10% of rotor C_x downstream of rotor trailing edge) using a three axis hot-wire probe in the relative frame of reference. These data are used to understand the interaction between hub passage vortex of the stator with the rotor row. The present "delta wing" test configuration has 21 delta wings, in comparison with 36 stator blades and 42 rotor blades. Hence, one appearance of the delta wing vortex behind the rotor can be expected over two-stator blade passing periods.

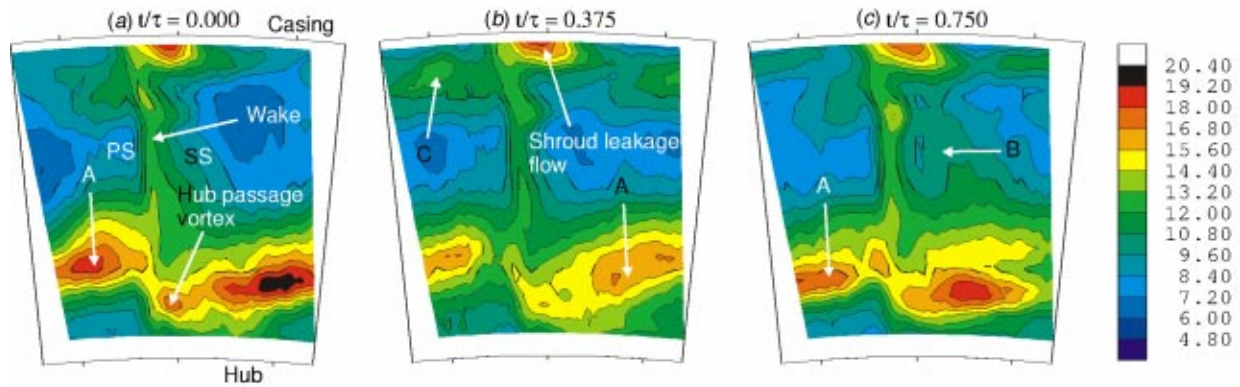


Fig. 15 Unsteady Tu contours at rotor exit (plane 3)

Figure 15 presents the contours of instantaneous turbulence intensity (Tu) at rotor exit (plane 3) over one stator wake passing period. The blade wake, hub and casing secondary flow, stator flow interaction regions can be observed with high turbulence intensities as shown in Fig. 15. The magnitude and size of the turbulence intensity corresponding to the stator interaction region (region A) varied periodically with time over one stator wake-passing period. Region A had a minimum value of 16.8% turbulence intensity at time $t/\tau=0.375$ (Fig. 15(b)) and a maximum value of 20.4% at time $t/\tau=0.00$ (Fig. 15(a)). This region occupied almost the whole of the blade pitch at 25% blade height. A comparison of the contours of the turbulence intensity between the datum configuration (not presented in the paper) and the present case indicated that the rotor flow field is very similar including the magnitudes of turbulence intensity. A large turbulence intensity core (region A) can be observed in the present test case covering whole of the rotor blade pitch compared to a much smaller region in datum case. The radial migration of the turbulence core on the pressure side is at higher radii than on the suction side of the blade, which is similar to the observed for the datum case. It has been shown from vortex dynamics by Chaluvadi et al. [3] that the stator vortex moves radially downwards on the suction surface and upward on the pressure surface from the action of image vortices inside the blade surfaces.

The size and magnitude of turbulence intensity varied little in the shroud region over one wake passing period. This suggests

that there is a negligible effect of stator vortex transport on the unsteadiness of shroud leakage flow. Another region B located to the right of the rotor wake can be observed with higher turbulence intensity than the surrounding at time $t/\tau=0.75$ (Fig. 15(c)). This region moves to the right towards the rotor wake and thickens the rotor wake width after quarter of stator passing period at $t/\tau=0.00$ (Fig. 15(a)). This periodic variation indicates that this region may be due to the transport of the stator wake in the rotor blade. The rotor blade wake can be distinguished from the rest of the secondary flow from 30% span to 75% span. In these spanwise locations the turbulence varied very little from 13.2–14.2% in one wake passing period. Another periodic variation in the turbulence structure can be observed near region C located to the left of the shroud leakage flow. This region has maximum turbulence intensity of 13.2% at time $t/\tau=0.375$ and minimum turbulence intensity 9.6% at time $t/\tau=0.75$. This may be due to the interaction of the passage vortex near the stator casing.

3.8 Unsteady Loss From Numerical Simulations. The steady and unsteady numerical simulations have been carried out with identical grids and solved using identical numerical schemes, mixing lengths, relaxation parameters, and boundary conditions. The steady and unsteady predicted flow fields were investigated to determine the contribution of the unsteady flow to the stage loss. Figure 16 presents the variations of the mass flow averaged entropy function with meridional distance for the steady and the

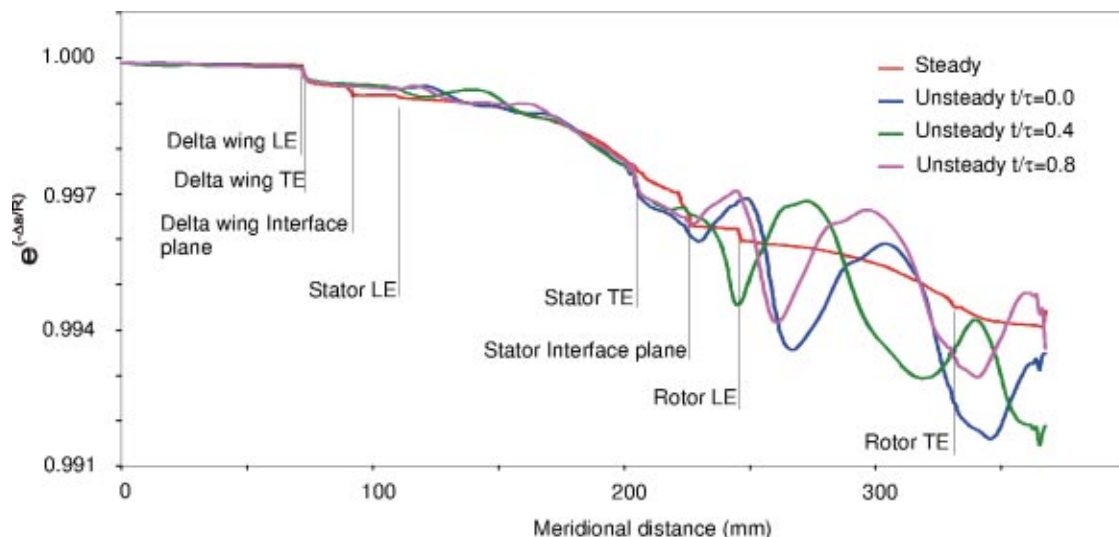


Fig. 16 Comparison of the steady and unsteady numerical simulations: entropy function

unsteady calculations. The variations of the entropy function for unsteady simulations were plotted at three time instants over a delta wing passing period. The locations of the interface planes, the leading and the trailing edges of the blade rows were marked. At any meridional location, the deviation of the entropy function from the value of 1.0 gives the cumulative loss generated up to that location.

It can be observed in **Fig. 16** that up to the first 72 mm of the meridional distance there is little variation in entropy function values between the steady and unsteady simulations and the magnitude is very close to 1.0. This indicates little or no additional loss generation until the leading edge of the delta wing. From the leading edge of the delta wing, the values of the entropy function start to reduce representing the loss generation from the development of the delta wing vortex. The reduction in entropy function continues until the delta wing row interface plane at 92 mm. After the trailing edge of the delta wing, the loss generation is from the mixing of the delta wing vortex with the surrounding flow. At the mixing plane behind the delta wing row the sudden decrease in the entropy function value for steady calculations can be observed due to the instantaneous mixing process being employed. For the unsteady calculations, the entropy function continues to reduce with meridional distance without any steep variations across the interface plane. The difference in entropy function between the two simulations at any axial location after the delta wing interface plane is considered to be due to the loss generated from unsteady flow.

It can be observed that after the delta wing interface plane (**Fig. 16**) until the stator mid-chord location, the value of the entropy function for unsteady simulations is higher than the steady simulations indicating lower losses from the unsteady calculations. The higher loss for the steady calculations is due to the instantaneous mixing of the delta wing vortex at the interface plane rather than mixing in the downstream blade row. Towards the end of the stator blade, the entropy function for the unsteady simulations is lower than the steady case indicating higher loss. The increase in loss is due to the interaction of the delta wing vortex with the stator blade. The difference between the steady and time average unsteady computations at the stator interface plane is 0.23% in efficiency while the total loss is 2.43% in efficiency. A loss audit at 8.4% C_x downstream of the stator trailing edge is carried out using the results from steady and unsteady simulations. This axial location is the same as the measurement location (plane 1) and hence an easy comparison can be made with the measurements. The loss from the unsteady interaction can be defined as

$$\omega_{\text{unsteady}} = \omega_{DW+\text{stator}} - \omega_{\text{stator}} - \omega_{DW} \quad (1)$$

where ω is the lost efficiency from inlet to the stage. The total loss in efficiency up to the 8.4% stator C_x ($\omega_{DW+\text{stator}}$) can be evaluated from unsteady simulation. The loss in efficiency from the stator (ω_{stator}) only and from the delta wings (ω_{DW}) only can be calculated from steady simulations. The unsteady loss is calculated to be 0.53% in efficiency from Eq. (1).

This unsteady loss as a percentage of the stator loss is 22%, which is in good agreement with the measured value of 21% of the stator loss coefficient (Y) as shown in **Table 2**. Similarly, large differences between the two simulations in the rotor blade row can be observed from stator interface plane (226 mm) to rotor exit plane located at 367 mm. The predicted efficiencies for the turbine stage with steady and time average unsteady simulations are 95.13% and 94.68% respectively. This also indicates the reduction in efficiency from unsteady flow is 0.45% and arise due to the additional loss generation from the interaction of the delta wing vortex with the stator and the rotor rows.

4 Conclusions

Half-delta wings were fixed to the rotating hub, in front of the stator row, to simulate the incoming upstream rotor passage vortices. The development of the steady and the unsteady three-

dimensional flow field behind the stator and the rotor blade rows has been described. The impact of the upstream delta wing vortices on the performance of the downstream blade is evaluated. Comparison of the stagnation pressure loss at stator exit between the datum configuration and delta wing configuration indicated that the additional losses were generated from the interaction of the delta wing vortex with the stator blade row. The increase in stagnation pressure loss is 21% of the datum stator loss, demonstrating the importance of this vortex interaction. Most of the increase in stagnation pressure loss is from the increase in stator secondary flow.

The transport of the delta wing vortices inside the stator row is described. At the exit of the stator in the present investigation, the pressure leg of the delta wing vortex was radially displaced upwards and the suction leg of the delta wing vortex was entrained into the stator passage vortex. A large variation in the stator flow field between 8.4% C_x and 25.2% C_x downstream of the stator trailing edge due to the downstream rotor potential field is observed.

The rotor exit flow was also affected by the interaction between the enhanced stator passage vortex and the rotor blade row. Flow underturning near the hub and overturning towards the midspan was observed, contrary to the classical secondary flow theory. The measured stagnation pressure at the exit of the rotor remained constant for the delta wing configuration compared to the datum configuration even with a stronger incoming stator passage vortex. The transport of the stator passage vortex inside the rotor blade is very similar to the delta wing vortex transport inside the stator row. The pressure leg of the stator passage vortex radially displaced upwards and the suction leg is entrained inside of the rotor hub passage vortex.

The unsteady numerical simulation results were further analyzed to identify the entropy producing regions in the unsteady flow field. It has been shown from the entropy function variations and the overall stage efficiency calculations that the additional loss was generated from the interaction of the delta wing vortex with the downstream blade row. The agreement between the experimental and computational results for the additional loss generation is good.

Acknowledgments

The authors would like to acknowledge the financial support of Mitsubishi Heavy Industries of Japan. In particular, thanks are extended to Mr. Eichiro Watanabe and Mr. Hiroharu Ohyama of MHI Turbine Engineering Department, for the kind sharing of their industrial experience and continuing support.

Nomenclature

- C = chord
- H = enthalpy
- H = blade span, boundary layer shape factor (δ^*/θ)
- P = pressure
- R = universal gas constant
- s = entropy, streamwise distance
- t = time from a datum point
- Tu = turbulence intensity = $\sqrt{1/3(\langle V_x \rangle^2 + \langle V_r \rangle^2 + \langle V_\theta \rangle^2)}/V_{\text{ref}}$
- U = blade speed
- V = velocity
- x = axial distance
- Y = total pressure loss coefficient = $(P_{01} - P_{02})/0.5\rho(V_{X1}/\cos 74 \text{ deg})^2$
- δ^* = boundary layer displacement thickness
- θ = boundary layer momentum thickness, flow angle
- τ = time for one wake passing period, time lag
- ω = efficiency loss

Subscripts

DW = delta wing
 M = midspan
 $o,0$ = stagnation
 r = radial
ref = reference
 x = axial
 θ = tangential
1 = blade row inlet
2 = blade row exit

Superscripts

$\bar{\quad}$ = time mean of the quantity

References

- [1] Hodson, H. P., 1985, "Measurements of Wake Generated Unsteadiness in the Rotor Passages of Axial Flow Turbines," *ASME J. Eng. Gas Turbines Power*, **107**.
- [2] Chaluvadi, V. S. P., Kalfas, A. I., Baniaghbal, M. R., Hodson, H. P., and Denton, J. D., 2001, "Blade Row Interaction in a High Pressure Turbine," *J. Propul. Power*, **17**, pp. 892–901.
- [3] Chaluvadi, V. S. P., Kalfas, A. I., Hodson, H. P., Ohyama, H., and Watanabe, E., 2003, "Blade Row Interaction in a High Pressure Steam Turbine," *ASME J. Turbomach.*, **125**, pp. 14–24.
- [4] Sharma, O. P., Renaud, E., Butler, T. L., Milsaps, K., Dring, R. P., and Joslyn, H. D., 1988, "Rotor-Stator Interaction in Multistage Axial Flow Turbines," *AIAA Paper No. 88-3013*.
- [5] Boletis, E., and Sieverding, C. H., 1991, "Experimental Study of the Three Dimensional Flow Field in a Turbine Stator Preceded by a Full Stage," *ASME J. Turbomach.*, **113**, p. 1.
- [6] Walraevens, R. E., Gallus, H. E., Jung, A. R., Mayer, J. F., and Stetter, H., 1998, "Experimental and Computational Study of the Unsteady Flow in a 1.5 Stage Axial Turbine With Emphasis on the Secondary Flow in the Second Stator," *ASME Paper 98-GT-254*.
- [7] Ristic, D., Lakshminarayana, B., and Chu, S., 1999, "Three-Dimensional Flow field Downstream of an Axial-Flow Turbine Rotor," *J. Propul. Power*, **15**(2), pp. 334–344.
- [8] Sharma, O. P., Pickett, G. F., and Ni, R. H., 1990, "Assessment of Unsteady Flows in Turbines," *ASME Paper No. 90-GT-150*.
- [9] Chaluvadi, V. S. P., Kalfas, A. I., and Hodson, H. P., 2003, "Vortex Generation and Interaction in a Steam Turbine," presented at 5th European Conference on Turbomachinery, Mar. 18–21, Prague, Czech Republic.
- [10] Chaluvadi, V. S. P., 2000, "Blade-Vortex Interactions in High Pressure Steam Turbines," Ph.D. thesis, Department of Engineering, Cambridge University, England.
- [11] Champagne, F. H., Schleicher, C. A., and Wehrmann, O. H., 1967, *J. Fluid Mech.*, **28**, p. 153.
- [12] Denton, J. D., 1986, "The Use of a Distributed Body Force to Simulate Viscous Effects in 3D Flow Calculations," *ASME Paper 86-GT-144*.
- [13] Denton, J. D., 1990, "The Calculation of Three Dimensional Viscous Flow Through Multistage Turbomachinery," *ASME Paper 90-GT-19*.
- [14] Denton, J. D., 1999, "Multistage Turbomachinery Flow Calculation Program (MULTIP99)—User's Manual," Whittle Laboratory, University of Cambridge.
- [15] Kuroumaru, M., Inoue, M., Higki, T., Abd-Elkhalek, F. A.-E., and Ikui, T., 1982, "Measurement of Three Dimensional Flow Field Behind an Impeller by Means of Periodic Multi-sampling With a Slanted Hotwire," *Bull. JSME*, **25**(209), pp. 1674–1681.
- [16] Goto, A., 1991, "Three Dimensional Flow and Mixing in an Axial Flow Compressor With Different Rotor Tip Clearances," *ASME Paper 91-GT-89*.
- [17] Arts, T., Boerrigter, H., Carbonaro, M., Charbonnier, J. M., Degrez, G., Olivari, D., Reithmuller, M. L., and Van den Braembussche, R. A., 1994, "Measurement Techniques in Fluid Dynamics," VKI LS-1994-01.
- [18] Denton, J. D., 1993, "Loss Mechanisms in Turbomachines," *IGTI Gas Turbine Scholar Lecture*, *ASME Paper 93-GT-435*.
- [19] Binder, A., 1985, "Turbulence Production Due to Secondary Vortex Cutting in a Turbine Rotor," *ASME J. Eng. Gas Turbines Power*, **107**, pp. 1039–1046.

Régis Houtermans
e-mail: houterma@vki.ac.be

Thomas Coton
Tony Arts

Von Karman Institute,
72 Ch. de Waterloo,
Rhode-St-Genèse 1640,
Belgium

Aerodynamic Performance of a Very High Lift Low Pressure Turbine Blade With Emphasis on Separation Prediction

The present paper is based on an experimental study of a front-loaded very high lift, low pressure turbine blade designed at the VKI. The experiments have been carried out in a low-speed wind tunnel over a wide operating range of incidence and Reynolds number. The aim of the study is to characterize the flow through the cascade in terms of losses, mean outlet flow angle, and secondary flows. At low inlet freestream turbulence intensity, a laminar separation bubble is present, and a prediction model for a separated flow mode of transition has been developed. [DOI: 10.1115/1.1748416]

Introduction

Gas turbines remain among the most compact engines available. The actual trend for improving them is to lower the maintenance and production costs while increasing the specific power. A suitable solution for any engine part consists of reducing the number of blades per row. This implies to increase the aerodynamic load of each blade. This requirement can be fulfilled by a combination between an increase of the suction side velocity peak level (limited by shock losses) and its position with respect to the leading edge (front or back loading). As the low pressure turbine can represent up to one third of the total engine weight, it is of first interest in this context.

Howel et al. [1], Brunner et al. [2], and Solomon [3] have illustrated the reliability of the wake induced transition for the high lift design in LP turbines. The present high lift and front loaded airfoil has been designed in such a way that the suction side velocity distribution presents a velocity peak at 32% of the suction side length with an almost constant velocity value downstream till $S/L=0.55$ (at zero incidence and in absence of separation). This velocity plateau makes the flow development along the channel very sensitive to incidence change. The influence of the variation of the Reynolds number and the inlet flow incidence on the profile losses, mean outlet flow angle and secondary flows will be investigated in this paper. As shown on **Fig. 1**, the pressure coefficient distribution is very close to the one of a blade designed at the VKI for compressible conditions. The two profiles are represented on **Fig. 2** (incompressible blade coordinates are provided in the Appendix). So, after a careful transposition, the conclusions of the incompressible study will allow to point out the influence of the Mach number.

As the LP turbine drives the fan providing the largest part of the thrust, the efficiency level must remain high. The position and the level of the velocity peak fix the deceleration length and the diffusion factor. But, in the LP turbine, the flow can be laminar over a large part of the blade profile, and consequently, cannot withstand a too strong adverse pressure gradient without separating. So, the transition process may occur in the free shear layer and the flow is susceptible to reattach to the wall, forming a bubble on the surface. As the evolution of the losses and the mean outlet flow angle are directly linked to the bubble physics, its correct prediction is of primary importance.

Contributed by the International Gas Turbine Institute and presented at the International Gas Turbine and Aeroengine Congress and Exhibition, Atlanta, GA, June 16–19, 2003. Manuscript received by the IGTI December 2002; final revision March 2003. Paper No. 2003-GT-38802. Review Chair: H. R. Simmons.

Roberts [4] provided a model for separated flow (considering transition as punctual) including the effects of Reynolds number and turbulent features (intensity and macroscale) combined in a turbulence factor. Mayle [5] gave relations for bubble development in the case of an extended transition process completed before the reattachment and in function of the bubble type: short or long. Walker [6] showed that the fully turbulent state can be also reached after reattachment. A few years later, Malkiel and Mayle [7], Lou and Hourmouziadis [8], Qiu and Simon [9], and Volino [10,11] gave qualitative and quantitative evolutions of the intermittency factor as a function of the freestream or local turbulence intensity.

Hatman and Wang [12] described the physical development and the main features of the transition for different bubble types. Their results showed that the bubble characteristics are well correlated by the value of some parameters at the separation position. They provided models but recommended caution for their extension to airfoils. Yaras [13] argued that the pressure gradient history of the boundary layer before the separation position has an influence on the transition process. This means that a model must include boundary layer integral parameters. Yaras [14] added the influence of the freestream turbulence intensity as more realistic conditions are needed to establish reliable models. Numerical simulations performed by Müller et al. [15] and [16] showed that more suitable test cases are needed to reach an accurate simulation of the separated flow mode of transition.

The aims of this paper are multiple. The first one is to provide the influence of incidence and Reynolds number on the aerodynamic performance of a front loaded very high lift blade at low turbulence intensity. The second one is to establish a model that, as a function of the boundary layer integral characteristics at the separation, gives the main bubble features for a very high lift LP turbine profile. Finally, this study is a part of a wider research conducted at the VKI, including the influence of freestream turbulence level and passing wakes in compressible flow conditions, as in Coton et al. [17].

Experimental Setup

Experiments were performed in the C1-low speed wind tunnel at the VKI. The flow enters the settling chamber through three mesh screens. From there, the flow is guided through a convergent and a honeycomb to the cascade. The latter is mounted on a rotating mechanism that can be easily turned to change the inlet flow incidence.

The cascade is composed of 13 blades and its main characteristics are given in **Table 1**. The pitch-to-chord ratio and the aspect

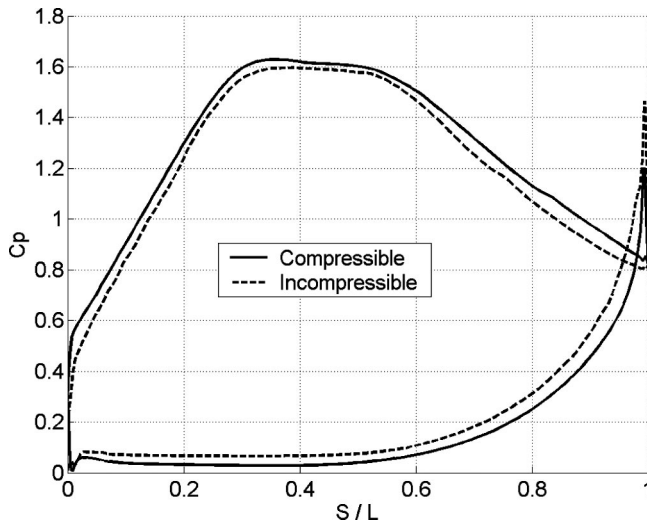


Fig. 1 C_p distribution for both compressible and incompressible profiles

ratio are, respectively, fixed to 1.05 and 2.5. The Zweifel coefficient is equal to 1.473. The isentropic exit Reynolds number ranged from 50,000 to 200,000. The incidences were set to -9 deg, -3 deg, 0 deg, 1.5 deg, and 5 deg. The inlet freestream turbulence level was 0.6%.

The uniformity of the upstream pressure and yaw angle distributions was checked with a four-hole probe in both pitchwise and spanwise directions. The upstream turbulent features were determined with a single hot wire. The sampling frequency was 50 kHz with a low pass filter set at 12 kHz. The turbulence is quite isotropic $\sqrt{v'^2}/\sqrt{u'^2}=0.95$. The Taylor's frozen turbulence pattern hypothesis was made to determine the length scales. The Taylor's macroscale is based on the integral time scale and the microscale is computed by using

$$\lambda \cong \frac{U \sqrt{u'^2}}{\sqrt{\left(\frac{\partial u'}{\partial t}\right)^2}}$$

whereas the Kolmogorov scale is determined by means of the turbulence dissipation rate

$$\varepsilon \cong \frac{15 \nu u'^2}{\lambda^2}$$

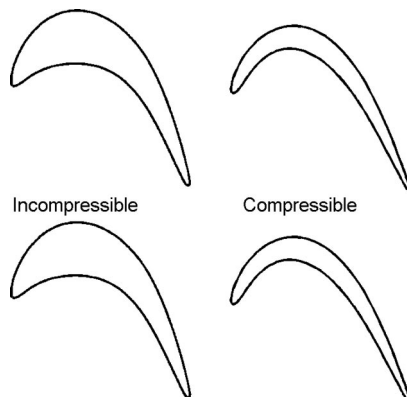


Fig. 2 Compressible and incompressible cascades

Table 1 Main cascade characteristics

c	c_{ax}	L_{SS}	g
0.05079	0.04498	0.08405	0.05333
H	γ	β_1	β_2
0.127	29.7	50	64

$$\eta = \left(\frac{\nu^3}{\varepsilon}\right)^{0.25}$$

The macroscale is equal to 14.89 mm; the microscale and the Kolmogorov scales are, respectively, equal to 1.85 mm and 0.23 mm for an exit Reynolds number of 130,000.

The characteristics of the upstream boundary layer developing along the endwalls were measured by means of a hot wire. The boundary layer extension is limited to one sixth of the channel height on each side and is turbulent (shape factor equal to 1.35). The downstream pressures and angles were determined with a five-hole pressure probe. This probe was calibrated from -37.5 deg to 22.5 deg for both angles. The static pressure distribution along the profile was measured with 25 pressure taps on the suction side and 18 on the pressure side. Introducing these results into a boundary layer code allowed to obtain the laminar boundary layer integral parameters up to the separation location.

The estimation of the uncertainties was performed for each measurement technique employed and each flow regime. Their maximum values are given for the lowest and highest Reynolds numbers (50,000 and 200,000). The absolute uncertainty on the pressure coefficient (maximum at the velocity peak) ranges between 0.02 and 0.002. For the losses, it ranges between 0.9 and 0.2 point, and for the angles between 0.25 and 0.13 (deg). Finally, the relative uncertainty on the hot wire data lies between 3.8 and 2.8%.

Results

Profile Losses. At midspan, the evolution of the profile losses and the mean outlet flow angle are presented on **Figs. 3 and 4** for five inlet flow incidences as a function of the Reynolds number. The incompressible profile loss coefficient is defined as

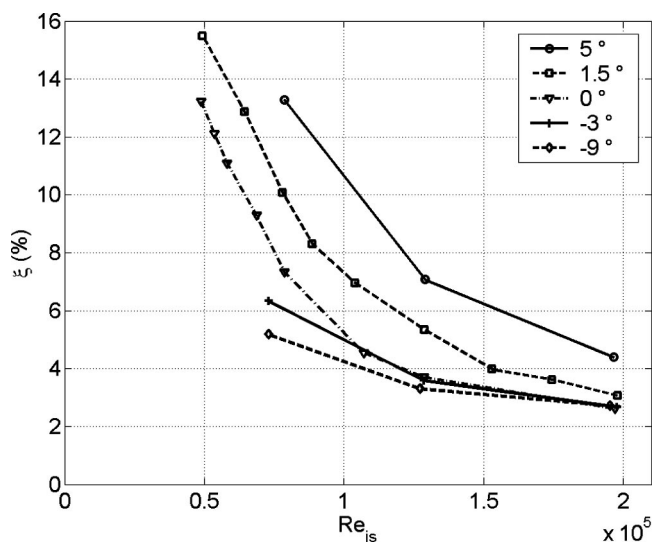


Fig. 3 Profile losses as a function of Re_{is} for five incidences

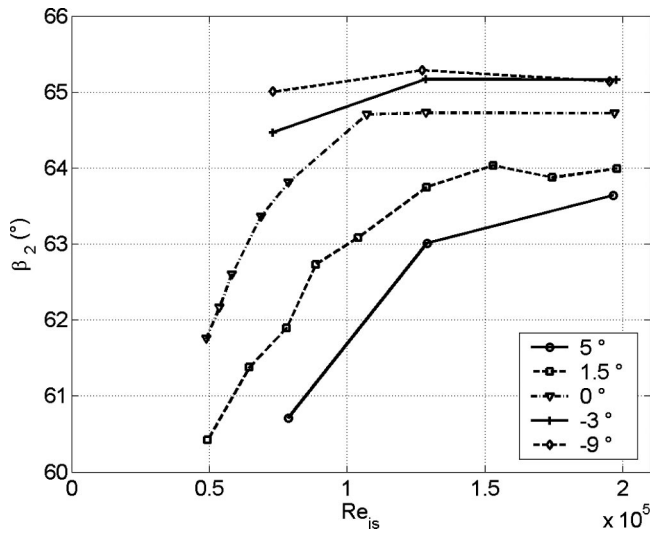


Fig. 4 $\bar{\beta}_2$ as a function of Re_{is} for five incidences

$$\xi = \frac{P_{01} - P_{02}}{P_{01} - P_2}$$

If the Reynolds number decreases or if, for a fixed Reynolds number, the incidence increases, the losses increase and the mean outlet flow angle reduces rapidly. Moreover, these variations are not linear. The aerodynamic performance seems to be more sensitive to a positive incidence than to a negative one. An incidence change influences the front velocity distribution. The velocity peak moves toward the leading (trailing) edge if the incidence becomes positive (negative) as shown on Fig. 5 ($Re_{is}=130000$). For an increasing incidence, the deceleration length and the diffusion factor increase. This influences the boundary layer development and thus the aerodynamic performance. For an increasing incidence, the separation position is shifted toward the leading edge. At fixed incidence, when reducing Reynolds number, the bubble length increases: the flow separates earlier and reattaches later. The pressure coefficient for three Reynolds numbers is shown on Fig. 6. As its interaction with the freestream flow is more and more important, the bubble deteriorates the aerodynamic performance.

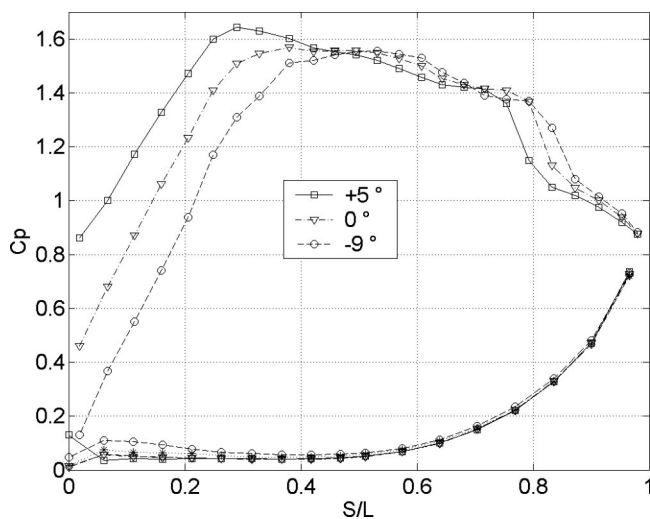


Fig. 5 C_p for three incidences at $Re_{is}=130000$

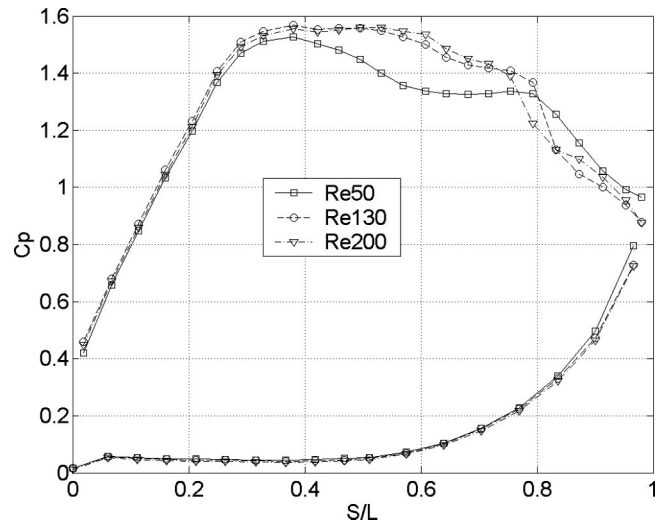


Fig. 6 C_p for three Re_{is} at zero incidence

Secondary Flows. The influence of incidence on the losses and the mean outlet flow angle (pitchwise mass averaged) is represented on Figs. 7 and 8, for $Re_{is}=130000$. On Fig. 8, one sees that the corner vortex in the region close to the endwall reduces the overturning of the flow. Also, the passage vortex induces an underturning and the trailing edge vortex influence is felt between midspan and the center of the passage vortex.

The pressure distribution, and so the loading, changes with incidence. The development of the secondary flows is directly linked to the loading level and distribution. As the separation bubble affects the pressure distribution, the evolution of the aerodynamic performance with incidence is linked to both the loading and the separation bubble features. With an increasing incidence, the secondary flows extension and level increase: the corner vortex becomes more and more important, the underturning increases, the passage vortex moves toward midspan. For the highest incidence, the secondary flows cover a huge portion of the span and will probably influence the flow at midspan.

The influence of the Reynolds number on the losses is represented on Fig. 9 for zero incidence. The influence of the secondary flows is more spread with an increasing Reynolds number.

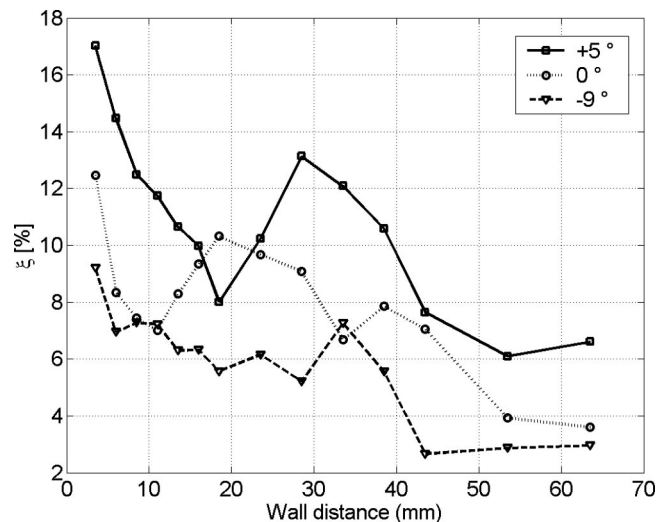


Fig. 7 Loss distribution along the span for several incidences with $Re_{is}=130000$

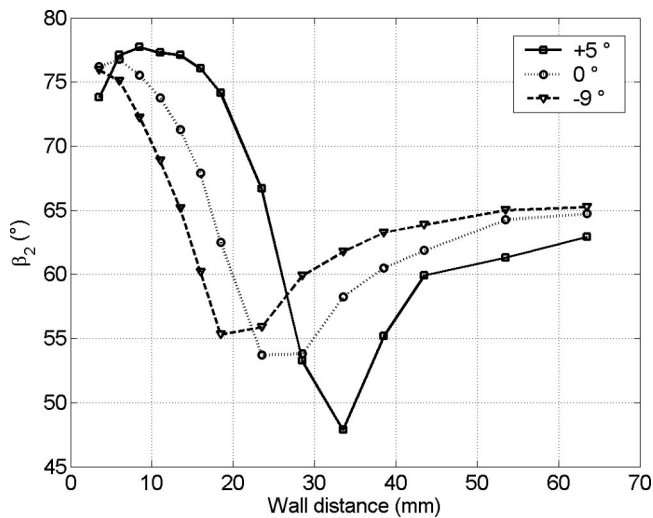


Fig. 8 $\bar{\beta}_2$ distribution along the span for several incidences with $Re_{is}=130000$

Prediction Model. In order to analyze the flow development, pressure taps have been placed along the blade surface. The measured pressure distribution has allowed the construction of a prediction model for the separated flow mode of transition. The goal is to provide the main bubble features at three positions namely the separation, the pressure recovery and the reattachment. These main bubble features are the acceleration parameter K , the local and momentum thickness Reynolds numbers at separation and the local Reynolds numbers at the pressure recovery and the reattachment.

Procedure. The procedure to determine the three characteristic points is represented on Fig. 10. Each line is drawn tangent to the pressure coefficient distribution. The intersections provide the position and the velocity for each point. The slope of the tangent upstream of the separation provides the variation of the velocity that will be introduced into the acceleration parameter at separation. This determination technique was inspired by Brunner et al. [2]. The comparison between results will show that this procedure is consistent with results of Roberts, Mayle, Hatman and Wang, and Yaras and is coherent with the bubble physics.

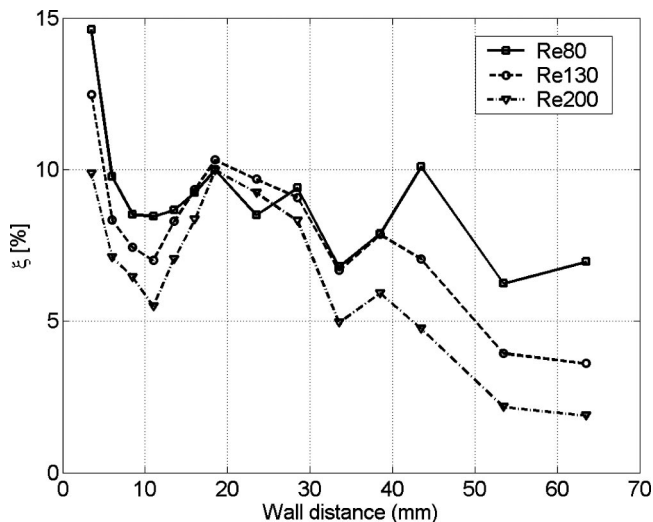


Fig. 9 Loss distribution along the span for several Re_{is} at zero incidence

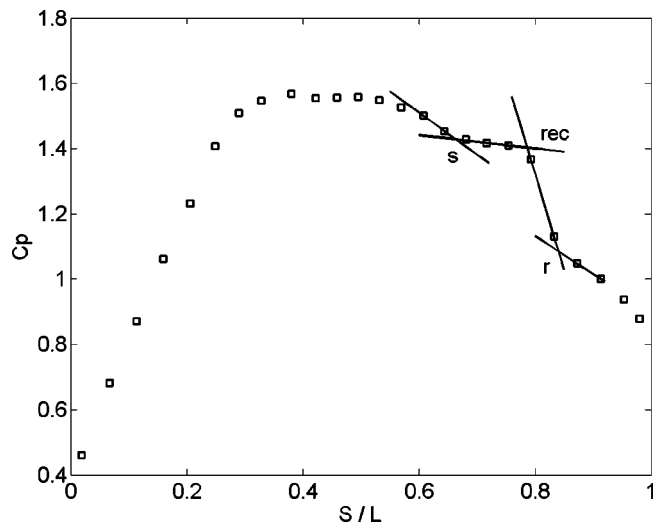


Fig. 10 Representation of the determination procedure

Due to the limited spatial resolution of the C_p distributions, the technique used by Yaras [13] consisting of searching the local minimum of the acceleration parameter to locate the reattachment point could not be used.

The Separation. As shown by previous authors, [12,13], it is necessary to include an integral parameter to accurately determine the separation position while taking into account the pressure gradient history of the boundary layer. Because of the cascade and hot wire dimensions, it was impossible to measure this characteristic before the separation without interfering with the flow. Consequently, the integral parameters were obtained from a laminar boundary layer computation (up to the separation point) with the measured velocity distribution as input.

The momentum thickness Reynolds number is represented as a function of the acceleration parameter at the separation on Fig. 11. This set of data can be correlated by Eq. (1) where the Polhausen parameter is equal to -0.1075 :

$$Re_{\theta,s}^2 K_s = -0.1075. \quad (1)$$

As for Yaras [13], it differs from the criterion given by Thwaites where the Polhausen parameter is equal to -0.082 . The

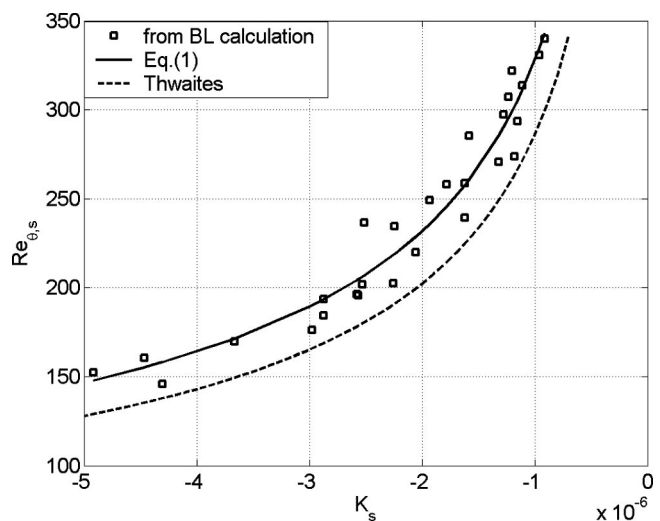


Fig. 11 $Re_{\theta,s}$ as a function of K_s

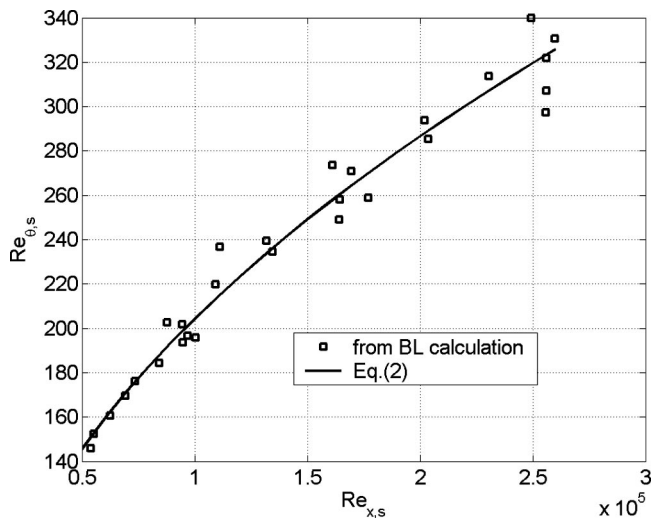


Fig. 12 $Re_{\theta,s}$ as a function of $Re_{x,s}$

momentum thickness Reynolds number is plotted as a function of the local Reynolds number at separation on Fig. 12. The best fit of these results is given by

$$Re_{\theta,s} = 0.74 Re_{x,s}^{0.488} \quad (2)$$

The present results are in good agreement with the theoretical proportionality (Schlichting, [18]) between the momentum thickness Reynolds number and the square root of the local Reynolds number. However, it can be noticed that the scatter increases with the local Reynolds number at separation. This could be linked to the determination procedure: as the physical length of the bubble decreases when the Reynolds number increases, the number of pressure taps used to deduce the main bubble characteristics is reduced.

The Pressure Recovery. The pressure recovery location is represented on Fig. 13 and is correlated to the separation by:

$$Re_{x,rec} = 6.777 Re_{x,s}^{0.8534} \quad (3)$$

It must be noticed that this relation is valid for both long and shorts bubbles.

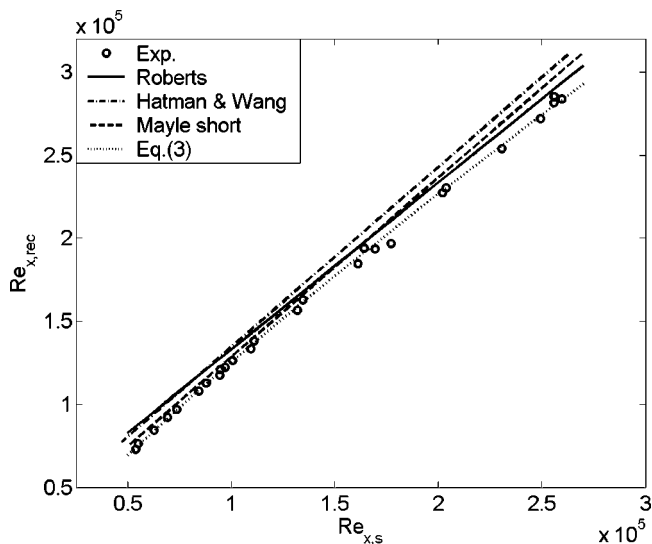


Fig. 13 $Re_{x,rec}$ as a function of $Re_{x,s}$

Table 2 Turbulence factor for three Re_{is}

Reynolds TF	80000	130000	200000
	0.0048	0.0046	0.0045

In 1975, Roberts provided a general overview of the bubble physics. The bubble was principally composed of two regions: a laminar part till its maximum displacement (where an instantaneous transition occurs) and a turbulent part up to reattachment. Roberts studied bubble development on compressor blades and established a relation for the laminar region length as a function of a turbulent factor incorporating the turbulence intensity and macroscale:

$$Re_{x,s-T} = Re_{x,T} - Re_{x,s} = 25000 \log_{10}(\coth(10TF)) \quad (4)$$

The turbulent factor is given in Table 2.

Afterwards, Mayle considered that the transition process extends over a short distance, taking place somewhere between the separation and the pressure recovery. He also made the distinction between the two types of bubble. The type is not directly linked to the bubble physical length but more to its influence on the losses and on the pressure coefficient distribution. He provided a relation for each kind of bubble:

$$Re_{x,s-T} = Re_{x,T} - Re_{x,s} = A Re_{\theta,s}^{0.7} \quad (5)$$

where the coefficient A is equal to 700 or 1300 if the bubble is respectively short or long.

From experiments on a flat plate, Hatman and Wang proposed a further classification: the short bubble can be laminar or already transitional at the separation. This last case has never been encountered during the present experiments. They correlated the maximum displacement location with the separation point by

$$Re_{x,md} = 1.0816 Re_{x,s} + 26805. \quad (6)$$

These last three relations (4), (5), and (6) are compared to Fig. 13 to Eq. (3) obtained from the present measurements. According to Roberts and Mayle, the transition ends at (or close to) the maximum displacement position. Moreover, it can be argued that the divergence of the streamlines from the maximum height of the bubble up to the reattachment corresponds to the pressure increase. So, the pressure recovery point can be considered as the maximum displacement position (as also done by Roberts). The difference appearing between the experimental results and the

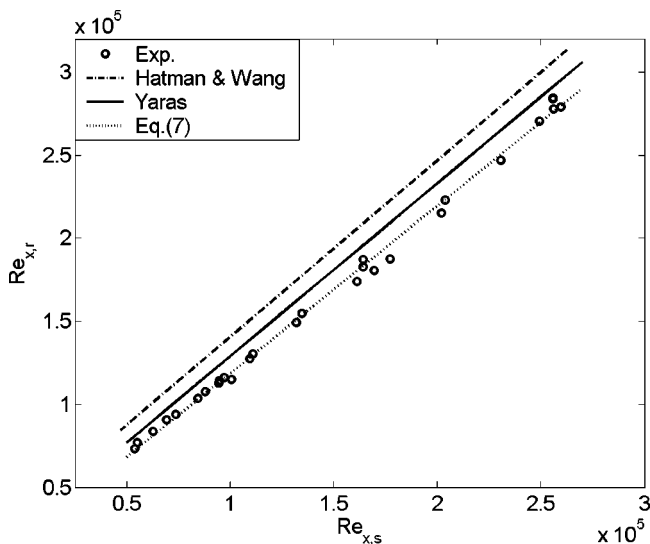


Fig. 14 $Re_{x,r}$ as a function of $Re_{x,s}$

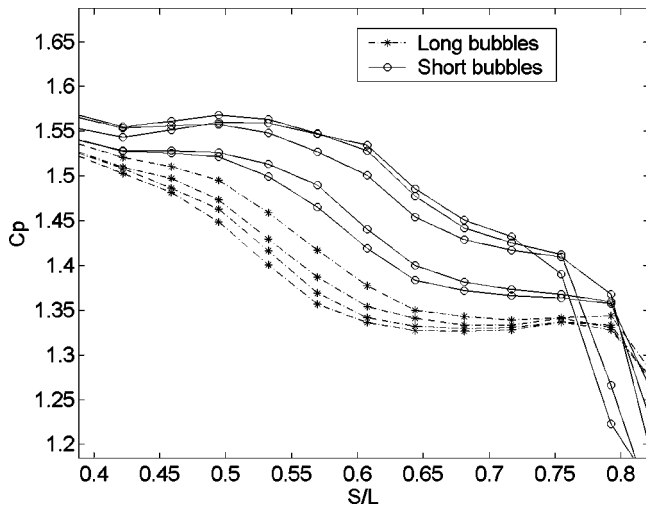


Fig. 15 C_p at several Reynolds numbers for long and short bubbles

various relations could be related to the pressure gradient history, the turbulent factor and the wall curvature which were not the same among the different sources.

The Reattachment. Finally, the bubble characterization ends up with the correlation for the reattachment point:

$$Re_{x,r} = 1.0074 Re_{x,s} + 17996 \quad (7)$$

which is compared to the relations of Yaras

$$Re_{x,r} = 1.04 Re_{x,s} + 80500(1 - \tanh^3(100TF')) - 20000$$

where $TF' = \max(0.01, TF)$, or Hatman and Wang

$$Re_{x,r} = 1.0608 Re_{x,s} + 34890$$

on Fig. 14. The difference between the experimental results and the other relations can be linked to the same reasons than for the separation correlation.

The Transition Characteristics. As shown by Hatman and Wang, the transition occurs differently in function of the bubble type. For each type, they provided the position of the transition onset and end, and of the maximum velocity fluctuations with respect to the bubble characteristic positions. As a consequence, the bursting needs to be detected to determine the bubble type and so the associated physics. From Roberts, Hatman and Wang, and Mayle, this non continuous process, occurring when the bubble changes from short to long can be assessed from the evolution of the aerodynamic performance, such as a strong increase in the profile losses and a reduction of the flow turning. This information is provided in Figs. 3 and 4. However, the accurate determination of this limit is always a matter of interpretation. As they contain useful information, the pressure distributions were also used. As shown in Fig. 15, the long bubbles present an increase of C_p just before the pressure recovery. This can be viewed as an evidence of a stronger recirculating flow inside the bubble induced after the onset of transition which occurs before the pressure recovery position. The results presented by Roberts (Fig. 4(b) in [4]) show the same tendency.

It is now possible to characterize the transition process for each type. In the case of short bubbles, some assumptions are required. As discussed on Fig. 13, the pressure recovery point is considered to be at the maximum of displacement. As opposed to Roberts and Mayle, it is precisely there that Hatman and Wang locate the transition onset. Walker [19] also argues along this direction. Hatman and Wang added that the intermittency factor was close to 0.7 at the reattachment. Consequently, knowing S_t from Eq. (3), S_r from

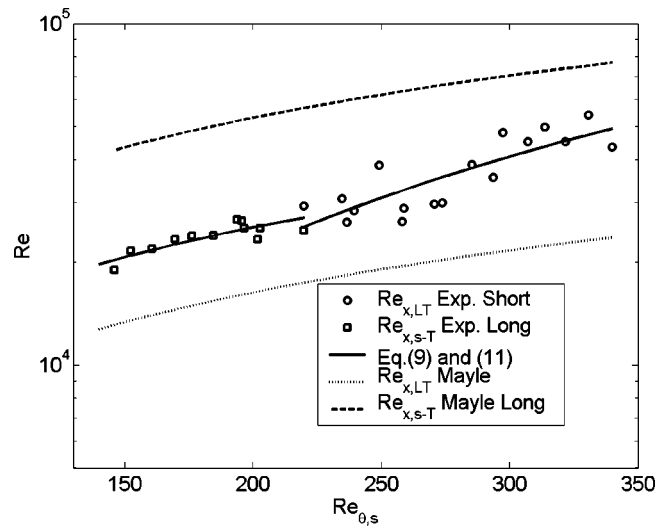


Fig. 16 $Re_{x,s-rec}$ as a function of $Re_{\theta,s}$ for long bubbles and $Re_{x,LT}$ as a function of $Re_{\theta,s}$ for short bubbles

Eq. (7), the transition end S_T can be computed by means of the universal evolution of γ provided by Narasimha [20] (with $S = S_r$):

$$\gamma(S) = 1 - \exp\left(-4.61 \frac{(S - S_t)^2}{(S_T - S_t)^2}\right) \quad (8)$$

This relation is independent of the pressure gradient and its applicability for transition in shear layer flows has been shown by Volino [10] and Qiu and Simon [9].

Finally, a Reynolds number based on the transition length and the velocity at the separation point can be computed for short bubbles:

$$Re_{x,LT} = \frac{U_s(S_T - S_t)}{\nu} = 6.94 Re_{\theta,s}^{1.5214} \quad (9)$$

This relation is very close to the one of Walker [6] and is compared on Fig. 16 to the correlation provided by Mayle for all bubble types:

$$Re_{x,LT} = 400 Re_{\theta,s}^{0.7} \quad (10)$$

This last equation underestimates the experimental data as foreseen by Walker [6].

For the long bubbles, it is generally agreed that the transition end is close to the pressure recovery position. A relation similar to the one of Mayle (Eq. (5)) can be obtained from the fit of our experimental data:

$$Re_{x,s-T} = 620 Re_{\theta,s}^{0.7} \quad (11)$$

and is compared on Fig. 16. Mayle's correlation is quite far from the present results. The transition onset should be deduced from one of the following relations provided by Mayle:

$$Re_{x,t} = 1000 Re_{\theta,s}^{0.7} + Re_{x,s} \quad (12)$$

Hatman and Wang

$$Re_{x,t} = 1.0816 Re_{x,s} + 26805 \quad (13)$$

or Yaras

$$Re_{x,t} = 1.04 Re_{x,s} + 63000(1 - \tanh^3(100TF')), \quad (14)$$

where $TF' = \max(0.01, TF)$. Nevertheless, all these relations give an onset of transition located after the recovery position of the

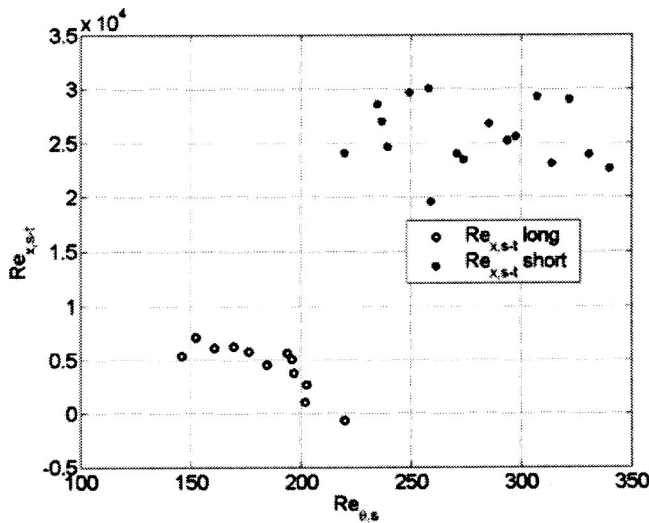


Fig. 17 $Re_{x,s-t}$ as a function of $Re_{\theta,s}$ for both long and short bubbles

present data. Thus, under the assumption that the pressure recovery is equal to the transition end, none of these relations can be used to determine the transition onset.

However, according to Mayle, "the difference between long and short bubbles is not the length of transition, but the length of the unstable laminar shear layer." Moreover, Walker [19] showed that the ratio of the transition length and its minimum value (LT/LT_{min}) evolves asymptotically for strong adverse pressure gradients (to a value very close to the one it passes by in case of incipient laminar separation at $Re_{\theta,s}^2 K_s = -0.08$). In these conditions, Eq. (9), established for short bubbles, could be used to provide the transition onset for long bubbles, with the pressure recovery taken as the transition end. Then $Re_{x,s-t}$ can be computed for the long bubbles and compared on Fig. 17 to $Re_{x,s-t} = Re_{x,s-rec}$ for short bubbles. This figure also confirms the thoughts of Mayle that the difference takes place in the laminar part of the separated flow.

The passage from long to short bubbles can be seen in the following way. The transition end takes place around the pressure recovery position, and the transition onset is located upstream, after the separation. As the Reynolds number increases, the transition onset moves toward the separation point. Physically, this can be linked to bigger and/or faster development of the instabilities in the shear layer. Approaching a value of $Re_{\theta,s} \approx 220$, the onset of transition stands close to the separation point. The transition process appears to be doped by the injection of instabilities and consequently, the mixing phenomenon is enhanced. The shear layer is able to reattach sooner in spite of the pressure gradient. This has to be linked with what Hatman and Wang were calling the tendency of reattachment for a long bubble in a point where the velocity fluctuations are maximum. Now that the bubble is short, the pressure coefficient distribution is modified which influences the transition process: the acceleration parameter at separation is smaller and the instability promotion is less important. Then the transition onset is located at the pressure recovery point (where is the maximum displacement) and the position of the maximum velocity fluctuations appears at the reattachment position.

In the opposite sense, if the bubble is short and the Reynolds number reduces, the transition onset is close to the pressure recovery position until $Re_{\theta,s} \approx 220$. If the Reynolds number decreases more, the velocity reduction appears to be translated by a weakening of the transition and mixing process. This prevents the bubble to reattach soon in an adverse pressure gradient. The limit between the two states (short or long) seems to be at $Re_{\theta,s} \approx 220$

which is different from Owen's bursting criterion ($Re_{\theta,s} = 125$). As shown on Fig. 17, the measurement point at $Re_{\theta,s} \approx 220$ could be of both types. It can be possible that the measured bubble which is a mean value oscillates between the long and the short one.

Conclusions

This paper provides the aerodynamic performance of a front loaded very high lift low pressure turbine blade for a wide operating range. It also points out that the position of the suction side velocity peak that changes with the incidence has a strong influence on the flow behavior and thus on the performance.

From pressure coefficient distributions, a simple model has been built, based on three characteristic points: separation, pressure recovery and reattachment whose determination has been shown reliable. These relations are valid as much for long as for short laminar bubbles. From these points, an interpretation has been attempted mainly about the transition process. Some incoherences among the already existing models have been pointed out. For instance, for short bubbles, the end of transition can not be considered at the maximum displacement. In this case, the models of Roberts and Mayle do not provide the transition end but the maximum displacement position. These models can lead to an underestimation of the transition length.

The results show a strong agreement with the bubble physics described by Hatman and Wang, and the bubble physics can be summarized as

1. for short bubbles, the transition onset is at the pressure recovery which corresponds to the maximum displacement position. The transition end can be computed by means of Eq. (9).
2. for long bubbles, the transition end can be considered as the pressure recovery position and the transition length also computed with Eq. (9) as discussed.

An interpretation of the bursting was provided based on the length of the bubble laminar portion. As mentioned by Mayle, this part seems to be the key of the passage between the two bubble states.

Finally, it has to be noticed that these results have been obtained in quite realistic conditions in terms of wall curvature, turning flow angles, boundary layer solicitations. The ranges of $Re_{\theta,s}$ and K_s were quite large, making from the present prediction model a well tested tool. However, more work is still required to improve the realism of the operating conditions by accounting for the influence of the compressibility, the unsteady effects and turbulence intensity (actually under study). For instance a low level ($Tu < 5\%$) enhances the transition process and leads to a reduction of the bubble influence on the aerodynamic performance; whereas a wake ($Tu = 15-20\%$) induces the transition avoiding therefore the separation.

Acknowledgments

The first author acknowledges the F.N.R.S. (Fonds National de Recherche Scientifique, Belgium) for the financial support to attend the conference.

Nomenclature

- c = blade chord (m)
- C_p = pressure coefficient = $(P_{01} - P_{wall}) / (P_{01} - P_2)$
- g = pitch (m)
- H = blade height (m)
- K = acceleration parameter = $(v/U^2)(dU/dS)$
- L = blade side length (m)
- P = pressure (Pa)
- Re_{is} = isentropic Reynolds number = $U_{2,is}c/\nu$
- Re_x = local Reynolds number = US/ν
- Re_θ = local momentum thickness Reynolds number = $U\theta/\nu$
- S = curvilinear coordinate (m)

Table 3 Blade geometry

X_{SS} (m)	Y_{SS} (m)	X_{PS} (m)	Y_{PS} (m)
0	0	0	0
-2.229e-4	2.491e-4	-2.229e-4	2.491e-4
-4.074e-4	9.874e-4	-4.074e-4	9.874e-4
-3.991e-4	1.811e-3	-3.991e-4	1.812e-3
-3.005e-4	2.635e-3	-3.005e-4	2.635e-3
7.065e-5	4.329e-3	7.065e-5	4.329e-3
1.369e-3	7.873e-3	1.369e-3	7.873e-3
3.671e-3	1.183e-2	3.671e-3	1.183e-2
6.737e-3	1.525e-2	6.737e-3	1.525e-2
1.140e-2	1.809e-2	1.140e-2	1.809e-2
1.599e-2	1.896e-2	1.599e-2	1.896e-2
2.057e-2	1.827e-2	2.057e-2	1.827e-2
2.520e-2	1.601e-2	2.520e-2	1.601e-2
3.158e-2	9.946e-3	2.989e-2	1.196e-2
3.616e-2	2.367e-3	3.359e-2	7.063e-3
3.968e-2	-6.311e-3	3.695e-2	6.608e-4
4.298e-2	-1.706e-2	3.9868e-2	-6.311e-3
4.454e-2	-2.393e-2	3.999e-2	-7.196e-3
4.455e-2	-2.446e-2	4.029e-2	-8.082e-3
4.421e-2	-2.501e-2	4.058e-2	-8.971e-3

t = time (s)

Tu = inlet turbulence intensity = $\sqrt{u'^2}/U_1$

TF = turbulence factor = $Tu(c/\Lambda)^{0.2}$

U = local velocity (m/s)

u' = velocity fluctuation (m/s)

β = yaw angle referring to the axial direction (deg)

γ = intermittency factor or stagger angle (deg)

ε = turbulent dissipation rate (m^2/s^3)

η = Kolmogorov turbulent scale (m)

Λ = turbulent macroscale (m)

λ = Taylor turbulent microscale (m)

ν = kinematic viscosity (m^2/s)

θ = momentum thickness (m)

ξ = loss coefficient

Subscript

0 = total condition

1 = inlet condition

2 = exit condition

ax = axial direction

is = isentropic

PS = relative to pressure side

r = reattachment position

rec = pressure recovery position

s = separation position

SS = relative to suction side

t = onset of transition

T = end of transition

wall = on the blade surface

Superscript

- = pitchwise mass averaged

Appendix

Incompressible Blade Geometry. Complete blade geometry is available upon request. See **Table 3** for some definition points.

References

- [1] Howel, R. J., Ramesh, O. N., Hodson, H. P., Harvey, N. W., and Schulte, V., 2001, "High Lift and Aft-Loaded Profiles for Low-Pressure Turbines," *ASME J. Turbomach.*, **123**, pp. 181–188.
- [2] Brunner, S., Fottner, L., and Schiffer, H.-P., 2000, "Comparison of Two Highly Loaded Low Pressure Turbine Cascades Under the Influence of Wake-Induced Transition," *ASME Paper 2000-GT-268*.
- [3] Solomon, W. J., 2000, "Effects of Turbulence and Solidity on the Boundary Layer Development in a Low Pressure Turbine," *ASME Paper 2000-GT-273*.
- [4] Roberts, W. B., 1975, "The Effect of Reynolds Number and Laminar Separation on Axial Cascade Performance," *ASME J. Eng. Power*, **97**, pp. 261–274.
- [5] Mayle, R. E., 1991, "The Role of Laminar-Turbulent Transition in Gas Turbine Engines," *ASME J. Turbomach.*, **113**, pp. 509–537.
- [6] Walker, G. J., 1993, "The Role of Laminar-Turbulent Transition in Gas Turbine Engines: A Discussion," *ASME J. Turbomach.*, **115**, pp. 207–218.
- [7] Malkiel, E., and Mayle, R. E., 1996, "Transition in Separation Bubble," *ASME J. Turbomach.*, **118**, pp. 752–759.
- [8] Lou, W., and Hourmouziadis, J., 2000, "Separation Bubble under Steady and Unsteady Main Flow Conditions," *ASME Paper 2000-GT-0270*.
- [9] Qiu, S., and Simon, T. W., 1997, "An Experimental Investigation of Transition as Applied to Low Pressure Turbine Suction Surface Flows," *ASME Paper 97-GT-455*.
- [10] Volino, R. J., and Hultgren, L. S., 2000, "Measurements in Separated and Transitional Boundary Layers Under Low-Pressure Turbine Airfoil Conditions," *ASME Paper 2000-GT-0260*.
- [11] Volino, R. J., 2002, "Separated Flow Transition under Simulated Low-Pressure Turbine Airfoil Conditions: Part I—Mean Flow and Turbulence Statistics," *ASME Paper GT-2002-30236*, and "Separated Flow Transition under Simulated Low-Pressure Turbine Airfoil Conditions: Part II—Turbulence Spectra," *ASME Paper GT-2002-30237*.
- [12] Hatman, A., and Wang, T., 1999, "A Prediction Model for Separated-Flow Transition," *ASME J. Turbomach.*, **121**, pp. 594–602.
- [13] Yaras, M. I., 2001, "Measurements of the Effects of Pressure-Gradients History on Separation-Bubble Transition," *ASME Paper 2001-GT-0193*.
- [14] Yaras, M. I., 2002, "Measurements of the Effects of Freestream Turbulence on Separation-Bubble Transition," *ASME Paper GT-2002-30232*.
- [15] Müller, M., Gallus, H. E., and Niehuis, R., 2000, "A Study on Models to Simulate Boundary Layer Transition in Turbomachinery Flows," *ASME Paper 2000-GT-274*.
- [16] Müller, M., Gallus, H. E., and Niehuis, R., 2001, "Numerical Simulation of the Boundary Layer Transition in Turbomachinery Flows," *ASME Paper 2001-GT-0475*.
- [17] Coton, T., Arts, T., Lefebvre, M., and Liamis, N., 2002, "Unsteady and Calming Effects Investigation on a Very High Lift LP Turbine Blade—Part I: Experimental Analysis," *ASME Paper GT-2002-30227*.
- [18] Schlichting, H., and Gersten, K., 2000, *Boundary Layer Theory*, Springer-Verlag, Heidelberg.
- [19] Walker, G. J., 1989, "Modeling of Transitional Flow in Laminar Separation Bubbles," *Ninth International Symposium on Air Breathing Engines*, Athens, Greece, Sept. AIAA ISABE, pp. 539–548.
- [20] Narasimha, R., 1985, "The Laminar-Turbulent Transition Zone in the Boundary Layer," *Prog. Aerosp. Sci.*, **22**(1), pp. 29–80.

Experimental Surface Heat Transfer and Flow Structure in a Curved Channel With Laminar, Transitional, and Turbulent Flows

P. M. Ligrani

C. R. Hedlund¹

Convective Heat Transfer Laboratory,
Department of Mechanical Engineering,
MEB 2202, 50 S. Central Campus Drive,
University of Utah,
Salt Lake City, UT 84112-9208

Heat transfer and flow structure are described in a channel with a straight portion followed by a portion with mild curvature at Dean numbers from 100 to 1084. The channel aspect ratio is 40, radius ratio is 0.979, and the ratio of shear layer thickness to channel inner radius is 0.011. The data presented include flow visualizations, and spanwise-averaged Nusselt numbers. Also included are time-averaged turbulence structural data, time-averaged profiles of streamwise velocity, spectra of longitudinal velocity fluctuations, and a survey of the radial time-averaged vorticity component. Different flow events are observed including laminar two-dimensional flow, Dean vortex flow, wavy Dean vortex flow (in both undulating and twisting modes), splitting and merging of Dean vortex pairs, transitional flow with arrays of Dean vortex pairs, and fully turbulent flow with arrays of Dean vortex pairs. Transitional events generally first appear in the curved portion of the channel at Dean numbers less than 350 in the form of arrays of counter-rotating Dean vortex pairs. At Dean numbers greater than 350, transitional events occur in the upstream straight portion of the channel but then continue to cause important variations in the downstream curved portion. The resulting Nusselt number variations with curvature, streamwise development, and Dean number are described as they are affected by these different laminar, transitional, and turbulent flow phenomena.

[DOI: 10.1115/1.1738119]

Introduction

Heat transfer in channels with transitional and turbulent flows are important for a range of practical applications, including cooling passages in gas turbine blades, internal combustion engine cooling ducts, heat exchangers, cooling systems for the nozzle walls of rocket motors, and medical treatment of the human cardiovascular system. Straight and curved channels are also interesting because they provide environments to investigate an assortment of transitional phenomena. In straight channels, these phenomena include regions of longitudinally distinct local instability referred to as “slugs” and “puffs” of turbulence, [1,2]. In curved channels, transition begins with the development of arrays of counterrotating Dean vortex pairs which form across the channel span, [3–5]. Whether in straight or curved channels, developing transitional flow events provide the initial conditions for the turbulent flows which follow. The interactions between these transitional phenomena and the subsequently developing turbulent flows can be quite complex, especially when a curved channel segment follows a straight segment, as in the present study.

Only a handful of investigations consider heat transfer in curved channels containing laminar and transitional flows. Of these, Cheng and Akiyama [6] present Nusselt numbers, velocity distributions, and pressure distributions determined from numerical analysis of curved channels with fully developed, laminar forced convection, no buoyancy, and constant heat flux boundary conditions. Mori et al. [7] present measured Nusselt numbers from a square channel with laminar, transitional, and turbulent

flow conditions, and numerically predicted Nusselt numbers, velocity data, and pressure surveys for fully developed laminar and turbulent channel flows. In another numerical description of curved channel heat transfer, Yee et al. [8] predict the streamwise development of Nusselt numbers and secondary motions in curved channels with aspect ratios of 1/3, 1, and 3, and steady, laminar flow with constant wall temperature boundary conditions. Chilukuri and Humphrey [9] numerically predict Nusselt numbers and secondary flows in a curved channel with a square cross-section and buoyancy both assisting and opposing the forced flow. Komiyama [10] presents numerically predicted Nusselt numbers from curved channels with fully developed flows and aspect ratios from 0.8 to 5, and constant wall heat flux boundary conditions.

Investigations of channels with fully turbulent flow are somewhat more numerous. Recent investigations consider the effects of curvature, [11–14], channel aspect ratio and geometry, [13–15], ribs and riblets placed along channel walls, [15–17], channel Reynolds number, [13,15,16], duct geometry, [14,15], flow tripping, [12], and different surface thermal boundary conditions, [11]. Of these investigations, several examine heat transfer behavior in channels with turbulent flow, [11,14–17]. Only Kobayashi et al. [11], Joye [14], and Mochizuki et al. [16] examine heat transfer in channels with curved sections. Kobayashi et al. [12] and Su and Friedrich [13] also investigate turbulent flows in curved channels without heating to illustrate structural characteristics of channel secondary flows. Only Kobayashi et al. [11] and Mochizuki et al. [16] consider the streamwise development of surface heat transfer distributions, channel secondary flows, and temperature distributions in curved channels.

Ligrani et al. [18] examine effects of curvature on measured heat transfer in channels with thermally fully developed, laminar, and transitional forced convection. Constant heat flux boundary conditions are applied to the surfaces of the channel, which has an aspect ratio of 40, a bend of 180 deg, $Pr=0.71$, and Dean numbers up to 300. The authors indicate that spanwise-averaged Nusselt

¹Carl Hedlund suddenly and unexpectedly passed from this world on June 25, 2003. For all those who knew Carl, he will always be remembered as a loving father and husband, and a person with exceptional technical abilities, an individual of exceptional integrity and honesty, a wonderful colleague, and a treasured friend.

Contributed by the International Gas Turbine Institute and presented at the International Gas Turbine and Aeroengine Congress and Exhibition, Atlanta, GA, June 16–19, 2003. Manuscript received by the IGTI Dec. 2002; final revision Mar. 2003. Paper No. 2003-GT-38734. Review Chair: H. R. Simmons.

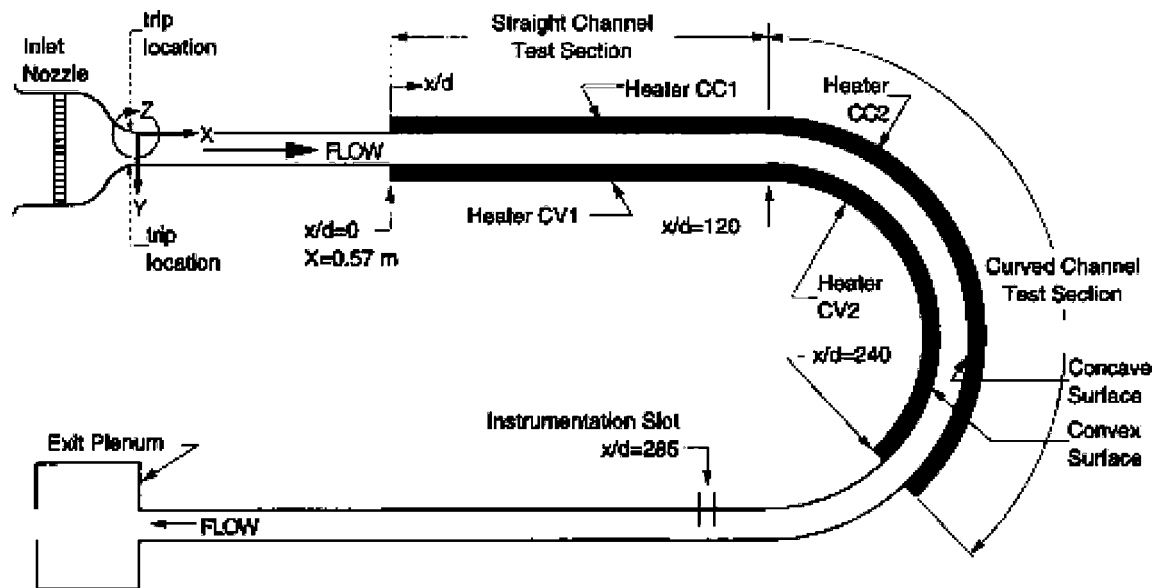


Fig. 1 Channel coordinate system and geometry

numbers are always higher on the concave surface than on the convex at all streamwise locations in the curved section, except just after curvature begins. Differences just downstream of the beginning of curvature result from initial development of Dean vortex pairs near the concave surface, [3–5], and the secondary flows and unsteadiness associated with them, [5,19]. Significant Nusselt number increases on the concave and convex surfaces also occur with x/d for $x/d > 156$ and $De > 150$ due to the twisting secondary instability, [5,20]. In the flows investigated by Ligrani et al. [18], fully developed laminar flow is always present at the inlet of the curved portion of the channel, and transitional events, such as Dean vortex pairs, are contained entirely in the curved portion of the channel. Using the same experimental facility, Hedlund and Ligrani [21] examine the effects of upstream transitional flows on curved channel Nusselt numbers at Dean numbers from 300 to 700. Results suggest that the thermal boundary layers responsible for the Nusselt number variations are dependent upon upstream initial conditions at the inlet of the curved portion of the channel, in addition to transitional disturbances and levels of turbulence intensity very near the measurement location. Local Nusselt number increases from transitional events in the upstream straight channel segment are believed to be due to local transitional “slugs” or “puffs” of turbulence, [1,2]. These cause initial Nusselt number augmentations relative to pure laminar values to be located progressively upstream as the Dean number increases.

In the present paper, Nusselt number characteristics at Dean numbers from 100 to 1084 are presented and discussed. Note that Reynolds numbers based on channel thickness Re are determined by dividing Dean numbers De by 0.1459. The present study uses the same channel employed by Ligrani et al. [18], and by Hedlund and Ligrani [21]. Included are descriptions of the influences of streamwise development, varying Dean number, and curvature on local Nusselt number behavior. Of the archival literature known to the authors, only Mori et al. [8], Ligrani et al. [18] and Hedlund and Ligrani [21] present *measured* heat transfer data from curved channels with laminar, transitional, and turbulent flows. The present work is thus important as it provides new information regarding effects of complex transitional and turbulent flows on channel heat transfer. Particular attention is devoted to the effects of different initial conditions at the entrance to the curved portion of the channel. These initial conditions are provided at this location by varying transitional phenomena which develop at different streamwise locations in the straight portion of the channel located

just upstream. As such, the present results provide an important tool for the development of numerical codes for the prediction of complex elliptic flows.

Experimental Apparatus and Procedures

Curved and Straight Channels. Detailed descriptions of the rectangular cross-section channel employed for the present study are given by Ligrani et al. [18] and Hedlund and Ligrani [21]. Dimensional details are also illustrated in Fig. 1. The channel is instrumented for heat transfer measurements, has a thickness d of 1.27 cm, an aspect ratio of 40, and is dimensionally similar to another transparent curved channel used for flow visualization and quantitative measurements of flow properties by Ligrani and Niver [5], and Ligrani et al. [19,20]. The ratio of shear layer thickness to convex radius of curvature is 0.011 in the curved section, which indicates mild curvature.

Just downstream of the channel inlet, the flow is conditioned to reduce spatial nonuniformities using arrays of screens, honeycombs, and a nozzle with a 20 to 1 contraction ratio. Figure 1 shows that the straight section is composed of an initial unheated section 0.57 m long followed by a heated section 1.52 m long. The straight section allows hydrodynamically and thermally fully developed channel flow to develop before entering the curved section under most conditions studied, [18,21]. With such conditions present, shear layer thickness is half of the channel thickness, $d/2$. The fluid then enters a 180 deg curved channel section with convex and concave surface radii of 59.69 cm and 60.96 cm. The interior walls of the heated section are made of 0.08 cm thick polycarbonate. Upon exiting the curved section, the flow enters a second straight section with a length of 2.44 m. As flow leaves the second straight portion, it passes through additional flow management devices and plenums to isolate the test section from the channel blowers and apparatus for measurement of mass flow rates.

Figure 1 additionally shows four heated sections of the channel walls, denoted CC1, CV1, CC2, and CV2. Each of these segments is instrumented with thermocouples to measure channel surface temperatures, etched foil heaters to heat channel surfaces, and insulation to minimize conduction losses, [18]. 100 copper-constantan thermocouples are placed between the heaters and non-flow side of the 0.08 cm Lexan at ten streamwise locations. These provide sufficient data to calculate spanwise-averaged Nusselt

numbers on concave and convex surfaces. At each location, thermocouples are placed in rows of five. The five thermocouples in each row extend across the channel span a distance of 20.32 cm. Rows of thermocouples on the straight portion of the channel are located at x/d of 12, 36, 60, 84, and 108. This first location corresponds to $X=0.722$ m. Rows of thermocouples on the curved portion of the channel are located at x/d of 132, 156, 180, 204, and 228.

To determine conductive losses from the heated portions of the channel, 40 additional thermocouples are placed in the insulation located behind the etched foil heaters. These thermocouples are placed in pairs along the channel centerline behind each row of thermocouples. One additional thermocouple is used to measure the mixed mean temperature at the channel inlet.

Voltages from the 141 T-type thermocouples are read sequentially using Hewlett-Packard relay multiplexer card assemblies, installed in a HP3497A low-speed data acquisition/control unit and a HP3498A extender. This system provides thermocouple compensation electronically such that voltages for type-T thermocouples are given relative to 0°C. A Hewlett-Packard 9836A computer processes signals from all 141 thermocouples to determine spanwise-averaged Nusselt numbers using procedures described below.

Nusselt Number Measurement. Procedures to measure local Nusselt numbers are described by Hedlund [22] and Ligrani et al. [18]. Details are also presented here for completeness.

For each test, heater power levels are adjusted to provide a constant surface heat flux boundary condition along the instrumented test surfaces. The channel is heated to thermal equilibrium during which time, the channel surfaces expand to the sizes that they assume as measurements are conducted. Metal C-type clamps are then installed along the curved test section to ensure that no leakage occurs from the exterior to the interior of the channel. A variety of quantities are then measured to determine local Nusselt numbers.

To do this, all thermocouple voltages and heater power levels are measured and converted into surface temperatures and a convective heat flux level \dot{q}''_{conv} . The latter are determined using energy balances which account for conduction losses from the test surfaces. The local mixed mean temperature t_m is determined at any streamwise channel location using the equation given by

$$t_m = t_{m-inlet} + (\dot{q}''_{conv} b \Delta x) / \dot{m} C_p. \quad (1)$$

Here, $t_{m-inlet}$ is the mixed mean temperature at the channel inlet. The temperatures measured by the thermocouples located within the test surface walls are then corrected to account for thermocouple contact resistance and the temperature drop which occurs in the polycarbonate between the thermocouple and the portion of the test surface located next to the air stream. With these data, local heat transfer coefficients and local Nusselt numbers are determined.

Overall energy balance checks are also conducted at Dean numbers less than 300, [18]. These are accomplished by direct measurements of the local mixed mean temperature just downstream of the heated portion of the channel. This is accomplished using a thermocouple probe to measure local fluid temperature and a miniature five-hole pressure probe, [18], to measure local velocity across the channel $Y-Z$ plane at $De=285$. These direct t_m results are then compared to mixed mean temperatures determined from energy balances using Eq. (2). In all cases, the two measurements of mixed mean temperature agree within a few percent, [18], which verifies the procedures employed to determine spanwise-averaged Nusselt numbers including conduction energy balances and energy balances to calculate mixed-mean temperatures.

Visualizations of Instantaneous Flow Structure. The visualizations and flow structure measurements are obtained in a second channel, which is transparent with the same internal dimensions (and flow management apparatus at the inlet) as the channel

employed for heat transfer measurements. To visualize the flow in this channel, smoke is injected into the channel inlet using a manifold and a rake of tubes to produce an array of laminar jets. Smoke patterns are illuminated in spanwise/radial planes using spot lights directed at spanwise slits in the black paper used to line the exterior of the convex surface of the channel. A video camera connected to a portable videocassette recorder is used to record the illuminated, time-varying patterns at rates as high as 60 frames per second. Additional details on this, as well as other aspects of the flow visualization techniques, are given by Ligrani et al. [19].

Local Mean Velocity Surveys. The miniature five-hole probe, described by Ligrani et al. [23], is used to measure total pressure and the three mean velocity components locally at different locations across the cross section of the transparent curved channel which is employed exclusively for such measurements. The tip diameter of the probe is 1.22 mm to minimize flow blockage and maximize spatial resolution in the confined channel interior. Additional corrections to account for finite spatial resolution and streamline displacement effects are made during data reduction following Ligrani et al. [24].

Longitudinal Velocity Fluctuation Surveys. Surveys of streamwise mean velocity and longitudinal velocity fluctuations are obtained using Dantec 55P04 single hot-wire probes. Sensor diameter and length are 5 microns and 1.25 mm, respectively. Each probe is operated at an overheat ratio of 1.8 using a Dantec 55M10 constant-temperature bridge. Individual probes are calibrated in the freestream flow of a wind tunnel using procedures for low velocity measurement described by Ligrani and Bradshaw [25]. These hot-wire probes are mounted in spanwise/radial planes 120 deg from the start of curvature in the transparent curved channel using the same automated two-dimensional traverse employed for the miniature five-hole pressure probe. Signals are conditioned with an amplifier gain of 2, a low-pass filter of 1.0 kHz, and no high-pass filter. Data are acquired at 2500 Hz using a Hewlett-Packard 6944A series 200 Multi-programmer with a buffered 69759A analog-to-digital conversion card capable of 12-bit binary resolution. This multi-programmer is controlled by a Hewlett-Packard model 320 series 9000 computer, which also stores and processes the data. With this acquisition system, 20,000 data samples are obtained at each measurement location which amounts to a sampling interval of 8.0 sec.

Experimental Uncertainty Estimates. Procedures described by Kline and McClintock [26] and Moffat [27] are employed to determine experimental uncertainty magnitudes based on a 95% confidence levels. The experimental uncertainty of spanwise-averaged Nusselt numbers is estimated to be $\pm 5.5\%$. Estimated uncertainty magnitudes of Dean number De , local streamwise velocity u_θ , time-averaged square of the longitudinal velocity fluctuation, and the normal or radial component of time-averaged vorticity ω_r , are $\pm 2\%$, $\pm 2.5\%$, $\pm 5\%$, and $\pm 7\%$, respectively.

Experimental Results

Table 1 summarizes the different types of flow behavior which are present in the present curved channel (with radius ratio of 0.979) at $\theta=112$ deg–115 deg, which are angular positions measured from the start of curvature. These different regimes of behavior are described in the sections which follow. Flow structural details are needed for the interpretation of surface Nusselt number variations, and for the development of numerical prediction models of flows in curved channels.

Development and Structure of Dean Vortex Pairs. As the influences of concave curvature impose themselves on the flow, secondary flows in the form of tiny Görtler-like vortices start to form near the concave surface of the channel. This is believed to occur just after the beginning of the curved portion of the channel as x/d exceeds 120 to 130. As the vortices are advected downstream, they grow in spatial extent, and produce spatially periodic

Table 1 Different types of flow behavior in the curved channel with radius ratio of 0.979 at $\theta=112$ deg–115 deg

De	Re	Flow Description
<60	<411	Curved channel Poiseuille flow
60–75	411–514	Partially formed Dean vortex pairs
>60	>411	Splitting and merging Dean vortex pairs
>75	>514	Fully formed Dean vortex pairs
60–125	411–860	Undulating Dean vortex pairs
129–200	884–1370	Twisting Dean vortex pairs
>700	>4800	Fully turbulent flow with Dean vortex pairs
36.9	253	Onset and presence of Dean vortex pairs from linear stability analysis

flow structures across the channel span, [5,28]. The unsteadiness of these layers is consistent with the initial development of Görtler vortices in boundary layers on concave walls, [5,19]. The resulting unsteadiness, along with the centrifugally induced secondary flows, augment thermal transport over that produced by laminar streamwise advection alone. As a result, unsteadiness and secondary flows both play important roles in increasing concave surface heat transfer coefficients relative to ones from the convex surface just after the imposition of curvature.

Such flow phenomena are illustrated by the flow visualization photographs presented in Fig. 2. These data are obtained at $De=122$. The images show typical flow visualization patterns of flow cross sections at different streamwise stations. Each covers one channel height in the Y direction and about 3.5 channel heights in the Z direction. The concave surface is at the bottom of each photograph, the convex surface is at the top, and flow is moving away from the observer. Observation locations range over θ from 85 deg to 135 deg, which correspond to x/d from 190 to 232.

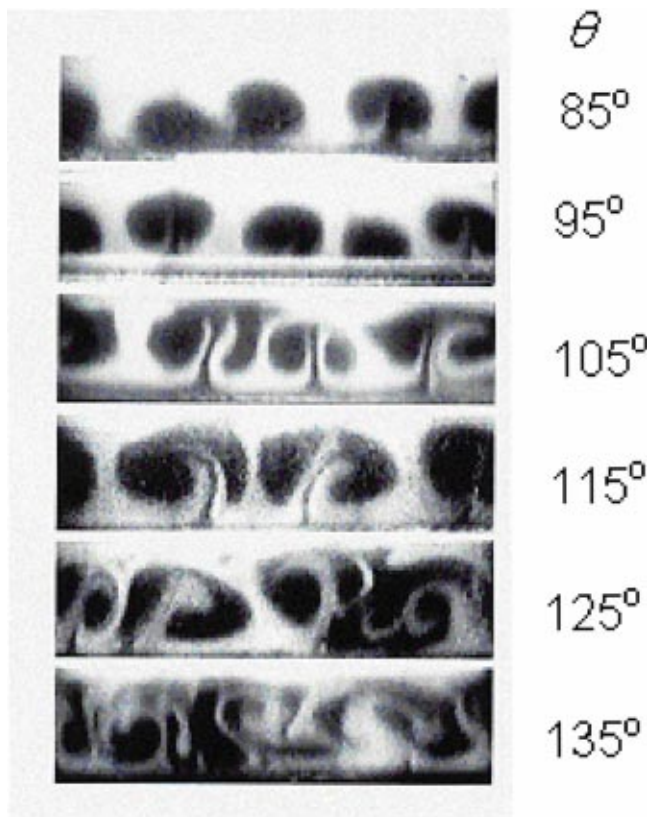


Fig. 2 Photographs of flow visualized using smoke at channel cross sections located at different streamwise locations for a Dean number of 122

At θ up to and including 85 deg and 95 deg, Fig. 2 shows smoke layers with spatial periodicity, which are present across the channel span. The periodicity of these layers increases in amplitude and definition with streamwise development, [18,19]. Such behavior is caused by the developing secondary flows in the array of partially formed vortex pairs located near the concave surface. The smoke enters the curved portion of the channel as a uniform layer about one-half channel height in extent next to the convex surface. As a result, events associated with secondary flows emanating from near the convex surface are smoke rich (bright), whereas ones from near the concave surface are relatively free of smoke (dark).

As θ increases from 95 deg to 105 deg, the smoke patterns in Fig. 2 show a dramatic change as they form into clearly defined mushroom-shaped patterns. Different portions of such patterns, with their occasional unsteadiness, are closely associated with different secondary flows. The dark mushroom “stems” with bright regions on each side are associated with upwash regions which emanate from near the concave surface between the two vortices in each pair. The mushroom “petals” correspond to vortex core regions. Bright regions between each mushroom pattern represent downwash regions (with respect to the concave surface) between vortex pairs [5,19]. Unsteadiness and spatial variations of secondary flows continue to be higher near the concave surface. Note that the flow visualization patterns probably lag slightly behind the secondary flow development in vortex pairs.

As the vortex pairs continue to convect downstream, flow visualization patterns in Fig. 2 for $\theta=105$ deg and $\theta=115$ deg show patterns which increase in radial extent to occupy the full channel height. Time-averaged radial vorticity distributions which illustrate these spatial variations are shown in Fig. 3 for $\theta=120$ deg, $x/d=219$, and $De=122$. These data are determined from measurements of the three mean velocity components made using the miniature five-hole pressure probe [23,24] in the transparent

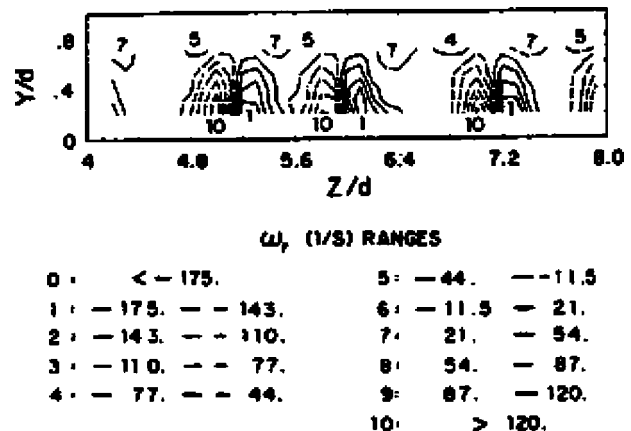


Fig. 3 Time-averaged distribution of radial vorticity for $De=122$, $\theta=120$ deg, and $x/d=219$. The associated vorticity scale is given below the plot.

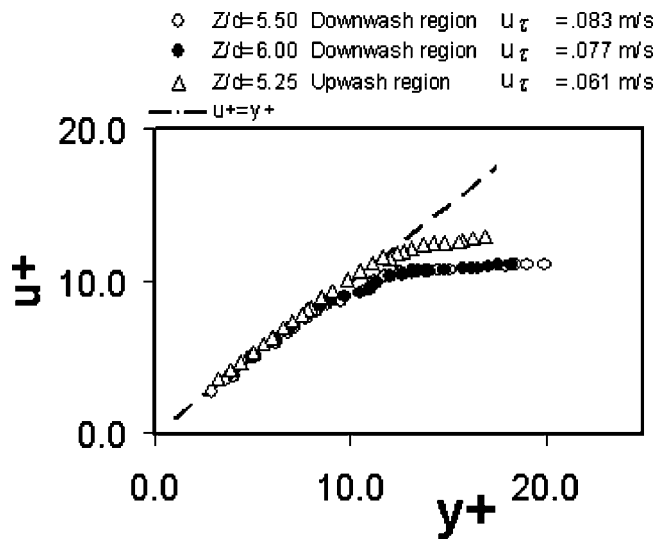


Fig. 4 Normalized streamwise mean velocity profiles at three different spanwise locations at $De=125$ and $x/d=219$

curved channel. In each plot, bulk flow direction is then into the plane of the page, $Y/d=0$ corresponds to the concave surface, and $Y/d=1$ corresponds to the convex surface.

The time-averaged radial vorticity distribution in **Fig. 3** shows alternating regions of positive and negative vorticity across the channel span. An individual vortex pair is indicated by a region of positive vorticity (dashed contour lines) immediately adjacent to a region of negative vorticity (solid contour lines). Three complete pairs are evidenced in the figure. Because these data are obtained at a different spanwise portion of the channel than where flow visualizations are observed, direct comparison between the two is precluded. Upwash regions are positioned between the two vortices in each pair where fluid with low streamwise momentum fluid is advected away from the concave surface by secondary flows. In **Fig. 3**, central portions of upwash regions are located at Z/d of about 5.1, 6.0, and 7.1 where gradients of radial vorticity are quite large and abrupt changes in the signs of these vorticity components occur as Z/d is changed at constant Y/d . Downwash regions are positioned between vortex pairs at Z/d of 4.5, 5.5, 6.6, and 7.6. These are responsible for convection of fluid with high streamwise momentum from near the channel center to regions near the concave wall. As a result, gradients of streamwise velocity are increased near the surface, [29]. Spanwise extents of upwash regions are smaller than the downwash regions as a result of higher pressure fluid existing on the downwash sides of individual vortices and lower pressure fluid existing on the upwash sides of individual vortices, [30].

Examples of velocity profiles measured with laminar flow and Dean vortex pairs in the channel are presented in **Fig. 4**. These data are measured at $De=125$ and $x/d=219$ near the downstream end of the curved portion of the channel. The linear behavior, which characterizes purely laminar behavior and no turbulent shear stresses near the channel surfaces, is evident for $y^+ < 10$. Streamwise mean velocities are lower in the upwash region than in the downwash region. However, in the normalized coordinates in **Fig. 5**, normalized upwash region velocities are higher due to locally lower friction velocity, [5,19,20].

Some distortion of the mushroom patterns is apparent in **Fig. 2** at $\theta=115$ deg which is associated with vortex pair unsteadiness especially in the spanwise direction. These motions and distortions are more apparent at $\theta=125$ deg and often associated either with undulating wavy motions, [20], and or spanwise wave number selection resulting from splitting and merging of vortex pairs, [19]. Undulations are unsteady oscillations and side-slipping of vortex pairs at relatively low frequency. Such wavy motions ap-

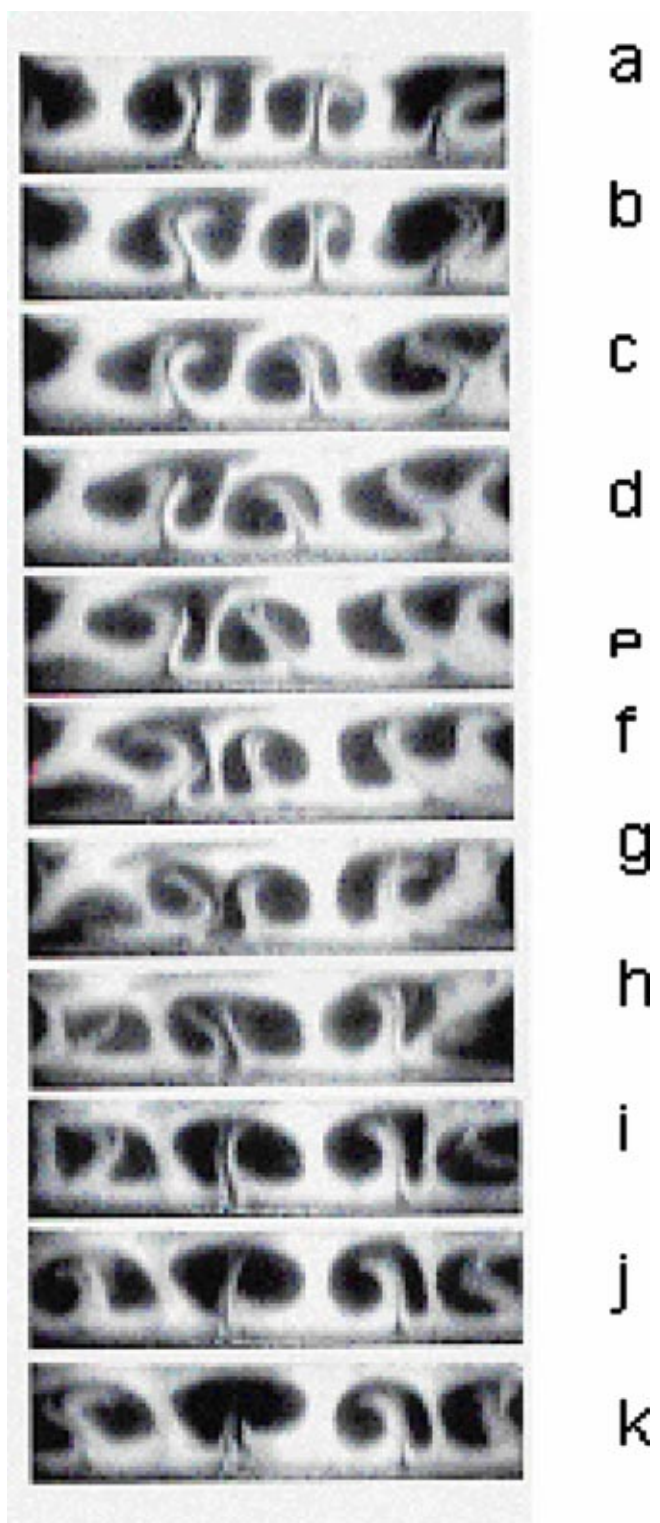


Fig. 5 Time sequence of 11 smoke visualization photographs and sketches illustrating how one vortex pair may be engulfed by an adjacent vortex pair followed by the emergence of a vortex pair from the near-wall region for $De=100$ at a streamwise location 105 deg from the start of curvature. Photographs are spaced apart by 1/30 second intervals. The streamwise direction is into the plane of the plot, the concave surface is on the bottom of each photograph, and the convex surface is on the top of each photograph.

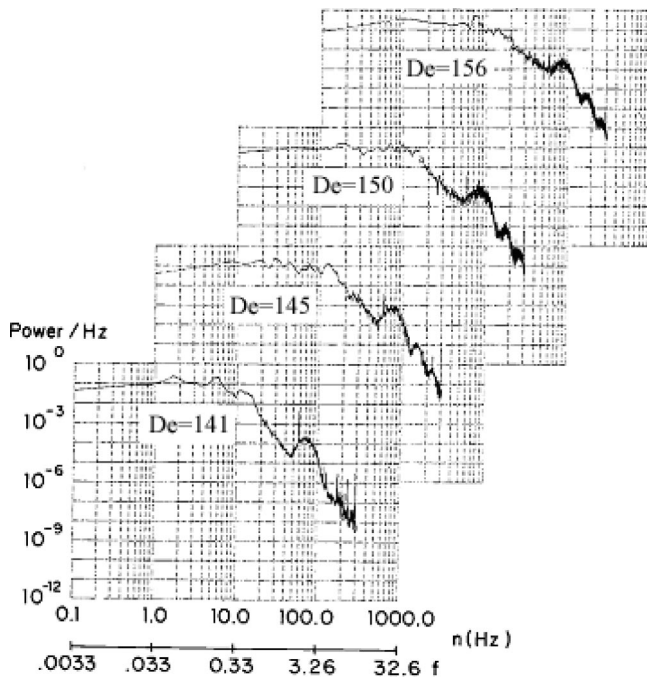


Fig. 6 Temporal power spectra of the voltage signals from a hot-wire sensor placed at $Y/d=0.5$ and $Z/d=-12.25$ (near an inflow region) at a streamwise location $\theta=112$ deg from the start of curvature. Individual spectra are given for De of 141, 145, 150, and 156 show the fundamental and two harmonic frequencies associated with twisting vortices.

pear as periodic spanwise-rocking of vortex pairs, along with periodic changes in the direction of upwash regions between vortex pairs [20].

Undulations are generally observed at θ greater than 95 deg from Dean numbers ranging from 40 to 125, [5,20]. Splitting and merging are apparent in visualizations at Dean numbers from 60 to 220, [5,19]. As θ increases from 125 deg to 135 deg, smoke patterns in Fig. 2 are increasingly convoluted and distorted. Higher levels of radial and spanwise unsteadiness are present from intense undulations, frequent splitting and merging, and possibly less organized motions.

Figure 5 shows a merging event observed at $De=100$ at a streamwise location 105 deg from the start of curvature. Here, the merging event occurs as the two vortices of opposite sign in two adjacent pairs move towards each other, collide, and then cancel. Initially, in photograph (a), about three and one-half vortex pairs are present each with a slightly different orientation. As time increases in photos (b), (c), (d), (e), and (f), the slightly smaller middle vortex pair starts to tilt such that the upwash region reaches an angle of about 60 deg from the plane of the concave wall. The left-most pair does the same thing, but in the opposite direction, as the two vortex pairs move closer to each other. The two pairs on the left sides of photographs in Fig. 5 then appear to collide in photograph (g). As this happens, the two adjacent vortex pairs cancel, and in doing so, cease to exist. A single vortex pair then replaces the prior existing two pairs in subsequent photographs (h)–(k). According to Bottaro [31], the bending of the vortices in Fig. 5 comes from an attraction or repulsion of neighboring vortex pairs caused by the Eckhaus instability. The initial step of merging (and splitting) processes thus involves instability of vortex pairs to spanwise perturbations [32], a part of the process which may be described by linear theory. As the process continues, nonlinear effects become important. Even though the photo sequence in Fig. 5 shows the timewise variation of flow

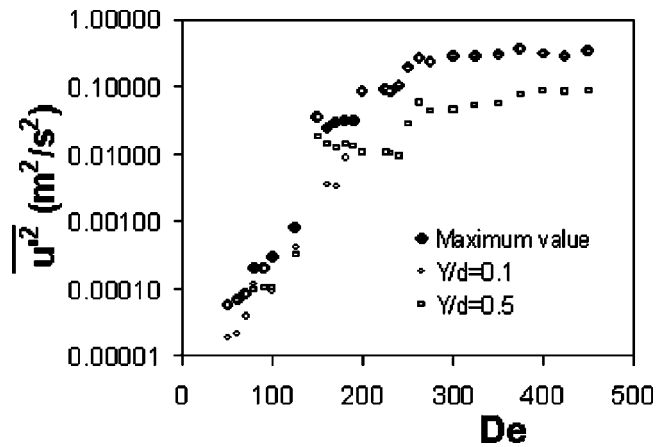


Fig. 7 Variation of the time-averaged magnitude of the square of the longitudinal fluctuating velocity with Dean number De at three different locations across the channel cross section at $x/d=219$

patterns, the merging event is the result of a flow which evolves spatially as well as temporally with significant changes over small streamwise distances.

Twisting and Longitudinal Velocity Fluctuations. Twisting is a high intensity vortex rocking motion of the Dean vortex pairs (when viewed in spanwise-normal planes), which generally occurs continuously at frequencies which depend upon the Dean number and location, with occasional transient occurrences at lower frequencies, [5,20]. As De increases at a particular x/d , or as x/d increases at a particular De , twisting first appears in upwash regions near the concave surface. With additional development, twisting produces intense large-scale oscillations about upwash regions which correspond to variations in time and space of the streamwise velocity and secondary flows near the concave wall, [20]. As the Dean number increases from 150 to 200, the largest time-averaged magnitudes of the square of longitudinal velocity fluctuations from twisting occur away from the channel walls at Y/d from 0.2 to 0.4, and then throughout upwash regions near the concave wall, [20].

Shown in Fig. 6 are power spectra of time records of voltages from a hot-wire probe sensing velocity fluctuations (mostly in the

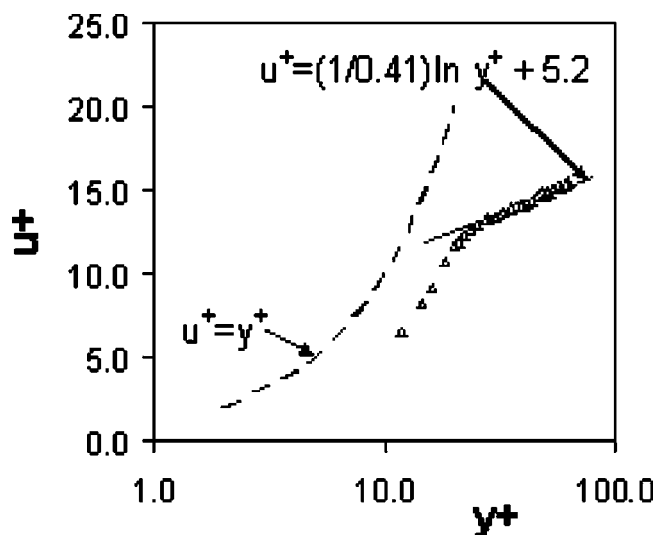


Fig. 8 Normalized streamwise mean velocity profile at $De=401$ and $x/d=219$

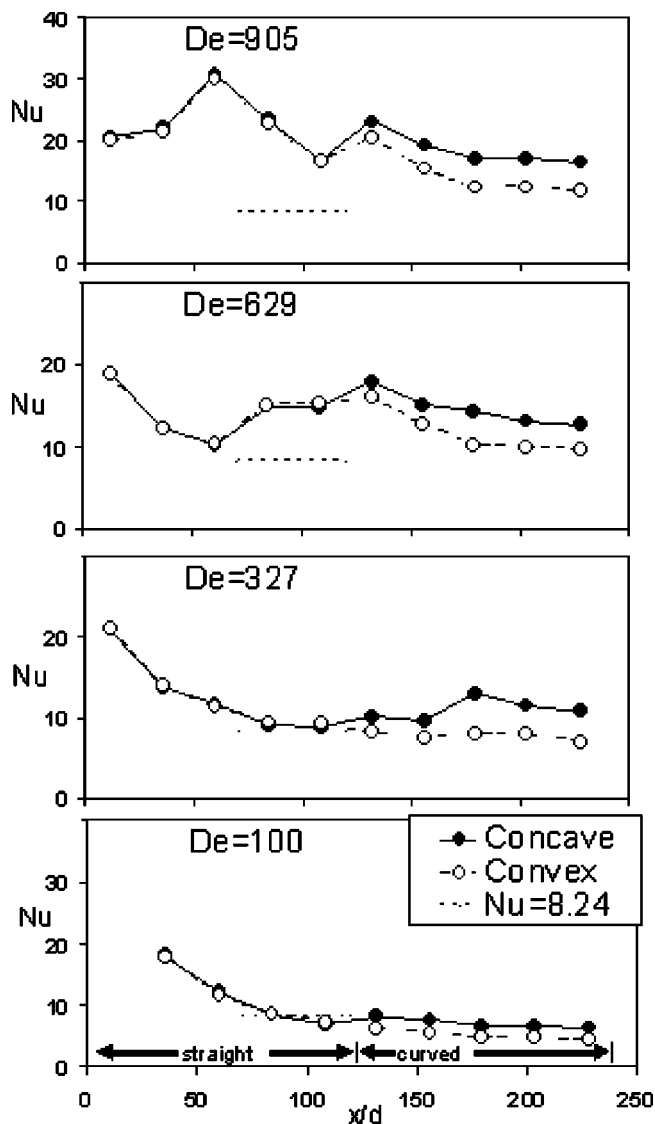


Fig. 9 Forced convection Nusselt numbers as dependent upon x/d for Dean numbers of 100, 327, 629, and 905

longitudinal direction) sampled at one point in the flow at $Y/d = 0.5$ and $Z/d = -12.25$ and a streamwise location $\theta = 112$ deg from the start of curvature. For De corresponding to 141, 145, 150, and 156, this location is within a vortex with negative vorticity levels and near an upwash region. In this figure, nondimensional frequencies are given as $f = 2\pi n(d/2)/\bar{U}$, where n is the frequency in Hz, and values of \bar{U} employed in Fig. 6 correspond to $De = 145$. Referring to data in Fig. 6 at this Dean number, the broad peak centered near $f = 2.5$ corresponds to the principal frequency of twisting vortices. Two harmonics are seen at $f = 4.9$ and $f = 7.4$. On the high frequency side of the principal peak, flow background noise levels are about two orders of magnitude lower than the local maximum. As the Dean number increases from 141 to 156 in Fig. 6, principal and harmonic peaks become higher in magnitude and more apparent relative to power levels of background fluid motions. Qualitatively similar spectra are observed at a variety of locations in spanwise/radial planes located from 112 deg to 120 deg from the start of curvature, and at a variety of De ranging from 129 to 200, [20]. The amplitudes of principal peaks from twisting are strongly dependent upon Dean number, as well as on the location within the vortex pair structure. The principal

frequency in the twisting portions of spectra usually lies between $n = 55$ Hz and 90 Hz (or between f ranging from 1.6 to 3.3).

Additional information on variations of time-averaged magnitudes of the square of the fluctuating velocity, u'^2 , is given in Fig. 7. These results provide additional insight into curved channel transition, and are obtained in a cross-sectional plane located at $x/d = 219$, which covers Z/d from 4 to 8 and Y/d from 0.1 to 0.8. Maximum u'^2 values are shown along with values measured in the upwash region of a vortex pair at $Y/d = 0.1$ and $Y/d = 0.5$. The u'^2 increases which occur as Dean number increases from 0 to 130 occur mostly from: (i) unsteadiness as the vortices initially form near the concave surface as tiny Görtler vortices and are particularly sensitive to small amplitude perturbations and spanwise wave number selection, [5,19], (ii) undulating motions, [20], (iii) splitting, merging, and spanwise wave number selection of fully formed vortex pairs, [19], and (iv) unsteadiness from random perturbations occurring at the channel inlet, [5,19,21]. The u'^2 variations shown in Fig. 7 at De from 130 to 200 are due to twisting, [20]. Here, significant u'^2 are present only within upwash regions between the vortices in each pair where twisting motions are initially most intense. The maximum u'^2 which occur within these upwash regions are located between $Y/d = 0.1$ and $Y/d = 0.5$.

At Dean numbers between 200 and 300, twisting continues to be present, as mentioned, and u'^2 continues to increase with De . In addition, the maximum u'^2 in the cross-sectional plane measured occurs at $Y/d = 0.1$. Time-averaged surveys of u'^2 at these conditions continue to show regions with locally increased u'^2 magnitudes located within and near vortex pair upwash regions. Afterwards, at higher De , the late-transitional "turbulent-like" behavior, characterized by the mean velocity profile in Fig. 8 is present. Time-averaged turbulence structure then increases only very gradually with Dean number at each cross-sectional plane location.

The normalized velocity profile presented in Fig. 8 is given for $De = 401$. The profile is at the downstream end of the curved portion of the channel at $x/d = 219$, which probably indicates that transitional events, like twisting, occur upstream. This is because the twisting secondary instability is important in initiating the transition process in curved channels. Twisting occurs at the downstream end of the channel after Dean vortex pairs are already present, and either partially developed or fully developed. Other transitional events then occur at locations which are progressively upstream as the Dean number increases.

Streamwise Development of Spanwise-Averaged Nusselt Numbers. Spanwise-averaged Nusselt numbers are presented as dependent upon normalized streamwise distance in Fig. 9 for Dean numbers of 100, 327, 629, and 905. Results from the concave and convex surfaces are given at different x/d for each Dean number to illustrate the effects of streamwise development and curvature (at x/d from 120 to 240). Note that the data presented for $x/d = 0 - 120$ are measured on the straight portion of the channel, and the data presented for $x/d = 120 - 240$ are measured on the curved portion of the channel shown in Fig. 1.

Results from the straight portion of the channel ($0 \leq x/d \leq 120$), presented in Fig. 9, provide several important checks on the experimental data for all four Dean numbers. First, Nusselt numbers measured on both sides of the channel (labeled concave and convex even though they are on the straight channel segment) are nearly equal at each streamwise location. This evidences two-dimensional velocity and thermal field development, and validates the measurement procedures used. This is additionally important because the flow at the end of the straight channel section, at $x/d = 120$, provides the thermal and velocity inlet conditions for the curved portion of the channel.

A second check is provided by the trends of the Nusselt number data with respect to streamwise distance in the straight portion of

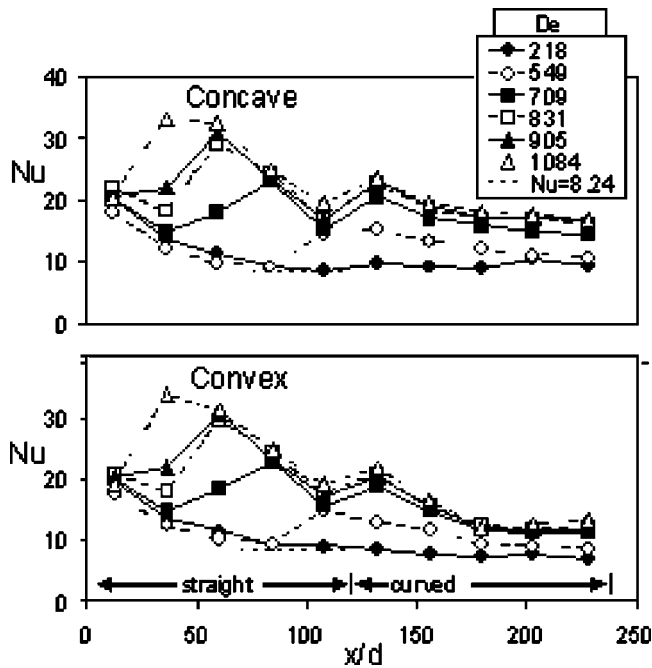


Fig. 10 Forced convection Nusselt numbers as dependent upon x/d for Dean numbers of 218, 549, 709, 831, 905, and 1084 for the concave and convex channel surfaces

the channel. For the lowest three Dean numbers, the decrease of Nu with x/d is consistent with thermal boundary layer development in the upstream part of the straight portion of the channel.

The third check is provided by Nusselt number data at $De = 100$, and $De = 327$. In both cases, Nu magnitudes near the downstream end of the straight portion of the channel (at x/d from 80 to 120 for $De = 100$ and $De = 327$) are near 8.24, the Nusselt number value expected for a spanwise-infinite, straight channel with fully developed, two-dimensional laminar flow and constant heat flux thermal boundary conditions.

Figure 9 shows that Nusselt numbers measured on the concave surface are generally consistently higher than values measured on the convex surface in the curved portion of the channel (at x/d from 120 to 240). This occurs regardless of the Dean number, as the influences of concave curvature impose themselves on the flow. The initial increases which occur as x/d exceeds 120 to 130 are due to secondary flows which result as tiny Görtler-like vortices initially form near the concave surface of the channel. These are formed by the unstable stratification of angular momentum in the curved portion of the channel which eventually results in the development of Dean vortex pairs. The Dean vortex pairs are generally associated with: (i) more intense secondary flows with greater spatial variations near the concave surface than near the convex surface, and (ii) more unsteadiness near the concave surface than near the convex surface, particularly at Dean numbers greater than 200 [19,20,29,31,32].

The Nusselt numbers in Fig. 9 for $De = 327$ show some similarities to the $De = 100$ data, but also important differences. For example, both data sets show higher Nusselt numbers on the concave surface compared to the convex surface in the curved part of the channel (at $x/d > 120$). At larger x/d , concave surface Nusselt numbers for $De = 327$ show another important increase (which is not present when $De = 100$) as the channel flow is advected downstream. This occurs as x/d increases from 156 to 180 at $De = 327$, and is associated with significantly increased flow unsteadiness, which is associated with the twisting secondary instability, which occurs either at these same streamwise locations or at locations upstream. Twisting is known to affect Nusselt number distribu-

tions and local flow behavior at Dean numbers as low as 130–150 depending on the streamwise location in the channel relative to the start of curvature.

Notice that the Nusselt number results for $De = 100$ in Fig. 9 do not show any significant change at positions corresponding to the flow visualization photographs presented in Fig. 2 for θ of 85 deg, 95 deg, and 105 deg. Thus, the dramatic flow visualization pattern changes associated with increased vortex development with streamwise distance shown in Fig. 2, do not cause significant changes to unsteadiness or thermal transport.

The Nusselt number increases (relative to pure laminar values), which are evident in Fig. 9 at $x/d < 120$ for $De = 629$ and $De = 905$, are due to transitional events which are present in the straight part of the channel. These events are probably similar to ones which nominally occur in straight pipes and channels with transitional flow. The most important events are “slugs” and “puffs” of turbulence, [1,2]. According to Stettler and Hussain [2], “slugs” originate from instability waves of entry region boundary layers, whereas “puffs” are “debris of relaminarization of fully turbulent flow induced at the entry by large disturbances or roughness (which can be an orifice, grid, disk, etc.)”. The instabilities which produce “slugs” include modified Tollmien-Schlichting waves which are often followed or accompanied by packets of small longitudinal vortices in near-wall boundary layer regions. Something similar to these events, most probably “slugs,” is speculated to be occurring quite frequently in the straight portion of our channel at $De > 400$ at locations evidenced by local Nusselt number increases with x/d relative to values for two-dimensional laminar channel flow. As mentioned earlier, these initial transitional flow events are located progressively upstream through the straight portion of the channel as the Dean number increases from 400 to 1084. These produce disturbances which then advect downstream by different distances as the Dean number changes to produce different initial conditions at the entrance of the curved portion of the channel at $x/d = 120$.

The results presented at different De in Fig. 9 are thus also important because they indicate that Dean vortex pairs are not only present in the channel at Dean numbers up to 1084, but that they also strongly influence thermal flow field behavior. As for the results at lower Dean numbers, significant differences in Nusselt numbers between the concave and convex surfaces occur for the different Dean numbers, when compared at the same x/d , in spite of (i) different transitional and turbulent flow events upstream, and (ii) different thermal and velocity conditions present at $x/d = 120$, at the inlet of the curved portion of the channel. Here, transition refers to local or global disturbances or turbulence which result in Nusselt numbers which are higher than values which exist with undisturbed laminar at the same location in the channel.

Spanwise-Averaged Nusselt Numbers at Different Dean Numbers. Some of the results from Fig. 9 are again plotted in Fig. 10, along with additional Nusselt number data sets for De of 218, 549, 709, 831, and 1084. In the top portion of Fig. 10, data measured on the concave surface for all Dean numbers are plotted together. In the bottom portion of Fig. 10, the convex surface data for all Dean numbers are plotted together.

The Nusselt number data in Fig. 10 for $De = 218$ represent pure laminar behavior in the straight portion of the channel ($0 < x/d < 120$). Here, Nu values first decrease with x/d and then become approximately constant with x/d at $x/d = 80$ –120, where values are close to 8.24. As mentioned, this Nusselt number is the expected value for fully developed flow in a straight channel with infinite aspect ratio and constant heat flux boundary conditions. As mentioned earlier, Dean vortex pairs form soon after the flow enters the channel at x/d just greater than 120. Near the downstream end of the channel, the Dean vortex pairs at $De = 218$ then develop the twisting secondary instability, [20], which causes Nusselt numbers from the concave surface to increase as x/d in-

creases from 180 to 204. Convex surface Nusselt numbers at these locations, on the other hand, are relatively unaffected by the twisting instability at this experimental condition.

Figure 10 shows that additional important Nusselt number increases with x/d occur at smaller x/d as the Dean number increases from 549 to 1084. In contrast to the Nusselt number variations from twisting, these changes occur in the straight portion of the channel and affect both channel surfaces. Such local Nusselt number increases occur as x/d increases from 36 to 84 at $De = 709$, as x/d increases from 36 to 60 at $De = 831$, as x/d increases from 12 to 60 at $De = 905$, and at x/d up to 36 at $De = 1084$. Each of these is due to transitional events, most likely local “slugs” of turbulence which originate from instability waves of entry region boundary layers, [1,2]. These cause initial heat transfer coefficient augmentations relative to pure laminar values to be located progressively upstream (at smaller x/d) as the Dean number increases.

Figure 10 also shows that Nusselt numbers on both the concave and convex channel surfaces at $De = 709$ are significantly higher than values measured at $De = 218$ and at $De = 549$, except for $x/d < 36$. This Nusselt number trend continues for $x/d < 84$ as the Dean number increases even further to 831, 905, and 1084, since Nusselt numbers continue to increase with De at each x/d within this range. Another interesting feature of the Nusselt number data in **Fig. 10** is the trend followed by the results measured in the straight portion of the channel ($0 < x/d < 120$). For each Dean number from 709 to 1084, Nusselt numbers just downstream of the transition region (i.e., $x/d > 84$ for $De = 709$, $x/d > 60$ for $De = 831$, 905, and 1084) follow a single family of curves. The curves in the family show weak dependence on Dean number, and each curve in the family has about the same slope when compared at the same x/d . This uniform x/d dependence of the curves in the family at x/d from 60–84 to 120 thus represents Nusselt number behavior for both channel surfaces in a near fully turbulent *straight* channel with developing thermal boundary layers.

As each of these flows ($De = 709$, 831, 905, and 1084) progresses through the curved portion of the channel ($120 < x/d < 240$), *concave side* Nusselt numbers in **Fig. 10** again follow a single family of curves. Here, Nusselt numbers again show uniform dependence on x/d when compared at the same x/d at all De in this range, and weak dependence on Dean number at each x/d . All of the curves thus have about the same slope when compared at the same x/d . In this case, the family of curves represents Nusselt number behavior on the concave surface in a fully turbulent (or near fully turbulent) *curved* channel with thermal boundary layers which are close to being fully developed.

Nusselt numbers measured at De equal to 709, 831, 905, and 1084 on the *convex* side of the channel in **Fig. 10** also roughly collect into a single family of curves, however, these data show different slopes at different Dean numbers when compared at the same x/d . Two distinctly different types of convex surface behavior are also apparent in **Fig. 10** for this range of Dean numbers, which are located at $120 \leq x/d < 180$, and $180 \leq x/d < 228$. For the latter region, *convex* side Nusselt numbers at different Dean numbers diverge slightly from each other as x/d becomes greater than 180.

Summary and Conclusions

Heat transfer and flow structure are described in a channel with a straight portion followed by a portion with mild curvature at Dean numbers from 100 to 1084. The channel aspect ratio is 40, radius ratio is 0.979, and the ratio of shear layer thickness to channel inner radius is 0.011. The data presented included flow visualizations, and spanwise-averaged Nusselt numbers. Also included are time-averaged turbulence structural data, time-averaged profiles of streamwise velocity, spectra of longitudinal velocity fluctuations, and a survey of the radial time-averaged vorticity component. Different flow events are observed including laminar two-dimensional flow, Dean vortex flow, wavy Dean vor-

tex flow (in both undulating and twisting modes), splitting and merging of Dean vortex pairs, transitional flow with arrays of Dean vortex pairs, and fully turbulent flow with arrays of Dean vortex pairs.

At all Dean numbers investigated from 100 to 1084, spanwise-averaged Nusselt numbers measured on the concave surface are significantly higher than values measured on the convex surface at x/d from 120 to 240 in the curved portion of the channel. Thus, Dean vortex pairs are not only present in the channel when the flow is laminar, transitional, and turbulent, but they also strongly influence thermal flow field behavior. Overall Nusselt number variations with De and x/d also suggest that the thermal boundary layers responsible for the Nusselt number variations are dependent upon upstream initial conditions in addition to transitional disturbances and levels of turbulence intensity very near the measurement location.

At De up to 300, the phenomena most responsible for the higher concave Nusselt numbers are (i) vortex pair secondary flows, and (ii) unsteadiness. Both of these result from the initial development of Dean vortex pairs near the concave surface in the form of tiny Gortler-like vortices whose spanwise wavelength selection mechanisms and growth rates are very receptive to small departures from ideal flow conditions and to disturbances in the oncoming stream.

As De become greater than 150, significant Nusselt number increases are present on the concave and convex surfaces in the downstream part of the curved channel segment at $x/d > 158$. After this initial increase, concave surface Nusselt numbers at a particular streamwise station continue to increase with Dean number by important amounts, whereas convex Nu values do not. This is due to the twisting wavy secondary instability, which, with the unsteady events caused by it, play important roles in augmenting local thermal transport levels.

At each Dean number investigated from 500 to 1084, important Nusselt number increases with x/d occur in the straight portion of the channel at each Dean number due to laminar-to-turbulent transitional phenomena. The Nusselt number increases are believed to be due to local transitional “slugs” or “puffs” of turbulence, [1,2], which cause initial Nusselt number augmentations relative to pure laminar values to be located progressively upstream as the Dean number increases.

Downstream of these events, flow is turbulent or near-fully turbulent at De from 500 to 1084, and Nusselt numbers in the straight portion of the channel at x/d from 0 to 120, and in the curved portion of the channel ($120 < x/d < 240$), collect into a single families of curves. These Nusselt number data thus represent fully turbulent or near fully turbulent *straight* channel flow and *curved* channel flow with thermal boundary layers which are close to being fully developed.

Acknowledgments

A number of other individuals participated in the research efforts which led to the results which are presented in this paper, including S. Choi, J. E. Longest, M. R. Kendall, W. A. Fields, S. J. Fuqua, A. R. Schallert, and P. Skogerboe.

This work was sponsored by the Propulsion Directorate, U.S. Army Aviation Research and Technology Activity-AVSCOM, through NASA-Defense Purchase Requests C-80019-F and C-30030-P. The program monitor was Mr. Kestutis Civinskas. Additional information is provided in Refs. [33] and [34].

Nomenclature

- A_{ch} = cross-sectional area of the channel
- b = spanwise width of heated test surface
- C_p = specific heat at constant pressure of air
- d = channel thickness
- De = Dean number, $(\bar{U}d/\nu)(d/r_i)^{0.5}$
- D_H = hydraulic diameter

f = nondimensional oscillation frequency
 h = spanwise-averaged heat transfer coefficient, $\dot{q}_{\text{conv}}''/(t_w - t_m)$
 k = thermal conductivity
 \dot{m} = mass flow rate of air in channel
 n = dimensional oscillation frequency
 Nu = spanwise-averaged Nusselt number, hD_H/k
 Pr = Prandtl number
 \dot{q}_{conv}'' = convective heat flux from test surface
 Re = Reynolds number, $\bar{U}d/\nu$
 r_i = radius of convex or inner channel surface
 t = time-averaged local temperature
 t_m = time-averaged mixed-mean temperature
 $t_{m-\text{inlet}}$ = time-averaged mixed mean temperature at channel entrance
 t_w = time-averaged local wall temperature
 u_θ = local streamwise velocity
 u' = fluctuating component of local streamwise velocity
 u^+ = nondimensional local streamwise velocity, u_θ/u_τ
 u_τ = friction velocity
 \bar{U} = spatially averaged bulk mean velocity
 x = streamwise distance from location where heating begins
 X = streamwise distance from channel inlet at nozzle exit
 Y = distance normal from the concave channel surface
 y^+ = nondimensional distance from concave surface, Yu_τ/ν
 Z = spanwise distance from channel spanwise centerline

Greek

ν = kinematic viscosity
 θ = angular position along curved portion of the channel
 Δx = streamwise distance from the beginning of heating to the streamwise location of interest
 ω_r = normal or radial component of time-averaged vorticity

Superscript

$-$ = time-averaged value

References

- Ligrani, P. M., Subramanian, C. S., Coumes, T. M., Greco, F. J., Koth, H., and Longest, J. M., 1992, "Study of the Imposition of Bulk Flow Pulsations on Plane Channel Flow at Moderate Stokes Numbers," *Exp. Therm. Fluid Sci.*, **5**, pp. 145–161.
- Stettler, J. C., and Hussain, A. K. M. F., 1986, "On Transition of the Pulsatile Pipe Flow," *J. Fluid Mech.*, **170**, pp. 169–197.
- Dean, W. R., 1928, "Fluid Motion in a Curved Channel," *Proc. R. Soc. London, Ser. A*, **121**, pp. 402–420.
- Brewster, D. B., Grosberg, P., and Nissan, A. H., 1959, "The Stability of Viscous Flow Between Horizontal Concentric Cylinders," *Proc. R. Soc. London, Ser. A*, **251**, pp. 76–91.
- Ligrani, P. M., and Niver, R. D., 1988, "Flow Visualization of Dean Vortices in a Curved Channel With 40 to 1 Aspect Ratio," *Phys. Fluids*, **31**, pp. 3605–3617.
- Cheng, K. C., and Akiyama, M., 1970, "Laminar Forced Convection Heat Transfer in Curved Rectangular Channels," *Int. J. Heat Mass Transfer*, **13**, pp. 471–490.
- Mori, Y., Uchida, Y., and Ukon, T., 1971, "Forced Convective Heat Transfer in a Curved Channel With a Square Cross Section," *Int. J. Heat Mass Transfer*, **14**, pp. 1787–1805.
- Yee, G., Chilukuri, R., and Humphrey, J. A. C., 1980, "Developing Flow and Heat Transfer in Strongly Curved Ducts of Rectangular Cross Section," *ASME J. Heat Transfer*, **102**, pp. 285–291.
- Chilukuri, R., and Humphrey, J. A. C., 1981, "Numerical Computation of Buoyancy Induced Recirculation in Curved Square Duct Laminar Flow," *Int. J. Heat Mass Transfer*, **24**, pp. 305–314.
- Komiyama, Y., 1984, "Laminar Forced Convection Heat Transfer in Curved Channels of Rectangular Cross Section," *Trans. Jpn. Soc. Mech. Eng., Ser. B*, **50**(450), pp. 424–434.
- Kobayashi, M., Maekawa, H., Takano, T., and Kobayashi, M., 1994, "Experimental Study of Turbulent Heat Transfer in a Two-Dimensional Curved Channel (Time-Mean Temperature and Multiple Temperature/Velocity Correlations in the Entrance Section)," *JSME International Journal, Series B: Fluids and Thermal Engineering*, **37**(3), pp. 545–553.
- Kobayashi, M., Maekawa, H., Shimizu, Y., and Uchiyama, K., 1992, "Experimental Study on Turbulent Flow in Two-Dimensional Curved Channel (Space/Time Correlations and Spectra of Velocity Fluctuations)," *JSME International Journal, Series B: Fluids and Thermal Engineering*, **37**(1), pp. 38–46.
- Su, M. D., and Friedrich, R., 1994, "Numerical Simulation of Fully Developed Flow in a Curved Duct of Rectangular Cross Section," *Int. J. Heat Mass Transfer*, **37**(8), pp. 1257–1268.
- Joye, D. D., 1994, "Optimum Aspect Ratio for Heat Transfer Enhancement in Curved Rectangular Channels," *Heat Transfer Eng.*, **15**(2), pp. 32–38.
- Lorenz, S., Nachtigall, C., and Leiner, W., 1996, "Permanent Three-Dimensional Patterns in Turbulent Flows With Essentially Two-Dimensional Wall Configurations," *Int. J. Heat Mass Transfer*, **39**(2), pp. 373–382.
- Mochizuki, S., Murata, A., and Fukunaga, M., 1995, "Effects of Rib Arrangements on Pressure Drop and Heat Transfer in a Rib-Roughened Channel With a Sharp 180 deg Turn," *ASME Paper No. 95-CTP-3*.
- Fusegi, T., 1995, "Turbulent Flow Calculations of Mixed Convection in a Periodically Ribbed Channel," *Journal of Enhanced Heat Transfer*, **2**(4), pp. 295–305.
- Ligrani, P. M., Choi, S., Schallert, A. R., and Skogerboe, P. E., 1996, "Effects of Dean Vortex Pairs on Surface Heat Transfer in Curved Channel Flow," *Int. J. Heat Mass Transfer*, **39**(1), pp. 27–37.
- Ligrani, P. M., Longest, J. E., Kendall, M. R., and Fields, W. A., 1994, "Splitting, Merging and Spanwise Wavenumber Selection of Dean Vortex Pairs," *Exp. Fluids*, **18**(1), pp. 41–58.
- Ligrani, P. M., Finlay, W. H., Fields, W. A., Fuqua, S. J., and Subramanian, C. S., 1992, "Features of Wavy Vortices in a Curved Channel From Experimental and Numerical Studies," *Phys. Fluids A*, **4**(4), pp. 695–709.
- Hedlund, C. R., and Ligrani, P. M., 1998, "Heat Transfer in Curved and Straight Channels With Transitional Flow," *Int. J. Heat Mass Transfer*, **41**(3), pp. 563–573.
- Hedlund, C. R., 1996, "Effects of Transition to Turbulence and Dean Vortex Pairs on Surface Heat Transfer in Curved and Straight Channels at Moderate and High Dean Numbers," M.S. thesis, Department of Mechanical Engineering, University of Utah, Salt Lake City, UT.
- Ligrani, P. M., Singer, B. A., and Baun, L. R., 1989, "Miniature Five-Hole Pressure Probe for Measurement of Mean Velocity Components in Low Speed Flows," *J. Phys. E*, **22**(10), pp. 868–876.
- Ligrani, P. M., Singer, B. A., and Baun, L. R., 1989, "Spatial Resolution and Downwash Velocity Corrections for Multiple-Hole Pressure Probes in Complex Flows," *Exp. Fluids*, **7**(6), pp. 424–426.
- Ligrani, P. M., and Bradshaw, P., 1987, "Subminiature Hot-Wire Sensors: Development and Use," *J. Phys. E*, **20**, pp. 323–332.
- Kline, S. J., and McClintock, F. A., 1953, "Describing Uncertainties in Single Sample Experiments," *Mech. Eng. (Am. Soc. Mech. Eng.)*, **75**, pp. 3–8.
- Moffat, R. J., 1988, "Describing the Uncertainties in Experimental Results," *Exp. Therm. Fluid Sci.*, **1**(1), pp. 3–17.
- Bippes, H., 1978, "Experimental Study of the Laminar-Turbulent Transition of a Concave Wall in a Parallel Flow," *NASA Tech. Memo.*, **75243**, pp. 1–69.
- McCormack, P. D., Welker, H., and Kelleher, M. D., 1970, "Taylor-Görtler Vortices and Their Effect on Heat Transfer," *ASME J. Heat Transfer*, **92**, pp. 191–112.
- Subramanian, C. S., Ligrani, P. M., and Tuzzolo, M. F., 1992, "Surface Heat Transfer and Flow Properties of Vortex Arrays Induced Artificially and From Centrifugal Instabilities," *Int. J. Heat Fluid Flow*, **13**(3), pp. 210–223.
- Botto, A., 1993, "On Longitudinal Vortices in Curved Channel Flow," *J. Fluid Mech.*, **251**, pp. 627–660.
- Guo, Y., and Finlay, W. H., 1991, "Splitting, Merging and Wavelength Selection of Vortices in Curved and/or Rotating Channel Flow due to Eckhaus Instability," *J. Fluid Mech.*, **228**, pp. 661–695.
- Ligrani, P. M., 1994, "A Study of Dean Vortex Development and Structure in a Curved Rectangular Channel With Aspect Ratio of 40 at Dean Numbers Up to 430," *NASA Contractor Report 4607*, Army Research Laboratory Contractor Report ARL-CR-144.
- Ligrani, P. M., 1996, "A Study of Heat Transfer in a Curved Rectangular Channel Including the Effects of Dean Vortex Pairs and Transition to Turbulent Flow," Department of Mechanical Engineering Report, University of Utah, Salt Lake City, UT.
- Ligrani, P. M., and Choi, S., 1996, "Mixed Convection in Straight and Curved Channels With Buoyancy Orthogonal to the Forced Flow," *Int. J. Heat Mass Transfer*, **39**(12), pp. 2473–2484.

Intermittency Transport Modeling of Separated Flow Transition

J. Vicedo¹

S. Vilmin²

W. N. Dawes

A. M. Savill³

CFD Laboratory,
Engineering Department,
University of Cambridge,
Cambridge, UK

An intermittency transport model is proposed for modeling separated-flow transition. The model is based on earlier work on prediction of attached flow bypass transition and is applied for the first time to model transition in a separation bubble at various degrees of freestream turbulence. The model has been developed so that it takes into account the entrainment of the surrounding fluid. Experimental investigations suggest that it is this phenomena which ultimately determines the extent of the separation bubble. Transition onset is determined via a boundary layer correlation based on momentum thickness at the point of separation. The intermittent flow characteristic of the transition process is modeled via an intermittency transport equation. This accounts for both normal and streamwise variation of intermittency and hence models the entrainment of surrounding flow in a more accurate manner than alternative prescribed intermittency models. The model has been validated against the well-established T3L semicircular leading edge flat plate test case for three different degrees of freestream turbulence characteristic of turbomachinery blade applications. [DOI: 10.1115/1.1748393]

Introduction

The proper prediction of the laminar-to-turbulent transition process is one of the most challenging and important problems hindering the development of more accurate computational tools. In fact, determining the state of the flow is of paramount importance if modeling complex flow for blade design optimization is to be achieved.

Transition is characterized by the eruption of turbulent spots first recorded by Emmons [1]. Subsequent studies have highlighted the intermittent behavior of the flow across the transition region. The concept of intermittency, as a measure of the probability of a given point to be inside the turbulent region, has evolved from the need to distinguish between uniform and random behavior of the flow along this intermittent region. The widely accepted function describing the streamwise evolution of the intermittency factor proposed by Dhawan and Narasimha [2] has led to the foundation of an extensive field of research in the field of transition modeling.

Various correlation methods accounting for the different parameters of the flow have been developed to account for the extent and form of the flow inside this region as reviewed by Dhawan and Narashima [2].

Despite performing in a wide range of flow types with various degrees of success, these methods are often restricted to the narrow range of flows which comply with the assumptions under which these were derived. The latter has motivated the search for alternative techniques to account for the intermittent nature of a transitional flow which may account for more of the physics involved and at the same time share enough degree of universality as to comply with the requirements posed by current aerodynamic design tools.

Thus, a transport equation for the intermittency is proposed in this study. It is based on the intermittency transport equations by Byggstøyl and Köllmann [3], Cho and Chung [4,5], and Savill [6,7]. The intermittency is not prescribed as a constant over a streamwise profile. Also, the application to three-dimensional flow

simulation is convenient. The mathematical formulation of the equation, and its coupling with a two-equation turbulence model is presented in the first part of the paper.

To illustrate its capabilities, the validation against a transitional bubble test case has been conducted. Such transitional flow is common in gas turbines as discussed by both Mayle [8] and Walker [9] and may occur in an overspeed region near an airfoil's leading edge as observed by Sommers [10].

Mathematical Model

Transition Model. The choice of transition model was motivated by the need to fulfill the three numerical requirements, namely, no use of normal-to-wall distance, simple source terms and straightforward boundary conditions as summarized by Katlitzin et al. [11]. The purpose of such an approach was to develop a method that could be applied to a wider range of test cases and could be extended to the prediction of three-dimensional geometries. Such approach is in clear contrast with most of the present correlation methods often restricted to two-dimensional geometries and dependent on flow parameters that make their application restricted to similar cases to those from which were initially derived.

Given the importance manifested by the intermittent effect of the flow at the outer portion of the boundary layer, the present work adopted a differential model for the intermittency factor. These tackle the problem of modeling the intermittency factor in the flow equations themselves. Two major arguments support the use of such approach. First, it allows the modeling of unbounded intermittent flows such as free-shear layers such as those encountered in separation bubbles and confluent wakes. Second, three-dimensional extension of the model does only require the computation of additional derivatives and is not restricted as correlations are.

The present study adopted a combination of earlier modeling approaches by Byggstøyl and Köllmann [2,12,13], Cho and Chung [4,5], and Savill [6,7]. Byggstøyl and Köllmann derived an intermittency transport equation which was coupled with conditioned Navier-Stokes equations and was used to compute free-shear wakes. Based on this work Cho and Chung presented an integrated high Reynolds $k-\varepsilon-\gamma$ approach which removed the conditioning and was successfully used to predict far wake turbulence and various jet flows. Savill [6] was the first to extend similar approaches to predict boundary layer transition by cou-

¹Present address: EADS, 16 Boulevard de Montmorency, 75016 Paris, France.

²Present address: Numeca, 5 Avenue Franklin Roosevelt, 1180 Brussels, Belgium.

³Chair of Computational Aerodynamics Design, Department of Aerospace Sciences, School of Engineering, Cranfield University, Cranfield MK43 0AL, UK.

Contributed by the International Gas Turbine Institute and presented at the International Gas Turbine and Aeroengine Congress and Exhibition, Atlanta, GA, June 16–19, 2003. Manuscript received by the IGTI Dec. 2002; final revision Mar. 2003. Paper No. 2003-GT-38719. Review Chair: H. R. Simmons.

pling it to a low-Re Reynolds stress model to model transition on a flat plate at various degrees of freestream turbulence.

The present departs from the exact intermittency transport equation in its form firstly derived by Dopazo [14]

$$\frac{\partial \gamma}{\partial t} + u_j \frac{\partial \gamma}{\partial x_j} = D_\gamma + S_\gamma \quad (1)$$

where D_γ represents the diffusion due to the relative motion of turbulent and nonturbulent zones and S_γ the combination of various terms determining the generation and destruction of intermittency across the interface.

The form adopted for the diffusion term kept the original form proposed by Byggstøyl and Kollmann [12]

$$D_\gamma = \frac{\partial}{\partial x_j} \left[\left(\nu_t + (1 - \gamma) \frac{\nu_t}{\sigma_\gamma} \right) \frac{\partial \gamma}{\partial x_j} \right] \quad (2)$$

based on the velocity jump model of Lumley [15].

Modeling of the source term S_γ required more detailed considerations with regard to the various factors determining the growth of intermittency across the transition region. The variation of intermittency across turbulent/non-turbulent interface was recast as the result of four major contributions

$$S_\gamma = S_\gamma^{(1)} + S_\gamma^{(2)} + S_\gamma^{(3)} + S_\gamma^{(4)} \quad (3)$$

The first term was modeled such as to account for the production of intermittency as proportional to the increase in turbulent kinetic energy while fulfilling the boundary condition, $0 < \gamma < 1$. The original form of the term was retained, reading

$$S_\gamma^{(1)} = C_{\gamma 1} \gamma (1 - \gamma) \frac{P_k}{k} \quad (4)$$

The second term in Eq. (3) was modeled to reflect the transport of mass and momentum caused by spatial inhomogeneity as discussed by Byggstøyl and Kollmann [12]. The present work adopted a modified form of the term proposed such that

$$S_\gamma^{(2)} = C_{\gamma 2} \gamma \frac{k^2}{\varepsilon} \frac{\partial \gamma}{\partial x_i} \frac{\partial \gamma}{\partial x_i} \quad (5)$$

Such modification was adopted in light of the extensive experimental studies on both boundary layer transition and edge intermittency effects suggesting that the inhomogeneity of the flow becomes more influential as the flow enters the turbulent state.

The dissipation of intermittency is accounted for by the third term, $S_\gamma^{(3)}$, which kept the form proposed by Byggstøyl and Kollmann which reads

$$S_\gamma^{(3)} = -C_{\gamma 3} \gamma (1 - \gamma) \frac{\varepsilon}{k} \quad (6)$$

in order to account for decaying homogeneous turbulence not maintained by external flow or boundary conditions.

The last term on the right-hand side of Eq. 3 was introduced based on the model of Cho and Chung [4] to account for the entrainment effect. The rate of entrainment is not dependent on the magnitude of the fluid viscosity. Thus, it is plausible to believe that the overall rate of entrainment is set by large-scale parameters of the flow. This term read

$$S_\gamma^{(4)} = -C_{\gamma 4} \gamma (1 - \gamma) \frac{\varepsilon}{k} \Gamma \quad (7)$$

where the intermittency interaction invariant, Γ , read

$$\Gamma \equiv \frac{k^{5/2}}{\varepsilon} \frac{u_i}{|\mathbf{u}|} \frac{\partial u_i}{\partial x_j} \frac{\partial \gamma}{\partial x_j} \quad (8)$$

The modeling of this term is of special concern for the prediction of separation bubbles. As argued by Roberts, in a discussion

of Mayle's work, [8], it is the entrainment process that ultimately determines the size of boundary layer separation bubbles.

The resulting transport equation for the intermittency factor thus reads

$$\begin{aligned} \frac{D\gamma}{Dt} = \frac{\partial}{\partial x_j} \left[\left(\nu_t + (1 - \gamma) \frac{\nu_t}{\sigma_\gamma} \right) \frac{\partial \gamma}{\partial x_j} \right] + C_{\gamma 1} \gamma (1 - \gamma) \frac{P_k}{k} \\ + C_{\gamma 2} \gamma \frac{k^2}{\varepsilon} \frac{\partial \gamma}{\partial x_i} \frac{\partial \gamma}{\partial x_i} - C_{\gamma 3} \gamma (1 - \gamma) \frac{\varepsilon}{k} - C_{\gamma 4} \gamma (1 - \gamma) \frac{\varepsilon}{k} \Gamma \end{aligned} \quad (9)$$

The transport equation could easily be introduced in the two-equation turbulence model framework by employing a conditioned eddy viscosity formulation as suggested by Simon and Stephens [16]. Thus, the effective eddy viscosity was defined as

$$\mu_t = \gamma \mu_t^* \quad (10)$$

where μ_t^* represents the eddy viscosity calculated from the base two-equation turbulence model employed.

As pointed out by Cho and Chung [5], indications suggest that the rate of dissipation at a point must be dependent on the intermittency. Such view is supported by those of Rodi and Scheuerer [17] with regard to the overpredicted skin friction values achieved by current two-equation models under adverse pressure gradient flows. These arguments motivated the introduction of an additional term into the dissipation rate equation with the form

$$S_\varepsilon = C_{\varepsilon 3} \Gamma \quad (11)$$

where the new defined constant had a value of $C_{\varepsilon 3} = 0.10$. The dependency of the additional source term on Γ is appropriate as its form suggests that its influence will be confined to regions with acceleration.

Finally, the model constants were defined as

$$C_{\gamma 1} = 1.60, \quad C_{\gamma 2} = 0.15, \quad C_{\gamma 3} = 0.10, \quad C_{\gamma 4} = 0.16, \quad \sigma_\gamma = 1.0 \quad (12)$$

based on those values derived by Savill [6].

Transition-Onset Location. Under high levels of freestream disturbances, the increased receptivity of the flow to these external perturbations at the separation point results in the failure of attached-flow correlations such as those of Dhawan and Narasimha [2], Abu-Ghannam and Shaw [18] Solomon et al. [19], and Mayle's, [8], attached-flow correlation. This is mostly due to the fact that the growth of these disturbances in the separated shear layer is not accounted for by any of these correlations.

Mayle [8] proposed, after gathering data from extensive experimental investigations on separation bubbles, the start of transition to be determined by

$$x_{st} \approx x_s + A \text{Re}_{\theta_s}^{0.7} \frac{\theta_s}{\text{Re}_{\theta_s}} \quad (13)$$

where the subscript s denotes separated flow conditions and θ and Re_θ denote momentum thickness and momentum thickness Reynolds number, respectively. In the present context, separation was detected once the pressure gradient parameter had reached the value of $\lambda_{\theta_s} = -0.082$. In the present study the constant A takes values of 300 suggested by Mayle [8].

Baseline Turbulence Model. The k - ε model of Yang and Shih [20] was chosen as baseline turbulence models following earlier assessment of the model by Vicedo [21]. The consistency of the model in freestream regions and the use of the Kolmogorov scale close to the wall, together with the implications of a unique well-behaved wall function and well-posed boundary conditions

were decisive factors for the choice of the model as baseline for the present work.

The addition of an upper bound for the turbulent time-scale based on the work by Durbin [22] was found necessary to avoid the overproduction of turbulent kinetic energy in stagnation regions such as those encountered at the leading edge of an airfoil.

The methodology used during the present investigation forced the eddy viscosity, μ_t , to be zero in regions inside the boundary layer where the flow was laminar. All source terms in the turbulence model and the intermittency transport equation were therefore multiplied by an indicator function, $I(x,y)$, such that $I=0$ in a laminar region and $I=1$ otherwise. Convection and diffusion terms were implemented without modifications to allow the turbulent quantities to convect and diffuse through the laminar region.

The final form of the model read

$$\frac{D}{Dt}(\rho k) = \frac{\partial}{\partial x_j} \left[\left(\mu_l + \frac{\mu_t}{\sigma_k} \right) \frac{\partial k}{\partial x_j} \right] + (P_k - \rho \varepsilon) I$$

$$\frac{D}{Dt}(\rho \varepsilon) = \frac{\partial}{\partial x_j} \left[\left(\mu_l + \frac{\mu_t}{\sigma_\varepsilon} \right) \frac{\partial \varepsilon}{\partial x_j} \right] + \frac{C_{\varepsilon 1} P_k - C_{\varepsilon 2} \rho \varepsilon}{T_t} I$$

with the eddy viscosity

$$\mu_t = \rho C_\mu f_\mu k T_t \gamma.$$

The time scale formulation follows the form proposed by Yang and Shih [20]. A bound is imposed based on the derivation by Durbin [22]

$$T_t = \frac{k}{\varepsilon} + \sqrt{\frac{\nu_l}{\varepsilon}} \leq \frac{2}{3} \frac{1}{C_\mu f_\mu \sqrt{2|\mathbf{S}|^2}}. \quad (17)$$

The reason behind this limiting value lies in the fact that it is common to come across unrealistic prediction of turbulent kinetic energy in stagnation points. This may result in leading-edge laminar flows to be predicted as turbulent with the consequent wrong estimation (if any) of the appearance of separation bubbles.

The wall function, f_μ , is given as a function of $Re = k^{1/2} y / \nu_l$

$$f_\mu = \sqrt{1 - \exp(-a_1 Re_y - a_2 Re_y^2 - Re_y^3)} \quad (18)$$

with $a_1 = 1.5 \times 10^{-4}$, $a_2 = 5.0 \times 10^{-7}$, and $a_3 = 1.0 \times 10^{-10}$. The dependency of the model on wall distance can be removed by employing $Re_y = k/S\nu_l$ and $a_1 = 3.0 \times 10^{-4}$, $a_2 = 6.0 \times 10^{-5}$ and $a_3 = 2.0 \times 10^{-6}$ as suggested by Yang and Shih [20].

Finally, the constants of the model read

$$C_\mu = 0.09, \quad C_{\varepsilon 1} = 1.44, \quad C_{\varepsilon 2} = 1.92, \quad \sigma_k = 1.0, \quad \sigma_\varepsilon = 1.3. \quad (19)$$

Computational Scheme

The CFD code NEWT developed by Dawes [23] was used to solve the equations of motion. In NEWT, equations are discretized in finite volume form on tetrahedral control volumes. Vertex-based storage is used and spatial discretization of the governing equations is achieved by means of a central differencing scheme which renders a system of equations in which the primary variables are assumed to have a linear variation over cell faces between vertices.

A four-stage Runge-Kutta method is employed to integrate the equations to a steady state solution and, to reduce the computational cost, viscous and artificial dissipation terms are frozen at the start of each time level. The time step is computed locally based on the maximum eigenvalues of the convective and diffusive operators.

The use of a pseudo-Laplacian form for the artificial dissipation operator has proved to be successful for a wide range of flows calculated in the framework of unstructured meshes as reflected by the work of Watterson [24]. It is nevertheless true that the

validity of such approach is restricted to meshes of equilateral tetrahedra and spurious numerical behavior may take place during the solution procedure in near-wall regions where highly stretched cells are often defined. Moreover, in near-wall regions, the strength of the fourth-order operator can be higher in magnitude than the physical viscous terms and affect the global convergence of the time-marching solution method.

To tackle these problems a directional scaling approach was adopted based on the work of Vilmin [25] on the same computational solver. Local stretching vectors are constructed locally at each node in the solution domain based on the skewness characteristics of the mesh.

Results and Discussion

Description of Test Case. The test case belongs to the battery of experiments performed within the ERCOFTAC Special Interest Group (SIG) on Transition (see Savill [26,27]) performed by Rolls-Royce Plc. (see Coupland [28]). The geometry employed is depicted in **Fig. 1** which sketches the semicircular leading-edge flat plate tested on the Rolls-Royce Applied Science Laboratory (RRASL) wind tunnel.

Reynolds number based on leading-edge diameter and freestream velocity were fixed to $Re = 3293$ and $U_0 = 5$ m/s, respectively, while the different freestream turbulence values measured at 6 mm from the leading edge are listed in **Table 1**. Following preliminary mesh refinement studies, the flow was computed on a mesh composed by 32,000 nodes and 64,000 cells with an average density of 30 nodes across the boundary layer with the first node laying at $y^+ < 1$.

The different results reported herein correspond to the three different models employed during the study. Results labeled $k-\varepsilon$ correspond to those predictions in which no transition-prediction tool was used. The set of results labeled by $k-\varepsilon-I$ correspond to simulations in which the point-transition criterion was employed in which transition onset was determined using the Mayle separated flow transition correlation described previously. A third model, labeled $k-\varepsilon-\gamma$, was employed which coupled Mayle's transition-prediction criterion with the intermittency transport equation.

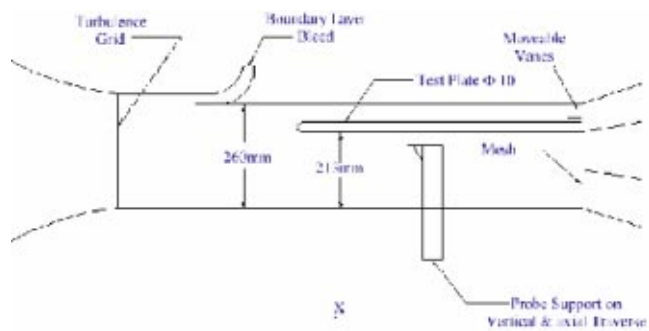


Fig. 1 RRASL wind tunnel working section and T3L model geometry

Table 1 T3L test case topology. Free stream turbulence level measured at $x = 6$ mm from leading edge.

Case	Re	$Tu_{\infty,6}(\%)$
T3LB	3293	0.63
T3LC	3293	2.39
T3LD	3293	5.34

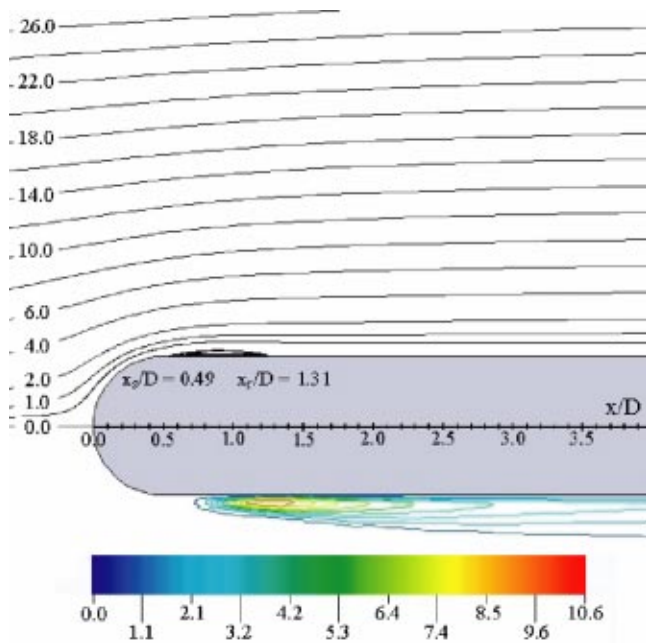


Fig. 2 Streamlines (above) and kinetic energy contours (below) for $k-\varepsilon$ transition free for $Tu_{\infty,6}=2.39\%$

Results for $Tu_{\infty,6}=2.39\%$

Streamline Patterns. Figure 2 shows the separated flow predicted by the baseline $k-\varepsilon$ model by means of streamlines and turbulence kinetic energy contours. Streamline coordinates are referred to the inlet position where the overall flow incidence is zero.

The first sign of separated flow is detected at the point at which the curved surface merges with the horizontal plate, $x_s/D=0.5$, and reattachment takes place at $x_r/D=1.31$. Despite the appearance of this separation bubble, both the point at which this initially takes place and the extent of it are not properly predicted as shall be illustrated by further comparison against experimental measurements.

Figure 3 shows the corresponding streamline pattern obtained by using the transition onset correlation proposed by Mayle. The use of such correlation resulted in transition onset being determined at $x_t/D=1.22$. This value is in clear disagreement with the value of $x_t/D=2.41$ reported by Papanicolaou and Rodi [29] who employed a different transition onset criterion based on both Re_θ and Tu_∞ on the same experiment.

As a consequence of the imposed laminarity of the flow along the boundary layer up to the point at which transition is being predicted, the turbulence generated due to the shearing effect of the separated flow takes longer to develop. Reattachment thus takes place further downstream ($x_r/D=1.65$) than with the base $k-\varepsilon$ model, resulting in a 50% increase in bubble length.

The separated flow pattern predicted by the transition model $k-\varepsilon-\gamma$ is shown in Fig. 4. Differences are visible when comparing previous results reported in Figs. 2 and 3. Despite separation and transition onset having been predicted at the same locations as when employing a point-transition criterion ($x_s/D=0.485$ and $x_t/D=1.22$, respectively), the extent of the separated flow is significantly larger. Reattachment was predicted at $x_r/D=2.43$, 66% longer with respect to the $k-\varepsilon-I$ model predictions, and three times as big as the predicted with the base $k-\varepsilon$ model.

Figure 5 shows the predicted intermittency distribution. Intermittency is, according to inlet boundary conditions, equal to unity in the freestream and, by means of the transition onset criterion used, a value of zero is specified inside the boundary layer region up to the point at which transition is predicted to take place.

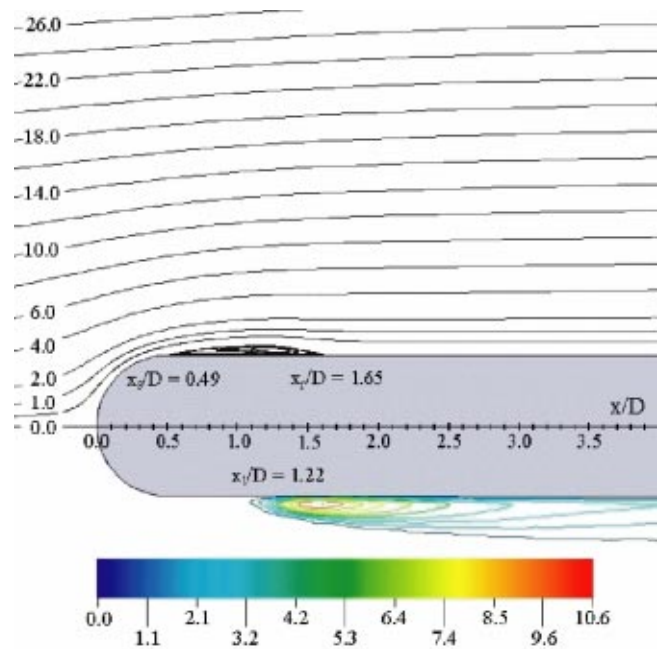


Fig. 3 Streamlines (above) and kinetic energy contours (below) for $k-\varepsilon-I$ model for $Tu_{\infty,6}=2.39\%$

Based on the available experimental data, there is no clear evidence on the location of both start and end of the transition region. There is, however, enough experimental data to suggest that the predicted values for intermittency in the recovery region is somehow underpredicted by the present model.

Despite the lack of intermittency data, Fig. 5 serves to illustrate the advantages of using the intermittency transport equation as an alternative to intermittency-prescribed models. The allowance of the model for diffusion and convection of kinetic energy from the freestream flow to the boundary layer and the varying normal

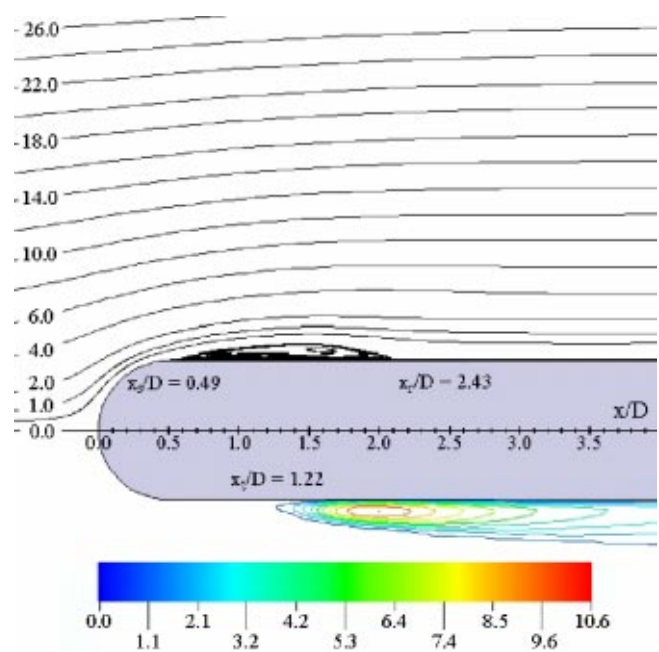


Fig. 4 Streamlines (above) and kinetic energy contours (below) for $k-\varepsilon-\gamma$ model for $Tu_{\infty,6}=2.39\%$

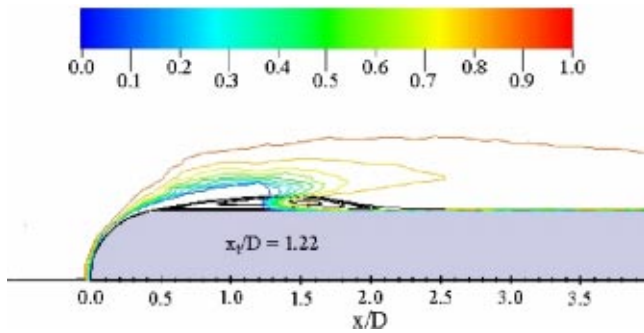


Fig. 5 Intermittency factor, γ , contours for $Tu_{\infty,6}=2.39\%$

distribution of intermittency across it are major strengths of the model and confirm the validity of the model for modeling edge intermittency as originally intended.

Additionally, streamwise development of intermittency is well accounted for, with transition length varying accordingly depending on the streamline chosen. Taking into account such effects is thought to be of utmost importance if the phenomena taking place on wake/boundary layer interactions are to be correctly modeled in the future.

The presence of intermittent flow inside the separation bubble is a common feature in separation bubbles and as shown by the predictions, such effect is accounted for by the model as opposed to other prescribed-intermittency models which do not account for normal variation of intermittency factor across the boundary layer. This has important implications with regard to the estimation of viscous losses in such types of flows as the use of a prescribed intermittency model for the present test case would have resulted in turbulent kinetic energy production being overpredicted in regions close to the computed transition onset location. This would inevitably result in improper account for entropy generation and thus in a wrong estimation of drag.

Boundary Layer Profiles. Figures 6 and 7 show a sequence of velocity profiles predicted with the three methods employed. Comparison is made against experimental measurements. Accordingly, all models predict the first signs of separation at the region where the curved surface becomes horizontal ($x=6$ mm) and a similar initial development of the separated flow ($x=8$ mm).

First significant discrepancies are observed at a streamwise location of $x=11$ mm. These are more pronounced with respect to the base $k-\epsilon$ model which denotes that the flow is already immerse in the recovery region and reaches reattachment shortly after the sequence at $x=13$ mm.

Both transition models, $k-\epsilon-I$ and $k-\epsilon-\gamma$, still predict values in agreement with experimental observations up to this stage. The width of the separated zone, however, is clearly underpredicted by the $k-\epsilon-I$ model. As a consequence earlier reattachment is predicted at $x=17$ mm.

Predictions with the $k-\epsilon-\gamma$ model, on the other hand, show a much closer agreement with the experiment. The prediction of the proper maximum width of the separation bubble results in closer agreement with the extent of the separated region. The closer agreement achieved with the transition model along the constant velocity region contrasts with the departure from experimental observations as the flow enters the pressure recovery zone and moves towards reattachment as demonstrated by measurements at $x=21$ mm and $x=23$ mm.

Integral Parameters. Skin friction values predicted with the various models are illustrated in Fig. 8 and compared against experimental calculations. Predictions for displacement thickness, δ^* , are also included.

Results confirm the behavior observed during the comparison between predicted and measured boundary layer velocity profiles.

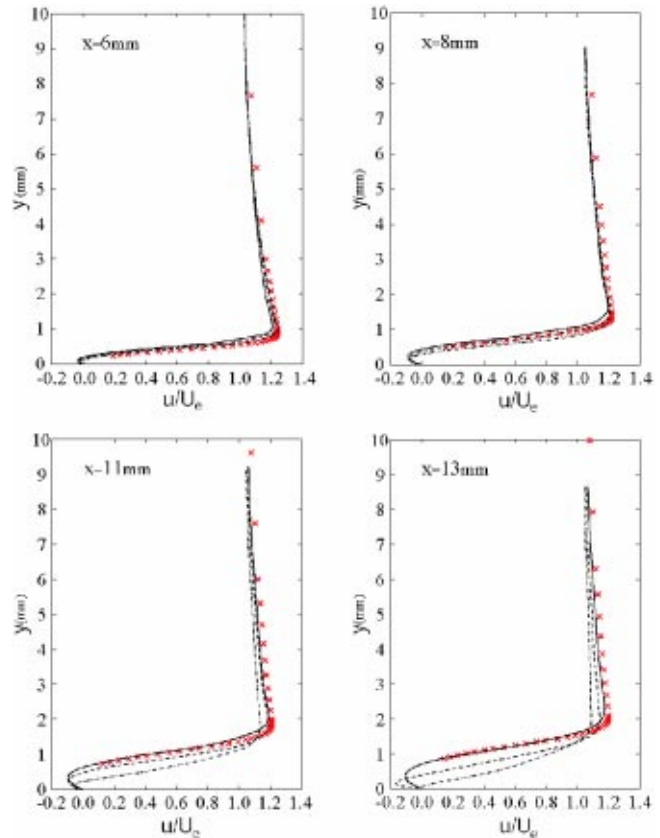


Fig. 6 Velocity profiles across the separation bubble, x experiments, --- $k-\epsilon$ model, -- $k-\epsilon-I$ model, — $k-\epsilon-\gamma$ model

The apparent overprediction of both δ^* in the separation bubble may not be so if special attention is placed on the measurement techniques employed during the experimental investigation. No negative flow measurements of the streamwise velocity were performed during data-gathering and hence experimental values should be expected higher if complete integration across the boundary layer was performed.

Results for $Tu_{\infty,6}=0.63\%$. Figure 9 shows predicted displacement thickness and skin friction values for case T3LB. Again the blockage imposed by the separation bubble is better perceived by the intermittency transport model which overpredicts measurements as expected due to the absence of reverse flow measurements.

Separation is again predicted similarly by all three models at the region where the curved surface merges with the horizontal plate, $x_s/D=0.485$. The differences in bubble extent predicted with both $k-\epsilon-I$ and $k-\epsilon-\gamma$ models are now more pronounced than in earlier cases with higher freestream turbulence levels. While reattachment is predicted at $x_r/D=1.82$ and $x_r/D=2.13$ with both $k-\epsilon$ and $k-\epsilon-I$ models, respectively, the use of the intermittency transport model, $k-\epsilon-\gamma$, significantly improves the predictions of bubble extent by predicting reattachment at $x_r/D=2.83$.

The other two models employed are shown to underpredict the width of the separation bubble, mostly as a consequence of an early prediction of flow reattachment as shown by skin friction predictions.

The close agreement of the $k-\epsilon-\gamma$ model contrasts with the results achieved by the prescribed intermittency model employed by Papanicolaou and Rodi [29]. They report predictions of reattachment at $x_r/D=2.91$ and thus overestimate the length of the separation bubble.

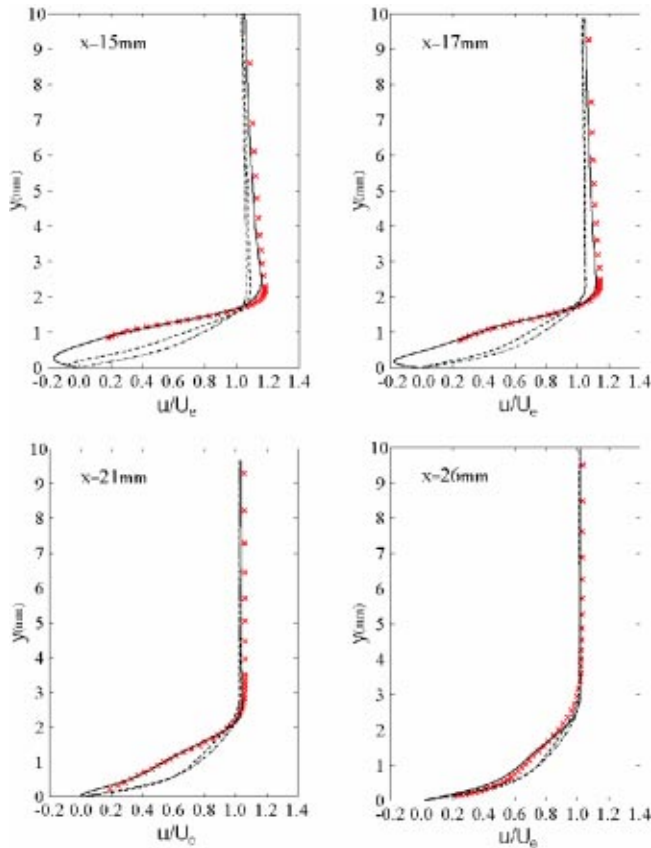


Fig. 7 Velocity profiles across the separation bubble, x experiments, \cdots $k-\epsilon$ model, $--$ $k-\epsilon-l$ model, $—$ $k-\epsilon-\gamma$ model

Reasons for improved modeling of the separated flow region can be traced to the predicted values for the intermittency factor shown by Fig. 10. The lower level of freestream turbulence results, accordingly, in a slower evolution of the intermittency factor along the transition region inside the separation bubble and across the viscous/inviscid interface. By comparing such predictions with those achieved for case T3LC, the capabilities of the intermittency transport equation for accounting for the influence of free-stream turbulence on the process of transition are thus manifested.

Results for $Tu_{\infty,6}=5.34\%$. Figure 11 shows intermittency contour plots for case T3LD. Transition is predicted to take place

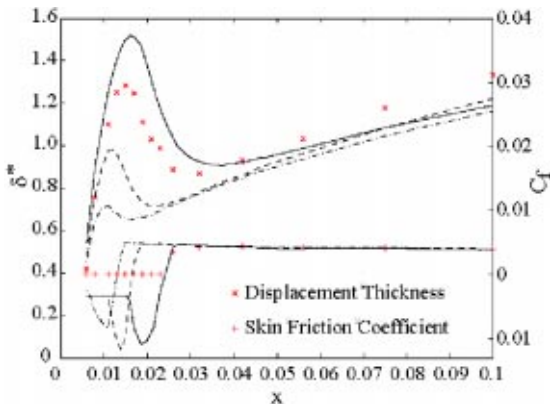


Fig. 8 Comparison of displacement thickness and skin friction predictions with experimental measurements for $Tu_{\infty,6}=2.39\%$: \cdots $k-\epsilon$ model, $--$ $k-\epsilon-l$ model, $—$ $k-\epsilon-\gamma$ model

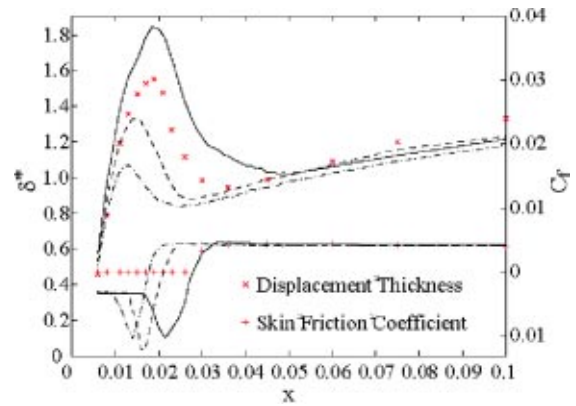


Fig. 9 Comparison of displacement thickness and skin friction predictions with experimental measurements for $Tu_{\infty,6}=0.63\%$: \cdots $k-\epsilon$ model, $--$ $k-\epsilon-l$ model, $—$ $k-\epsilon-\gamma$ model

at $x_t/D=1.18$, at a location close to that reported for lower freestream turbulence levels. This places some concern on the validity of a transition onset criterion independent of freestream turbulence levels for the present study.

Regarding the evolution of intermittency across the transition region, this is predicted to evolve more rapidly, as expected, for an increased freestream turbulence level. The turbulent kinetic energy diffused across the boundary layer edge results in intermittency increasing more rapidly in this region, while a stronger shearing effect results in transition taking place rapidly inside the separation bubble.

Again, the decrease in intermittency growth rate as the recovery stage takes place manifests as an ambiguous feature of the model. Despite the increased intermittency growth expected for such levels of freestream turbulence, transition is still predicted to reach a stage near completion at which the intermittency factor experiences a lower growth than should initially be expected.

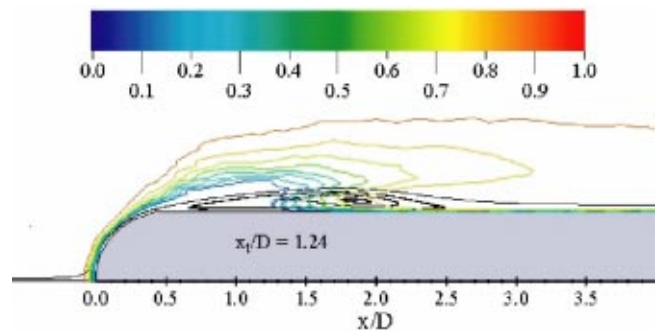


Fig. 10 Intermittency factor, γ , contours for $Tu_{\infty,6}=0.63\%$

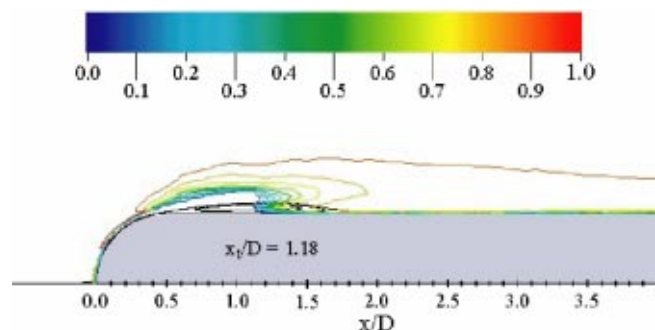


Fig. 11 Intermittency factor, γ , contours for $Tu_{\infty,6}=5.34\%$

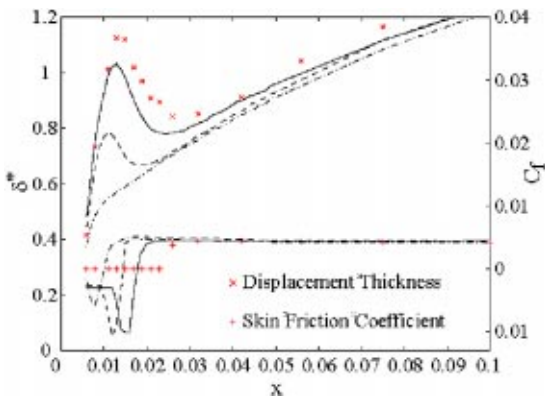


Fig. 12 Comparison of displacement thickness and skin friction predictions with experimental measurements for $Tu_{\infty,6} = 5.34\%$: \cdots $k-\epsilon$ model, $--$ $k-\epsilon-I$ model, $—$ $k-\epsilon-\gamma$ model

The presence of higher turbulence intensity in the free-stream results in shorter separated flow regions. **Figure 12** shows the predicted displacement thickness and skin friction values. The differences in bubble extent are now not as pronounced as with lower levels of turbulence. There is, however, noticeable agreement on the predictions with the $k-\epsilon-\gamma$ model of the displacement effect due to the presence of the separated flow and marked differences from those achieved with the other models.

The base $k-\epsilon$ model barely predicts any blockage effect caused by the separation bubble, and the use of a transition onset criterion such as the one employed by the $k-\epsilon-I$ model, although improving predictions, still does not model correctly the displacement induced on the flow by the presence of a separation bubble. The use of the intermittency transport equation in the $k-\epsilon-\gamma$ model enables predictions to bear a closer resemblance with experimental observations and predicts reattachment at $x_r/D = 2.12$.

Conclusions

The object of the present study was to test the ability of the proposed model to predict the effect of variable intensity, freestream turbulence on the initial development and subsequent transition to turbulence of a laminar boundary layer undergoing separation.

Results for various moderate levels of freestream turbulence have illustrated the improved results achieved in the prediction of these type of complex flows. The closer resemblance of the results achieved with the intermittency transport model have shown that modeling the intermittent behavior of such complex flows leads to improved predictions than when transition is specified by using a point-transition criterion.

For higher freestream turbulence levels the validity of the transition onset criterion has been put into evidence with regard to the inability to predict sufficient upstream displacement of transition onset with increasing freestream turbulence as argued by Walker [9]. Results with the modified intermittency model have nevertheless shown improved capabilities with regard to predicting the extent of the separation bubble.

With regard to the use of the intermittency transport model as opposed to production term modifications and prescribed models, the $k-\epsilon-\gamma$ model has shown an improved performance when predicting separation-bubble parameters when compared to earlier work on the same test case. The differences underlining both approaches suggest that the allowance of the intermittency model for the diffusion of freestream turbulence into the boundary layer by means of modeling the entrainment process is the reason behind the improvements achieved.

Results have also served to confirm the views posed by Roberts (Mayle [8]) with regard to the entrainment process being the one phenomenon determining the extent of boundary layer separation

bubbles. This has further assessed the validity of the form of the term modeling this phenomenon adopted for modeling this process in the intermittency transport equation.

Acknowledgments

This work was done as part of an EPSRC/BAE SYSTEMS CASE award. The authors would like to express their most profound gratitude to both Mr. Alan Gould from BAE SYSTEMS and Dr. John Coupland from Rolls Royce for their support and contribution throughout the entire length of the research.

Nomenclature

- C_f = skin friction coefficient = $\tau_w / (\rho U_\infty)$
- D = diameter of semicircular leading-edge geometry
- D_γ = intermittency factor diffusion term
- I = indicator function
- k = turbulent kinetic energy
- Re = Reynolds number based on characteristic length
- S_{ij} = mean strain-rate rate tensor
- S_γ = intermittency factor source term
- T_t = turbulence time scale
- Tu = freestream turbulence, percent
- u_i = instantaneous velocity in tensor notation
- γ = intermittency factor
- Γ = intermittency interaction invariant
- δ = boundary layer thickness
- δ^* = displacement thickness
- ϵ = rate of dissipation of turbulent kinetic energy
- λ_θ = pressure gradient parameter
- μ = molecular viscosity of air
- μ_t = turbulent viscosity
- ρ = density of the fluid
- $\sigma_k, \sigma_\epsilon$ = Prandtl number for the turbulent kinetic energy and its rate of dissipation
- θ = momentum thickness

Subscripts

- r = reattachment point
- s = separation point
- st = start of transition
- w = wall boundary
- ∞ = local freestream conditions
- $\infty,6$ = freestream conditions 6 mm from the leading edge

References

- [1] Emmons, H. W., 1951, "The Laminar-Turbulent Transition in a Boundary Layer—Part I," *J. Aerosp. Sci.*, **18**(7), pp. 490–498.
- [2] Dhawan, D., and Narasimha, R., 1958, "Some Properties of Boundary Layer Flow During Transition From Laminar to Turbulent Motion," *J. Fluid Mech.*, **3**, pp. 418–436.
- [3] Byggstoyl, S., and Kollmann, W., 1986, "Stress Transport in the Rotational and Irrotational Zones of Turbulent Shear Flows," *Phys. Fluids*, **29**(5), pp. 1423–1429.
- [4] Cho, J. T., and Chung, M. K., 1990, "Intermittency Transport Modeling Based on Interactions Between Intermittency and Mean Velocity Gradients," *Engineering Turbulence Modelling and Experiments*, W. Rodi and E. Ganic, eds., Elsevier, New York.
- [5] Cho, J. T., and Chung, M. K., 1992, "A $k-\epsilon-\gamma$ Equation Turbulence Model," *J. Fluid Mech.*, **237**, pp. 301–322.
- [6] Savill, A. M., 1995, "The Savill-Launder-Younis (SLY) RST Intermittency Model for Predicting Transition," *ERCOFTAC Bulletin*, (24), pp. 37–41.
- [7] Savill, A. M., 1996, "One-Point Closures Applied to Transition," *Turbulence and Transition Modeling*, M. Hallböck, D. S. Henningson, A. V. Johansson, and P. H. Alfredsson, eds., Kluwer, London.
- [8] Mayle, R. E., 1991, "The Role of Laminar-Turbulent Transition in Gas Turbine Engines," *ASME J. Turbomach.*, **113**, pp. 509–537.
- [9] Walker, G. J., 1993, "The Role of Laminar-Turbulent Transition in Gas Turbine Engines: A Discussion," *ASME J. Turbomach.*, **115**, pp. 207–217.
- [10] Sommers, D. M., 1981, "Design and Experimental Results for a Natural-Laminar-Flow Airfoil for General Aviation Applications," NASA TP-1861.
- [11] Kalitzin, G., Gould, A. R. B., and Benton, J. J., 1996, "Application of Two-Equation Turbulence Models in Aircraft Design," *AIAA Paper 96-0327*.
- [12] Byggstoyl, S., and Kollmann, W., 1981, "Closure Model for Intermittent Turbulent Flows," *Int. J. Heat Mass Transfer*, **24**(11), pp. 1811–1822.

- [13] Byggstoyl, S., and Kollmann, W., 1986, "A Closure Model for Conditioned Stress Equations and its Application for Turbulent Shear Flows," *Phys. Fluids*, **29**(5), pp. 1430–1440.
- [14] Dopazo, C., 1977, "On Conditioned Averages for Intermittent Turbulent Flows," *J. Fluid Mech.*, **81**, pp. 433–438.
- [15] Lumley, J. L., 1980, "Second Order Modelling of Turbulent Flows," *Prediction Methods for Turbulent Flows*, W. Kollmann, ed., **1**, Hemisphere, Washington, DC.
- [16] Simon, F. F., and Stephens, C. A., 1991, "Modeling of Heat Transfer in Bypass Transitional Boundary-Layer Flows," NASA TP-3170.
- [17] Rodi, W., and Scheuerer, G., 1986, "Scrutinizing the $k-\epsilon$ - I Turbulence Model Under Adverse Pressure Gradient Conditions," *ASME J. Fluids Eng.*, **108**, pp. 174–179.
- [18] Abu-Ghannam, B. J., and Shaw, R., 1980, "Natural Transition of Boundary Layers—The Effects of Turbulence, Pressure Gradient and Flow History," *J. Mech. Eng. Sci.*, **22**(5), pp. 213–228.
- [19] Solomon, W. J., Walker, G. J., and Gostelow, J. P., 1996, "Transition Zone Predictions for Rapid Varying Flows," *Transitional Boundary Layers in Aerodynamics*, R. A. W. M. Hengen and J. L. van Ingen, eds.
- [20] Yang, Z., and Shih, T. H., 1993, "New Time Scale Based $k-\epsilon$ Model for Near-Wall Turbulence," *AIAA J.*, **31**(7), pp. 1191–1197.
- [21] Vicedo, 2001.
- [22] Durbin, P. A., 1996, "On the $k-\epsilon$ Stagnation Point Anomaly," *Int. J. Heat Fluid Flow*, **17**, pp. 89–90.
- [23] Dawes, W. N., 1992, "The Simulation of Three-Dimensional Viscous Flow in Turbomachinery Geometries Using a Solution-Adaptative Unstructured Mesh Methodology," *ASME J. Turbomach.*, **114**, pp. 528–537.
- [24] Watterson, J. K., 1994, "A New, Pressure-Based, Unstructured Mesh, Navier-Stokes Solver and Application to 3D Compressible Vortex/Boundary Layer Interaction," Ph.D. thesis, University of Cambridge, Cambridge, UK.
- [25] Vilmin, S., 1998, "Turbulence Modeling on Unstructured Meshes for 3D Turbomachinery CFD," Ph.D. dissertation, École Polytechnique Fédérale de Lausanne, Lausanne, Switzerland.
- [26] Savill, A. M., 1993, "Some Recent Progress in the Turbulence Modeling of By-Pass Transition," *Near-Wall Turbulent Flows*, R. M. C. So, C. G. Speziale, and B. E. Launder, eds., Elsevier, New York, pp. 829–848.
- [27] Savill, A. M., 1993, "Further Progress in the Turbulence Modelling of By-Pass Transition," *Engineering Turbulence Modeling and Experiments 2*, W. Rodi and F. Martinelli, eds., Elsevier, New York, pp. 583–592.
- [28] Coupland, J., 1995, "Transition Modelling for Turbomachinery Flows," *ERCOFTAC Bulletin*, (**24**), pp. 5–8.
- [29] Papanicolaou, E. L., and Rodi, W., 1999, "Computation of Separated-Flow Transition Using a Two-Layer Model of Turbulence," *ASME J. Turbomach.*, **121**, pp. 78–87.
- [30] Kovaszny, L. S. G., Kibens, C., and Blackwelder, F., 1970, "Large-Scale Motion in the Intermittent Region of a Turbulent Boundary Layer," *J. Fluid Mech.*, **41**, pp. 283–325.
- [31] Driver, D. M., 1991, "Reynolds Stress Measurements in a Separated Boundary Layer Flow," *AIAA Paper 91-1787*.
- [32] Menter, F. R., 1994, "Two-Equation Eddy-Viscosity Turbulence Models for Engineering Applications," *AIAA J.*, **32**(8), pp. 1598–1605.
- [33] Roberts, W. B., 1980, "Calculation of Laminar Separation Bubbles and Their Effect on Airfoil Performance," *AIAA J.*, **18**(1), pp. 25–31.
- [34] Schmidt, R. C., and Patankar, S. V., 1991, "Simulating Boundary Layer Transition With Low-Reynolds Number $k-\epsilon$ Turbulence Models: Part 1—An Evaluation of Prediction Characteristics," *ASME J. Turbomach.*, **113**, pp. 10–17.
- [35] Tennekes, H., and Lumley, J. L., 1972, *A First Course in Turbulence*, MIT Press, Cambridge, MA.
- [36] Townsend, A. A., 1956, *The Structure of Turbulent Shear Flow*, Cambridge University Press, Cambridge, UK.

A. J. Cooper

School of Engineering,
University of Warwick,
Gibbet Hill Road,
Coventry CV4 7AL, UK

A. B. Parry

Rolls-Royce plc,
P.O. Box 31,
Derby DE24 8BJ, UK

N. Peake

Department of Applied Mathematics and
Theoretical Physics,
University of Cambridge,
Centre for Mathematical Sciences,
Wilberforce Road,
Cambridge CB3 0WA, UK

Acoustic Resonance in Aeroengine Intake Ducts

A theoretical model is used to investigate the effect of geometry, flow conditions and acoustic lining on the occurrence of acoustic resonance within aeroengine ducts. Semi-analytical methods are used to demonstrate that two types of acoustic resonance can be excited. The first is an intake resonance arising due to axial variation of the intake shape and the presence of swirling flow downstream of the rotor. The second occurs as a result of mode trapping between the rotor and stator. Such resonance phenomena may be relevant to the destabilization of the fan and the onset of flutter and rotating stall.

[DOI: 10.1115/1.1776586]

1 Introduction

The excitation of fluid-dynamical and acoustic instabilities within aeroengines can be a serious problem, particularly since engines are usually required to operate over a wide range of conditions. The onset of such instabilities can lead to substantial degradation in engine performance and of practical interest are flutter and/or rotating stall in the fan. In the aerospace industry there has been much discussion of aerodynamic instabilities associated with the fan and of the link between these instabilities and the installation (type of intake/bypass duct) in which the fan is sited. More specifically, it has been suggested that the link between the instabilities and the installation is driven by the acoustics of the system, with frequent reference to “cut-on” and “cut-off” acoustic modes. As might be expected, most relevant information is anecdotal and remains unpublished. However, Vahdati et al. [1] have recently published a detailed computational study of the effects of civil aeroengine intake on fan flutter instability. They made unsteady CFD calculations of a civil fan with two intakes. The first was a straight duct, representative of rig intakes. The second was a flight intake (though modeled as axisymmetric). The study found that the flutter stability dropped sharply for some very narrow speed ranges. Moreover, they found that there were significant differences between the results obtained for the two intakes. Separate calculations for the intake alone showed that the instabilities occurred close to the cut-on frequency ahead of the fan, and that fan flutter and intake duct acoustics are inextricably linked. Prior to this publication, an analytical model was developed by Cooper and Peake [2] to represent an aeroengine intake and fan system (including both the fan and the outlet guide vanes). A generic aeroengine geometry was used in order to show how, in certain parameter regimes, acoustic modes can become trapped in the intake leading to pure acoustic resonance and the development of large-amplitude, saturated-state oscillations. In practice, the detection of this type of instability would generally occur at a late stage in the design process, and there is heavy reliance on rig, or even full-scale engine testing. Clearly an analytical model of the form described in [2] could be of great use in defining design criteria at an early stage.

The physical mechanism for mode trapping identified in Cooper and Peake [2] arises from properties of the aeroengine geometry and flow. Axial changes in cross-sectional area of the intake give rise to turning points within the duct, where an acoustic mode

changes from being cut on (propagating) to cut off (evanescent). At a turning point a mode propagating upstream from the fan must be reflected into a downstream-propagating mode. Swirling flow behind the fan plays a crucial role, since a mode which is cut on ahead of the fan can be cut off by the mean swirl. Therefore an acoustic mode may become trapped between the fan and a turning point upstream in the intake duct, leading to pure acoustic resonance. In this paper specific aeroengine geometries and flow conditions are analyzed, and the model of Cooper and Peake [2] is extended in order to establish which characteristics of the geometry and flow influence mode trapping.

The steady flow in the duct is characterized by bulk axial Mach numbers in the intake and downstream of the stator, and axial and swirl Mach numbers between the rotor and stator. The effect of the fan rotation is expressed in terms of an average blade Mach number. In Cooper and Peake [2] the flow parameters were treated as independent, whereas in practical cases they are related by the fan aerodynamic design. In this paper, by assuming specific relations between the Mach numbers which approximate real engine properties, we determine how acoustic resonance is affected by different model geometries and flow conditions. The condition for the onset of acoustic resonance depends on the modulus of the reflection coefficient for acoustic modes at the fan. This reflection coefficient depends on: the dimensions of the duct at the fan location, the fan speed, the flow Mach numbers, the gap between the fan and the stator, and the frequency of the incoming acoustic mode. The reflection coefficient can be determined without any prior assumption of intake shape. The specific geometry of the intake determines where, and at which frequencies, turning points occur within the duct and thus defines the frequency range over which acoustic resonance is theoretically possible. We concentrate on frequencies and circumferential mode numbers which could be considered typical of aeroacoustic instability. This corresponds to relatively low frequencies (typically 200–600 Hz at full scale) and low-order circumferential mode numbers ($m=2-5$). The effects of fan-stator gap, fan speed-swirl relationship, duct shape, and acoustic lining on the occurrence of acoustic resonance are investigated.

In this paper the model devised to study intake resonance is developed further in order to investigate a second type of acoustic resonance, not considered in Cooper and Peake [2], which can occur as a result of modes being trapped between the rotor and the

Contributed by the Turbomachinery Division of THE AMERICAN SOCIETY OF MECHANICAL ENGINEERS for publication in the JOURNAL OF TURBOMACHINERY. Manuscript received by the ASME Turbomachinery Division, April 2003; final revision, February 2004. Associate Editor: T. Okiishi.

stator. Mode trapping in the intake relies on mean swirl cutting off a mode behind the fan, and only occurs for modes co-rotating with the swirl. For counter-rotating modes the effect of mean swirl is to cut on a mode. This creates the possibility of acoustic resonance between the rotor and the stator, which occurs when modes are cut on by swirl in the rotor-stator gap but cut off upstream and downstream of the swirling flow region. The possibility of this type of mode trapping has been discussed by Hanson [3].

2 Modeling the Aeroengine Duct

The intake duct is assumed to be axisymmetric with a circular cross-section varying slowly in the axial direction, containing irrotational steady flow and upstream and downstream propagating acoustic modes. The model does not represent the effects of droop present on inlets of modern gas turbines, but the significant effects of area variation in the duct are included in the model. This allows the aeroacoustic flow field in the duct to be determined following the approach of Rienstra [4]. The fan is represented in our model by an actuator disk. Horlock [5] gives an excellent discussion of the many possible applications of actuator disks, including turbomachinery cascades. More recently Joo and Hynes [6,7] have used actuator disks, embedded within a CFD scheme, to model a representative fan on a high bypass ratio civil turbofan engine with great success. An actuator disk relates the flow on either side of the disk (blade row) by appropriate jump/conservation conditions; it is assumed implicitly that the flow field varies slowly in the circumferential direction (i.e., the length scale over which the flow field varies is much greater than the blade pitch). This assumption is clearly valid here as we focus on low-order circumferential modes. The acoustic wavelength is also much greater than the axial chord of the blade rows, so that the resonant field is not created, or influenced, by direct scattering of modes at the trailing and leading edges of the blades. Note that, to be precise, the actuator disk model used here is a 'thick' actuator disk, where the conditions imposed represent jumps in value and also location—from a blade entry plane to a blade outlet plane. The entry and exit planes are positioned normal to the x -axis at average leading-edge and trailing-edge locations.

Downstream of the fan the duct is taken to be a uniform annulus carrying a steady vortical flow consisting of uniform axial flow and a swirling azimuthal component. Mean vorticity couples the potential and vorticity equations and gives rise to coupled acoustic-vorticity modes which can propagate both upstream and downstream. This type of mean swirling flow has been studied by Golubev and Atassi [8] and Tam and Auriault [9].

At some distance downstream of the rotor, a stator acts to straighten the flow. The stator row is also represented by an actuator disk, with appropriate jump/conservation conditions which are derived for a stationary (nonrotating) turbomachinery row. Like the rotor, the stator is represented by a thick actuator disk in order to preserve the rotor-stator gap. Downstream of the stator the perturbation flow fields are described in the usual way for uniform mean axial flow in a parallel annulus.

The form of the perturbation solutions in each region is discussed in Appendix A. The standard cylindrical coordinate system (x, r, θ) is used throughout, and lengths are nondimensionalized by the average duct radius at the fan, r_m^* , velocities by a reference sound speed, c_∞^* , density by ρ_∞^* , pressure by $\rho_\infty^* c_\infty^{*2}$, and time by r_m^*/c_∞^* .

3 Acoustic Resonance in the Intake

The change in intake cross-section can give rise to turning points in the intake where a mode changes from cut on to cut off. This is indicated by changes in the reduced axial wave number

$$\sigma = \pm [1 - \alpha^2 (C_0^2 - U_0^2) / \omega^2]^{1/2}, \quad (1)$$

where α is the radial wave number (defined in Appendix A), ω is the frequency, C_0 is the local sound speed and U_0 is the local

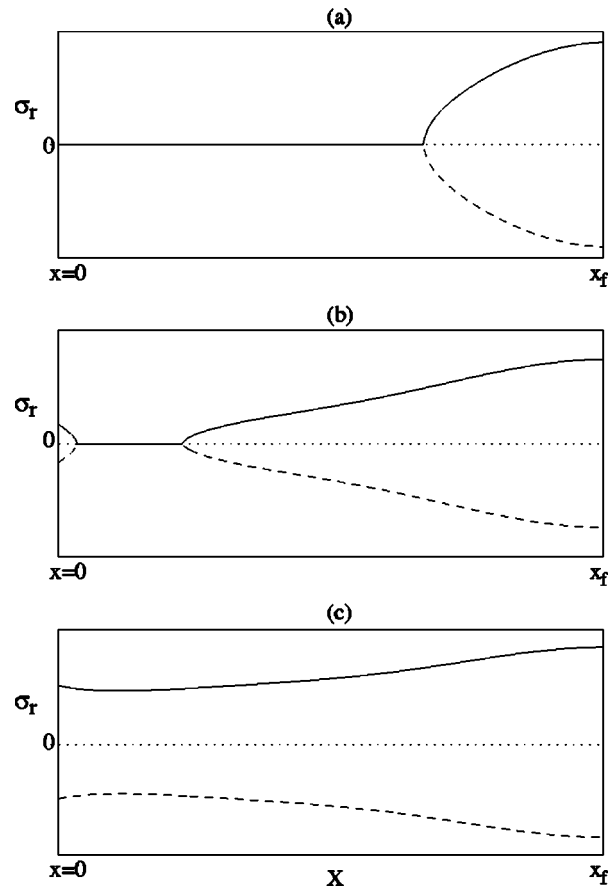


Fig. 1 Variation in the real part of the reduced axial wave number, σ , of the first radial mode along a slowly varying duct. Solid lines represent right-propagating modes and dashed lines left-propagating modes; modes are cut off when $\text{Re}(\sigma)=0$. (a) Single turning point upstream of the fan, $\omega_1 < \omega < \omega_2$, (b) two turning points in the intake, $\omega_2 < \omega < \omega_3$, (c) mode cut on along the entire length of the duct, $\omega_3 < \omega < \omega_4$. All higher-order radial modes are cut off when $\omega < \omega_4$. Duct inlet is located at $x=0$ and fan located at $x=x_f$.

axial velocity. When a mode is cut on σ is purely real and when a mode is cut off σ is purely imaginary. **Figure 1(a)** shows, for a typical intake shape, how a mode which is cut on at the fan becomes cut off at some point further upstream. Typically the turning point first arises at the fan location at a critical frequency, ω_1 , and then moves upstream as the frequency is increased. At a second critical frequency, ω_2 , a second turning point can arise in the duct (**Fig. 1(b)**). Further increases in frequency see the mode become cut on along the entire length of the duct when $\omega = \omega_3$ (**Fig. 1(c)**). One mode remains cut on along the entire length of the duct until, at a frequency ω_4 , a second mode becomes cut on at the fan. ω_1 and ω_4 are governed by the duct dimensions at the fan, while ω_2 and ω_3 are governed by the intake shape. The frequency range of practical interest generally corresponds to the case where there is just a single mode cut on at any point along the duct, and we therefore restrict attention to this parameter regime.

For acoustic resonance in the intake duct we are interested in the relationship between the coefficients of the upstream and downstream-propagating modes in the intake, \mathbf{A}^u and \mathbf{A}^d . The vectors \mathbf{A}^u and \mathbf{A}^d consist of all the intake cut-on coefficients and a finite number of the cut-off coefficients. The conditions imposed by the actuator disks (Eqs. (29)–(31) in Appendix A) can be rearranged to give the following condition at the fan location, $x = x_f$,

$$\mathbf{A}^u = \mathbf{K} \mathbf{A}^d. \quad (2)$$

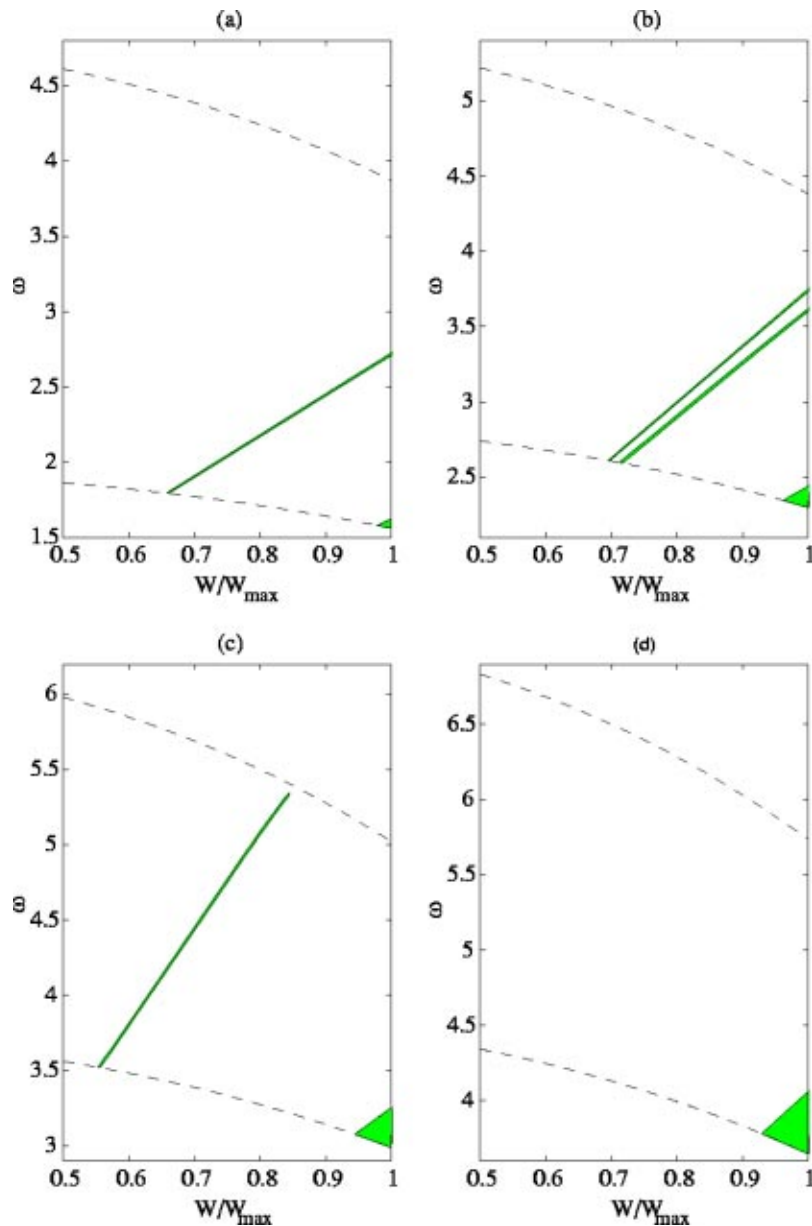


Fig. 2 Frequencies and fan speeds corresponding to potential acoustic resonance in an arbitrary intake. Dashed lines denote the frequency range for which there is, at most, one mode cut on along the duct. The lower line is ω_1 , and the upper line is ω_4 . The shaded (gray) regions correspond to $|K| > 1$, the edges of the bands are where $|K| = 1$, and elsewhere $|K| < 1$. (a) $m = 2$, (b) $m = 3$, (c) $m = 4$, (d) $m = 5$.

For the case of a single cut-on mode (2) can be reduced to a scalar expression

$$A^u(x_f) = KA^d(x_f), \quad (3)$$

where K can be thought of as the fan reflection coefficient.

In addition to reflection at a turning point it is also possible to have reflection of a propagating acoustic mode at the open (inlet) end of the duct (see Cooper and Peake [2] for details on how the reflection coefficients are determined). Acoustic resonance in this case relies on energy which is lost at the inlet being replaced by energy extracted from the fan and mean flow to sustain it. If the reflection coefficient at a turning point or the inlet is R then a necessary condition for unforced acoustic resonance to occur is $|K| = 1/|R|$. If there exists a single turning point, $R = \exp(i\pi/2)$, and the upstream-propagating wave is totally reflected at the turn-

ing point. The $\pi/2$ phase jump between incident and reflected waves can be derived by considering an inner region around the turning point in which the wave amplitude satisfies Airy's equation—see Rienstra and Hirschberg [10] for details. The resonance condition for the single turning point case is then $|K| = 1$.

In the frequency range $\omega_2 \leq \omega \leq \omega_3$ the resonance condition depends on the length of the cut-off region. If the gap between the two turning points is large, very little energy can escape across the cut-off region and the system acts like the single turning point case. As the gap shortens, energy can leak across the cut-off region producing a phenomenon analogous to barrier penetration (see Dowling and Ffowcs Williams [11]). If the gap then becomes sufficiently short, much more energy can leak across the cut-off region and the system behaves as if the mode is cut on along the entire length of the duct.

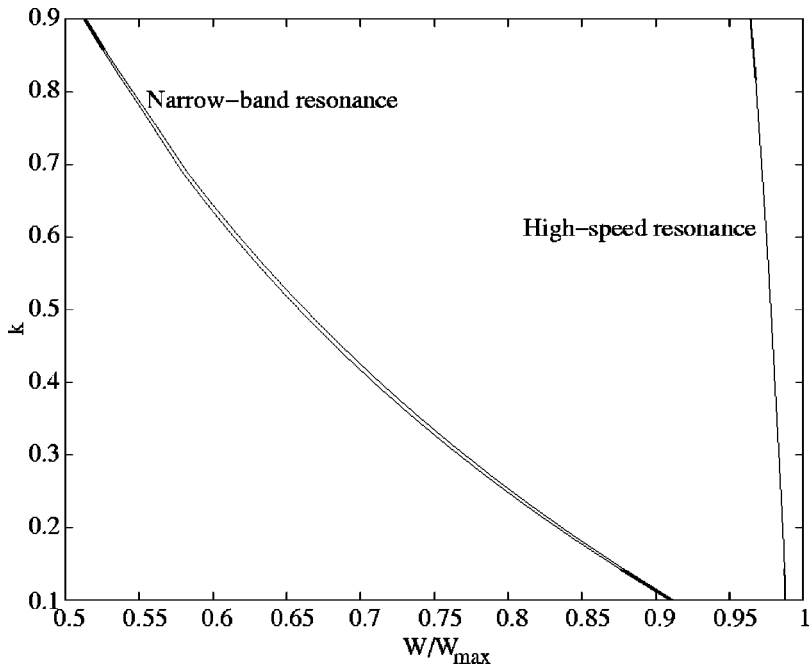


Fig. 3 Effect of degree of mean swirl on the resonance bands for $m=2$, where $M_{\Omega} = kW/W_{\max}$. Lines correspond to fan speeds where $|K|=1$ along the line $\omega = \omega_1$.

The value of $|K|$ depends only on duct dimensions and flow conditions at the fan and further downstream. Essentially it represents the effect of the fan system (the fan, outlet guide vanes and interrow swirl region) on downstream propagating waves in the intake. Parameters which give values of $|K| \geq 1$ can therefore be determined independently of intake shape in the frequency range $\omega_1 \leq \omega \leq \omega_4$. Once these have been calculated the effect of intake shape can be assessed by determining the critical frequencies ω_2

and ω_3 and the values of $|K|$ can then be matched accordingly. In this way it is possible to identify aspects of the intake shape which have a direct influence on the resonance.

3.1 Example. This section considers an industrially representative duct where axial, swirl, and blade Mach numbers are expressed in terms of fan speed. This leaves the frequency, ω , and fan speed as free parameters to be varied in order to find under

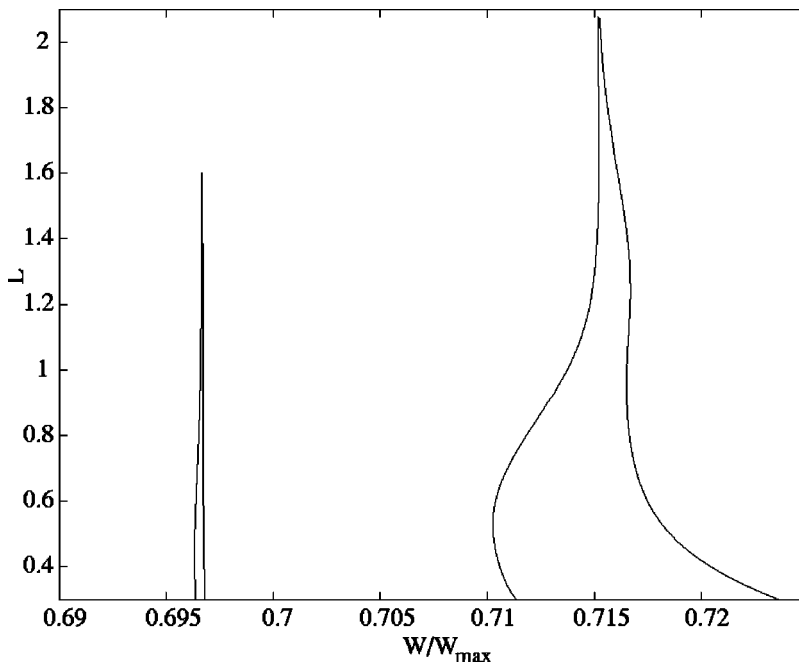


Fig. 4 Effect of rotor-stator gap length, L , on the narrow-band resonance for $m=3$. Lines correspond to fan speeds where $|K|=1$ along the line $\omega = \omega_1$.

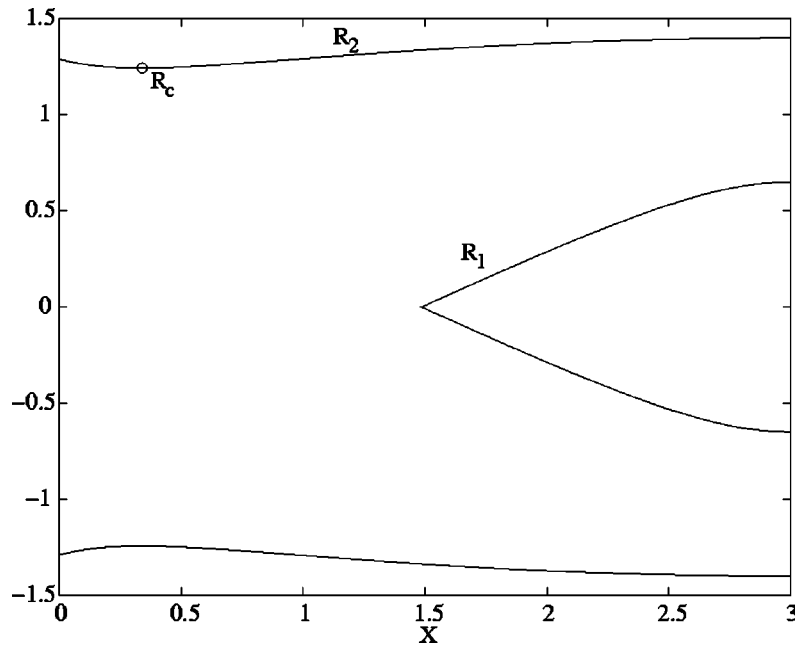


Fig. 5 Intake shape used in examples. The duct dimensions at the fan, inlet and throat (denoted here by R_c) are important aspects of the duct shape which define the frequency ranges for the cut on/cut off characteristics shown in Fig. 1.

which conditions $|K| \geq 1$. The nondimensional radii of the duct at the fan, and further downstream, are taken to be $R_1(x_f) = 0.65$, $R_2(x_f) = 1.4$, and the rotor-stator gap $L = x_s - x_f = 0.7$. It is assumed that the fan rotates with an angular velocity $W \text{ rad}^{-1}$, and has a maximum design angular velocity $W_{\max} \text{ rad}^{-1}$. The average blade Mach number is given by

$$M_b = \left(\frac{W}{W_{\max}} \right) \frac{W_{\max} r_m^*}{c_{\infty}^*}, \quad (4)$$

where it is assumed that $W_{\max} r_m^* / c_{\infty}^* = 0.8$. The mean flow behind the rotor consists, in general, of a radially varying axial velocity and a swirl velocity comprised of solid-body rotation and free-vortex components. The model formulation is applicable to the general velocity distribution but qualitative results can be obtained by approximating the mean velocity field by a uniform axial flow and solid-body rotation. This approximation allows more efficient computation of the eigenvalues and eigenvectors. The effects of a more general velocity field are discussed at the end of this section.

The axial and average swirl Mach numbers are taken to be

$$\begin{aligned} M_x^{(1)} &= 0.6W/W_{\max} & M_x^{(2)} &= 0.5W/W_{\max}, \\ M_x^{(3)} &= 0.45W/W_{\max}, & M_{\Omega} &= 0.5W/W_{\max}, \end{aligned} \quad (5)$$

where superscript (1) denotes the intake section, (2) the swirl region, and (3) downstream of the stator.

Calculations were carried out for circumferential mode numbers $m = 2-5$ and for fan speeds in the range $0.5 \leq W/W_{\max} \leq 1$. The dimensional frequency is given by $f = \omega c_{\infty}^* / 2\pi r_m^*$, and for this example the range $1.5 \leq \omega \leq 6.5$ corresponds to $208 \text{ Hz} \leq f \leq 905 \text{ Hz}$.

Figure 2 shows frequencies as a function of relative fan speed where the necessary condition for resonance is satisfied. At the edges of the shaded regions $|K| = 1$, regions where $|K| > 1$ are shaded gray, and elsewhere $|K| < 1$. The results show very narrow regions which vary in position and number with m , and these families of resonances will be termed “narrow-band” resonance. In addition to this there are wider regions of “high-speed” reso-

nances. The results indicate the general areas where acoustic resonance may be a factor. Resonances for a specific intake shape are identified later. The effect of swirl is considered by calculating resonance points along the line $\omega = \omega_1$ for different swirl Mach numbers given by $M_{\Omega} = k(W/W_{\max})$, where $0.1 \leq k \leq 0.9$. In **Fig. 3** it can be seen that as the degree of swirl increases, the resonance condition is satisfied at lower fan speeds. The high-speed resonance is less sensitive to changes in swirl than the narrow-band resonance. The effect of rotor-stator gap length, L , can also be demonstrated by considering resonance points along the line $\omega = \omega_1$, and results are shown in **Fig. 4**. The width of the narrow band resonance is found to decrease as the gap length increases, and beyond some critical value of L the resonance bands disappear. The high-speed resonance (not shown) is generally insensitive to changes in gap length and remains present for large values of L . Similar trends to those shown in **Fig. 3** and **Fig. 4**, for changes in mean swirl and rotor-stator gap length, are observed for all values of m of interest.

The results presented above suggest different physical explanations for the occurrence of the two families of acoustic resonance. The insensitivity of the high-speed resonance to both swirl distribution and gap length suggests that the mechanism relies solely on the presence of swirl to cut off the incident wave. Acoustic resonance then occurs as a result of direct reflection at the fan face. The effects of swirl and rotor-stator separation on the narrow-band resonance indicate that propagation through the swirl region and the stator must be involved in this case. The effects of gap length suggest that the physical process must involve reflection of cut-off waves at the stator. The disappearance of this resonance beyond a critical separation appears to support this theory, as increases in gap length would attenuate the incident cut-off waves to such a degree at the stator location, removing the possibility of reflection.

We now consider the intake effect using the duct of a CFM56-inspired turbofan engine, as in Rienstra [4]. The intake shape is given by

$$R_1(x) = \max\{0, 0.985 - [0.112 + 3.37(1-x/3)^2]^{1/2}\}, \quad (6)$$

$$R_2(x) = 1.4 - 0.25(1-x/3)^2 + 0.14 \exp(-11x/3), \quad (7)$$

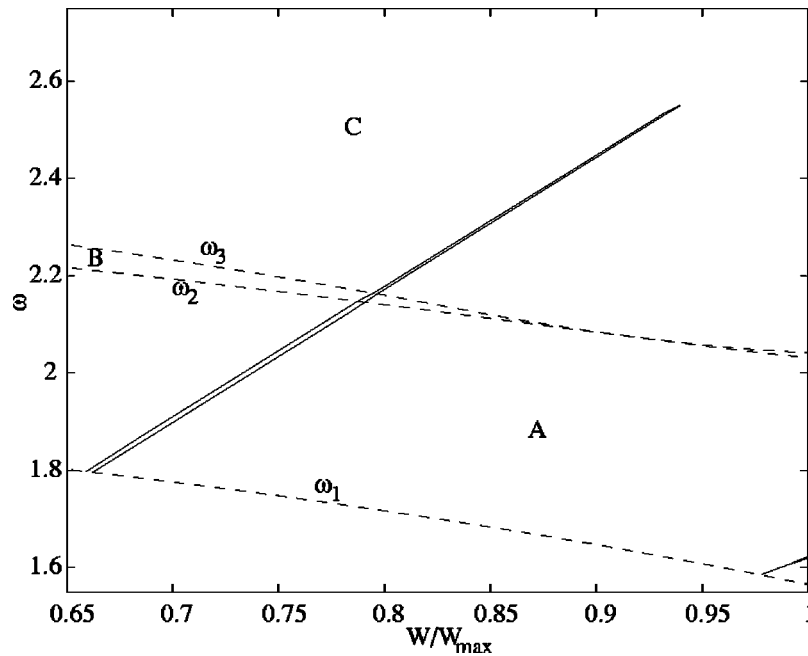


Fig. 6 Solid lines show when the resonance condition is satisfied for $m=2$ with the intake shape given by Eq. (6) and Eq. (7). Dashed lines show the frequencies ω_1 , ω_2 and ω_3 . Region A corresponds to the behavior shown in Fig. 1(a) and here $|K|=1$. Region B denotes the situation in Fig. 1(b). Region C corresponds to the case in Fig. 1(c) and here $|K|=1/|R|$.

with $0 \leq x \leq 3 = x_f$, and shown in Fig. 5. The characteristics shown in Fig. 1 are dependent on two critical radii. The frequency at which a mode becomes cut on at the duct inlet (Fig. 1(b)), depends on the inlet radius, $R_2(0)$. The frequency at which the mode becomes cut on along the entire length of the duct (Fig. 1(c)) depends on the radius of the duct at the point of maximum contraction, R_c , termed the throat radius. These radii determine ω_2 and ω_3 as functions of relative fan speed and indicate which form of the resonance condition must be satisfied, i.e., for $\omega < \omega_2$ we must have $|K|=1$, and for $\omega > \omega_3$ we must have $|K|=1/|R|$, where R is the reflection coefficient at the duct inlet.

The inlet reflection coefficient $|R|$, which decreases with increasing fan speed and increasing frequency, can be used to identify specific resonance points. Figure 6 shows the frequency ranges determined by the intake shape and the resulting resonance points when $m=2$. In this case the general areas of possible resonance shown in Fig. 2(a) give a good indication of actual resonances when a specific intake shape is assumed. The main difference is that for $\omega > \omega_3$ the resonance band narrows and vanishes for $W/W_{\max} > 0.95$.

Changing the intake shape has an effect on the lines ω_2 and ω_3 . Increasing/decreasing the radius $R_2(0)$ will lower/raise the line ω_2 and also change the reflection coefficients at the duct inlet. Increasing/decreasing the throat radius R_c will lower/raise the line ω_3 . The intake shape can also be modified by changing the axial location of the throat. If the value of R_c remains unchanged, then this has no effect on the position of the lines ω_1 , ω_2 or ω_3 , but may change the length of the cut-off region in the frequency range $\omega_2 \leq \omega \leq \omega_3$ and the amount of energy leakage across the cut-off region. The value of R_c is much more important than the axial location of the throat.

The inclusion of a more general swirl distribution is expected to have little impact on the qualitative results presented here, in that two families of resonance may be generated and the basic mechanisms for their occurrence remain valid. Since the high-speed resonance simply relies on the action of the swirl to cut off the incident wave it is expected that this family of resonances would

not be affected significantly by changes in the swirl distribution. The conditions at which the narrow-band resonance arises may be affected by the addition of a free-vortex component in the swirl, since it is hypothesized that propagation through the swirl region is involved in the generation of this type of resonance.

3.2 Lined Intake Duct. If the intake duct is lined with a finite impedance material then this acts to attenuate the cut-on modes. Even though these modes are attenuated they still carry energy, unlike cut-off modes in a hard-walled duct. The effect of an acoustic lining is to remove any turning points within the intake duct, leaving reflection from the open end of the duct as the only mechanism for acoustic resonance to occur. It should be noted that in practice intake treatment usually starts some distance upstream of the fan and extends to the neighborhood of the inlet highlight. As such, mode scattering at the interface between lined and unlined sections of the duct may have an impact on the resonance condition. These effects are not included at this stage and we assume the duct is lined completely. Some differences to the hard-walled duct arise since the radial and reduced axial wave numbers for upstream and downstream-propagating modes now differ. In order to obtain a resonance condition in this case the general solution for the amplitude variation along the duct must be considered. Following Rienstra [4] the amplitudes of the downstream and upstream-propagating modes, at the fan location x_f , can be written as

$$A^d(x_f) = S^+(x_f) P^+ A^d(0) / S^+(0), \quad (8)$$

$$A^u(x_f) = S^-(x_f) P^- A^d(0) / S^-(0), \quad (9)$$

where

$$P^\pm = \exp\left(-i \int_0^{x_f} \mu^\pm(\varepsilon y) dy\right).$$

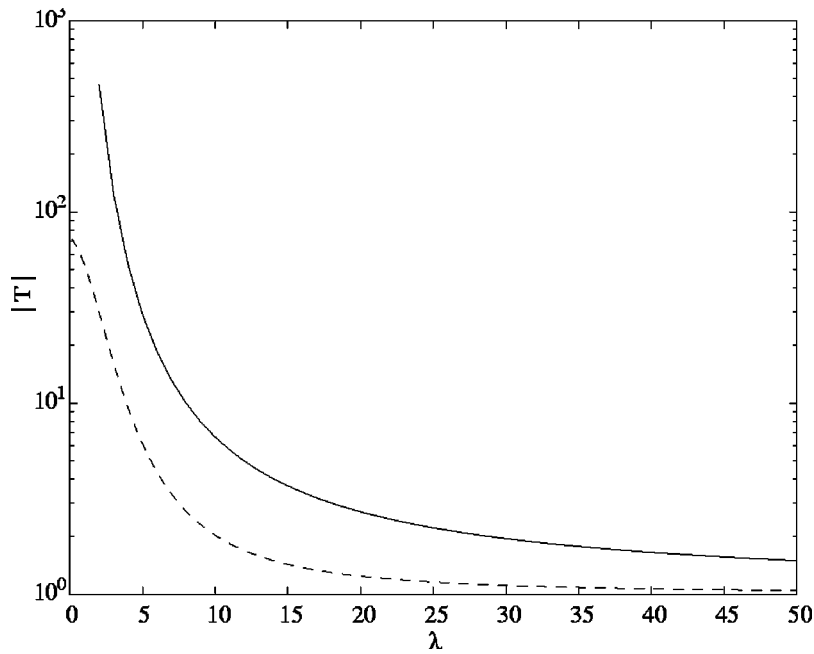


Fig. 7 Effect of wall impedance on the parameter $|T|$ defined in Eq. (10), when $m=2$, $W/W_{\max}=0.5$, $\omega=2.5$. Solid line: $Z_2=\lambda-i$; dashed line: $Z_2=4-\lambda i$.

The axial wave number, μ^\pm , is defined in Appendix A (Eq. (12)) and expressions for $S^\pm(x)$ are given in Appendix B. This leads to the resonance condition

$$|K|=|T/R|, \quad (10)$$

where $T=S^-(x_f)S^+(0)P^-(S^-(0)S^+(x_f)P^+)$. **Figure 7** shows the variation of $|T|$ as a function of wall impedance, for a given fan speed and frequency. The value of $|T|$ is dominated by the exponential factor $|P^-/P^+|$, which increases significantly with the degree of wall compliance. These trends are maintained across all fan speeds and frequencies. As a result, unless the liner material is very stiff, it is generally not possible to extract sufficient energy from the fan and the mean flow in order to satisfy the resonance condition, and the acoustic lining is able to attenuate the resonant acoustic modes. If the intake is lined the lining impedance and intake length, which govern the size of P^\pm , are therefore significant factors to be considered.

4 Acoustic Resonance in the Rotor-Stator Gap

The mechanism for acoustic resonance in the intake relies on mean swirl cutting off a mode which is cut on in the absence of swirl. This only arises for modes co-rotating with the swirl (i.e., $m>0$ given $M_\Omega>0$). For counter-rotating modes ($m<0$) the effect is opposite. This provides a potential mechanism for mode trapping in the gap between the rotor and the stator. At low frequencies no modes are cut on upstream of the fan and downstream of the stator, but a counter-rotating mode can be cut on in the swirling flow region. In order to derive a resonance condition for this type of acoustic resonance we return to the relations between coefficients. For resonance in the rotor-stator gap rearrangement of Eqs. (29)–(31) leaves an expression of the form

$$\mathbf{Q}\mathbf{A}^+=0, \quad (11)$$

where \mathbf{A}^+ is the vector of coefficients for the downstream-propagating modes in the interrow swirl region. The condition for resonance in this case is that the matrix \mathbf{Q} be singular, i.e. \mathbf{Q} has zero determinant.

In numerical systems there are problems in using the zero determinant condition to prove a matrix is singular due to numerical

rounding errors. Woodley and Peake [12] discussed these problems and adopted the method of singular value decomposition (SVD) to establish whether a matrix is singular. The SVD factorization can be used to obtain the condition number, which is defined as the ratio of the largest and smallest singular values. Strictly a matrix is singular if the reciprocal of the condition number (RCond) is zero. Again, due to errors accumulated in the numerical procedures preceding the calculation of the condition number, this condition cannot be obtained exactly. We therefore define resonance as occurring when RCond is significantly smaller than elsewhere across the parameter range. The determinant is also monitored to ensure that the reciprocal of the condition number is small due to a zero eigenvalue, rather than one large eigenvalue.

4.1 Example. The case of zero cut-on modes upstream of the fan corresponds to the frequency range $0<\omega<\omega_1$. **Figure 8** shows contours of $\ln(\text{RCond})$ for $m=-2$ when $M_\Omega=0.5W/W_{\max}$ and the axial Mach numbers are those given in Eq. (5). There are several regions where the contours are concentrated denoting sharp extrema. The dashed lines indicate the fan speeds where RCond displays a sharp minimum. The subplots in this figure show the value of RCond as a function of frequency at these fan speeds and indicate the frequencies at which the system is numerically singular. Although there exist discrete points where the matrix can be said to be singular it might be expected that frequencies and fan speeds in the vicinity of these singular points may excite an acoustic resonance given small fluctuations in flow conditions or geometry. **Figure 8** shows several regions where the system may be particularly sensitive to small changes in conditions and where acoustic resonant modes may be excited. The position and number of resonance points is found to vary with the rotor-stator gap length (more resonance points are found for smaller gap lengths) and the resonance is only sustained for sufficiently high degrees of swirl.

If the intake is lined modes are no longer cut on in the intake, and $\mathbf{A}^d=0$ since the modes \mathbf{A}^u are attenuated to such an extent when the inlet is reached that there are no modes reflected back downstream. An acoustic lining therefore effectively extends the frequency range for which there are zero modes cut on in the

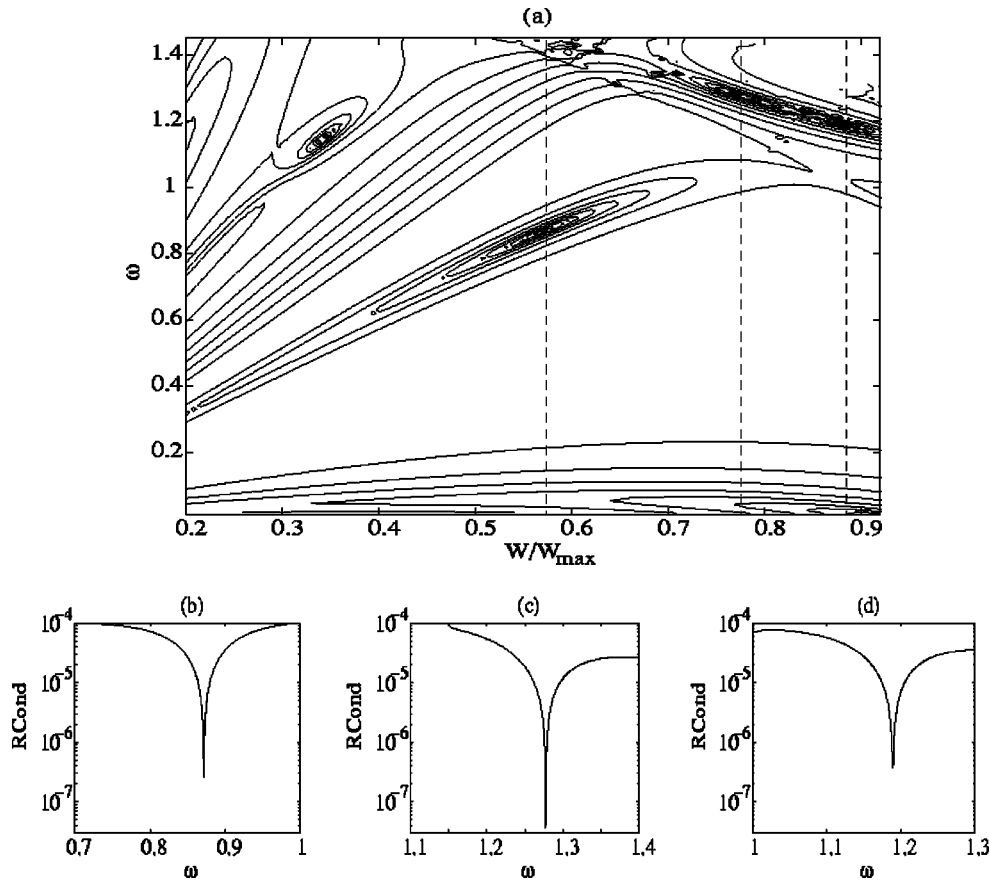


Fig. 8 (a) Contours of $\ln(RCond)$ when $m = -2$, $L = 0.7$ and $M_{\Omega} = 0.5W/W_{max}$. The dashed lines denote fan speeds at which $RCond$ displays a sharp minimum corresponding to numerical singularity. The variation in $RCond$ at these fan speeds is shown in the subplots (b) $W/W_{max} = 0.575$, (c) $W/W_{max} = 0.775$, (d) $W/W_{max} = 0.885$.

intake and is likely to enhance the possibility of the rotor-stator gap resonance. This form of unforced interstage acoustic resonance would lead to the formation of large-amplitude, saturated-state oscillations in the same manner as the intake resonance, suggesting another possible route to instability or loss of performance within the engine.

5 Conclusions

A theoretical model of an aeroengine has been developed and used to demonstrate the phenomenon of acoustic resonance. Two forms of resonant state have been identified. One corresponds to the trapping of acoustic modes in the intake which arises, in part, due to the cross-sectional variation of the intake. The second form of resonance occurs between the rotor and the stator. The presence of swirling flow is involved in the physical mechanism of both forms of resonance. Modes corotating with the mean swirl which are cut on upstream of the fan can be cut off in the swirling region downstream of the fan, and counter-rotating modes can be cut on in the swirling-flow region and cut off elsewhere. For the intake resonance mode trapping occurs between the fan and a point upstream in the intake. If a turning point exists in the intake then an upstream-propagating mode is totally reflected into a downstream propagating mode. For a mode cut on along the entire length of the intake partial reflection occurs at the inlet. In this case energy lost in reflection must be extracted from the fan and mean flow in order for resonance to occur.

The intake resonance is comprised of two families. The first is generally a high-speed resonance occurring at fan speeds above 90% of the maximum speed, and is insensitive to the degree of swirl and rotor-stator gap length. This suggests that the physical

process involves the action of swirl to cut off the incident mode, effectively generating a barrier to the incident acoustic wave which becomes reflected at the fan face. The second family occurs over a wider range of fan speeds and is completely eliminated if the rotor-stator gap exceeds some critical value. This suggests that these resonant states involve the evolution of cut-off modes through the swirl region and arise from reflection of these modes off the stator. The formulation of the acoustic resonance model makes no assumption about the form of the mean flow distribution in any region, and is therefore applicable to the more general velocity distribution in the swirl region. The difficulty in implementing this arises in the computation of the vorticity-dominated eigenvalues and eigenfunctions. A significant increase in numerical complexity would be required in order to obtain the vorticity-dominated modes sufficiently accurately in the general case. Since the degree of swirl strongly affects the latter family of resonances, it may be important in practical terms to account for the actual swirl profile produced by the fan. The construction of this model has identified important duct characteristics which are significant for intake resonance. Critical parameters are the inlet radius and annulus dimensions at the fan, together with the flow conditions at the fan and further downstream, which determine the overall frequency range across which acoustic resonance is possible. Furthermore the value of the duct radius at the throat governs which form of resonance condition is appropriate. A larger throat radius extends the frequency range over which the condition $|K|=1$ must hold. The model also demonstrates that acoustic resonance in the rotor-stator gap can be excited, but only if the degree of swirl is large enough. The position of these resonances in frequency-fan speed parameter space and the number of resonance

points changes with rotor-stator gap length. The effect of acoustic lining in the intake is to attenuate the intake acoustic resonance states. In practice it may be more attractive to line only a section of the intake, in which case a tailoring of properties to eliminate all resonant modes would be required. A lined intake is thought to increase the frequency range over which the gap resonance is possible.

In conclusion, if the frequency of any of these resonant states coincides with a natural vibrational frequency of the fan then this may lead to destabilization of the fan and the onset of phenomena such as flutter and/or rotating stall. The model provides an efficient alternative to full numerical simulation and allows physical mechanisms to be investigated over a wide range of parameter values. The authors anticipate that the model will prove to be a useful tool in the design process, allowing potentially damaging resonant phenomena to be investigated prior to full-scale testing.

Acknowledgments

The work described in this paper was supported by a research grant from EPSRC, reference GR/L80317. AJC also acknowledges support from The Royal Society. The authors would like to acknowledge useful discussions with R. V. Brooks and Dr N. H. S. Smith.

Appendix A

Flow Upstream of the Fan. The intake section is modelled as a slowly varying duct. A slow axial scale $X = \varepsilon x$ is introduced, where ε is a small parameter of the order of the axial slope of the duct walls. The duct is defined by $R_1(X) \leq r \leq R_2(X)$ with mean axial velocity $U_0^{(1)}(X)$. Details of the full mean flow solution can be found in Rienstra [4]. The local axial Mach number is given by $M_x^{(1)}(X) = U_0^{(1)}(X)/C_0^{(1)}(X)$, where $C_0^{(1)}$ is the relative speed of sound along the intake.

For a mode of nondimensional frequency ω and circumferential wavenumber m , the acoustic field, at leading order, is expressed in terms of a potential with slowly varying amplitude and axial wave number. The axial wave numbers, μ_n^\pm , are given by

$$\mu_n^\pm(X) = \frac{-k_0 M_x^{(1)} \pm (k_0^2 - \alpha_n^2 \{1 - M_x^{(1)2}\})^{1/2}}{1 - M_x^{(1)2}}, \quad (12)$$

where $k_0 = \omega/C_0^{(1)}$, n denotes radial order and α_n is the radial wave number determined from the boundary condition $\partial\phi^{(1)}/\partial r = 0$ at the (hard) duct walls. A typical eigenvalue spectrum consists of a finite number of cut-on modes ($\text{Im}\{\mu_n\} = 0$) corresponding to the lowest radial orders, and an infinite, discrete, set of cut-off modes ($\text{Im}\{\mu_n\} \neq 0$).

Just upstream of the fan, located at $x = x_f$, the potential field can be expressed as

$$\begin{aligned} \phi_m^{(1)}(x, r, \theta, t) = & \sum_{n=1}^{\infty} \{A_{mn}^u e^{-i\mu_{mn}^-(x-x_f)} \\ & + A_{mn}^d e^{-i\mu_{mn}^+(x-x_f)}\} C_m(\alpha_{mn} r) \exp\{i\omega t - m\theta\}, \end{aligned} \quad (13)$$

where A_{mn}^u and A_{mn}^d are coefficients of upstream and downstream propagating waves, respectively, $C_m(z) = J_m(z) + \kappa Y_m(z)$, with J_m and Y_m the m th-order Bessel functions of the first and second kind, respectively, and $\kappa = -J'_m(\alpha R_2)/Y'_m(\alpha R_2)$.

Flow Between the Rotor and the Stator. Behind the fan the steady flow is swirling and taken to consist of uniform axial flow, $U_0^{(2)}$, and mean swirl expressed as a sum of rigid body rotation Ωr and free vortex Γ/r . The perturbation velocity, \mathbf{v} , is first decomposed into potential and vortical parts,

$$\mathbf{v} = \nabla\Phi + \mathbf{a}. \quad (14)$$

With the form

$$[\Phi, a_x, a_r, a_\theta] = [\phi_{mn}(r), X_{mn}(r), R_{mn}(r), T_{mn}(r)] \exp\{i\omega t - im\theta - ik_{mn}(x-x_f)\}, \quad (15)$$

the coupled acoustic and vorticity equations give rise to a generalized eigenvalue problem,

$$\mathbf{B}\mathbf{Y}_{mn} = k_{mn}\mathbf{Y}_{mn}, \quad (16)$$

where $\mathbf{Y}_{mn} = [\phi_{mn}, \eta_{mn}, R_{mn}, T_{mn}]$, and $\eta_{mn} = k_{mn}(1 - U_0^2/C_0^2)\phi_{mn}$. Equation (16) is solved numerically using a Chebyshev spectral-collocation method to determine the values of k_{mn} and the associated eigenvectors. The eigenvalue relation for this type of flow produces two distinct sets of coupled acoustic-vorticity modes. One set is pressure dominated and consists of upstream and downstream-propagating cut-on modes and an infinite discrete set of cut-off modes. The second set is vorticity-dominated and consists of two branches of eigenvalues which asymptotically approach a critical value corresponding to pure convection. These modes are labeled $+$, $-$, l and r , respectively. The perturbation to the flow field is written as a sum over these modes and detailed mathematical descriptions are given in Cooper and Peake [2].

Flow Downstream of the Stator. Behind the stator, located at $x = x_s$, the steady flow is purely axial with velocity $U_0^{(3)}$, and the unsteady flow field consists of downstream-propagating acoustic and vorticity modes. The acoustic field is given by

$$\phi_m^{(3)} = \sum_{n=1}^{\infty} B_{mn}^d e^{-is_{mn}^+(x-x_f)} C_m(\alpha_{mn} r) \exp\{i\omega t - im\theta\}, \quad (17)$$

where the axial wave numbers, s_{mn}^+ , differ to μ_{mn}^+ in region 1 if $M_x^{(3)} \neq M_x^{(1)}$.

The radial component of the purely convected vorticity field, \mathbf{a} , is expressed in terms of Bessel functions which satisfy the impermeability condition at the walls,

$$\begin{aligned} a_r^m = & \sum_{n=1}^{\infty} B_{mn}^r e^{-ik_x(x-x_f)} \{J_1(\beta_{mn} r) + \nu Y_1(\beta_{mn} r)\} \exp\{i\omega t \\ & - im\theta\}, \end{aligned} \quad (18)$$

where $k_x = \omega/U_0^{(3)}$ is the convected wave number, $\nu = -J_1(\beta_{mn} R_2)/Y_1(\beta_{mn} R_2)$ and the radial eigenvalues, β_{mn} , are chosen to satisfy the boundary conditions. The vorticity field must satisfy $\nabla \cdot \mathbf{a} = 0$ which leads to the expansions

$$\begin{aligned} (a_\theta^m, a_x^m) = & \sum_{n=1}^{\infty} (r B_{mn}^\theta, i B_{mn}^x) e^{-ik_x(x-x_f)} \{J_0(\beta_{mn} r) \\ & + \nu Y_0(\beta_{mn} r)\} \exp\{i\omega t - im\theta\}. \end{aligned} \quad (19)$$

The coefficients are related by the condition

$$\beta_{mn} B_{mn}^r - im B_{mn}^\theta - ik_x B_{mn}^x = 0, \quad (20)$$

which allows one set of unknown coefficients to be eliminated.

Twin Actuator Disk Model for Rotor-Stator Pair. The unknown constants in the three flow regions are related through conservation of mass flow, conservation of radial velocity, conservation of rothalpy and the Kutta condition applied at each disk. A condition on the stagnation pressure is not applied since we are assuming the flow to be isentropic.

Using superscripts (1) and (2) to denote the unsteady flow fields in regions 1 and 2, respectively, the (linearized) mass and radial velocity conditions at the rotor are

$$\frac{M_x^{(1)}}{C_0^{(1)}} p^{(1)} + u_x^{(1)} D_0^{(1)} = \frac{M_x^{(2)}}{C_0^{(2)}} p^{(2)} + u_x^{(2)} D_0^{(2)}, \quad (21)$$

$$u_r^{(1)} = u_r^{(2)}, \quad (22)$$

where C_0 , D_0 are the relative mean speed of sound and mean density, and p is the perturbation pressure. The linearized conservation of rothalpy condition is

$$\frac{p^{(1)}}{D_0^{(1)}} + C_0^{(1)}(M_x^{(1)}u_x^{(1)} - rM_b u_\theta^{(1)}) = \frac{p^{(2)}}{D_0^{(2)}} + C_0^{(2)} \left(M_x^{(2)}u_x^{(2)} + r \left\{ M_\Omega + \frac{M_\Gamma}{r^2} - M_b \right\} u_\theta^{(2)} \right), \quad (23)$$

where $M_b = W r_m^*/(C_0^{(1)}c_\infty)$ is the average blade Mach number (W is the angular velocity of the fan). The mean swirl velocity is assumed to be composed of solid-body rotation and free-vortex components and the associated swirl Mach number are given by $M_\Omega = \Omega r_m^*/(C_0^{(1)}c_\infty)$ and $M_\Gamma = \Gamma/(r_m^{*2}C_0^{(1)}c_\infty)$, respectively. The Kutta condition leads to

$$M_x^{(2)}u_\theta^{(2)} = r \left\{ M_\Omega + \frac{M_\Gamma}{r^2} - M_b \right\} u_x^{(2)}. \quad (24)$$

The corresponding conditions imposed at the stator are

$$\frac{M_x^{(2)}}{C_0^{(2)}} p^{(2)} + u_x^{(2)} D_0^{(2)} = \frac{M_x^{(3)}}{C_0^{(3)}} p^{(3)} + u_x^{(3)} D_0^{(3)}, \quad (25)$$

$$u_r^{(2)} = u_r^{(3)}, \quad (26)$$

$$\begin{aligned} \frac{p^{(2)}}{D_0^{(2)}} + C_0^{(2)} \left(M_x^{(2)}u_x^{(2)} + r \left\{ M_\Omega + \frac{M_\Gamma}{r^2} \right\} u_\theta^{(2)} \right) \\ = \frac{p^{(3)}}{D_0^{(3)}} + C_0^{(3)} M_x u_x^{(3)}, \end{aligned} \quad (27)$$

$$u_\theta^{(3)} = 0. \quad (28)$$

The conditions in Eqs. (21)–(28) give rise to expressions involving a summation over the number of radial orders, n . If the summations are truncated at some value $n = N$, then these conditions can be transformed into a set of eight matrix equations in terms of A_{mn}^u , A_{mn}^d , A_{mn}^+ , A_{mn}^- , A_{mn}^l , A_{mn}^r , B_{mn}^d , B_{mn}^x and B_{mn}^r , by multiplying both sides by $r C_m(\alpha_j r)$ ($j = 1, \dots, N$) and integrating from $R_1(X_f)$ to $R_2(X_f)$ (see Cooper and Peake [2] for details). By eliminating the coefficients A_{mn}^l , A_{mn}^r , B_{mn}^d , B_{mn}^x and B_{mn}^r these equations can be reduced to the form

$$\mathbf{C}_1 \mathbf{A}^u + \mathbf{D}_1 \mathbf{A}^d + \mathbf{E}_1 \mathbf{A}^+ + \mathbf{F}_1 \mathbf{A}^- = 0, \quad (29)$$

$$\mathbf{C}_2 \mathbf{A}^u + \mathbf{D}_2 \mathbf{A}^d + \mathbf{E}_2 \mathbf{A}^+ + \mathbf{F}_2 \mathbf{A}^- = 0, \quad (30)$$

$$\mathbf{C}_3 \mathbf{A}^u + \mathbf{D}_3 \mathbf{A}^d + \mathbf{E}_3 \mathbf{A}^+ + \mathbf{F}_3 \mathbf{A}^- = 0, \quad (31)$$

where \mathbf{C}_j , \mathbf{D}_j , \mathbf{E}_j , and \mathbf{F}_j are $N \times N$ matrices, and $\mathbf{A}^u = [A_{m1}^u, A_{m2}^u, \dots, A_{mN}^u]$, etc. In the calculations a value of $N = 10$ was found sufficient to obtain a convergent solution.

Appendix B

The general amplitude variation along a lined duct was determined by Rienstra [4] and is given by

$$A(x) = Q_0 S(x),$$

where Q_0 is an arbitrary constant and, if $R_1 \neq 0$,

$$S(x) = \frac{1}{2} \pi \left(\frac{2C_0}{D_0 \omega \sigma} \right)^{1/2} \left[\frac{R_2^2 \left(1 - \frac{m^2 - \zeta_2^2}{\alpha^2 R_2^2} \right) + \frac{D_0 U_0 \zeta_2}{\Omega}}{[\alpha R_2 Y_m'(\alpha R_2) - \zeta_2 Y_m(\alpha R_2)]^2} - \frac{R_1^2 \left(1 - \frac{m^2}{\alpha^2 R_1^2} \right)}{[\alpha R_1 Y_m'(\alpha R_1)]^2} \right]^{-1/2},$$

otherwise

$$S(x) = \left(\frac{2C_0}{D_0 \omega \sigma} \right)^{1/2} \left[\left\{ R_2^2 \left(1 - \frac{m^2 - \zeta_2^2}{\alpha^2 R_2^2} \right) + \frac{D_0 U_0 \zeta_2}{\Omega} \right\} J_m(\alpha R_2)^2 \right]^{-1/2},$$

where $\Omega = \omega - \mu U_0$ and $\zeta_2 = \Omega^2 D_0 R_2 / (i \omega Z_2)$, with Z_2 the outer wall impedance.

References

- [1] Vahdati, M., Sayma, A. I., Br ard, C., and Imregun, M., 2002, "A Computational Study of Intake Duct Effects on Fan Flutter Stability," *AIAA J.*, **40**(3), pp. 408–418.
- [2] Cooper, A. J., and Peake, N., 2000, "Trapped Acoustic Modes in Aeroengine Intakes With Swirling Flow," *J. Fluid Mech.*, **419**, pp. 151–173.
- [3] Hanson, D. B., 1992, "Unsteady Coupled Cascade Theory Applied to the Rotor/Stator Interaction Noise Problem," DGLR/AIAA Paper 92-02-084.
- [4] Rienstra, S. W., 1999, "Sound Transmission in Slowly Varying Circular and Annular Lined Ducts With Flow," *J. Fluid Mech.*, **380**, pp. 279–296.
- [5] Horlock, J. H., 1978, *Actuator Disk Theory. Discontinuities in Thermo-Fluid Dynamics*, McGraw-Hill, New York.
- [6] Joo, W. G., and Hynes, T. P., 1997, "The Simulation of Turbomachinery Blade Rows in Asymmetric Flow Using Actuator Disks," *ASME J. Turbomach.*, **119**, pp. 723–732.
- [7] Joo, W. G. and Hynes, T. P., 1997, "The Application of Actuator Disks to Calculations of the Flow in Turbofan Installations," *ASME J. Turbomach.*, **119**, pp. 733–741.
- [8] Golubev, V. V., and Atassi, H. M., 1998, "Acoustic-Vorticity Waves in Swirling Flows," *J. Sound Vib.*, **209**, pp. 203–222.
- [9] Tam, C. K. W., and Auriault, L., 1998, "The Wave Modes in Ducted Swirling Flows," *J. Fluid Mech.*, **371**, pp. 1–20.
- [10] Rienstra, S. W., and Hirschberg, A., 1999, "An Introduction to Acoustics," Rep. IWDE 99-02, TU Eindhoven.
- [11] Dowling, A. P., and Ffowcs Williams, J. E., 1983, *Sound and Sources of Sound*, Ellis-Horwood, London, p. 93.
- [12] Woodley, B. M., and Peake, N., 1999, "Resonant Acoustic Frequencies of a Tandem Cascade. Part 1. Zero Relative Motion," *J. Fluid Mech.*, **393**, pp. 215–240.